THE SIMULATION OF FIRE GROWTH AND SPREAD WITHIN ENCLOSURES USING AN INTEGRATED CFD FIRE SPREAD MODEL

Fuchen Jia

BSc
(Peking University)

MSc
(Beijing Institute of Technology)

Submitted as partial fulfilment of the requirement
for the Degree of Doctor of Philosophy

FIRE SAFETY ENGINEERING GROUP
CENTER OF NUMERICAL MODELLING AND PROCESS ANALYSIS
SCHOOL OF COMPUTING AND MATHETICAL SCIENCES
UNIVERSITY OF GREENWICH

September 1999

ACKNOWLEDGEMENTS

I am deeply indebted to my supervisors, Professor E. R. Galea and Dr. M. K. Patel, for their great interest, enthusiasm and guidance in carrying out this work. They provided me with many helpful comments and suggestions on the writing of research papers and this thesis. The author would also like to thank them for rectifying the drafts of this thesis and my other research papers.

Experiments were carried out at the Home Office Fire Experimental Unit, Fire Research and Development Group(FRDG). These experiments were aimed to provide experimental data to validate the fire spread model presented in this work. The author would like to thank Mr. J. Foster, Mr. G. Roberts and other staff at the Fire Experimental Unit for setting up the instrumentation and carrying out the tests. I would also like to thank Dr. David Peace, director of FRDG, for approving and funding the experimental program.

I gratefully acknowledge the financial support of the University of Greenwich through its research bursary system. I also wish to thank all my friends and colleagues at the University of Greenwich for their assistance and advice.

Finally, I would like to acknowledge that without the understanding, support and patience of my wife, Jun Ma, this work would not have been realised.

ABSTRACT

The main objective of this thesis is to develop relatively simple but reasonable engineering models within a CFD software framework to simulate fire in a compartment and fire growth and propagation in enclosures in which solid combustibles are involved through wall or ceiling linings. Gas phase combustion, radiation and solid fuel combustion are addressed in this study. At the heart of this study is the integration of the three sub-models representing the key elements mentioned above in compartment fire development and other auxiliary calculations such as the evaluation of the radiative properties of gas-soot mixture, temperature calculation for non-burning solid surfaces, etc. into a complete fire spread model.

Shortcomings in the conventional six-flux radiation model are highlighted. These were demonstrated through a simple artificial test case and corrected in the modified six-flux model. The computational cost and accuracy of the six-flux model and the discrete transfer method (DTM) using different number of rays are also investigated.

A simple empirical soot model is developed based on experimental observations that soot formation occurs in the fuel rich side of the chemical reaction region and the highest soot concentration is found in the same region. The soot model is important to evaluate the radiative properties of the gas-soot mixture in fires.

By incorporating the gas-phase combustion model, the radiation models and the soot model, substantial improvement in the predicted upper layer temperature profiles is achieved in the simulations of one of the Steckler's room fire test. It is found that

radiation plays an important, perhaps dominant role in creating the nearly uniform temperature distribution in the upper layer.

The integral method to calculate temperatures of non-combustible solids is extended to be capable of dealing with the non-linearity of the reradiation at the solid surface(top surface) exposed to a fire and the convective heat loss at the opposite surface. The integral method is economic and simple for the calculation of temperatures of non-combustible solids.

Pyrolysis models for noncharring and charring solid combustibles are developed. The mass loss rates produced by the noncharring model for PMMA are in excellent agreement with experimental data. The charring model produced predictions for the mass loss rates and temperature distribution of a wood sample in very close agreement to that measured.

Finally, qualitative and quantitative verifications for the integrated fire spread model are carried out. The model is demonstrated to be capable of both qualitatively and quantitatively predicting fire, fire growth and development within compartment fire scenarios.

CONTENTS

Chapter 1

INTRODUCTION

1.1 Background

Fire is a process of combustion in which combustible species react intensely with oxygen in air. Combustion reactions liberate the potential energy stored in the chemical bonds holding together the molecules of fuel. Consequently, burning of a typical fuel releases energy. As a result of incomplete combustion, fires also generate soot and toxic gases. In an enclosure scenario, the high temperature of the hot gases, strong radiation emitted primarily from small soot particles, and toxic gases arising from incomplete combustion, all pose a lethal environment to the people remaining in the enclosure.

Unwanted fires not only claim a great toll in terms of property damage, but also endanger people's lives. Throughout the world, 65-75,000 people die in fire annually[Brushlinsky, 1997]. The cost of fires including direct damage, indirect damage, fire service maintenance, fire protection to building and fire insurance is about 1% of each country's gross national product(GNP)[Brushlinsky, 1997]. In 1995 in the United Kingdom, 808 fire deaths were reported in which nearly 600 people were killed in dwelling fires[Home Office Statistics Bulletin, 1997]. In China(the home of the author), in 1994, 2748 people died in fires, while direct property losses were about 1240M Yuan(approximately £100M), accounting for 3.8 per cent of GNP[Wang and Fan, 1997]. Particularly devastating fires include the fire in the Kings Cross underground station(November, 1988) in London which claimed 31 people's

lives. While, in 1977, a fire at the Beverley Hill Supper Club in Kentucky killed 164 people[Canter, 1990]. Furthermore, "80 percent of the people killed by fires are at home or at leisure elsewhere in hotels or other publics places; a full 80 percent of these are killed in their own homes"[Lyons, 1985]. Therefore protection of life and property from enclosure fires has become a major concern.

In real enclosure fires, following the initiation of the fire, three phases of fire development generally occur:

a) growth stage, in which the local fire grows smoothly, the end of this phase is usually followed by flashover which is marked by a sharp increase in fire growth rate;
b) fully developed stage, in which all combustible materials are involved in combustion, this is marked by a period of almost steady burning, and finally;
c) decay stage, in which the fire begins to decline having consumed most of the fuel.

If there is not sufficient oxygen available during the early stage of fire development, the fire may self extinguish. But an extremely devastating event—backdraft may also be possible to occur due to the shortage of oxygen. Although the flaming combustion is restrained due to insufficient supply of oxygen, the pyrolysis of combustible materials may still continue to release combustible gases. A sudden fresh air supply, for instance the opening of a door or breaking of a window by a fire fighter, may create an explosive fire due to the mixing of the extremely vitiated combustible mixture in the room with the fresh air.

Flashover is a hazardous phenomenon since once it takes place the people remaining in the fire compartment are unlikely to survive. The initial phase of fire growth is essential for people to evacuate, and so concerns arise to predict fire growth in its

early stage. In recent years, there has been considerable experimental and theoretical research regarding the growth of compartment fires and fire spread. This has generated considerable experimental data about fires and flammability of combustibles and understanding of fire behaviour. This in turn has lead to the development and use of mathematical models to simulate and predict fire development in buildings. The motivation to utilise fire models is twofold. Firstly, for a specified room fire scenario, due to low cost and ease of use compared with experiments, it is desirable to predict the fire development using mathematical models in terms of measurable material properties, the geometric configuration of the compartment and the physical state of the environment. Secondly and perhaps more importantly, "from a life-safety and operational standpoint, the ability to make accurate predictions of the spread of fire, smoke, and toxic gases opens up many possibilities for combating these problems, as well as for taking effective preventive measures. The ability to prevent the hazards from developing becomes especially important as new and exotic materials become available"[Jones, 1984].

There are essentially two types of fire models. One kind of fire modelling is called zone modelling. This approach divides the fire compartment into several distinct zones deemed relatively uniform in temperature and composition. Generally two zones are used: "upper layer zone" for hot upper layer beneath the ceiling and the fire plume and "lower layer zone" for the remaining part of the compartment. In each zone variables are assumed to be uniform but can vary with time. Conservation equations for mass and energy in each zone are derived in the form of ordinary differential equations and solved numerically. Advanced zone models include the effects of the fire plume, radiation, convective energy losses through walls, ceiling and the floor and

the fire spread over solid fuel surfaces[Karlsson, 1992; Quintiere et al., 1995]. However, the shortcomings of zone models stand out as the problems grow more complex. First of all, it is not easy to determine the number and locations of zones representing the fire situation since they are not always obvious. Secondly, zone models include empirical relationships and constants derived from experiments. They may not be valid in certain applications as configurations change and become more complex. Thirdly, the underling assumption that the uniform fire characteristics such as air temperature, density and smoke concentration are held in each zone may break down in complicated fire scenarios[Galea, 1989].

As relatively inexpensive powerful computers emerge, the mathematical modelling based on computational fluid dynamics (CFD) becomes an alternative attractive approach to investigate the behaviour of the enclosure fire growth. This kind of modelling technique is often called "field modelling". Compared with zone models, it appears the more versatile and involves a minimum of empiricism and builds the empiricism on a more fundamental level. The fluid flow is described by a set of three-dimensional, partial differential equations that govern fluid flow. This set consists, in general, of the following equations: the continuity equation, the three momentum equations that govern the conservation of momentum per unit mass in each of the three space dimensions, the equation for conservation of energy, the equations for a turbulence model and other equations for scalar variables such as species concentration, soot concentration and so on. A general purpose CFD package numerically solves these governing equations at discrete moments in time and points in space. Field models can provide quantitative differences in physical variables throughout the computational grid. Fire field models have been used to investigate the development of hazardous conditions

within fire enclosures such as high rise building[Galea et al., 1996], underground[Simcox et al., 1988], aircraft cabin[Galea and Markatos, 1991], road tunnel[Kumar and Cox, 1985] and fire-sprinkler interactions[Hoffman et al., 1988]. A description of other fire field model applications can be found in Stroup[1995].

Simulation results produced by fire field models have the potential of providing more detailed information than what can easily be gathered from real fire tests. The numerical simulations may be repeated several times with the same geometric configuration but different environmental conditions. This will help establish the conditions leading to flashover or backdraft and hence take effective preventive measures accordingly. However, fire field modelling is still in its preliminary stage of development. The potentials of this technique have not been fully exploited. The fire simulation problems represent one of the most difficult areas in CFD: the numerical solution of recirculating, three-dimensional turbulent buoyant fluid flow with heat and mass transfer. Combustion is often ignored in engineering applications and the fire is treated as a simple prescribed source of heat and smoke. Generally, when combustion is included, it is approximated using relatively simple one-step reaction mechanisms for gaseous or liquid fuels such as methane. While these combustion models increase the complexity of the simulation, they still ignore or greatly simplify many important combustion aspects. One of the major simplifications is the use of fluid rather than solid fuels. In these cases, in addition to the simplifications associated with turbulence, chemical mechanisms, reaction rate, soot formation and thermal radiation, the charring and pyrolysis processes, as well as the flame spread over solid surfaces are ignored.

1.2 The Aims of My PhD Study

This study is motivated by the desire to construct a potentially useful tool to quantitatively predict the fire growth and propagation in enclosures. Reasonably accurate predictions to fire spread process in room fires are helpful to understand the fire behaviour and its interactions to the environmental conditions. More importantly, however, as the protection of life in home is a central concern, fire prevention technology must address the earliest stages of the ignition and growth of the unwanted fire.

Fire and fire spread are extremely complex processes involving chemical and physical changes of combustible materials and surrounding conditions, simplifications must be made when simulating the development of fire in enclosures. A fundamental question arises when it is expected to develop an integrated model incorporating major essential aspects of fire spread such as gaseous combustion, soot formation and thermal radiation and solid phase processes:

- Is it possible to arrive at reasonably accurate predictions of fire behaviour in a compartment from using relatively simple models representing these aspects mentioned above?
- Furthermore, will it be possible to use these models to predict the onset of flashover and backdraft conditions?

This question is associated with the confidence in use of this advanced modelling technique. To answer it systematic validation should be done by comparing model predictions with experimental results and theoretical analyses. If the answer is yes, the practical problems are:

- Is it affordable to integrate the primary essential elements of fire spread into the simulations of fire spread processes if only limited computing power is available which is not uncommon in the applications of engineering purpose?
- Is it possible to reduce the cost by introducing relatively simple sub-models to simulate fire development for engineering application purposes?
- What kind of data are required as an input of the integrated model? It is important for engineering applications that the input data required in the integrated model are measurable and can be obtained from bench or small-scale experiments or can be found from the literature.

An essential phenomenon in enclosure fires, in particular domestic fires, is that most of fuel is in condensed phase such as wood tables, chairs, lining materials etc.. Fire spread over lining materials will reduce the time to flashover especially when vertical upward fire progress is involved. And standard full-scale tests of fire spread over lining materials have been designed to evaluate the flammability of building materials. When solid fuels are burning, interactions between the gas-phase and solid-phase processes become important. An elemental problem is:

- How to express these interactions in some relatively simple way so that reasonable predictions of fire development can be obtained from the integrated fire spread model?

Many materials char when burnt. The mass loss processes of charring materials involve many very complicated physical and chemical material interactions and the associated mathematical description of these changes may be extremely complex. Reasonable approximations are demanded to form a relatively simple mathematical representation of

the complex mass loss processes. This relatively simple formulation is also required if a potentially versatile integrated fire spread model applicable to various engineering purposes is to be developed.

Due to the very high temperature (usually above 1000K) at the char surface, the boundary condition at the surface becomes highly non-linear due to the surface reradiation. Numerically, this high non-linearity needs to be dealt with carefully if reasonably accurate, yet flexible and efficient predictions of mass loss rates are to be made.

Radiation is the dominant mode of heat transfer in a large-scale enclosure fire. Radiation models should be included in the integrated fire spread model to improve the prediction accuracy. However, radiation calculations are tedious and time consuming. Since better accuracy requires more calculations in general, a balance between the accuracy and the expense must be taken into consideration to select an appropriate radiation model.

Nowadays, field models have few limitations in terms of geometrical configuration that can be considered. Accordingly the component models used in the integrated model and the associated input data required are expected to fit this high level of flexibility to increase the possibility to numerous engineering applications.

Efforts have been made in this thesis to develop simple but reasonable engineering models within a CFD software framework to simulate gas fires in a compartment and fire growth and propagation in enclosures in which solid combustibles are lined on walls or ceiling. Attention has been focused on all the problems and issues presented above.

1.3 Layout of the Thesis

An overview of the key aspects of fire behaviour together with a summary of the relevant experimental data is provided in chapter 2. In addition, a review of the field modelling approach to fire simulation is also provided in chapter 2.

A simple heat source fire field model of the type commonly used in engineering applications is developed and through comparison with experimental data its shortcomings are analysed in chapter 3. This model forms a basis of comparison for the more complex models developed in later chapters.

In chapter 4, a simple gas phase combustion model is developed and its capabilities are demonstrated through comparison with one such similar model.

Chapter 5 is devoted to the soot formation process and the thermal radiation. The soot formation process is briefly described and a simple soot model is developed. The calculations of the radiative energy exchanges are then presented.

In chapter 6, the models, the gaseous combustion model, the radiation models and the soot formation models, described in the preceding chapters are incorporated into an integrated model to simulate the experimental test used in chapters 3. These simulations serve as part of validation for the final integrated fire spread model that is presented in chapter 8.

In chapter 7, a pyrolysis model for non-charring material is developed and compared

with experimental data, The model is then extended to include the effects of char that is also compared with experimental data.

An integrated model for the simulation of fire development within enclosures is finally developed and presented in chapter 8. This model contains all the work performed in the previous chapters and is a result of the efforts trying to resolve all the questions raised in the last section. To partially verify the model, the model is used to simulate two real fire tests involving the burning of the non-charring and charring combustible solids.

Finally, a summary of the achievements of work reported in this thesis is presented in chapter 9.

Chapter 2

COMPARTMENT FIRES AND MODELLING

2.1 Compartment Fires

A compartment fire refers to a fire that starts, grows and develops within a room or similar scenario within a building. The fire that eventually burns down a house or a large building first starts as a localised fire. The localised fire is small at its initial stage and grows smoothly. Depending on availability of sufficient oxygen the fire may develop into two different patterns after incipience. A schematic description of fire development is depicted in figure (2.1.1). If sufficient fresh air is supplied through ventilation, the fire growth will continue. When the fire is large enough, radiation becomes the dominant mode of heat transfer. Radiation from the fire, the hot upper layer and the hot solid surfaces will preheat remote combustible objects that may eventually become involved in the fire. Thus the fire will increase rapidly.

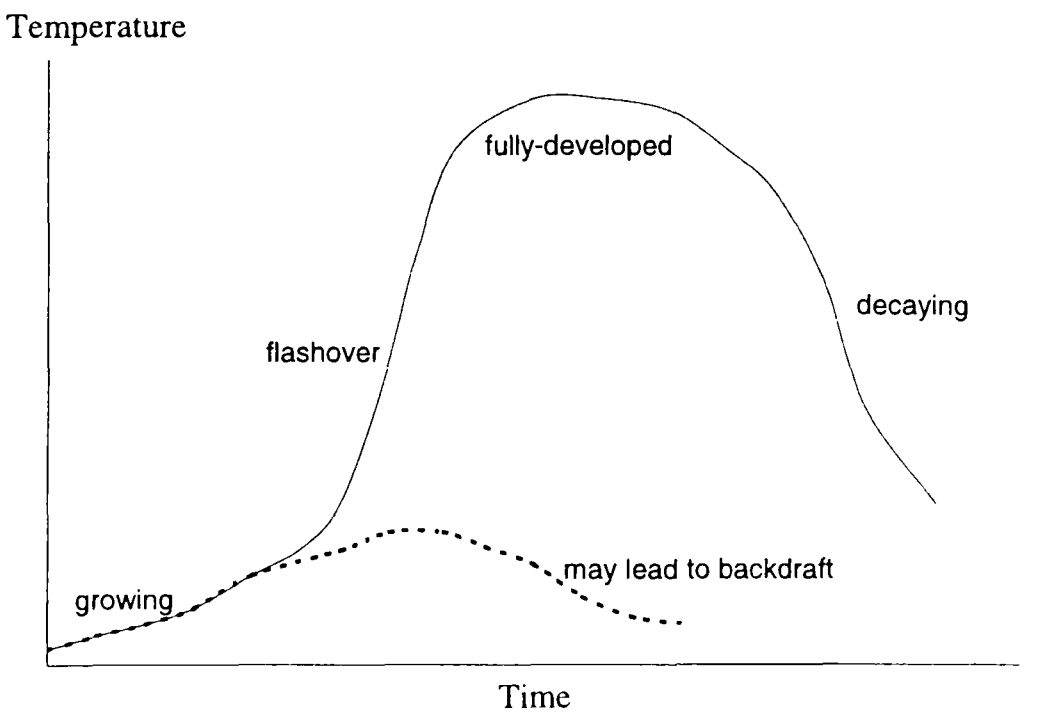

Fig. 2.1.1: Schematic of the course of the fire development within enclosures.

At the end of the growth stage, a sharp increase in fire growth rate takes place. In a very short space of time, all combustible surfaces and objects erupt into flames. This phenomenon is called flashover. Time to flashover is critical for life since after flashover occurs people remaining in the fire compartment are unlikely to escape. At onset of flashover, the temperature of the upper hot layer typically approaches over 500 °C[Hägglund et. al., 1974] and the heat flux at the floor may reach a level of 20kW/m^2[Waterman, 1968], thus making the atmosphere lethal.

Another type of flashover may occur within the combustible gases themselves. Unburnt combustible gases may form a deepening hot upper layer beneath the ceiling. The concentration of unburnt pyrolysed fuel within the layer increases with time. A critical point will be reached when the combination of the concentration of these gases and their temperature is such that they themselves rapidly combust creating a flashover which engulfs the entire compartment.

After flashover, the fire is in a fully developed stage. All combustible objects are involved in burning. The fire is usually ventilation controlled since much more pyrolysis products are released than can be consumed by the fire. The unburned gasified volatiles flow out the fire room through openings and may burn outside the compartment. Eventually the combustibles are consumed one by one and the fire dies away.

If there is insufficient oxygen to allow flaming combustion to continue, or flashover to occur, the fire will be throttled back and vitiated burning may develop. This is extremely hazardous, for while flaming combustion may be greatly reduced, pyrolysis

of the fuel may continue to produce combustible gases within the hot compartment. A sudden in rush of fresh air created by for example, the opening of a door or breaking of a window by a fire fighter, may cause the room to erupt into flame with large flames emerging from the opening posing a significant threat to firefighters. This phenomenon is known as backdraft.

As protection of life from fires is the central concern of the fire safety and protection engineering, fire prevention technology must address the earliest stage of growth of the unwanted fires. In recent years, considerable research has been performed regarding the spread of fires within compartments. Bench, small-scale and full-scale fire experiments have been conducted to understand and establish the conditions at which a fire develops and spreads.

Flashover is the short transition from a growing fire to a fully developed fire. During this short period, all solid combustible surfaces erupt into flame and the fuel controlled fire becomes a ventilation controlled fire. Since the unburnt combustible volatiles flow out of the fire compartment with the hot gas mixture, it is very often observed that there is an intense fire protruding from the fire compartment after flashover. It is generally accepted that flashover occurs when the gas temperature beneath the ceiling is above approximately 500 ^{o}C. Based on experimental results, Waterman[1968] concluded that at the onset of flashover the heat flux at the floor may reach around 20kW/m. Experiments[Waterman, 1968; Hagglund et al., 1974] suggest that there is a critical burning rate which must be exceeded for a flashover occurrence. Another important condition for the occurrence of flashover concerns the heat release rate from the fire. Several correlation have been derived to estimate the

heat release rate required for flashover, the most common of which are:

1) Babrauskas[1980]

$$Q = 750 A_o \sqrt{H_o}\ , \tag{2.1.1}$$

where A_o is the area of the door opening and H_o is the height of the door.

2) McCaffrey et al.[1981]

$$Q = 610 (h_k A_w A_o \sqrt{H_o}\ )^{1/2}, \tag{2.1.2}$$

where h_k is an effective heat transfer coefficient and A_w is an effective surface area.

3) Thomas[1981]

$$Q = 0.78 A_T + 378 A_o \sqrt{H_o} \tag{2.1.3}$$

where A_T is the total internal surface area.

These correlation are derived from the concept of the two-layer zone model. The coefficients appearing in the correlation are based on data from a limited number of experiments. For Babrauskas's correlation(equation (2.1.1)), the ventilation factor ($A_o \sqrt{H_o}$) ranged from 0.03 to 7.51 $m^{5/2}$ and the surface area to ventilation factor ratios ($A_T/A_o \sqrt{H_o}$) ranged from 9 to 65 $m^{-1/2}$. The derivation of McCaffrey's correlation(equation (2.1.2)) did not take the heat loss through radiation into account and the experiments used to obtain data did not contain combustible lining material on walls and ceiling. The fires in those experiments were generally located near the centre of the room.

Although the backdraft phenomenon has not been as widely investigated as flashover,

some characteristics have been obtained from experiments[Fleischmann et al., 1994; Gottuk et al., 1997]. Gottuk et al.'s study showed that the fuel mass fraction is the key factor for backdraft development. Gottuk et al. conducted a series of full-scale backdraft experiments using diesel as fuel. They concluded that the critical fuel mass fraction for backdraft is 0.16 for fully vitiated conditions. This conclusion may be expected to extend to other hydrocarbon fuels due to the same lower flammability limit on a mass basis[Gottuk et al., 1997]. A series of small scale backdraft experiments were carried out by Fleischmann et al.[1994]. The tests were carried out in a half scale residential room that was 1.2m high, 1.2m wide and 2.4m long. The window or door was simulated by a 0.4m high and 1.1m wide opening hatch centred in the short wall opposite the burner. A methane burner was placed against the wall opposite the opening. In each experiment the fuel flow to the burner was left on for a predetermined time period. 5 seconds after the gas flow was terminated the hatch was opened. A spark to re-ignite the fuel was either left on the entire time or not turned on until the hatch was opened. In the experiments, it was observed that the vertical temperature distribution is nearly uniform after the sealed compartment is fully vitiated. Before the hatch was opened, the gaseous fuel concentration increased steadily and the O_2 and CO_2 levelled off. A gravity current immediately moves into the room after opening the hatch. After re-ignition, a flame travels through the mixed layer driving the combustible gases out of the room. The re-ignited flame burns along the front and the top of the entrained air. It takes about 2 to 3 seconds to observe a large fireball exiting the compartment. During this short period of the backdraft explosion, there are intense pressure pulses generated. When flames exit the compartment the pressure reaches its first peak value. Then the second significant rise of the pressure takes place as the large fireball erupts outside the compartment. The

pressure then drops rapidly due to a repercussion of the fireball. After the backdraft explosion, the fuel mass fraction dramatically drops to a very low level.[Fleischmann et al., 1994]

Sufficient data and insight into the fire evolution within compartments obtained from bench, small-scale and full-scale experiments have made it possible to numerically simulate fires in compartments. The simulation results produced by a model may provide us more detailed information than could have been learnt from a real fire test. As more powerful computers emerge, the mathematical modelling based on computational fluid dynamics (CFD) becomes an alternative attractive approach to investigating the behaviour of the enclosure fire growth because of its ease of use and low cost compared to fire trials. For a specified room fire scenario, it is desirable to be able to predict the fire development in terms of measurable material properties, the geometric configuration of the compartment and the physical state of the environment. However, this is not to say that models are capable of replacing experimentation entirely. Experimentation is still vital for validation purpose and for the collection of fundamental data to be used in these models. Computer models can be used to better target the scenarios that need experimental investigations.

2.2 CFD Fire Modelling for Enclosure Fires

Simulation of fire growth and spread within enclosures is a very difficult task. Not only are the gas-phase and solid-phase combustion processes complex in their own right, but in addition we must also contend with the interaction between turbulence, gas-phase combustion, radiation and solid phase behaviours. Over the past 15 years

considerable effort has been expended in developing fire field models capable of predicting the development of hazardous conditions within fire enclosures [Galea, 1989; Galea and Markatos, 1991; Markatos and Cox 1984; Simcox et al., 1988; Yeoh et. al., 1995]. At the heart of these fire field models is the Computational Fluid Dynamics (CFD) code and a large proportion of these models are based on commercial CFD software such as PHOENICS [Spalding, 1981] and CFX [Burns and Wilkes, 1987]. The former is, for example, the core of the JASMINE [Markatos et al., 1982] code and an aircraft cabin fire model [Galea and Markatos, 1991] while the latter has been used, for example, in the Kings Cross Underground fire [Simcox et al., 1992] investigation, as well as aircraft [Galea et al., 1993] and high rise building fire scenarios [Galea et al., 1996].

The CFD based fire field model is essentially made up of two components, i.e., transport and combustion. The transport phenomena are core to the fire field model and consider the manner in which mass, momentum and energy is transported and conserved throughout the flow domain. The convection (and conduction) component is generally provided by the CFD code to which is added a radiation model.

The majority of practical fire modelling applications has been concerned with the spread of heat and smoke in complex structures and so combustion has either been ignored or greatly simplified. In cases where combustion is ignored the fire is treated as a simple prescribed source of heat and smoke. While this approximation may appear crude it can produce good agreement with experimentally derived temperature measurements [Kerrison et al., 1994a,b] for room fire scenarios. Generally, when combustion is included, it is approximated using relatively simple one-step reaction

mechanisms [Kumar et al., 1991; Yeoh et al., 1995] for liquid or gaseous fuels such as methane. While these simple combustion models increase the complexity of the simulation, they still ignore or greatly simplify many important combustion aspects. One of the major simplifications is the use of fluid rather than solid fuels. In these cases, in addition to the simplifications associated with turbulence, chemical mechanisms, reaction rate, soot formation and thermal radiation, the charring and pyrolysis processes, as well as flame spread over solid surfaces are ignored. Some recent work has attempted to predict fire spread in enclosures through the use of field models incorporating the primary elements affecting fire spread within compartments such as turbulence, gas-phase combustion, radiative energy exchanges, solid fuel combustion and so on [Luo and Beck, 1996; Opstad, 1995; Yan and Holmstedt, 1996; Jia et al., 1997, 1999a, 1999b].

The motivation to develop such fire spread models that are capable of producing reasonably accurate predictions to fire growth and development within enclusours is twofold. For a specified room fire scenario, it is desirable to predict the fire development in terms of measurable material properties, the geometric configuration of the compartment and the physical state of the environment. Reasonably accurate predictions to fire spread process in room fires are helpful to understand the fire behaviour and its interactions to the environmental conditions. Perhaps more importantly, from a life-safety and operational standpoint, as the protection of life in home is a central concern, fire prevention technology must address the earliest stages of the ignition and growth of the unwanted fire. "The ability to make accurate predictions of the spread of fire, smoke, and toxic gases opens up many possibilities for combating these problems, as well as for taking effective preventive

measures"[Jones, 1984].

In the work of Luo and Beck[1996], a very simple empirical flame spread model on polyurethane surfaces was used. The radiative energy exchanges were described by the discrete transfer method and radiative properties of the gas-soot mixture were calculated by considering the local concentrations of CO_2, H_2O and soot. The sooting processes were modelled using the soot formation model proposed by Magnussen et al.[1977]. This compartment fire spread model was used to simulate the full-scale multi-room fire spread experiments conducted by the authors. In these tests foam mattresses were used as fuel. Reasonable predictions of the trends for the experiments were obtained.

Attempts to model fire spread within enclosures have been reported by Opstad[1995]. His idea was to apply small-scale measurements into CFD-modelling. Cone Calorimeter test data were used to derive the thermal properties of building products and burning of lining materials was modelled by direct use of heat release measurements obtained from the tests. The ignition temperature concept was employed to determine the ignition of solid fuels. The ignition temperature was supposed to be a function of exposure as a way of correction of fixed thermal properties and simplification of deriving thermal properties from the heat conduction equation. In this treatment the obvious assumption is that the behaviour of burning building materials in a large room fire is the same as that in the bench scale tests. However, in reality the reaction of combustible materials in a large-scale fire to the exposure may be significantly different from that in a small-scale fire. And the behaviour of combustible solids also depends on the exposure time, in particular when the heat wave in the solid hits the back face. Therefore it is very important to select

proper heat release data as input to produce reasonable predictions.

Recognising the disadvantages of the method above, Yan and Holmstedt[1996] used a pyrolysis model to simulate the mass loss processes of the combustible solid. The ablation approach was adopted. The material properties, called the optimised equivalent properties, were derived from the Cone Calorimeter test results. By using these properties, it was expected that the pyrolysis model could be applicable to realistic composite materials. However, it was not clear how they dealt with the interactions between the gas phase combustion and the solid phase response. Furthermore, it was not clear how the highly non-linearity of the solid surface reradiation was treated.

The recently developed CFD software SOFIE[Rubini, 1996] was utilised by Lewis et. al.[1997] to simulate a real compartment fire experiment[Steckler et. al., 1982] using methane. The simulations included systematic variations of model elements such as with/without radiation, use of different models to represent the burner and different mesh densities. The most distinguished feature of the work is the demonstration of the flamelet gas phase combustion model that "offers the additional prospect of incorporating more detailed chemistry such as in relation to the generation of CO into the room fire prediction"[Lewis et. al., 1997]. However, application of the flamelet approach to the more complex process of fire spread over solid fuel surfaces still remains questionable.

2.3 The Governing Equations of Turbulent Diffusion Flames

Fires within enclosures involve turbulent diffusion flames. The fluid flows of turbulent diffusion flames contain aspects of fluid dynamics, transport processes, thermodynamics and chemistry. The central equations governing the phenomena of interest here consist of the Navier-Stokes equations and supplementary consevation equations for species concentrations. They are a set of three dimensional, time-dependent, non-linear partial differential equations, representing conservation of mass, momentum, energy and chemical species. Due to the random fluctuations in the turbulent flow pattern, statistical rather than instantaneous treatment is used to develop these conservation equations. This is achieved by averaging the fluctuations of both flow and thermochemical properties.

The mean value $\bar{\phi}$ of a variable ϕ can be defined as

$$\bar{\phi} = 1/\Delta t \int_{t-1/2\Delta t}^{t+1/2\Delta t} \phi \, dt \qquad (2.2.1)$$

where Δt is the time interval which is large compared with the time scale of the turbulent fluctuations while is small relative to the time scale of macroscopic change of the variable. This is referred to as ensemble averaging.

The time dependent variables are split into mean and fluctuating parts. For compressible flows the Favre average is density-weighted averaging, defined by

$$\tilde{\phi} = \overline{\rho\phi} / \bar{\rho} \qquad (2.2.2)$$

$$\phi = \tilde{\phi} + \phi'' \qquad (2.2.3)$$

with $\overline{\rho\phi''} = 0$, where ϕ'' is the fluctuating part and the superposed bar indicates the

mean value. For simplicity, in the following discussion the tilde over any single variable is omitted and the superposed bars over the tensor product and the product of a variable and a vector indicate Favre averages.

With Favre averaging, the equations of continuity, momentum equation and scalar are given by

$$\partial\rho/\partial t + \nabla(\rho\,\vec{u}\,) = 0 \tag{2.2.4}$$

$$\partial\,(\rho\,\vec{u}\,)/\partial t + \nabla(\rho\,\vec{u}\otimes\vec{u}\,) = \vec{b} + \nabla(\sigma - \rho\,\overline{\vec{u}\otimes\vec{u}}\,) \tag{2.2.5}$$

$$\partial\,(\rho\phi)/\partial t + \nabla(\rho\,\vec{u}\,\phi) = \nabla(\Gamma\nabla\phi - \rho\,\overline{\vec{u}\phi}\,) + S_\phi \tag{2.2.6}$$

where $\vec{b}$ is the body force vector, Γ is the diffusion coefficient, S_ϕ is the source term and σ is the stress tensor.

The two unkonwn terms $\rho\,\overline{\vec{u}\otimes\vec{u}}$ and $\rho\,\overline{\vec{u}\phi}$ are respectively called the Reynolds stress and the Reynolds flux. They need modelling to close the governing equations. The k-ε turbulence model is one of the most widely used turbulence models. Based on the eddy viscosity hypothesis, two additional variables k, the turbulent kinetic energy, and ε, the dissipation rate, are introduced to model directly the Reynolds stress and Reynolds flux. The transport equations for k and ε [AEA Technology, 1991] are

$$\partial(\rho\varepsilon)/\partial t + \nabla(\rho\,\vec{u}\,\varepsilon) - \nabla((\mu+\mu_T/\sigma_\varepsilon)\nabla\varepsilon) = C_1\varepsilon/k(P+C_3\max(G,0)) - C_2\rho\varepsilon^2/k \tag{2.2.7}$$

and

$$\partial(\rho k)/\partial t + \nabla(\rho\,\vec{u}\,k) - \nabla((\mu+\mu_T/\sigma_k)\nabla k) = P+G-\rho\varepsilon \tag{2.2.8}$$

respectively, where P is the shear production defined by

$$P = \mu'\nabla\vec{u}\,(\nabla\vec{u} + (\nabla\vec{u}\,)^T) - \frac{2}{3}\nabla\vec{u}\,(\mu'\nabla\vec{u} + \rho k) \tag{2.2.9}$$

and G is the buoyant production defined by

$$G = -\mu'/\rho\, \vec{g}\, \nabla\rho \tag{2.2.10}$$

which, with the Boussinesq buoyancy approximation, can be written as

$$G = -\mu'\beta\, \vec{g}\, \nabla T \tag{2.2.11}$$

where $\vec{g}$ is the gravity vector.

Using the k-ε turbulence model, the governing equations can be rewritten as

$$\partial\rho/\partial t + \nabla(\rho\, \vec{u}\,) = 0 \tag{2.2.12}$$

$$\partial\,(\rho\, \vec{u}\,)/\partial t + \nabla(\rho\, \vec{u} \otimes \vec{u}\,) = \vec{b} - \nabla p' + \nabla(\mu'(\nabla\, \vec{u} + (\nabla\, \vec{u}\,)^{T})) \tag{2.2.13}$$

$$\partial\,(\rho\phi)/\partial t + \nabla(\rho\, \vec{u}\, \phi - \Gamma'\nabla\phi) = S_{\phi} \tag{2.2.14}$$

where $\mu' = \mu + \mu_T$, $\Gamma' = \Gamma + \Gamma_T$ with $\mu_T = C_{\mu}\rho k^2/\varepsilon$ and $\Gamma_T = \mu_T/\sigma_T$ where σ_T is the turbulent Prandtl number.

The governing equations for all fluid variables can be expressed in the general form:

$$\frac{\partial\rho\phi}{\partial t} + \mathrm{div}(\rho\vec{u}\phi) = \mathrm{div}(\Gamma_{\phi}\, \nabla\phi) + S_{\phi} \tag{2.2.15}$$

where S_{ϕ} is the source term and ϕ stands for any one of the following variables: the velocities u, v, w in three co-ordinate directions, the enthalpy h, the turbulent kinetic energy k, its dissipation rate ε, the mixture fraction ξ, the mass fraction of fuel m_f, the soot concentration and so on. For the continuity equation ϕ takes the value of one. The four terms in the general form of governing equations represent accumulation, convection, diffusion and source respectively.

Since fire is a gas phase phenomenon involving the production and destruction of chemical species and small particles, heat release and radiative heat transfer, it is

necessary to represent all these processes in the governing equations. They may be incorporated as a part of the source term of the appropriate individual governing equation. The flow can only be determined from the governing equations with models describing these complex processes.

In a fire system, heat is released during the processes of chemical reactions. It should be represented as a part of the source term in the equation of energy conservation. In cases where combusiton is ignored the fire is treated as a simple prescribed source of heat release. When combustion is included, gas-phase combustion models will provide the mathematical expressions of the rate of the heat release. Chapter 4 will present a brief review of combustion models aimed at identifying a represnetative gas-phase combustion model for the simulation of fire growth and spread within enclosures.

Radiative heat transfer is the dominant mode of heat transfer in most fire systems. It creates source and sink terms in the energy equation. Radiation models should be included in numerical simulations for these fire systems to calculate the source and sink terms in the energy equation due to the contributons from radiation. In Chapter 5, two radiation models commonly used in fire simulations are briefly described and the method used to incorporate the model into the CFD based fire model is outlined.

The chemical species and particles such as soot may be created and destroyed in the chemical reactions associated with combustion. These phenomena are described by source terms in the corresponding conservation equation for each individual species or particle. To complete the closure of the governing equations, models for the

creation and destruction of these species and particles are needed. These models may be gas-phase models or soot formation models. Some sooting models are presented in Chapter 5.

Flame spread over solid fuel surfaces is controlled by two central mechnisms—heat tranfer to the solid fuel and the gas-phase combustion[Fernandez-Pello and Hirano, 1983]. It is a result of complex interactions between the gas-phase behaviour and the solid-phase behaviour. The solid-phase behaviour can be modelled by solid-phase models which may describe the heat conduction in the solid fuel and mass loss processes involving complex physical and chemical changes and transport processes in the condensed phase, while the gas-phase behaviour may be represented by the governing equations. Furthermore, the solid-phase processes and the gas-phase processes may be coupled together by the boundary conditions at the interface of the gas phase and solid phase. These boundary conditions embody the interactions between the two phases. A detailed description of the boundary conditions at the gas/solid surface will be mathematically expressed in Chapter 7 and 8.

The CFD code used in this study, i.e. CFDS-FLOW3D(an early version of the CFX code) did not include gas-phase combustion models, radiation models and solid fuel pyrolysis models. The main objective of this research was to develop and test these models and corresponding computer codes within the framework of the selected CFD software. The models developed in the present studies and their integration within the CFD software are expected to be able to quantitatively predict the fire growth and propagation within enclosures for engineering applications.

2.4 The Numerical Solutions to the Governing Equations

The governing equations for turbulent reacting flows described in the preceding section consist of a set of three dimensional, time dependent, non-linear partial differential equations. In general their exact solutions can not be obtained by analytical methods. Consequently, the numerical techniques called Computational Fluid Dynamics(CFD) have been developed to solve them numerically and approximately.

The basic principle of CFD is to replace the continuous differential governing equations with simple discretised algebraic equations that can be solved with relative ease. The first step is to partition the calculation domain into a number of small volumes or cells. This partition also creates a number of grid points associated with the small cells. The discretised algebraic equations derived from the governing differential equations represent the relations of the values of the dependent variables at a group of grid points. Thus the solutions of these algebraic equations are expected to come close to the exact solutions of the governing equations with increase in the number of the small volumes or the grid points.

A general purpose CFD software is a suite of programs for the simulation of complex processes involving fluid flow, heat transfer and chemical reactions. It provides numerical codes to solve these discretised algebraic equations in each cell to obtain the various parameters of interest such as temperature, pressure, flow velocities, species concentrations, etc.

The CFDS-FLOW3D software Version 2.3.3 [Burns and Wilkes, 1987] (Note: later

version of this software is called CFX) was selected as a numerical tool for these studies. This is a general purpose CFD package. Compressibility is assumed and the perfect gas law is used to describe the equation of state. In this software, all solid surfaces are modelled with non-slip conditions for the velocities. The usual 'wall functions' [AEA Technology, 1991] are used to compute shear stresses at solid surfaces.

Since the differential governing equations and hence the derived discretised algebraic equations are, in general, non-linear and coupled, it is not practical to solve them simultaneously. Actually a sequential rather than simultaneous procedure is adopted for calculating fluid flow. This numerical procedure is called outer iteration, in contrast to the so-called inner iteration in which the algebraic equations for one dependent variable at a time are solved. In the outer iteration, the equation for each variable is solved in sequence. A set of nominally linear algebraic equations for the particular variable at the nodes of the mesh is obtained by substituting the current values of the other variables into the corresponding discretised equation. The linear algebraic equation at a control volume is mathematically expressed as[AEA Technology, 1991]

$$\sum_m A_m(\phi_p - \phi_m) = S_u + S_p\phi_p \qquad (2.4.1)$$

where the summation is over the neighbouring cells of the control volume p. In equation (2.4.1), A_m is commonly known as the coefficients and the source term is linearized. An updated solution for this particular variable is generated by iteratively solving the linear equations by using a particular linear equation solver that is designated to the equations by the CFD software or by the user. For example, the CFDS-FLOW3D code has the following linear equation solver: LINE SOVLVER,

ICCG(preconditioned conjugate gradients), STONE(full field stone's method) and so on[AEA Technology, 1991]. In principle, the inner iteration for each variable is not completely converged since the calculation for the flow is at an intermediate stage and hence excessive amount of work for each variable at this stage is a waste of time and effort. In the next outer iteration, the tentative coefficients, A_m, in the algebraic equations will be refined using the updated values of the variables. This process will carry on until a stopping criterion for the outer iteration is satisfied or the maximum number of iteration is performed.

In this way, it appears that the approximate solutions of one particular variable can be obtained without major difficulties provided the flow field is known. However, the central obstruction blocking the obtainment of the flow field is the unknown pressure field. The source terms for the momentum equations contain the pressure gradient and no equation is particularly specified to obtain the pressure field. But the pressure field is indirectly governed by the continuity equation. The velocity field generated from the momentum equations by using appropriate pressure field values must satisfy the continuity equation. Thus, a mechanism of iterative pressure correction and velocity correction is established aimed at reducing the mass residual source term of the continuity equation to zero. The best known method implementing this mechanism is called the SIMPLE algorithm. Its detailed description can be found in [Patankar, 1980].

In CFDS-FLOW3D(Version 2.3.3), the sequence of the equations solved in the outer iteration is listed below in terms of the variables:

1) u—the velocity component in the x co-ordinate;

2) v—the velocity component in the y co-ordinate;

3) w—the velocity component in the z co-ordinate;

4) p—the pressure. The pressure field is obtained using the pressure correction algorithm. Two options, SIMPLE and SIMPLEC[AEA Technology, 1991], of the algorithm are provided by the software;

5) k—the turbulence kinetic energy(if the flow is turbulent);

6) ε—the turbulence dissipation rate(if the flow is turbulent);

7) T—the temperature;

8) H—the enthalpy;

9) ,..., n) s_n—extra scalars.

Of course, the technique is of no value if a converged solution cannot be reached. In the CFDS-FLOW3D software (Version 2.3.3) the standard convergence criterion for the outer iteration is based on the mass source residual reducing to a tolerance specified by the user. If the outer iteration is not stopped by the measure, then a maximum number of iteration set by the user will be performed.

Under-relaxation is a technique to enhance the possibility of generating convergent solutions at the end of the outer iteration. Under-relaxation slows down the changes of the variables and coefficients. Thus, instability due to nonlinearity and interlinkage of the governing equations may be surmounted. Linear under-relaxation may be implemented by letting the updated values of one dependent variable being between the previous values and the values newly obtained from the inner iteration for the corresponding dependent variable. The linear under-relaxation is in a range of 0 to 1. In addition, linear under-relaxation can also be applied to other quantities and

coefficients such as density, diffusion coefficient, source terms and even boundary conditions.

When the source term S_ϕ in equation (2.2.15) depends on the corresponding variable ϕ, S_ϕ should be linearised in terms of ϕ since the discretised equation for ϕ solved in the inner iteration is required to be linear algebraic and diagonally dominant. This is done also because in many applications it is too crude to treat the source term as a constant. In this way, S_ϕ can be expressed as

$$S_\phi \approx S_c + S_p\phi. \tag{2.4.2}$$

The basic rule for this expression is that S_p must be negative. Negative S_p may help yield a strongly diagonally dominant matrix[Patankar, 1980], and hence, is conducive to obtain more accurate and stable solutions from the nominally linear algebraic equation for ϕ.

The wall shear stress and convective heat transfer at the wall are calculated using the so-called wall functions[AEA Technology, 1991]. This is because there is a thin laminar sub-layer close to the wall in which "turbulent motion must be damped down by the action of viscosity and the shear stress must ultimately be transmitted to the wall in the same manner as in a laminar boundary layer"[Kay and Nedderman, 1985]. Consequently, the governing equations for the turbulent main flow do not accurately represent the flow motion in the region near the wall. The description below for the wall functions follows the treatment in the user manual of The CFDS-FLOW3D software Version 2.3.3[AEA Technology, 1991]. Let τ denote the wall shear stress. By introducing a new quantity τ_k defined as

$$\tau_k = \rho C_\mu^{1/2} k\,, \tag{2.4.3}$$

the dimensionless velocity and the dimensionless distance from the wall are defined as

$$u^+ = (\rho\tau_k)^{1/2} u/\tau \tag{2.4.4}$$

and

$$y^+ = (\rho\tau_k)^{1/2} y/\mu. \tag{2.4.5}$$

The dimensionless velocity u^+ has a functional relation with the dimensionless distance y^+ as

$$u^+ = y^+ \text{ if } y^+ < y^+_0, \text{ or, } u^+ = 1/\kappa \ln(E\, y^+) \text{ if } y^+ > y^+_0 \tag{2.4.6}$$

where κ and E are constants, y^+_0 is the upper root of

$$y^+ = 1/\kappa \ln(E\, y^+). \tag{2.4.7}$$

Similarly, a dimensionless temperature is defined as

$$T^+ = (\rho\tau_k)^{1/2} C_p (T_w - T)/Q_w \tag{2.4.8}$$

where T_w and Q_w are the wall temperature and the wall heat flux respectively. The dimensionless temperature is a function of y^+ as

$$T^+ = P_r\, y^+ \text{ if } y^+ < y^+_T, \text{ or, } T^+ = \sigma_T/\kappa \ln(F\, y^+) \text{ if } y^+ > y^+_T\,, \tag{2.4.9}$$

where $P_r = \mu C_p/\lambda$, σ_T and F are constants, and y^+_T is the larger root of

$$P_r\, y^+ = \sigma_T/\kappa \ln(F\, y^+). \tag{2.4.10}$$

2.5 Verification of the CFD Based Fire Models

While field models of compartment fires incorporate increasing number of complex elements of physical and chemical processes which may occur, concerns are arising about the accuracy and credibility of the models and elaborate numerical methods essentially associated with these models. The systematic comparison of fire field

model predictions with experimental data (often termed 'validation') is a crucial step in the general acceptance of this technique and in determining the scope of its application. While no degree of successful validation will prove a fire model correct, confidence in the technique is established the more frequently it is shown to be successful in as wide a range of applications as possible.

The experimental data selected to validate the model developed in this study will briefly be described below. The detailed description for these experiments will be provided in the appropriate chapters.

One set of experimental benchmark fire data that has been used to validate fire field models[Kerrison, 1994a,b; Lewis et. al., 1997] is provided by the series of compartment fire tests investigated by Steckler et. al.[1982]. This involved a gas burner located at various positions on the floor of a small room with various openings. The burner was supplied with commercial grade methane at a fixed rate to produce a constant fire strength. In the series of fire tests the size of the ventilation, the burner power and position were systematically changed to investigate the nature of the fire induced flows in the compartment. The experimental data consists of the detailed velocity and temperature distribution in doorway, the vertical temperature distribution at the room corner and mass flux flowing into and out of the room. Data from this series of tests are often used to validate basic fire models.

Quintiere et al.[1979] carried out a series of small-scale compartment fire tests using PMMA as fuel. The door width and the PMMA sample size were systematically varied. Some key measured data characterising the steady state of the compartment

fire, such as upper layer gas temperature, ceiling temperature, heat flux at the floor, air entrained rate etc., were provided. This series of tests is satisfactory to validate models describing the burning of non-charring solid fuel in a compartment.

Bench scale tests of burning PMMA [Rhodes, 1994] can be used to validate sub-models attempting to simulate non-charring solid fuel pyrolysis. The PMMA samples were burned in a Cone Calorimeter at three different levels of external radiation fluxes. The comparing quantity is the mass loss rate.

Charring model can be verified by comparing the model predictions with the experiment conducted by Kashiwagi et al.[1987]. Kashiwagi et al. carried out several experiments to investigate wood burning under different surrounding conditions. The varied conditions included the oxygen concentration in the air flow and the external radiation flux level. In these cases the comparison can focus on the history of the mass loss rate and temperatures of the solid fuel at different positions.

Finally, a series of experiments[Jia et al., 1999e] were conducted by the Home Office Fire Experimental Unit, Fire Research and Development Group(FRDG), specially for the task of validating the fire spread model developed as part of this research. A sheet of chipboard was lined over the whole expansion of the ceiling of a half scale compartment. The experimental data consists of temperatures in the solid fuel, the vertical air temperature distribution near the door, upper layer temperature and radiation fluxes at different positions.

As mentioned before, the aim of this study is to develop a fire growth and spread

model integrating sub-models representing gaseous combustion, radiative energy exchanges and solid phase combustion. This integrated model has been developed and validated step by step and the results are presented in this thesis. First, a model including the gas phase combustion model and radiation model will be verified in Chapter 6 by comparing the model predictions for the Steckler's room fire with the experimental data. Then the pyrolysis sub-models of non-charring and charring material burning are examined in Chapter 7 by comparing the model predictions with the experimental data obtained from the specifically designed bench scale tests[Rhodes, 1994; Kashiwagi et al., 1987] for the two different types of solid fuels. Finally, the integrated model for fire spread over solid surfaces will be validated in Chapter 8 by comparing the model results with appropriate measured data obtained from the fire experiments in compartments conducted by Quintiere et al.[1979] for PMMA burning and by FRDG, Home Office, for wood products[Jia et al., 1999e].

2.6 Concluding Remarks

A small fire at the initial stages of fire growth and spread in an enclosure may end up producing hazardous outcomes—flahsover or backdraft. The early stage of the fire growth is crucial to evacuate people from the fire room. Therefore, the simulation and prediction of the early stage of the fire spread in enclosures is the most concern of fire modellers. CFD fire modelling is a promising approach due to its flexibility and low cost compared with conducting real fire experiments. However, this technique is at an early stage of development. The simplest fire field models treat fire as a prescribed heat and smoke source. Some primary elements in fire development such as gas phase combustion, radiation, soot formation and transportation, solid fuel combustion, etc.

are often neglected due to complication associated with their incorporation into the basic model. The driving force of the present study is to surmount the weakness of these simplifications in a fire field model by incorporating the primary aspects of fire spread into the model.

In the remainder of this thesis a fire field model will be developed that takes account of fire propagation over solid surfaces. The model is being developed as a possible means of including simple solid fuel combustion consideration into practical engineering fire field models. Thus, the aim is to use relatively simple radiation and combustion models in order to keep computational overheads down to a practical level. The process commences with the development and analysis of a standard heat release model of the type often used in simple engineering applications.

Chapter 3

A HEAT SOURCE FIELD MODEL FOR A ROOM FIRE SCENARIO

3.1 Introduction

In this chapter the simplest form of fire field models will be developed and the predictions from the model will be compared with experimental data. The experimental data corresponds to a room fire scenario involving a non-spreading fire[Steckler et al., 1982]. The model, in which radiation is ignored, simulates the fire as a volumetric heat source. This model represents the simplest form of fire field model of the type often employed in engineering applications. The fire model is developed within the framework of the commercial CFD code CFDS-FLOW3D(version 2.3.3)[Burns and Wilkes, 1987]. The purpose of this study is to provide a starting point and a point of reference for the proposed model development that constitutes this thesis. This work is also intended to highlight the limitations of this approach and suggest areas of possible further model development.

3.2 Steckler Room Fire Tests

Steckler et al.[1982] carried out a series of fire experiments within a compartment to investigate fire induced flows. The experimental data obtained from these fire tests are of sufficient quality to be used to validate fire field models of non-spreading fires in small compartments. In this chapter, one of the Steckler room fire tests is simulated using a simple heat source model established within CFDS-FLOW3D and a

comparison is made of the model predictions with the experimental data.

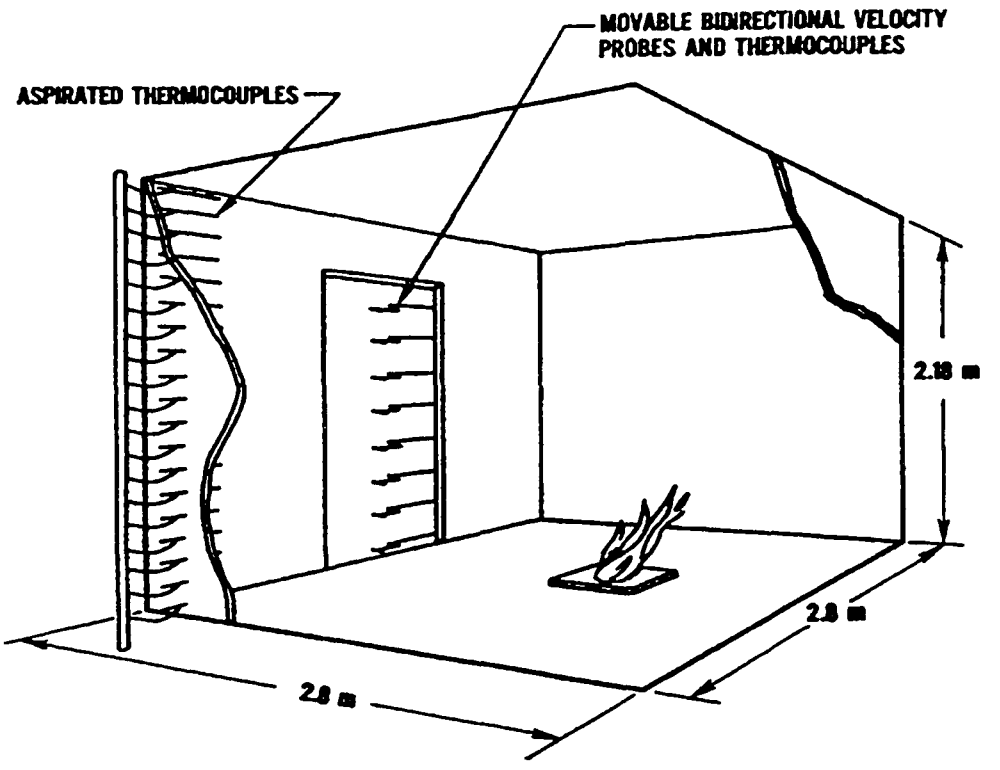

Fig. 3.2.1: Schematic room fire experiment(copied from Steckler *et al.*[1982]).

A series of 45 experiments were conducted by Steckler et al.[1982] to investigate the characteristics of fire induced flows within a compartment. The compartment used in the experiments was 2.8m × 2.8m in plan and 2.18m in height. Figure (3.2.1) is a schematic view of the experimental set-up of the Steckler room fire tests. The walls and ceiling were 0.1m thick and they were covered with a ceramic fibre insulation board to establish near steady state conditions within 30 minutes. In the series of experiments, a 0.3m diameter gas burner supplied with commercial grade methane at a fixed rate producing constant fire strengths of 31.6, 62.9, 105.3 and 158 kW was systematically placed in 8 different floor locations and the opening was varied ranging from small windows to wide doors. The door openings were 0.24m to 0.99m.

Bi-directional velocity probes and bare-wire thermocouples were placed within the room opening on a two-dimensional grid of 28 to 144 depending on the size of the opening to measure velocities and temperatures within the centre of the door jamb.

The measured velocities may be subject to up to 10 percent error. A stack of aspirated thermocouples was placed in the front corner of the room to measure the gas temperature profile.

Mass flow rates within the opening were reported there. They were determined by integrating the local mass velocities (ρv) over the area of the opening either above or below the neutral plane level. The local velocity (v) and the local temperature (T) were obtained from the corresponding experimental data and the local density (ρ) was calculated by ideal gas law. The error in the mass flow measurements may be up to approximately 10 percent.

In the test selected here, the door measured 0.74m wide and 1.83m high and the fire, which was centrally located on the floor, was represented by a gas burner measuring 0.3m in diameter. The burner power selected was 62.9 kW.

3.3 The Simulation of the Selected Steckler Room Fire Test

The fire is simulated as a simple volumetric source of heat appropriate to the case under consideration. The heat source representing the fire is described as a rectangular burner of which the surface area is the same as the round burner used in the experiment. As the wall boundary conditions are adiabatic, the heat release rate is modified in order to account for heat loss through the walls and ceiling and via radiation during the experiment. This is achieved by calculating from the provided experimental data, for each configuration examined, the heat convected out of the room during the experiment and using this value as the heat release rate for the

numerical calculations. The mathematical formula for the calculation of the heat convected out of the room is given by

$$\dot{Q}_c = \iint_{An} \rho v C_p (T - T_0) dA \qquad (3.3.1)$$

where A_n is the area in the door way above the neutral plane and T_0 is the ambient temperature. The local mass flow (ρv) and the local temperature (T) were obtained from the corresponding experimental data. Equation (3.3.1) is numerically integrated over the grid of thermocouples and bi-directional velocity probes placed within the opening. In this simulation the heat loss is approximately 3.9 kW.

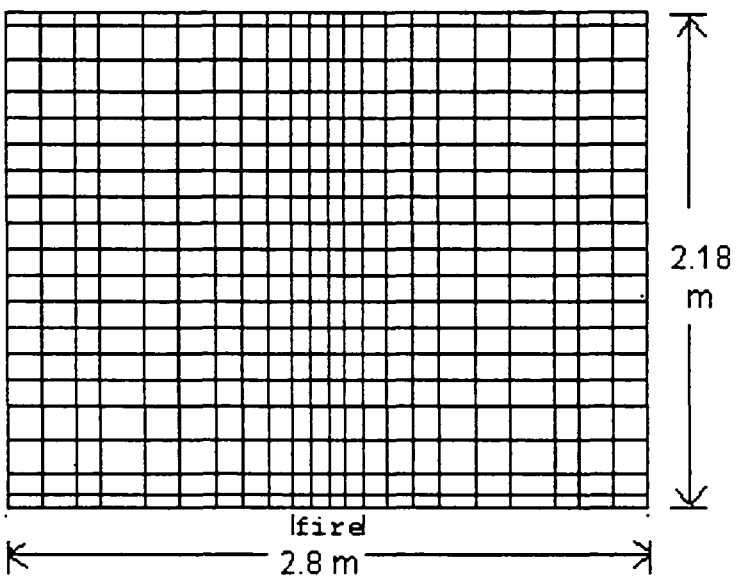

the mesh in x-y plane

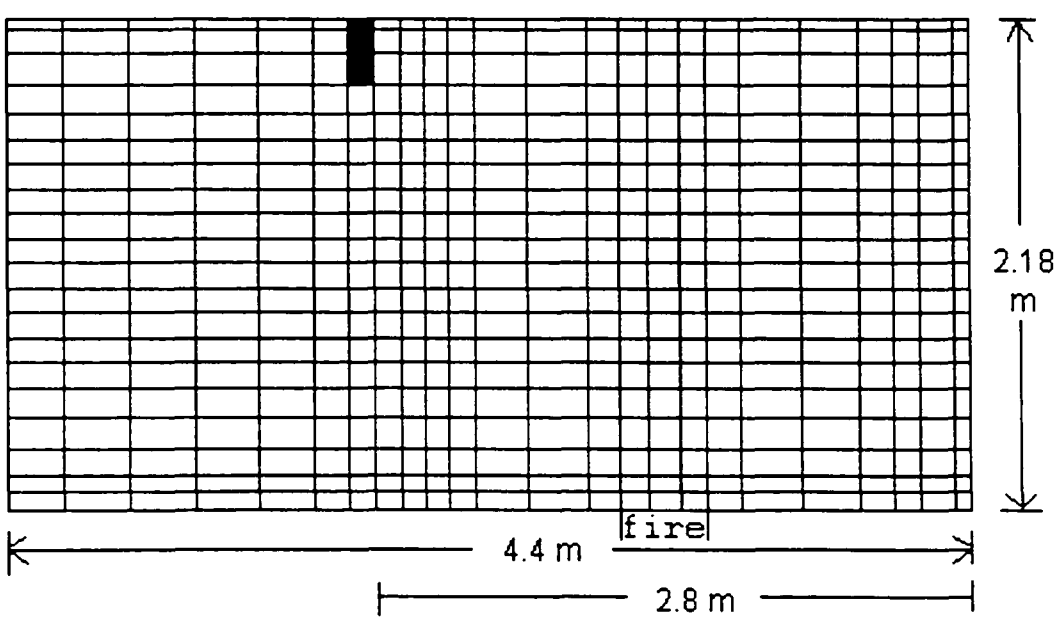

the mesh in y-z plane

Fig. 3.3.1: The mesh used in the model.
Note: the black region in the second figure represents the soffit.

A mesh of 10120 cells in total (7480 internal and 2640 external cells) is used to discretise the geometry. The mesh consists of 23 cells in length, 22 cells in width and 20 cells in height. The mesh is non-uniformly distributed with refinements in the wall, floor, ceiling, fire and doorway regions. In order to correctly model the flow through the open door, the numerical grid is extended by 1.6m to include a region outside the fire compartment. A fixed pressure boundary condition is applied on all external boundaries.

The differential equations involved in this simulation include the momentum equations for three velocity components, the continuity equation, the energy conservation equation and two equations for κ and ε describing turbulence. These equations are expressed in a general form in equation (2.2.15).

CFDS-FLOW3D is run in transient mode until steady-state conditions were achieved. Only the steady-state results are considered here, typically requiring 200 time steps to reach steady-state conditions. Within each time step, a convergence criterion is if the mass source residual falls below 1×10^{-4} (and the other key residual measures, e.g. enthalpy by corresponding amounts). If the time step iteration is not stopped by these measures then a maximum of 100 iterations will be performed during the time step. Steady-state is assumed to be achieved when the maximum change between spot values is below 1% between time steps.

The simple fire field model presented here will be referred in chapter 6 for a comparison with an improved fire field model. For the ease of the comparison, this model is called the base fire field model.

While these results are not strictly mesh independent, small variation in model results were found with mesh refinement. For the purposes of this thesis, the mesh is considered to be adequate.

3.4 Results and Discussion

Some main characteristics of a room fire observed by the experiment and the simulation are summarised in table (3.4.1) for comparison.

Table 3.4.1 The predicted and experimental data of some main characteristics in the room fire.

model elements	upper layer temperature	Neutral plane height	inflow	outflow
	°C	m	kg/s^{-1}	kg/s^{-1}
Prediction	144	1.0	0.546	0.551
Experiment	129	1.027	0.554	0.571

The experimental upper layer temperature was determined by averaging the experimental temperature values in a column through the upper layer as measured by the thermocouple stack located in the corner of the room. In table (3.4.1), the predicted upper layer temperatures represent a mean temperature determined in a similar manner to the experimental value, i.e., the same thickness of the upper layer is used to calculate the average upper layer temperature for both the measured and predicted values.

The neutral plane within the opening is the position at which the flow velocity is zero. The hot gas mixture flows out of the room through the portion of the opening above the neutral plane while the fresh air enters the room through the portion of the opening below the neutral plane. Thus the outflow (inflow) rate was determined by

integrating the local mass velocities (ρv) over the area of the opening above (below) the neutral plane level. The location of the neutral plane is determined by calculating the approximate location of the zero velocity line within the doorway. The prediction of the location of the neutral plane is in very good agreement with the experiment. The predictions of mass flux into and out of the room also show good agreement with experimental data.

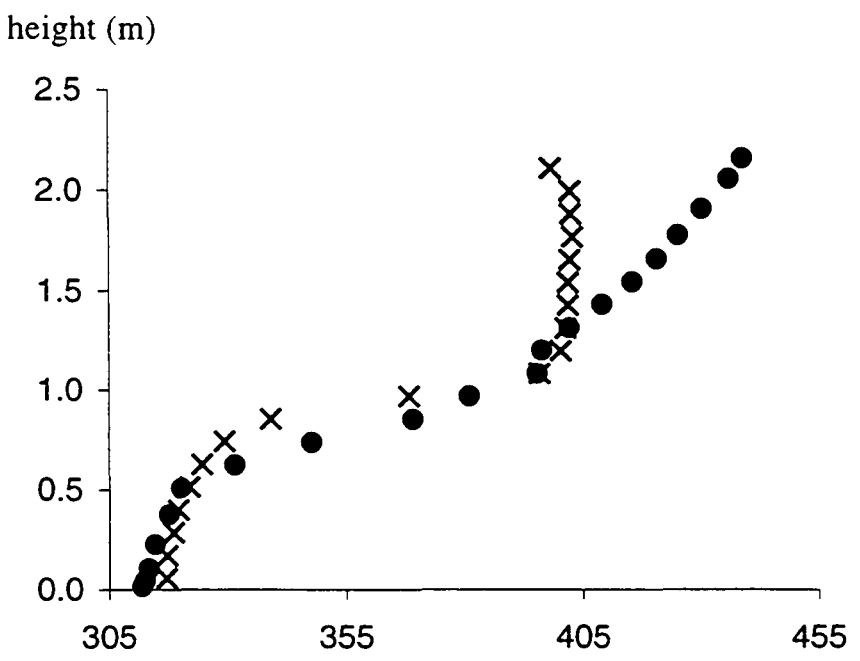

Fig. 3.4.1: Vertical temperature profiles measured and predicted in the corner of the Steckler room.
• : predicted by the heat source model; × : measured.

The measured and predicted vertical stack temperature profiles in the corner of the Steckler room are depicted in figure (3.4.1). While the predicted temperatures in the lower layer agree very well with the measured values and in the upper part the predicted temperatures are of the same order as the measured values, the basic characteristic of the temperature distribution in the upper layer is completely missed by the predictions. The measured stack temperatures show a nearly uniform distribution in the upper layer and a small drop near the ceiling, while the simulation temperatures present a monotonic increasing trend. The temperatures in the upper layer produced by the simulation are considerably higher than the experimental data.

The maximum difference reaches 10.2%.

The sharp transition of the temperature distribution from the cool low part to the hot upper part is somewhat smeared by the simulation. The numerical inaccuracies of false diffusion due to coarseness of the mesh could make a contribution to it. However, Kerrison et al.[1994a,b] have shown that a fine mesh would not help produce much improvement.

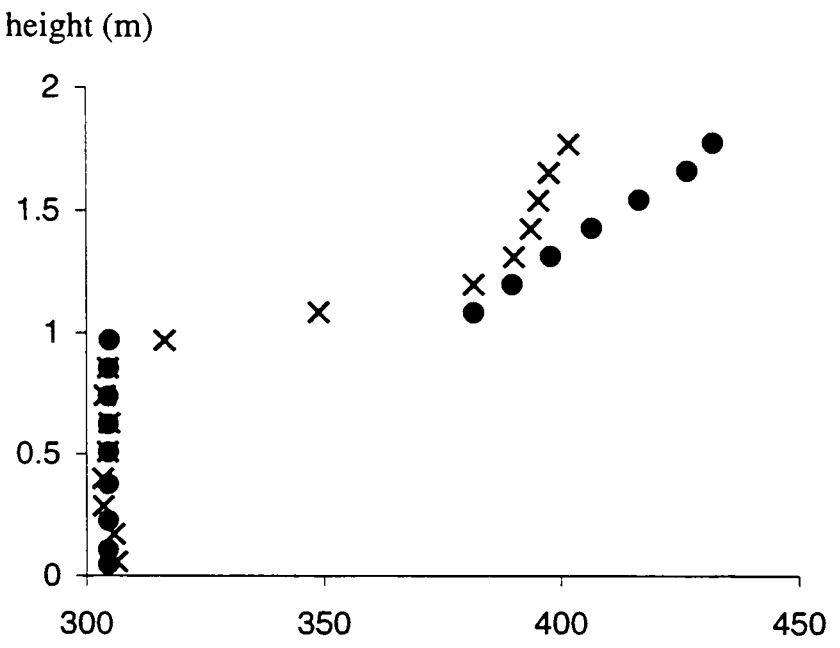

Fig. 3.4.2: The measured and predicted vertical temperature profiles in the doorway central line.
• : predicted by the heat source model; × : measured.

Figure (3.4.2) plots the temperature profiles along the doorway centreline. The simulation quantities are in reasonable agreement with the experimental data. The existence of the cold and hot layer in the doorway is predicted. The simulation captures the sharp increase of the temperature from the cold lower part to the hot upper layer. However, the upper layer temperatures are overpredicted again with differences of up to 7.5%.

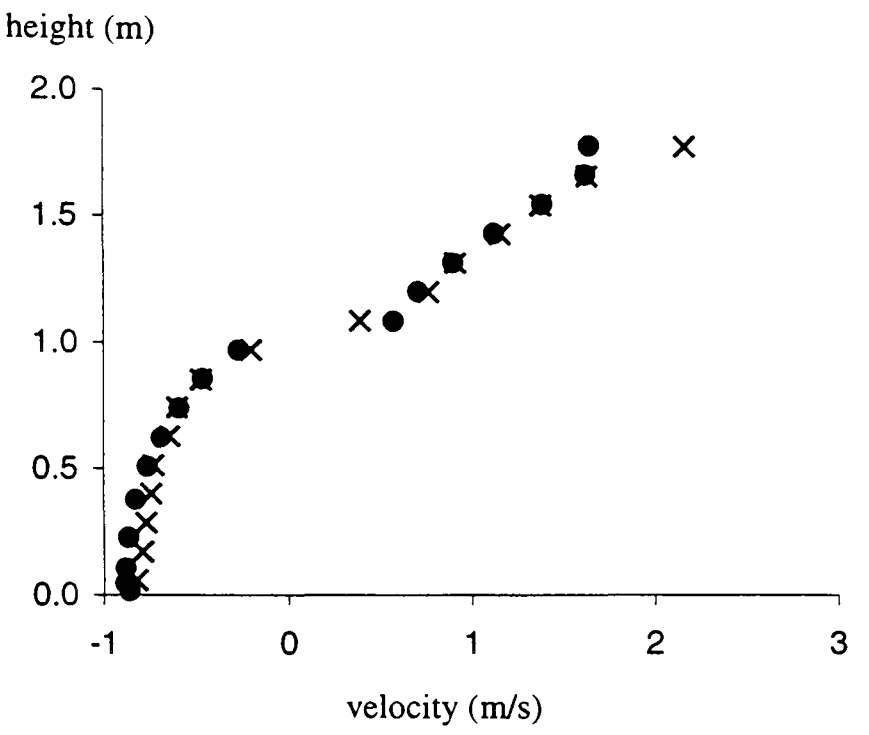

Fig. 3.4.3: The measured and predicted velocity profiles of the vertical middle line in the doorway.
• : predicted by without radiation models; × : measured.

The vertical velocity profile in the middle of the door is depicted in figure (3.4.3). Except just under the upper edge of the door the model predictions produce excellent agreement with the experimental data. The velocity just under the upper edge of the door is underpredicted. This behaviour was also found in several other model predictions[Kumar et al., 1991; Hadjisophocleous, 1993; Kerrison et al., 1994a,b]. The accuracy of the experimental data in this region was questioned by Kerrison et al.[1994a,b]. "In order to achieve meaningful results, the bi-directional velocity probes must be aligned parallel to the velocity streamlines. The velocity probes in the experiment were placed with their axes horizontal - i.e. parallel to the floor. However, in the vicinity of the door edges - particularly the top edge where the hot buoyant gases exit the room - the streamlines intercept the door plane at acute angles leading to the possibility of substantial measurement errors."[Kerrison et al., 1994a,b]

Figure (3.4.4) plots the predicted flow velocities in the plane passing the doorway central line and the centre of the Steckler room. It is obvious that there is a neutral

plane within the door. It is clearly demonstrated that within the doorway the fresh air flows into the room through the lower portion below the neutral plane while the hot gases rush out of the room through the upper portion above the neutral plane. The incoming fresh air is accelerated towards the fire due to entrainment. As a result, the fire is tilted backwards. The fresh air is entrained into the fire from its front and the hot gases are pumped into the upper layer due to buoyancy.

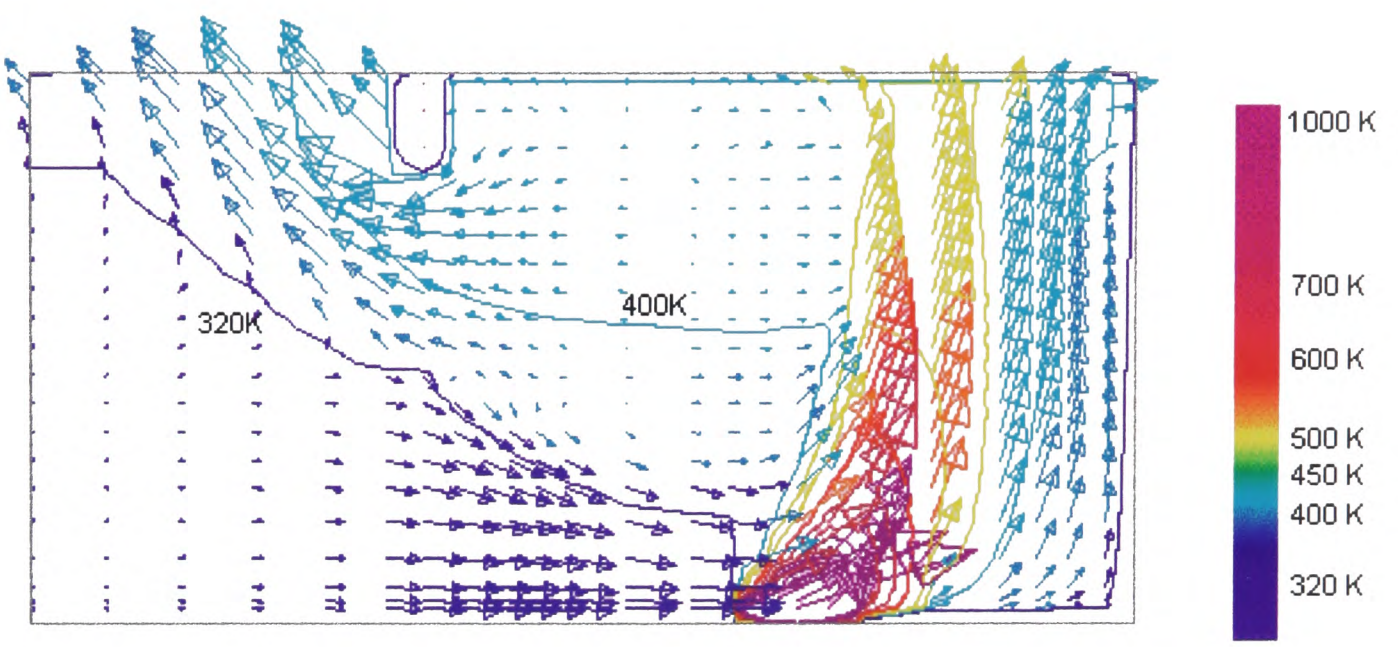

Fig. 3.4.4: The predicted flow velocities in the plane passing the doorway central line and the centre of the Steckler room.
Note: the solid lines in the figure are temperature contours. The colour of the velocity vectors represents the flow temperature.

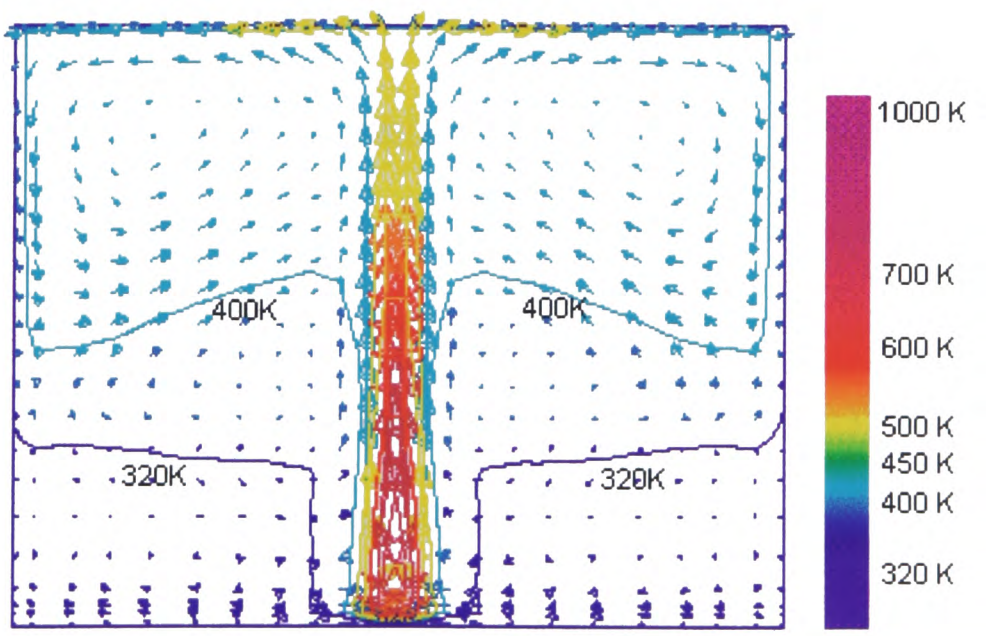

Fig. 3.4.5: The flow velocities in the xy plane 0.15m behind the burner.
Note: the solid lines in the figure are temperature contours. The colour of the velocity vectors represents the flow temperature.

In figure (3.4.5), the velocities in the xy plane 0.15m behind the burner is depicted. The hot gas flow of the buoyant plume of the fire is deflected horizontally due to the confinement of the ceiling. Two large re-circulation regions of hot gas flow are clearly observed in the hot upper layer beside the upper part of the fire plume. It is also shown that the fresh air near the base of the fire is pushed away due to the expansion of the hot gases in the fire. But the fresh air is entrained into the fire from its flanks above the firebase.

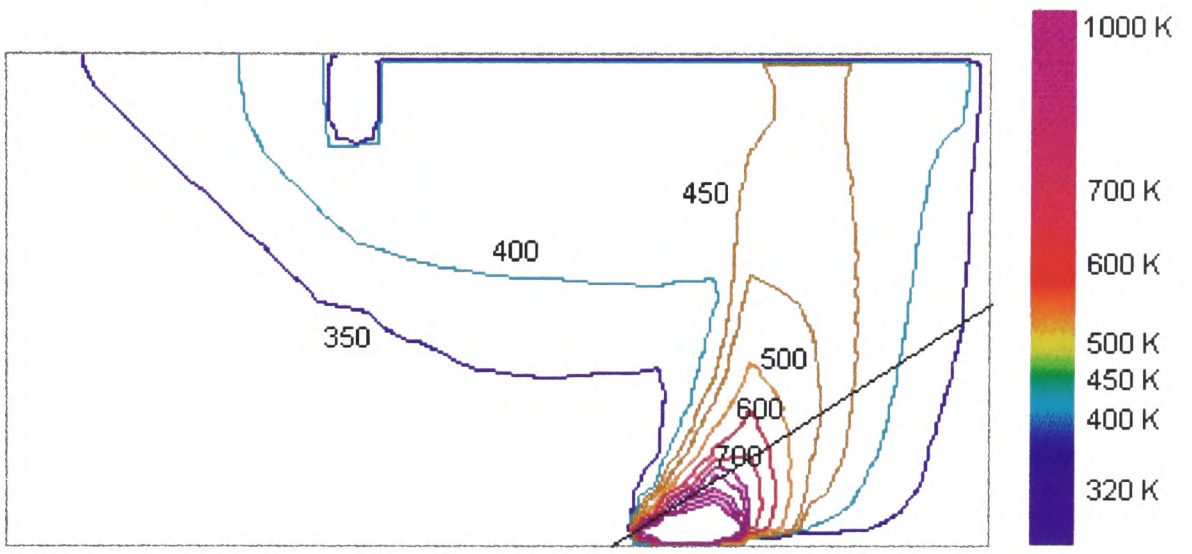

Fig. 3.4.6: the temperature contours in the plane passing the doorway central line and the centre of the Steckler room (Unit: K).

Finally, figure (3.4.6) illustrates clearly that the thermal plume is blown backwards by the induced incoming flow and that the flame drifts back away from the burner. This effect was also observed in the experiment and earlier numerical results[Kerrison et al., 1994a,b]. Furthermore, from this figure, the angle of inclination of the fire to the horizontal can be estimated. This is estimated to be approximately in the range of 40^{o} to 44^{o}. This result is close to the flame angle in the range of 33^{o} to 43^{o} observed by Quintiere et al.[1981] in an earlier series of experiments using an identical experiment setup.

3.5 Concluding Remarks

The field model predictions using the simple heat source to simulate the burner fire capture the main trends of a non-spreading room fire situation. The predicted neutral plane height, the mass flow into and out of the room and the profiles of velocity and temperature in the doorway centreline are in good agreement with the experimental results. The qualitative predictions of the effects of the incoming fresh air and the ceiling jet are also consistent with the observation of real burner fires.

However, large differences occur between the predicted and measured vertical temperatures in the hot upper part region of the room. The predicted temperatures in this region are quite higher than those measured. The overpredicted temperatures may result from the neglect of radiation in the simulation. In fact, radiation plays a significant part in the heat transfer in room fire situations. Upper layer temperatures will reduce due to radiative heat losses. Radiation heat losses also decrease the temperature of the burner fire. Thus less energy will pump into the upper layer through the fire plume. However, of greater significance is the fact that the simulation completely missed the approximately uniform characteristic of the upper layer temperature distribution. Once again, the possible reason for the incorrect predictions of these trends is that radiation in the simulation was neglected. Radiation may help create a nearly uniform temperature distribution in the upper layer since higher gas-soot mixture temperatures cause more radiative heat losses.

Another factor contributing to the higher predicted vertical temperatures is the neglect of conduction heat losses through the walls and ceiling. Although the energy loss due

to radiation and conduction through bounding surfaces was taken into account by using the reduced fire power of the heat source, the estimated energy loss may be too crude to represent the real energy losses. Since heat losses through the ceiling was not considered, the predicted vertical temperatures produce a monotonic increasing trend that is against the observed trend of the measured vertical temperature distribution.

Improvement of the simulation predictions of the Steckeler room fire tests may be achieved by taking the radiative energy exchanges and conduction heat losses through walls and ceiling into account. However the radiative properties of the gas-soot mixture will not be appropriately evaluated without the simulation of gas-phase combustion since the concentrations of soot, CO_2 and H_2O are centrally important for the evaluation. Gas-phase combustion models are also required to simulate fire spread over solid fuel surfaces since the gas-phase combustion is one of the two central mechanisms to control the flame spread over a solid surface.

Concerning the heat loss through the walls, it is very computationally expensive and unnecessary to calculate the temperature distribution within the non-burning solid walls by solving the conduction equation for solids using the finite difference method. An easy and economical method to calculate the solid surface temperature must be found and used.

Most fuels involved in room fires are solid fuels such as lining materials on walls and ceiling, upholstered furniture and so on. Solid combustion models must be included to simulate a real fire development within an enclosure.

Thus, while capable of producing reasonable results, the fire model presented in this chapter needs further development before it can reliably be used in fire engineering calculations. The elements mentioned above need to be incorporated into an integrated model to form a useful tool to predict fire growth and spread within enclosures. These elements and their models will be discussed and developed in the following chapters.

Chapter 4

GAS PHASE COMBUSTION AND MODELLING

4.1 Introduction

Most fuels involved in compartment fires are combustible solids such as upholstered furniture, wall and ceiling lining materials. At high surface temperature, the solid fuel is gasified by absorbing heat from the fire to yield combustible gases that meet oxygen and burn in the fire. These combustible gaseous products flow and diffuse to the reaction zone where they react with oxygen and liberate heat. Sufficient heat must be transferred back to the solid fuel in order to maintain the endothermic pyrolysis process. Thus gas phase chemical reaction is one of the central controlling mechanisms of solid fuel burning. Consequently it is important to incorporate an appropriate gas phase combustion model into the integrated model simulating compartment fire spread which involves solid fuels. Gas-phase combustion models are also required to evaluate the radiative properties of the gas-soot mixture since the concentrations of soot, CO_2 and H_2O are centrally important for the evaluation.

In this chapter, a characteristic description of diffusion flames is given. Some gas phase combustion models for diffusion flames are reviewed. Then the gas phase combustion model used in this study is described and a verification of the model is presented.

4.2 Diffusion Flames

Fire is a combustion process in which chemical reactions between fuels and oxidisers occur and heat is released. Most enclosure fires involve solid material as fuels. Since fire is a gas phase phenomenon, solid fuels must be gasified under high temperature to form combustible volatiles before mixing and reacting with oxidants in the gas phase. Therefore fires are diffusion flames in nature. In diffusion flames, fuel and oxidant are separate initially before the chemical reactions occur. At the mixing layer, the fuel and oxidant diffuse into each other(hence the name "diffusion flame").

The study of diffusion flames concerns their internal structure, their rate of energy release, the rate of transport of fuel and oxidant into the flame(burning rate) and the necessary conditions of their existence and extinction[Linan and Williams, 1993].

The real mechanisms of gas phase combustion are very complex. Gas phase combustion may create tens even hundreds of short living intermediate species during a series of elementary steps. It is extremely difficult to describe and model the detailed kinetics of real chemical reactions due to the lack of current knowledge and data concerning the mechanism. For the well understood fuels, the large number of elementary chemical steps and associated intermediate radicals usually prevents modelling the chemical kinetics in detail due to the limit of computer capacity in engineering applications. To reduce this complexity and hence lead to reduction of computation, one step global chemical reaction is generally assumed to represent the chemical reaction of a diffusion flame. For example, the following representation of the methane and air diffusion flame is widely used in engineering applications,

$$CH_4 + 2O_2 \rightarrow CO_2 + 2H_2O + \text{heat}\ .$$

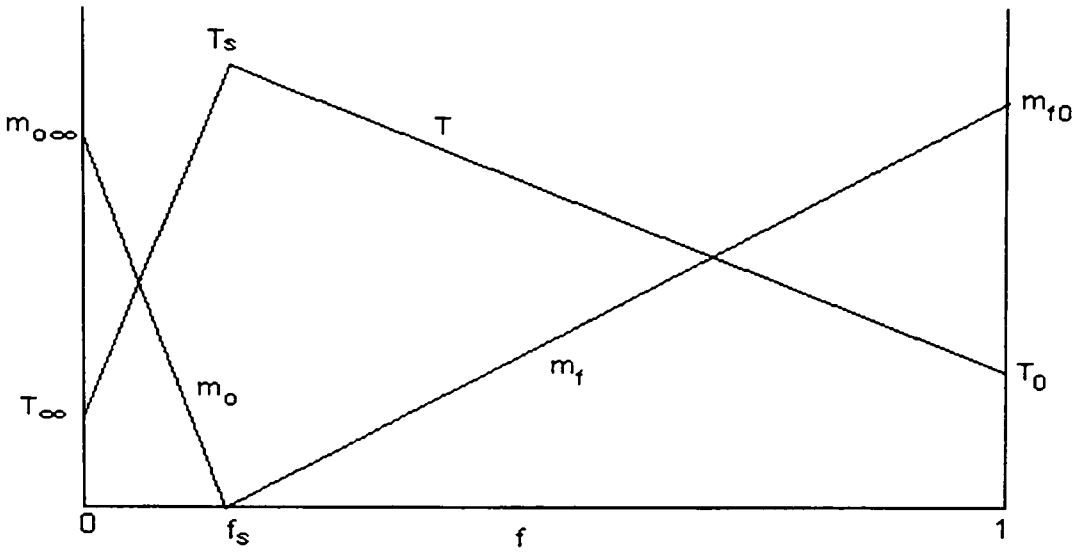

Fig. 4.2.1: Illustration of the structure of a laminar diffusion flamelet with infinite fast chemistry.

Under the assumption of one-step reaction and infinite fast chemistry, chemical equilibrium means that the fuel and oxidant can not coexist. This leads to that the mass fraction of fuel (m_f) or oxidant (m_o) must be zero, where $m_f = c_f/\rho$ and $m_o = c_o/\rho$ are the mass fractions of the fuel and oxidant, c_f and c_o are the concentrations of the fuel and the oxidant respectively and ρ is the density of the gas mixture. This situation is only valid when $m_f = 0$ for $f < f_s$ and $m_o = 0$ for $f > f_s$, where $f = (\chi - \chi_{o\infty})/(\chi_{f\infty} - \chi_{o\infty})$ is the mixture fraction—a conserved scalar, f_s (= $1/(1+s)$) is its stoichiometric value, s is the stoichiometric ratio of fuel to oxidant, $\chi = m_f - m_o/s$ and the subscripts of f_∞ and o_∞ refer to the initial conditions of the fuel and the oxidant. Within the thin sheet where $f = f_s$, fuel and oxidant meet and react at an infinite fast rate and all the energy stored in the bonds of molecules is released and conducted away from the flame sheet. Oxygen diffuses into the flame from the zone $f < f_s$ while fuel diffuses into the flame from the zone $f > f_s$. The laminar flamelet structure is illustrated in figure (4.2.1). Within the reaction sheet the accumulation and convection are negligible compared with the diffusion and the latter are balanced with the reaction. Thus the singular

reaction zone is a reactive-diffusive zone.[Linan and Williams, 1993]

Soot particles may be formed due to incomplete combustion. The soot formation process is extremely complex. However, C_2H_2 is commonly recognised as an important, probably dominant intermediate species in the sooting processes. Soot particles are the dominant source of heat losses from the flame. Consequently, flame temperature is considerably lower than the adiabatic flame temperature.

Diffusion flames are usually turbulent. So great interests lie in turbulent combustion. When the Reynolds number of a fluid flow is sufficiently high, turbulence is generated in the flow. The distinctive feature of a turbulent flow is the highly random or irregular nature of the fluid motion. Within the turbulent flow, the larger eddies generate smaller eddies due to vortex stretching. The smallest eddies have an isotropic nature. The process in which the kinetic energy is transferred into internal energy takes the form of an energy cascade[Kay and Nedderman, 1985]. The kinetic energy is extracted from the mean flow by the largest eddies. Energy is then transferred to smaller eddies. This energy transferring process continues until in the smallest eddies the kinetic energy is finally dissipated into internal thermal energy by the direct action of viscous stress.

In turbulent flames, the chemical reactions interact with the turbulence. So the combustion process is very complex. Turbulent diffusion flames appear to be highly wrinkled, bumpy and rough. Several experiments have demonstrated that the large-scale vortices transport the unmixed ambient fluid across the entire extent of the mixing layer[Pivovarov *et al.*, 1993]. The mixing layers are therefore strongly

corrugated. The eddy mixing results in more efficient combustion as it enhances the reactant mixing process.

In turbulent reactive flow, intermittence is a distinctive phenomenon. In turbulent diffusion jet flames, it is found that curves of measured time-averaged fuel mass fraction and oxidant mass fraction significantly overlap[Spalding, 1979]. Spalding argued that the fluctuations result in one reactant being in large excess at one moment, and the other one at next moment.

A non-dimensional parameter to describe the feature of combustion is Damkohler number which is defined as the ratio of a flow time to a chemical reaction time[Linan and Williams, 1993]. Let τ_c denote the chemical reaction time and the flow time is expressed in $l/\sqrt{2k}$, where l is the integral scale of turbulence and k is the turbulent kinetic energy. Then the Damkohler number is defined as

$$D_a = (l/\sqrt{2k})/\tau_c . \tag{4.2.1}$$

Two limiting cases are discussed here. When $D_a << 1$, the chemical reaction rate is slow compared with the fluid dynamics. The concentration fluctuations of the reactants are smoothed by the turbulent eddy mixing before the chemical reactions take place. Consequently, the combustion proceeds slowly and occurs throughout the region in which the reactants exist and are well mixed due to the turbulence. On the other hand, when D_a is sufficiently large($D_a >> 1$), the reaction rate is rapid in comparison with the fluid dynamics. The combustion reactions occur in wrinkled thin sheets where the fuel and oxidant meet and diffuse into each other.[Linan and

Williams, 1993]

Another complexity created by turbulence is the interaction between radiation and turbulence. Firstly, the temperature fluctuations cause significant variation of radiative heat losses as radiative heat losses are a function of T^4. Secondly, the temperature fluctuations also substantially affect soot concentration in the flame as soot formation is sensitive to temperature. In turn, the variation of soot concentration produce changes of absorptivity and emisitivity of the reactive flow. Since soot particles play a dominant role in the radiation from the fire, the fluctuations of the soot concentrations will then significantly affect the radiation from the fire.

Buoyancy is important in fires. Buoyant flow is created by differences in density between the hot gases and the relatively cool surrounding atmosphere. Buoyancy is the driving force which makes hot combustion products move upwards in fires. In the situation of fire spread over combustible solids, buoyancy dominates the flame spread type(wind aided or opposed spread) and even changes the chemistry involved.

4.3 Gas-phase Combustion Models

4.3.1 Introduction

Since the number of parameters involved is enormous, it is generally too difficult to completely describe the chemical reactions in fires. Combustion models are introduced to model them under simplifications. A common practice is to use the probability density functions to store the statistical information of turbulent flames. A

key task of combustion models is to determine the combustion rate at which the reactants are consumed and products are produced. In this section several combustion models commonly used in fire safety engineering applications are reviewed.

4.3.2 The probability density functions

Because of the random nature of turbulent flames, it is useful to introduce the probability density functions (pdf) to maintain the statistical information of turbulent flames. A wide range of pdfs are discussed by Tuovinen[1995].

According to the classification made by Linan and Williams[1993], the pdfs are used in two strategies, the approximation of pdfs using moments and calculation of the evolution of pdfs. When the first strategy is employed, a specific pdf form is selected. The parameters in the pdf are obtained from the properties of a pdf and equations derived from flow properties. For example, if the reaction rate is assumed to be infinite, the chemical equilibrium means that the fuel and the oxidizer can not coexist at the same point and moment. Thus, all of state variables are uniquely determined in terms of the mixture fraction f such that the intermittence can be described by the pdf for f. Suppose the pdf of f takes the form of a delta function, i.e.,

$$p(f) = a\delta(f-f_-) + b\delta(f-f_+) \tag{4.3.1}$$

where $f_- = \bar{f} - \alpha$, $f_+ = \bar{f} + \alpha$, $\bar{f}$ stands for the mean value of f which is governed by

$$\partial \rho \bar{f} / \partial t + \nabla (\rho \mathbf{U} \bar{f}) - \nabla ((\mu_t / \sigma_t + \mu_l / \sigma_l) \nabla \bar{f}) = 0 \tag{4.3.2}$$

where μ_t and μ_l are laminar and turbulent viscosities, and σ_t and σ_l are the effective Prandtl/Schmidt numbers respectively. The constants a, b and α are

calculated from the following equations

$$\int_0^1 p(f)df = 1 \tag{4.3.3}$$

$$\int_0^1 fp(f)df = \bar{f} \tag{4.3.4}$$

$$\int_0^1 (f-\bar{f})^2 p(f)df = G \tag{4.3.5}$$

where G is the variance of the mixture fraction which satisfies the equation below [Tuovinen, 1995]

$$\partial\rho G/\partial t + \nabla(\rho \mathbf{U} G) - \nabla((\mu_t/\sigma_t + \mu_l/\sigma_l)\nabla G) = c_1 \mu_t/\sigma_t \nabla f \bullet \nabla f - c_2 \rho\varepsilon/kG. \tag{4.3.6}$$

In the second strategy, the turbulent combustion process is treated as a stochastic process governed by the transport equations. All the statistical information of the turbulent flame is stored in a joint pdf of the velocity and state variables. The pdf is governed by an equation derived from the basic transport equations.

When a pdf, for instance p(*f*), for the mixture fraction is introduced to contain the statistical information of a turbulent flame, the mean value and the variance of fluctuations of a scalar variable Ψ can be expressed by

$$\bar{\Psi} = \int_0^1 \Psi p(f)df \tag{4.3.7}$$

$$\overline{(\Psi - \bar{\Psi})^2} = \int_0^1 (\Psi - \bar{\Psi})^2 p(f)df \tag{4.3.8}$$

4.3.3 The flamelet model

In laminar flames, the chemical equilibrium is reached provided infinite rate chemistry is presented. Then all of the state variables such as reactant concentrations and temperature are uniquely determined by a conserved scalar, the mixture fraction f. The laminar flamelet model treats the turbulent flame as an assembly of microscopic laminar flame elements interacting with vortices. In each of these elements, the instantaneous state variables are expressed in terms of the mixture fraction f, i.e. $\psi = \psi(f(x,t))$ where ψ stands for a scalar variable. The mean values of these scalars are obtained through a calculated probability density function. A second parameter, the dissipation rate of the mixture fraction χ, is introduced to describe the strain effects.

The mixture fraction and mass transport are governed by equation (4.3.2) and

$$\partial \rho Y_\alpha / \partial t + \nabla (\rho \mathbf{U} Y_\alpha) - \nabla (\rho D \nabla Y_\alpha) = W_\alpha \qquad (4.3.9)$$

respectively[Tuovinen, 1995; Linan and Williams, 1993], where Y_α is the mass fraction of the species α, D is the common diffusion coefficient and W_α is the source term of the species α due to chemical reaction. In the mixing layer of a laminar flame, the accumulation and convective effects are of little importance compared with the diffusion effects, thus a diffusive-reactive balance is established. Hence equation (4.3.9) can be approximately simplified to describe this balance as

$$-\rho D |\nabla f|^2 \, d^2 Y_\alpha / d f^2 = W_\alpha \qquad (4.3.10)$$

$D|\nabla f|^2$ is called scalar dissipation rate χ[Buriko et al., 1994; Linan and Williams, 1993].

From equation (4.3.10), it is obvious that the chemical calculation is decoupled from the turbulent flow field calculation. At each strain rate a table of the scalars versus mixture fraction is calculated and stored in a look-up table prior to the calculation of the flow field.

The flamelet model is widely used to investigate the structure of diffusion or premixed flames[Sanders and Lamers, 1994; Bradley et al., 1994; Moss et. al., 1995].

4.3.4 The eddy break-up model

Spalding[1971] found that the Arrhenius form did not represent the chemical reaction rate correctly. The predicted flame spread rate and concentration profiles were not in agreement with experimental data simultaneously. He suggested that the influence of the local turbulence level on the reaction rate should be taken into account. The larger eddies are broken down into smaller ones. It was supposed that the reaction rate must be controlled by the rate at which the larger unburned gas eddies are successively broken down into smaller ones until the size of the small eddies allow the chemical reaction to occur. This suggests that the chemical reactions take place in the fine turbulent structure. The rate of energy decay in the turbulence be estimated by[Spalding, 1971]

$$\dot{e}_t = 0.35\rho \left| \frac{\partial u}{\partial y} \right| e_l \qquad (4.3.11)$$

where $\dot{e}_t$ and e_l denote the rate of energy decay and local energy respectively, ρ stands for density and $\frac{\partial u}{\partial y}$ is the local velocity gradient.

To combine the influences of the chemical kinetic and the eddy break-up process on the combustion rate, Spalding introduced the concept of reactedness τ, defined by

$$\tau = (m_f - m_{f,u}) / (m_{f,b} - m_{f,u}) \qquad (4.3.12)$$

where m_f is the mass fraction of fuel and the subscripts u and b stand for the unburned and burned conditions respectively. Obviously, τ changes from 0 to 1 according to the unburned and completely burned state respectively. The reactedness τ characterises the intermittence of turbulent flames because the fluid in the combustion region is composed of alternating fragment of unburned gas and almost fully burned gas. The instantaneous reaction rate $\dot{m}_f'''$ is a function of τ. At a given point, the reactedness can have a reaction rate $\dot{m}_{f,\max}'''$, which can be relatively high[Spalding, 1971].

Spalding assumed that the eddy break-up rate could be expressed in the same form as the rate of energy decay. Thus, the eddy break-up rate is equal to $C(1-\tau)\rho\left|\partial u/\partial y\right|$, where C is a constant. When the simultaneous influences of chemical kinetic and eddy mixing on combustion rate are considered, the combustion rateis given by[Spalding, 1971]

$$R_f = \{ (\tau \dot{m}_{f,\max}''')^{-1} + [C(1-\tau)\rho|\partial u/\partial y|]^{-1} \}^{-1} \qquad (4.3.13)$$

4.3.5 The eddy dissipation model

To the author's best knowledge, the eddy dissipation model was first proposed by Magnussen and Hjertager[1977]. Like the eddy break-up model, the eddy dissipation

model assumes that the chemical reactions occur at the smallest eddy level, i.e. where the molecular transfer process is significant to heat conduction and chemical reaction. When the chemistry is fast, Magnussen et al.[1977] suggested that the combustion process be dominated by eddy mixing processes. Therefore, the combustion rate can be determined by the rate of intermixing on a molecular scale of fuel and oxygen eddies, in other words, by the rate of dissipation of the eddies[Magnussen et al., 1977]. Unlike the pdf's approach, Magnussen et al. tackled the mean scalar variables directly. Thus, the combustion rate is expressed by[Magnussen et al., 1977]

$$R_f = A\bar{C}_f \frac{\varepsilon}{k} \tag{4.3.14}$$

where $\bar{C}_f$ is the time-averaged fuel concentration, k and ε are the turbulent kinetic energy and the turbulence dissipation rate respectively. Equation (4.3.14) represents the lean fuel and rich oxygen situation. If the time-averaged oxygen concentration is low and the time-averaged fuel concentration is high, oxygen will show a remarkable intermittence. Therefore, the combustion rate in this region is given by

$$R_f = A(\bar{C}_o / s)\frac{\varepsilon}{k} \tag{4.3.15}$$

where $\bar{C}_o$ stands for the time-averaged oxidant concentration, and s is the stoichiometric ratio of oxidant to fuel. Thus, the real time-averaged combustion rate is the combination of equations (4.3.14) and (4.3.15), given by[Magnussen et al., 1977]

$$R_f = A\min(\bar{C}_f, \bar{C}_o / s)\frac{\varepsilon}{k} \tag{4.3.16}$$

It is obvious that the eddy dissipation model has a close relation with the eddy break-up model. However, the difference between the two models requires some comments.

In the eddy break-up model, the intermittence of the turbulent flame is expressed by the reactedness τ, while in eddy dissipation model, the intermittence is embodied in the formulation $A\min(\bar{C}_f, \bar{C}_o / s)$. Because the time-averaged reactant concentrations are dealt with directly, this model does not include the equations for concentration fluctuations. Magnussen et al.[1977] argued that this is a great advantage, especially when taking into consideration the lack of certainty with which concentration fluctuations of reactants can be determined.

4.4 A Combustion Model of Turbulent Diffusion Flames

4.4.1 Description of the model

Since the chemical mechanism involved in most enclosure fires is extremely complicated and there is insufficient knowledge and kinetic data to model the chemical reactions of fires in detail, the common assumption, in engineering applications, is that the chemistry involved in fires is infinitely fast. Consequently, it is assumed that the combustion rate is dominated by the mixing rate. Among the models reviewed in the previous section, the eddy dissipation concept is most suitable to model the combustion in fires given the above limitation as the time-averaged reactant concentrations are dealt with directly in this model and in most fire situations of interest the statistical information about turbulent fluctuations is uncertain. Therefore, the eddy dissipation concept is selected in the present study to simulate the gas phase combustion. In this section, a combustion model of turbulent diffusion flames is described by using the eddy dissipation concept.

A simple one-step global chemical reaction is adopted, i.e.,

$$F + sO \rightarrow (1+s)\,P + \text{heat} \tag{4.4.1}$$

where F is the fuel, O is the oxidant, P is the product and s is the stoichiometric constant. The heat released through the consumption of one unit mass fuel is denoted by H.

The numerical simulation of combustion is governed by a set of partial differential equations: continuity, momentum, energy and mass transport equations. These equations have already been described in detail in section 2.3.

Four scalar variables are used in this model. They are mixture fraction(f), mass fraction of fuel(m_f), mass fraction of air(m_a) and mass fraction of products(m_p).

The source term of the governing equation for mass fraction of fuel employs the eddy dissipation concept, i.e.,

$$R_f = A\min(\bar{C}_f, \bar{C}_o / s)\frac{\varepsilon}{k} \tag{4.4.2}$$

where A takes 4.0[Magnussen et al., 1977]. To guarantee the numerical stability, the source term is linearized using the method proposed in Patankar[1980]. The mass fraction of air and products are determined by the algebraic equations

$$m_a = 1 - m_f - (f - m_f)/f_s \tag{4.4.4}$$

$$m_p = 1 - m_f - m_a \tag{4.4.5}$$

rather than differential equations, where f_s is the stoichiometric value of f, defined by $f_s = 1 / (1 + s)$.

Since flow is assumed to be compressible, the ideal gas law is adopted

$$\rho = \frac{pW_g}{RT}, \tag{4.4.6}$$

where R is the universal gas constant and W_g is the molecular weight of the gas mixture, given by

$$1/W_g = m_f/W_f + m_a/W_a + m_p/W_p \tag{4.4.7}$$

where W_f, W_a and W_p are the molecular weights of the fuel, air and products respectively.

The static enthalpy is calculated using

$$h = (\int_0^T c_p(T')dT' - h_0) + m_f H \tag{4.4.8}$$

where $c_p(T)$ is the specific heat of the gas mixture, and $h_0 = \int_0^{T_{ref}} c_{pa}(T')dT'$, c_{pa} is the specific heat of air and T_{ref} is a reference temperature at which the static enthalpy of the air is zero.

The specific heat of each component is assumed to be a polynomial function of temperature, which is expressed as

$$c_p = a + bT + cT^2 + dT^3. \tag{4.4.9}$$

The specific heat of the gas mixture is defined by

$$c_p = m_f c_{pf} + m_a c_{pa} + m_p c_{pp} \tag{4.4.10}$$

where c_{pf}, c_{pa}, and c_{pp} are the specific heat of the fuel, air and the products respectively.

A disadvantage of the model presented above is to neglect the chemical kinetics of the

combustion. In fact, this model can not simulate the complex processes of extinction and ignition of diffusion flames. Therefore, as long as fuel and oxidant statistically co-exist at a point, i.e., the average local mass fraction m_f and m_a are not zero at the same time, this combustion model predicts that chemical reactions take place even if the mixture is beyond the range of flammability. However, since the aim of the present study is to predict the fire growth and spread within enclosures after ignition of flames, the model presented here is suitable for this aim. Actually combustion models based on the eddy dissipation concept are widely used in fire engineering applications. Future work is directed at this deficiency.

4.4.2 Implementation of the model within CFDS-FLOW3D

A computer programme of the gas phase combustion model described above has been developed by the author using the FORTRAN language and has been incorporated in the commercial CFD software CFDS-FLOW3D(version 2.3.2) .

To implement the model described in the previous subsection, two additional scalars are introduced to represent the fuel mass fraction m_f and the mixture fraction f. Consequently, two additional governing equations are added. This is activated by using a keyword under OPTIONS subcommand in the data file of Command Language Frontend of CFDS-FLOW3D. The air mass fraction m_a and the products mass fraction m_p are algebraically calculated in terms of the equations (4.4.4) and (4.4.5).

CFDS-FLOW3D provides a user subroutine named USRSRC to allow users to add

sources and sinks of the governing equations. Since the mixture fraction is a conserved variable, no source and sink terms are added into its governing equation. But a sink term is added into the governing equation for the fuel mass fraction. The sink term is calculated according to equation (4.4.2). Since in the USRSRC subroutine the discrete equation is dealt with, the actual sink term is the product of R_f in equation (4.4.2) and the current cell volume, i.e.,

$$R_f^n = -R_f \times \text{volume}(n) = -A\min(\bar{C}_f, \bar{C}_o/s)\frac{\varepsilon}{k} \times \text{volume}(n)$$

$$= -A\rho\min(m_f, m_a c_o/s)\frac{\varepsilon}{k} \times \text{volume}(n) \qquad (4.4.11)$$

where n is the index of the current cell and c_o stands for the oxygen mass fraction in the fresh air. To enhance numerical stability, equation (4.4.11) is linearised according to Patankar[1980], as follows:

$$R_f^n = S_{fu} + S_{fp}\, m_f \qquad (4.4.12)$$

where

$$\text{if } m_{fs} = m_f^\circ,\ S_{fp} = 0,\ S_{fu} = 0; \qquad (4.4.13)$$

if $m_{fs} < m_f^\circ$,

$$S_{fu} = -A\rho\min(m_f^\circ, m_a^\circ c_o/s)\, m_{fs}/(m_{fs} - m_f^\circ)\frac{\varepsilon}{k} \times \text{volume}(n), \qquad (4.4.14)$$

$$S_{fp} = A\rho\min(m_f^\circ, m_a^\circ c_o/s)/(m_{fs} - m_f^\circ)\frac{\varepsilon}{k} \times \text{volume}(n), \qquad (4.4.15)$$

where m_f° and m_a° are the current values of the fuel mass fraction and the air mass fraction respectively, c_o is the mass fraction of oxygen in the fresh air and m_{fs} [$= (f - f_s)/(1-f_s)$] is the stoichiometric value of the fuel mass fraction.

Since the heat released due to combustion is represented by the modified

enthalpy(equation (4.4.8)), there is no source term added into enthalpy equation for combustion. Furthermore, the gas temperature is calculated by solving equation (4.4.8). After the enthalpy equation is solved in each outer iteration of a time step, the tentative enthalpy (h) at every node of the mesh is known. The local temperature is then calculated from equation (4.4.8) using the Newton iterative method. The temperature calculation is performed in three user subroutines provided by CFDS-FLOW3D named USRDEN, USRDND and USRDNN. The subroutine USRDEN is for internal nodes of the mesh while the subroutines USRDND and USRDNN are for the Dirichlet boundary conditions and the Neumann boundary conditions respectively. In addition, the density calculations in terms of equations (4.4.6) and (4.4.7) are also performed in the same three user subroutines.

4.5 A Demonstration of the Gas Phase Combustion Model

In this section the capabilities of the computer programme of the eddy dissipation model used for gaseous combustion described in the previous section is demonstrated. The demonstration involves a standard test case known as the Harwell Furnace[Harwell Lab., 1994]. Predictions from the model are compared with results generated by the standard commercial package. The results have been reported in [Jia et. al., 1995].

The Harwell Furnace is a standard test case included in the CFDS-FLOW3D (version 3.3) software. This version of CFDS-FLOW3D has an eddy dissipation combustion model as a standard component of the software. Comparison data is generated for this test case using this software. The geometry of the furnace is cylindrical and is 1m in length and 0.15m in radius(figure (4.5.1)). The fuel (methane) and oxidant (air) are

injected into the furnace from its circular base. The fuel enters the furnace from a circular inlet while the oxidant flows into the furnace through a concentric annulus inlet. An outlet is provided at the opposite circular end of the furnace.

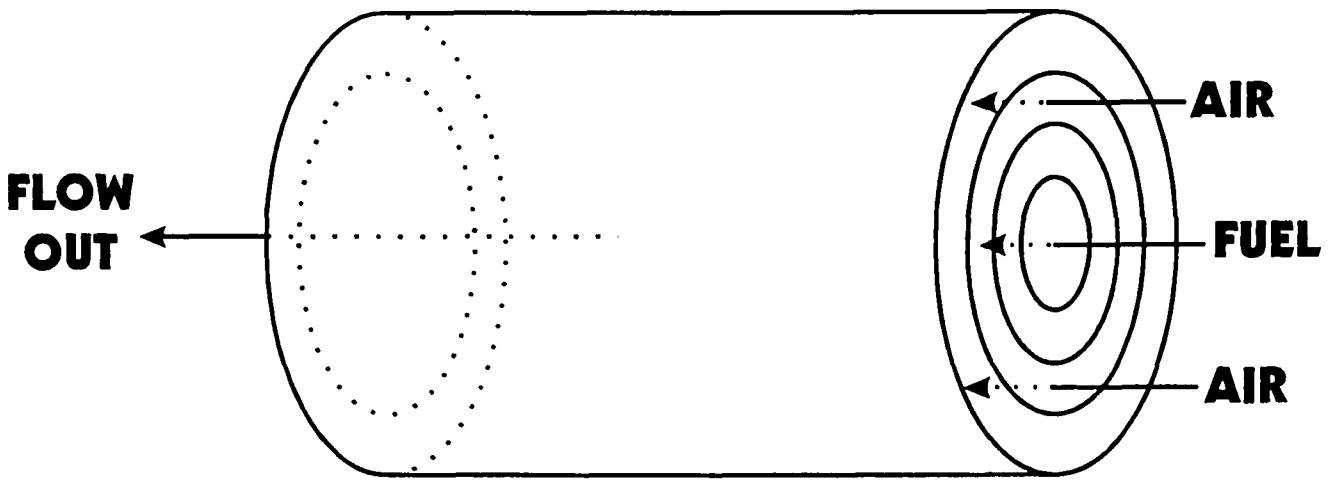

Fig. 4.5.1: schematic representation of the Harwell Furnace.

The geometry is modelled using a cylindrical coordinate system. The flow is symmetrical to the central line of the furnace thus allowing a two dimensional representation. Both the CFDS-FLOW3D combustion model and the model presented here use identical computational meshes, boundary conditions, initial conditions and physical properties.

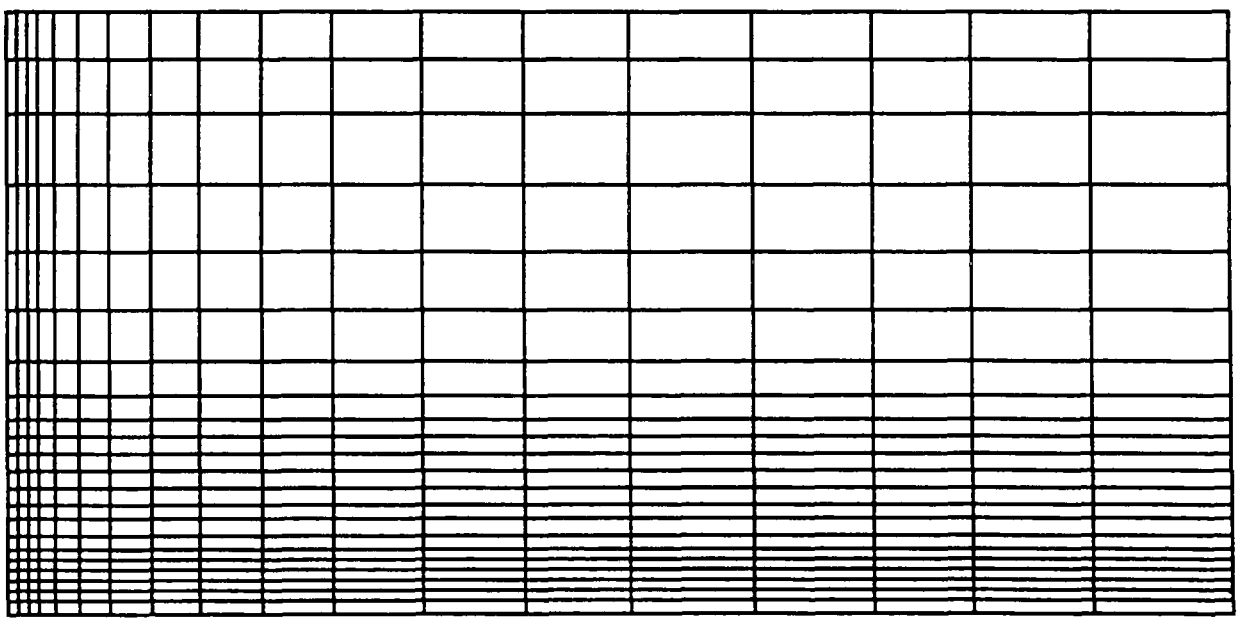

the central axis

Fig. 4.5.2: The mesh used for the computation of the Harwell Furnace.

The two dimensional mesh consists of 18×22(396) cells. The mesh is plotted in figure (4.5.2). A cylindrical coordinate system is used. The boundary condition for the central axis of the furnace is set as a symmetry plane. The walls are assumed to be isothermal with a temperature of 400K. Both the models are run in steady-state mode and convergence is assumed when the mass source residual falls below 5×10^{-6}.

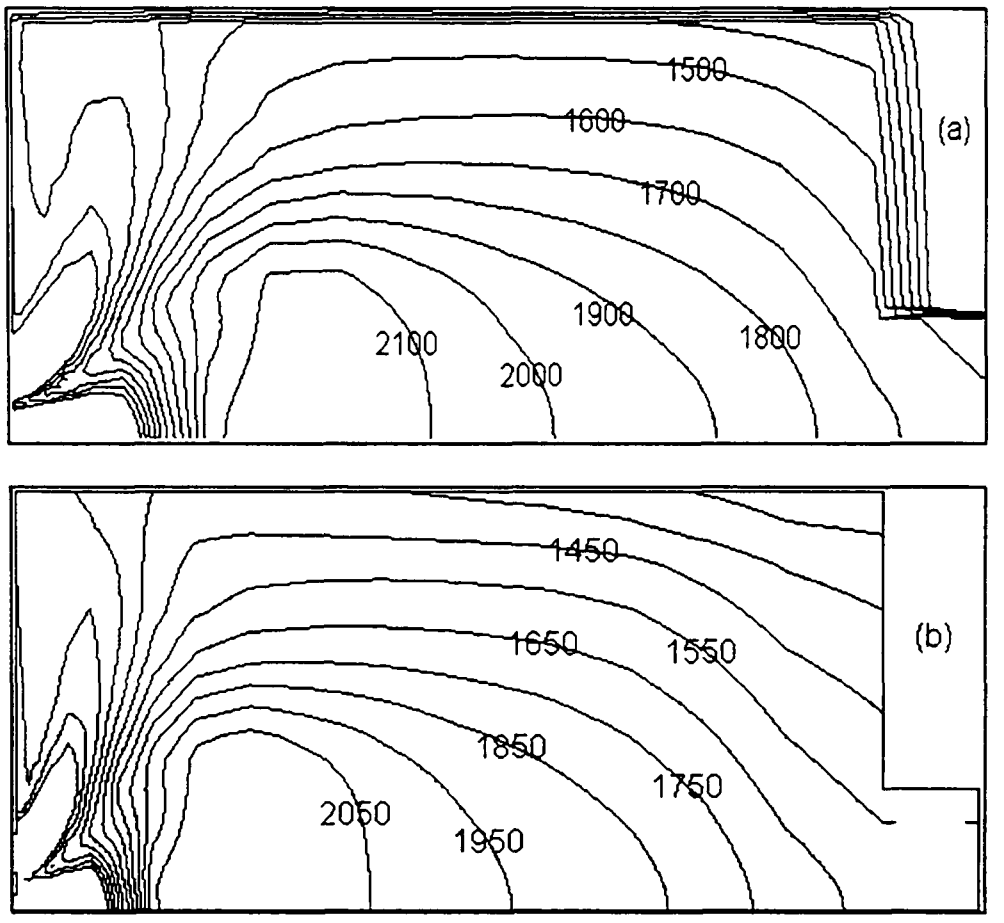

Figure 4.5.3: Temperature contours in the Harwell Furnace(unit:K):
a) produced by the CFDS-FLOW3D combustion model(MODEL2),
b) produced by the model described in section 4.4 of this thesis(MODEL1).

To facilitate the discussion below, the model presented in this study is named as MODEL1 while the standard model in the CFDS-FLOW3D (version 3.3) is named as MODEL2.

The temperature contours and the flame structure produced by both models are depicted in figure (4.5.3). While as may be expected, both models produce similar predictions, the numerical performance of each model is significantly different. MODEL1 produced a converged solution in 125 seconds and required only 441 iterations while MODEL2

required 258 seconds and 562 iterations. The difference in efficiency is possibly due to the nature of the linearization of the source term for the fuel mass fraction.

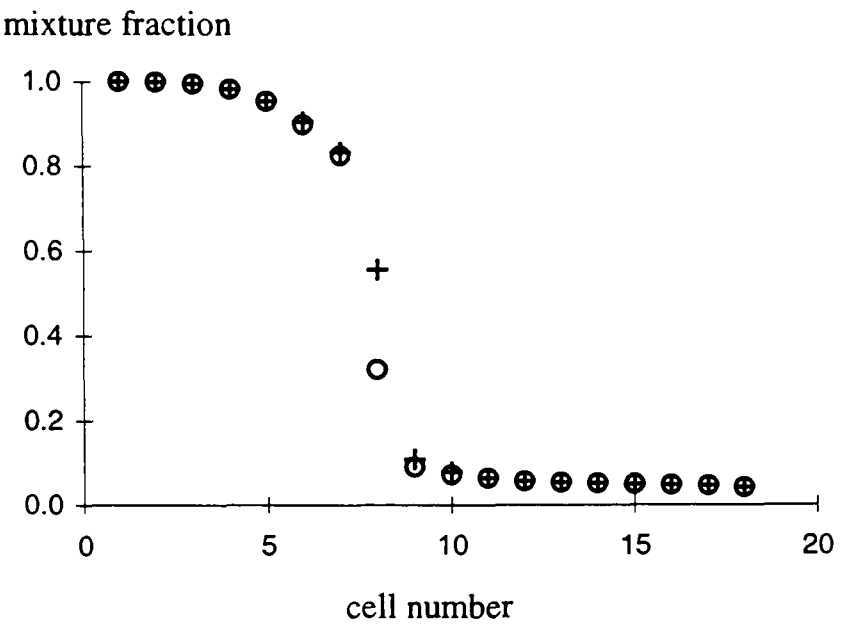

Fig. 4.5.4: The mixture fraction profiles along the central line.
+ : predicted by the model in CFDS-FLOW3D (MODEL2);
o : predicted by the model described in section 4.4 of this thesis(MODEL1).

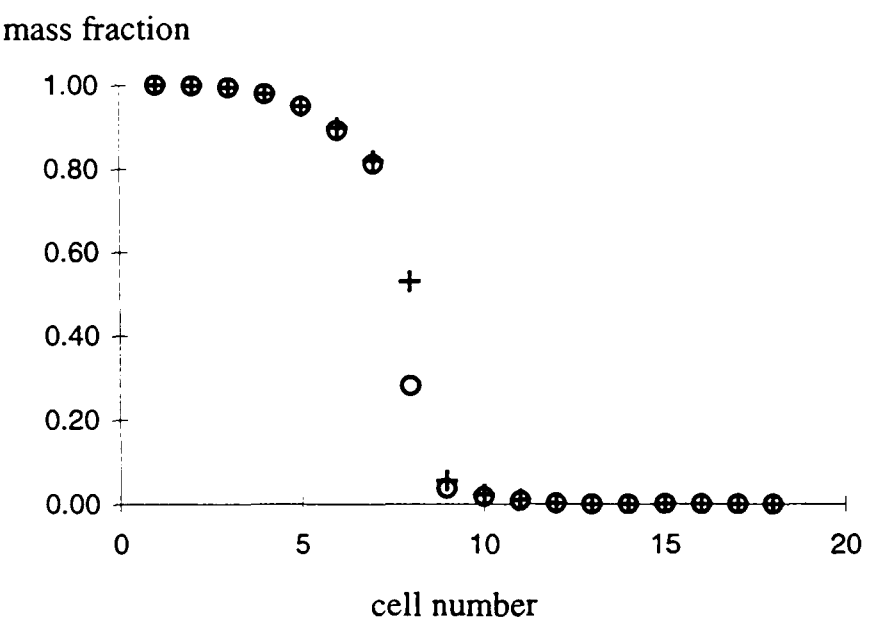

Fig. 4.5.5: The fuel mass fraction profiles along the central line.
+ : predicted by the model in CFDS-FLOW3D(MODEL2);
o : predicted by the model described in section 4.4 of this thesis(MODEL1).

Figure (4.5.4) plots the mixture fraction profiles along the axis of the furnace. Except at the 8^{th} cell, both the models produced nearly identical results. MODEL1 predicts a lower mixture fraction at the 8^{th} cell when compared with MODEL2. The fuel mass fraction profiles along the axis of the furnace are presented in figure (4.5.5). Corresponding to lower MODEL1 prediction of the mixture fraction, MODEL1

produces lower fuel mass fraction than MODEL2 while the two models generate almost the same predictions of fuel mass fraction elsewhere along the axis of the furnace. From figures (4.5.4) and (4.5.5) it can be inferred that the flame sheet along the central line locates at the 8th cell because there is a steep drop in the values for the mass fraction of fuel and the mixture fraction at that cell.

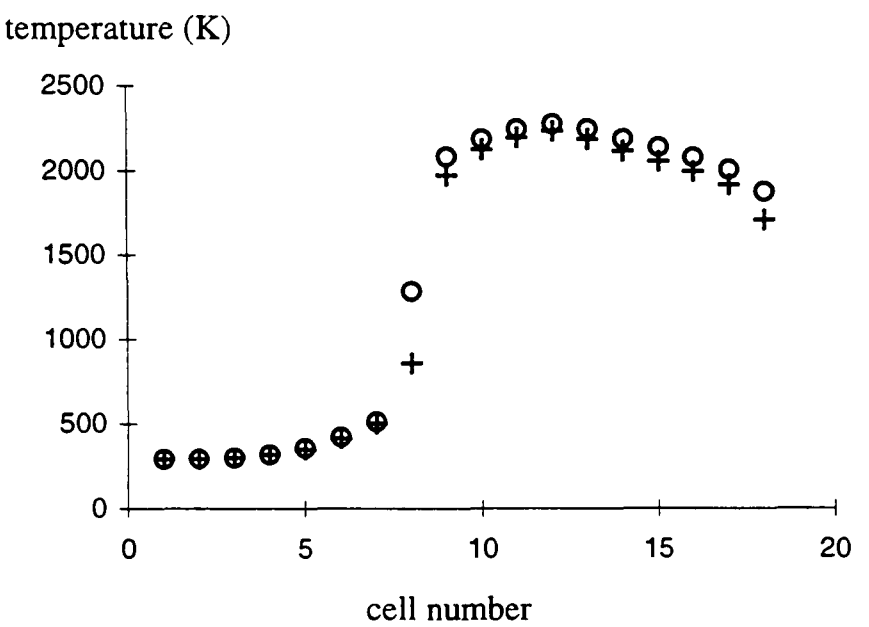

Fig. 4.5.6: The temperature profiles along the central line.
+ : predicted by the model in CFDS-FLOW3D(MODEL2);
o : predicted by the model described in section 4.4 of this thesis(MODEL1).

Figure (4.5.6) outlines the temperature profiles along the axis of the furnace. The fact that MODEL1 generates the lower mixture fraction and fuel mass fraction at the 8^{th} cell along the axis indicates that MODEL1 predicts more intense chemical reaction at this cell than MODEL2. Consequently, MODEL1 yields a higher temperature prediction at this cell. Meanwhile, the temperatures along the axis calculated from both models are very close elsewhere.

Finally, the comparison between the two models for the values of the mixture fraction at the cross section plane of the flame tip are demonstrated in figure (4.5.7). Once again the predictions from both the models are almost identical.

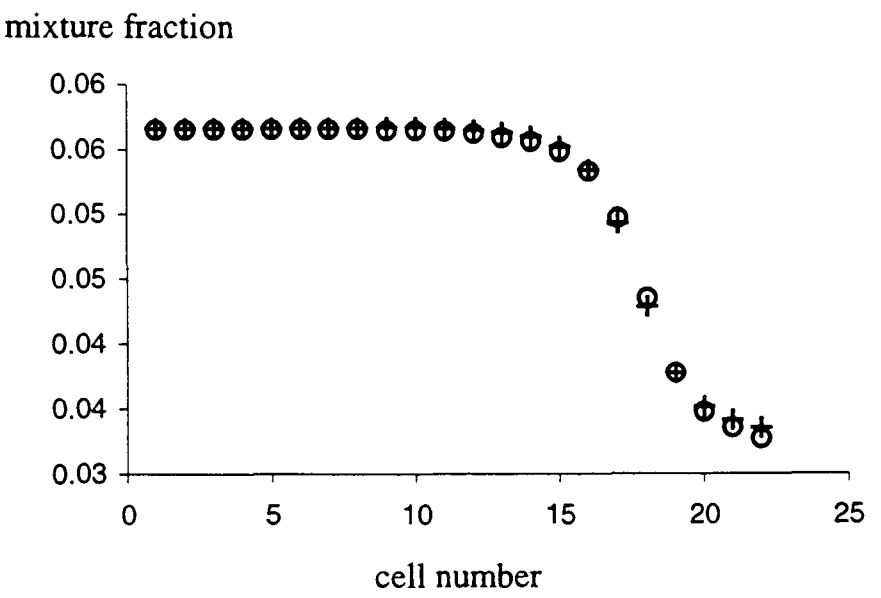

Fig. 4.5.7: The cross-section mixture fraction profiles at the flame tip.
+ : predicted by the model in CFDS-FLOW3D(MODEL1);
o : predicted by the model described in section 4.4 of this thesis(MODEL1).

Figures (4.5.3) to (4.5.7) demonstrate that the results of the two models are in extremely good agreement except the values at the flame sheet. This fact verifies the computer programme for the gas phase combustion model developed in the present study.

4.6 Concluding Remarks

A brief description of diffusion flames has been presented. Most compartment fires involve combustion in the regime of the diffusion flame. Consequently, in order to simulate the flame spread within the enclosures, it is essential to model diffusion flames. Several gas phase combustion models have been reviewed. The gaseous combustion model based on the eddy dissipation concept was selected to simulate the gas phase combustion in the present study. A field model code was developed using the eddy dissipation concept. The code was examined by comparing the predictions from the code with the predictions from the eddy dissipation combustion model as supplied in the commercial CFD software CFDS-FLOW3D (version 3.3) for the

Harwell Furnace which is a standard test case in the software. The two models produce results in excellent agreement. The model code for the gas phase combustion developed here will be further validated in chapter 6 by using it to simulate the same Steckler room fire as the one reported in chapter 3.

Chapter 5

SOOT FORMATION AND RADIATION

5.1 Introduction

Thermal radiation is an important, often the dominant, heat transfer mode in compartment fires. The amount of the radiative heat losses from the flames is substantial and is transmitted by electromagnetic waves to the surroundings. Radiation from the hot layer, accumulated beneath the ceiling, and the fire is responsible for preheating distant objects and even heating them up to a condition ready to burn. The energy required to sustain the endothermic solid gasification processes are also mainly transferred by radiative flux from the fire to the solid surface.

Due to radiative heat losses, the flame temperature is less than the adiabatic flame temperature. Simulations using models with and without radiation components may produce quite different results[Kaplan et al., 1994]. This is because the model with radiation will yield lower flame temperatures due to the radiative heat losses, leading to a lower chemical heat release rate. Consequently, the reduced heat release rate decreases the volumetric expansion causing the flame to shrink. As a result, the overall temperature distribution within the flame changes, which further alters the distribution of species concentrations and soot volume fraction.[Kaplan et al., 1994]

Except energy exchange by radiation between surfaces(i.e. walls, ceilings, floors furniture, etc.), participating media also emit, absorb or scatter radiation. From the thermal radiation viewpoint, the primary gaseous species in hydrocarbon fires are

water vapour and carbon dioxide. They strongly absorb and emit in the thermal radiation spectrum of 1 to 100 μm[Tien et al., 1995]. Soot particles usually form as the result of incomplete combustion of the hydrocarbon fuels and their contribution often becomes important and dominant in many radiation calculations.

Exact calculations of radiative heat transfer are often very tedious and time consuming due to the spectral structure of radiative properties of the combustion products and the huge calculations required by the resolution of the transfer equation. To alleviate this problem, simplifications are needed. The simplifying assumptions and models used in the integrated flame spread model to evaluate the radiative properties and resolve the radiative transfer equation will be presented in this chapter.

In section 5.2, the mechanisms of soot formation and the soot model used in this study are briefly discussed. Some basic conceptions of radiation and the transfer equation will be outlined in section 5.3. The evaluation of the radiative properties of the soot-gas mixture is presented in section 5.4. The two radiation models used in the present study, the six-flux model and the discreet transfer method are described in section 5.5. Section 5.6 is concerned with the technical treatments in the radiation models used in this study. Finally, some concluding remarks are made in section 5.7.

5.2 Soot Formation and Modelling

The formation of soot has attracted considerable attention due to its importance. It is associated with incomplete combustion. It not only reduces combustion efficiency, but also generates hazardous effects on human health and environments. Due to radiative

heat losses, the flame temperature is reduced. And surrounding combustible solid material can be heated and ignited by radiative heat fluxes from the fire. Soot volume fraction is essential to obtain radiative properties to predict radiative heat flux in fire. In fire, soot plays a dominant role in radiative heat transfer.

5.2.1 Soot formation

The formation of soot is an extremely complicated series of chemical and physical processes. In these sequential or paralleling processes, a hydrocarbon fuel molecule containing few carbon atoms is converted into a carbonaceous agglomerate containing some millions of carbon atoms through interactions of intermediate radicals, coagulation and agglomeration and surface reactions. Before stepping into modelling these complex processes, it is necessary to have a basic understanding of their features although soot processes are poorly understood in many aspects.

The formation of soot can be roughly described in four distinct phases: 1) precursor formation; 2) particle inception; 3) particle growth; and 4) particle oxidation [Glassman, 1988]. First of all, hydrocarbon fuel molecules are broken down to small intermediate radicals, which leads to precursors from these species. Through interactions of these small hydrocarbon radicals, aromatic rings are created. They further grow to larger polycyclic aromatic hydrocarbons (PAH) mainly via addition of acetylene. When the aromatic structures contain sufficiently large number of carbon atoms, particle nuclei are formed. Such condensed phase carbon particles coagulate simultaneously and surface growth by adsorbing gaseous hydrocarbon species takes place. Surface growth causing a large soot mass increase mainly determines the final

soot concentration. Coagulation leads to an increase of particle size and decrease of the particle number density. Paralleling to all these chemical and physical processes, the precursors and all subsequent structures are also attacked by OH radicals and O_2 molecules. [Glassman, 1988]

"The chemistry of fuel pyrolysis, and thus fuel structure, plays an important, and possibly dominant role, in sooting diffusion flames"[Glassman, 1988]. However, the decisive influence of the fuel molecular structure occurs only at the early stages of the formation of soot, "first by providing more efficient reaction partners for formation of aromatic molecules and second by affecting the generation of hydrogen atoms"[Frenklach et al., 1986].

"There must be an underlying fuel independent general mechanism that is modified only with respect to alternative routes to intermediates. These routes are simply affected by the combustion system temperature and the general character of the initial. The relative propensity of one fuel to soot compared to another may arise primarily from a difference in the initial rate of formation of the first and second ring structures and that the mechanisms controlling the growth of large condensed ring aromatics, soot nucleation, soot growth, etc., remain not only essentially unchanged, but that the growth steps of the large aromatic structures leading to soot nucleation are significantly faster than the formation of the initial rings. Thus the formation of the initial rings controls the rate of incipient soot formation. Consequently, the incipient soot formation particle concentration determines the soot volume fraction or the total amount of soot formed"[Glassman, 1988].

It is noted that the process of soot formation is relatively slow compared with the production of other chemical species(H_2O, CO_2)[Coppalle et al., 1994]. Due to this chemically kinetic limited character, the effects of temperature and concentration on soot formation are important. "The higher the temperature the greater is the pyrolysis rate and precursor formation and thus the incipient soot formation rate". "Since the soot formation mechanism could involve a relatively high activation energy step, the whole process could be so highly temperature dependent that there may be a critical temperature for soot onset that only above this threshold temperature are the kinetic rates fast enough for soot to be formed."[Glassman, 1988]

Soot formation starts on the fuel rich side in the reaction zone. This process takes place in thin sheets with comparatively narrow range of mixture fractions and high temperatures[Moss et al., 1988; Honnery et al., 1992; Gore and Faeth, 1988]. Nucleation takes place on the fuel side close to the flame front[Kim et al., 1984]. Unlike gaseous molecules, soot particles are not diffused due to the concentration gradients. The existence of soot particles in fuel lean region is attributed to convection. It appears that soot growth is temperature-time history dependent[Honnery et al., 1992], which may cause complexity and uncertainty to models. In turbulent diffusion flames, soot production is influenced by the turbulent mixing. Experimental data show that the soot volume fraction can not be expressed as a unique function of the mixture fraction[Coppalle et al., 1994; Kent and Honnery, 1987]. Unlike gaseous species whose concentrations are functions of the mixture fraction, a conserved variable in the flamelet approach, soot formation rate rather than concentration is supposed to be functional dependence on the mixture fraction and temperature[Moss et al., 1988].

Since soot volume fraction is essential to obtain radiative properties to predict radiative heat flux and soot plays dominant roles in radiation heat transfer in fire, it is necessary to model soot formation.

5.2.2 Review of soot modelling

There are two kinds of sooting models - kinetic soot models and empirical models. Even though parameters of models in the first category need calibrating based on experimental data to produce good agreement with experimental measurements, these models try to simulate kinetically the processes of nucleation, surface growth, coagulation and oxidation. They incorporate the flamelet or PDF technique hopefully creating good predictions in the soot concentration and the flame structure. One of their aims is to provide a tool to give insight into the processes of soot formation. Detailed or reduced chemical mechanisms are employed leading to tens of chemical steps and species involved in the computation. Consequently powerful computers are required. Models in the second category are expected to produce rough but reasonable soot concentration. They are aimed at engineering applications where only limited computer power is available and reasonable predictions are required.

Generally, empirical soot models do not take detailed kinetic mechanisms of soot formation into account. However, some key features of soot formation such as the locations of this process are included in models. Only one equation for soot volume fraction or soot concentration is used to describe soot transport. The production rate of soot is derived directly from experimental data. Therefore, these soot models are simple, rely on empirical data and are expected to produce only reasonable results.

5.2.2.1 Kinetic soot models

Mechanisms of soot formation and oxidation are taken account into these models. Detailed measurements of soot and species distributions and temperatures in flames provide the basis of constructing the model structure and variables and calibration of model parameters.

Magnussen et al.[Magnussen et al., 1977; 1978] proposed a soot model for turbulent diffusion flame based on the eddy dissipation concept, which assumed combustion takes place in the fine structures with Kolmogorov microscale responsible for the dissipation of turbulence into heat. "Soot was assumed to form both in the heated fine structures and in the surrounding fluid"[Magnussen et al., 1978]. Soot formation is assumed to undergo two stages - radical nuclei formation and soot particle formation. The rates of nuclei and particle formation are determined by the local fuel concentration, temperature, nuclei density and particle density. The oxygen is supposed to be responsible for the destruction of the soot particles and radical nuclei. The oxidation rate is determined by the rate of dissipation of the eddies. This soot formation and oxidation model was used to simulate jet C_2H_2 diffusion flames. With the rate constants adjusted to match the corresponding experimental data, the model produced reasonable levels of soot concentrations.

A simple soot model was developed by Kenndey et al.[1990]. Only a single equation for soot volume fractions was used to describe the soot transportation process in laminar flames. The rates of soot volume formed by nucleation, surface growth and destruction due to oxidation were taken into account. Particle number density was

assumed constant based on the two following experimental measurements: a) similar number densities in different flames and b) the weak dependence of the rate of surface area on the particle number density. The rate of surface growth was expressed in terms of the mixture fraction. Both the molecular oxygen and OH radicals were assumed to attack the soot particles in the oxidising process. The model was calibrated by experimental data.

A model proposed by Moss et al.[Moss et al., 1988; 1995] included all essential steps of soot formation: nucleation, surface growth, coagulation and oxidation. Soot volume fraction and particle number density were selected to represent the balance between the soot transport and production. This model exploited the key feature of soot formation that soot formation is confined in a comparatively narrow range of mixture fraction values. "The critical features to be established in respect of the model are evidently the mixture fraction and temperature fields in the sooting region and, in particular, the extent to which the simplification afforded by flamelet modelling can be sustained in the presence of increasing soot formation"[Moss et al., 1988]. Like the models outlined above, the parameters in this model were also adjusted from detailed experimental measurements.

The pyrolysis of the fuel plays a dominant role in soot formation. Based on this fact, Leung et al.[1991] proposed a model "in which global reaction rates for soot formation are related to the concentration of a characteristic pyrolysis product, taken to be acetylene". Nuclei are formed as acetylene is broken down and surface growth is attributed to adsorption of acetylene on the surface of the particles. To take the ageing effect on soot particles into account, a function of surface area was used to determine

the growth rate.

The model parameters in the models referred to previously need calibrating from individual experimental data to produce reasonable estimates of soot formation in the specific flame. "Since the amount of soot formed from a particular fuel has a complex dependence on the overall combustion process, there is no one characteristic parameter that can define the amount formed per unit weight of fuel consumed. Both the flame type and various physical parameters determine the extent of soot formation from a given fuel"[Glassman, 1988]. Therefore, it is questionable and uncertain to directly apply these models to different flames, particularly to building fires. Consequently, some empirical soot models were proposed to fit the circumstances of building fires or flames in which solid fuels are involved.

5.2.2.2 Empirical soot models

Generally, empirical soot models do not take detailed kinetic mechanisms of soot formation into account. However, some key features of soot formation such as the locations of this process are included in models. Only one equation for soot volume fraction or soot concentration is used to describe soot transport. The production rate of soot is derived directly from experimental data. Therefore, these soot models are simple and expected to produce only reasonable results.

A soot model proposed by Novozhilov et al.[1996] contains carbon as a kind of product in the one-step global chemical reaction. The carbon represents soot formed in flames. Soot is created near the reaction zone and transported by convection. The soot

concentrations are derived from the local mixture fraction. However, how to empirically obtain the coefficient before the carbon in the formula of the one-step global reaction was not mentioned in the article.

In Yan and Holmstedt's paper[1996], the converting efficiency from fuel to soot was assumed constant and chosen with reference to some experimental measurements. "The soot formation rate is simply assumed to be locally proportional to either fuel supply rate or fuel consumption rate. No oxidation is considered." A transport equation for soot concentration was used and the soot volume fraction was calculated from the soot concentration with a constant soot density.

5.2.3 The soot model used in the present study

The soot model used in this study is based on the fact that soot formation takes place in the fuel rich side of chemical reaction region and the highest soot concentration is found in the same region[Moss et al., 1988; Honnery et al., 1992; Gore and Faeth, 1988]. The measured mean soot concentration in the region of soot formation is considered as a final result of the soot formation processes: nucleation, surface growth, coagulation and oxidation. Therefore, in this region soot concentrations are assumed to remain constant, taken as the measured mean values. While outside the soot formation region it is assumed that soot formation and oxidation has ceased due to the lower temperatures thus soot particles are transported by convection.

According to the description in chapter 4, when the gas phase combustion is used, two scalar variables, the mixture fraction(f) and the fuel mass fraction(m_f), are employed.

When the soot formation and transportation are to be modelled, in addition to the already used two scalars, one extra scalar variable is introduced in this study to represent the mass fraction of soot particles(m_{soot}). An arbitrarily small value is assigned to the diffusion coefficient of this scalar since the soot particles do not diffuse due to the difference of the soot concentration. The soot volume fraction(f_v) essentially required for the radiation calculation is obtained by

$$f_v = m_{soot}\rho/\rho_{soot}, \tag{5.2.1}$$

where ρ and ρ_{soot} are the densities of the gas mixture and the soot respectively. A constant soot density ($2000kg/m^3$)[Fairweather et al., 1992] is used. Measurements show that the soot formation takes place in thin sheets representing a narrow mixture fraction range. Moss et al.[1988] suggested that this range be between 0.07 to 0.2 for ethylene-air flames. The soot model used in this study assumes that within this mixture fraction range the soot volume fractions remain constant, taking the measured mean values which vary from one solid fuel to another. Mean soot volume fractions in various flames have been measured by Hubbard and Tien[1978]. Soot particles are then transported somewhere else in the flow domain by convection.

5.3 Thermal Radiation in Participating Media

Radiative heat transfer is the dominant pattern of heat transfer in many combustion systems. It is known that radiation becomes the dominant mode of heat transfer when the characteristic lengths of fires exceed 0.2m[Tien et al., 1995]. In the room fire scenario, radiation from the hot layer, accumulated beneath the ceiling, and the fire is responsible for preheating distant objects and even heating them up to a condition ready to burn. The energy required to sustain the endothermic solid gasification

processes are also mainly transmitted by radiation from the fire to the solid surface.

To calculate radiation for a room fire scenario, we need to know radiative properties of the participating medium. In this section, some basic concepts of thermal radiation are introduced and some methods to calculate the radiative properties of participating media are described.

5.3.1 Blackbody thermal radiation

The monochromatic radiant intensity per unit area from a blackbody will be denoted by $I_{b\nu}$. By Planck's law, $I_{b\nu}$ is given as

$$I_{b\nu} = 2h\nu^3 n^2 / \{ c_0^2 [\exp(h\nu/kT) - 1 \} \tag{5.3.1}$$

where h is the Planck constant, ν is the frequency of the radiation, n is the index of refraction for the medium and c_0 is the speed of light in the medium.

The total radiant intensity per unit area from a blackbody, I_b, can be obtained by integrating over all frequencies, giving

$$I_b = \int_0^\infty I_{b\nu} \, d\nu = n^2 \sigma T^4 / \pi \tag{5.3.2}$$

Since the radiation intensity of a blackbody is independent of direction and the differential solid angle $d\Omega = \sin\theta d\theta d\phi$, the total hemispherical power per unit area of a blackbody, E_b, is given by the integration over the entire hemisphere

$$E_b = \int_0^{2\pi} \int_0^{\pi/2} I_b \cos\theta \sin\theta d\theta d\phi = n^2 \sigma T^4 \tag{5.3.3}$$

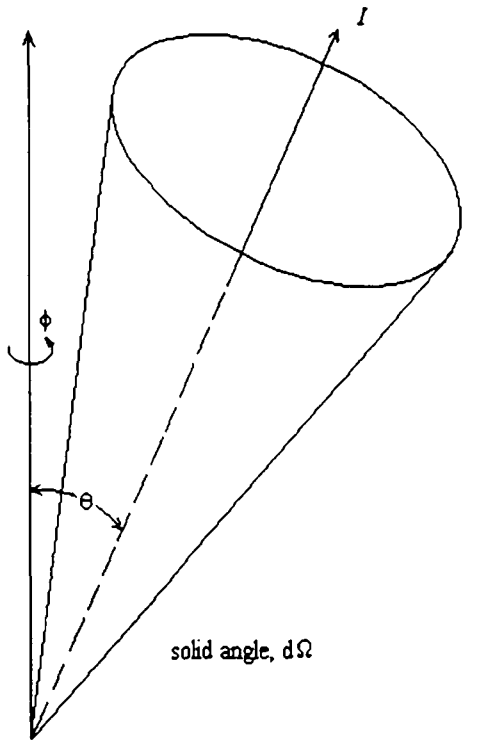

Fig. 5.3.1: Coordinate system for radiation intensity.

5.3.2 The equation of radiation transfer in participating media

The radiative heat transfer in a medium is described by

$$\frac{d}{dl} I(\Omega,r) = -(a + s)\, I(\Omega,r) + aI_b(r) + \frac{s}{4\pi} \int_{\Omega'=4\pi} I(\Omega',r)\, \Phi(\Omega' \rightarrow \Omega) d\Omega' \qquad (5.3.4)$$

where Ω is a specified direction; l represents the physical pathlength along Ω; r is the position of a point; $I(\Omega,r)$ stands for radiation intensity along Ω at position r; a and s are absorption and scattering coefficients of the medium respectively; $I_b(r)$ is the blackbody radiation intensity; and $\Phi(\Omega' \rightarrow \Omega)$ is the scattering phase function. This equation is the base of developing any reasonable numerical calculations of radiative heat transfer.

In many engineering applications, the effect of scattering are negligible, since "scatter is important only when considering the impact of fly ash in coal combustion systems

and sometimes in the dense oil spray in diesel engines or the near burner region of furnaces"[Sarofim, 1986]. When scatter is neglected, the equation (5.3.4) is simplified as

$$\frac{d}{dl} I(\Omega,r) = -aI(\Omega,r) + aI_b(r) \qquad (5.3.4a)$$

5.3.3 Surface radiation

The monochromatic radiation from a blackbody represents the maximum amount of radiant energy emitted at a given temperature and a given frequency(or wavelength). The monochromatic emissive power of a real surface (non-blackbody) is expressed as

$$I_\lambda = \varepsilon_\lambda I_{b\lambda} \qquad (5.3.5)$$

where ε_λ is the monochromatic emissivity of the real surface and λ is the wavelength of the radiation. ε_λ is less than unity.

Real surfaces also absorb a fraction of the energy reaching on them. By Kirchhoff's law, the emissivity and absorptivity must be equal to maintain thermodynamic equilibrium, i.e.

$$\alpha_\lambda = \varepsilon_\lambda \qquad (5.3.6)$$

The spectral dependence of emissivity of a real body is simplified by introducing the concept of a grey body for which the emissivity is independent of wavelength. In this case, the subscript is hence removed and the equal relationship between emissivity and absorptivity is still held, i.e.

$$\alpha = \varepsilon \qquad (5.3.7)$$

5.3.4 Emissivity of participating media

The emissivity of a participating medium is defined as

$$\varepsilon_\lambda = I_\lambda / I_{b\lambda} \tag{5.3.8}$$

When a monochromatic beam of radiation with zero incident radiation passes through a medium having uniform temperature and radiative properties, the emissivity for pathlength S is explicitly expressed by

$$\varepsilon_\lambda = 1 - \exp(-\kappa_\lambda S) \tag{5.3.9}$$

where κ_λ is the spectral extinction coefficient which includes the effects of both absorption and scattering within the medium.

$\kappa_\lambda S$ is called the optical thickness. For nonhomogeneous media it is defined as

$$\tau_\lambda = \int_0^x \kappa_\lambda dx \tag{5.3.10}$$

The optically thin limit occurs when $\tau_\lambda << 1$. In this situation any intervening absorption of radiation by the medium will be negligible. The radiant beam will freely travel to the bounding surfaces. Radiative interaction between various parts of the medium is trivial. The Planck mean absorption coefficient for optically thin media is defined as

$$\kappa_P = \pi/(\sigma T^4) \int_0^\infty \kappa_\lambda I_{b\lambda}\, d\lambda \tag{5.3.11}$$

, representing the average property over the whole range of wavelength.

The opposite extreme of $\tau_\lambda << 1$ is the optically thick limit under the condition of $\tau_\lambda >> 1$. In this case the radiant flux is only affected by the local emission and the

radiation transfer within the medium can be treated as a diffusion process, i.e.,

$$q_\lambda = -4/(3\kappa_\lambda)\mathrm{d}E_{b\lambda}/\mathrm{d}s \tag{5.3.12}$$

where q_λ is the radiant flux[Tien et al., 1995]. Correspondingly, the mean absorption coefficient for optically thick media, called Rosseland mean absorption coefficient, is defined as

$$1/\kappa_R = \int_0^\infty 1/\kappa_\lambda \, \mathrm{d}E_{b\lambda}/\mathrm{d}E_b \mathrm{d}\lambda \tag{5.3.13}$$

For the media neither optically thin nor optically thick, the total emissivity of a medium is defined as

$$\varepsilon_t = \pi/(\sigma T^4) \int_0^\infty \varepsilon_\lambda I_{b\lambda} \, \mathrm{d}\lambda \tag{5.3.14}$$

which is an average property over all wavelength.

5.4 The Radiative Properties of Gas-soot Mixtures

For homogeneous and isothermal mixture of soot, CO_2 and H_2O, the total mixture emissivity, ε_m, is approximated by[De Ris, 1979]

$$\varepsilon_m = \varepsilon_s + \varepsilon_g - \varepsilon_s \varepsilon_g \tag{5.4.1}$$

where ε_g is the gaseous emissivity of CO_2 and H_2O, ε_s is the soot emissivity. The absorption coefficient, α_m, of the mixture is given under gray assumption by

$$\alpha_m = \alpha_s + \alpha_g \tag{5.4.2}$$

where α_s and α_g are the absorption coefficient of soot and gases respectively. The evaluation of the radiative properties of soot and CO_2 and H_2O is described below.

5.4.1 The radiative properties of gases

The dominant gaseous species for absorption and emission in fires are CO_2 and H_2O. As the calculation of the integration over the entire wavelength in equation (5.3.14) is complicated and time consuming, some approximate models have been proposed.

A very simple expression for the absorption(emission) of CO_2 and H_2O in hydrocarbon fires was proposed by Magnussen and Hjertager[1977]. The absorption coefficient of CO_2 and H_2O is evaluated by

$$\alpha_g = 0.1(m_c + m_w) \tag{5.4.3}$$

where m_c and m_w are the mass concentration of CO_2 and H_2O respectively.

More accurate evaluation of radiative properties of CO_2 and H_2O was reported by Modak[1979]. The emissivity of the gaseous mixture of CO_2 and H_2O is given by

$$\varepsilon_g = \varepsilon_c + \varepsilon_w - \Delta\varepsilon_{cw} \tag{5.4.4}$$

where ε_c is the emissivity of a pathlength S of CO_2 at a temperature T and partial pressure p_c; ε_w is the eimissivity of a pathlength S of H_2O at a temperature T and partial pressure p_w; $\Delta\varepsilon_{cw}$ is the 2.7 and 15 μm overlap correction for a pathlength S. ε_c and ε_w are approximated by three parameter(partial pressure, pressure-pathlength and temperature) curve fits to spectral calculation of ε_c and ε_w at 1 atmosphere total pressure[Modak, 1979]. "The curve fits for emissivities are accurate to within 5% in the temperature range 300 to 2000 K for a gas partial pressure range of 0 to 1 atm and a pressure-pathlength range of 0 to 6 atm. These ranges encompass most practical combustion systems"[Modak, 1979].

5.4.2 The radiative properties of soot

It is well established that "soot absorption and emission is proportional to the soot volume fraction(f_v) provided the radiation wavelength is greater than the soot particle diameter." "This is usually the case for infrared radiation from flames. Under these conditions scattering of radiation by the particles is also negligible"[De Ris, 1979]. Under these assumptions the soot emissivity becomes

$$\varepsilon_s = 1-15/\pi^4\psi^{(3)}(1+x) \tag{5.4.5}$$

with the definition $x = cSf_vT/c_2$, where $\psi^{(3)}(z)$ is the pentagamma function

$$\int_0^\infty t^3\exp(-zt)/(1-\exp(-t)dt \tag{5.4.6}$$

and c is a dimensionless constant between 4 and 10 associated with the soot chemical composition.[De Ris, 1979]. It is very difficult to derive the value of c from experimental data. The recommended value of c is 7 which lies in the middle of the reported range 4-10[Hottel and Sarofim, 1967].

Under gray-soot assumption, a further simplified calculation of soot emissivity is given by[Yuen and Tien, 1977]

$$\varepsilon_s = 1-\exp(-\kappa s) \tag{5.4.7}$$

where s is the physical pathlength and κ is the effective soot-emission parameter independent of s. And κ is given as

$$\kappa = 3.6\gamma T/c_2 \tag{5.4.8}$$

where c_2 is the Planck second constant and γ is the effective soot-concentration parameter defined as

$$\gamma = 36\pi f_v(n^2k)/\{[n^2-(nk)^2+2]^2+4n^2k^2\} \tag{5.4.9}$$

According to equation (5.4.9), soot extinction coefficient can be also expressed as

$$\kappa = af_v T \tag{5.4.10}$$

where a is a constant depending on the soot chemical composition. A similar expression for soot extinction coefficient was obtained by Kent and Honnery[1990] based on their experimental data for ethylene-air diffusion flames. As scattering is neglected, the extinction coefficient represents only absorption. Kent and Honnery expressed the absorption coefficient for soot as

$$\alpha_s = 2.66 \text{const} f_v T(\text{cm}^{-1}) \tag{5.4.11}$$

Under gray-soot assumption, equation (5.4.1) is further simplified as

$$\varepsilon_m = [1-\exp(-\kappa S)] + \varepsilon_g \exp(-\kappa S) \tag{5.4.12}$$

[Yuen and Tien, 1977], where ε_g is the emissivity of the radiating gases calculated easily from the method presented in subsection 5.4.1.

5.5 Radiation Models

5.5.1 Introduction

Due to the huge calculations required by the resolution of the transfer equation (5.3.4), it is prohibitively expensive to obtain exact radiative energy exchanges in a fire system. Consequently approximate numerical calculations of radiation transfer are demanded.

Among the radiation models are the zone method[Hottel and Sarofim, 1967] and

Monte Carlo method[Howell, 1968]. In the zone method, the flow domain and the bounding surfaces are partitioned by a number of small zones. Exact radiation transfer can be approached by increasing the zone number. However, since all radiative exchanges between each zone pair are considered, this method becomes very expensive as the number of zone increases. To lessen the cost, Monte Carlo method can be used for obtaining the exchange factors between each zone pair. A large number of random rays are required to obtain satisfactorily accurate radiation fluxes. As a result, demanding calculations are needed. Therefore both methods are only practically used for relatively coarse meshes. It is not efficient to incorporate these two methods into field fire models without modification since quite fine grids are used in this modelling technique.

More suitable (i.e. computationally less demanding) models have been proposed for incorporating into fire field models. The six-flux model and the discrete transfer method are two radiation models widely used. Because these two models are also employed in this study, they are outlined here in detail.

5.5.2 Six-flux model formulation

As a first approximation, the six-flux model [Hoffmann and Markatos, 1988] has successfully been applied to a number of practical problems involving radiation [Sarofim, 1986], including fires [Hoffmann and Markatos, 1988; Jia et al., 1997; 1999a, b]. Since "scatter is important only when considering the impact of fly ash in coal combustion systems and some times in the dense oil spray in diesel engines or the near burner region of furnaces"[Sarofim, 1986], scatter is ignored in the following

model description.

The six radiation fluxes in the positive and negative directions of x, y, and z are denoted by F_x^+, F_x^-, F_y^+, F_y^-, F_z^+ and F_z^- respectively. Thus

$$\mathrm{d}F_\alpha^+/\mathrm{ds} = -aF_\alpha^+ + aE_\mathrm{b} \tag{5.5.1}$$

$$\mathrm{d}F_\alpha^-/\mathrm{ds} = aF_\alpha^- - aE_\mathrm{b} \tag{5.5.2}$$

where α represents the coordinate directions, a is the absorption coefficient and $E_\mathrm{b} = \sigma T^4$ is the black-body radiation power and σ is the Stefan-Boltzmann constant.

By adding equation (5.5.1) and equation (5.5.2) we have the result that

$$\mathrm{d}(F_\alpha^+ + F_\alpha^-)/\mathrm{ds} = -a(F_\alpha^+ - F_\alpha^-) \tag{5.5.3}$$

Subtracting equation (5.5.2) from equation (5.5.1) gives

$$\mathrm{d}(F_\alpha^+ - F_\alpha^-)/\mathrm{ds} = -a(F_\alpha^+ + F_\alpha^-) + 2aE_\mathrm{b} \tag{5.5.4}$$

From equation (5.5.3) we have

$$\mathrm{d}[1/a\mathrm{d}(F_\alpha^+ + F_\alpha^-)/\mathrm{ds}]/\mathrm{ds} = -\mathrm{d}(F_\alpha^+ - F_\alpha^-)/\mathrm{ds} \tag{5.5.5}$$

Let $R_x = (F_x^+ + F_x^-)/2$, $R_y = (F_y^+ + F_y^-)/2$, $R_z = (F_z^+ + F_z^-)/2$. Then if we now substitute equation (5.5.4) in equation (5.5.5), we have the following second-order ordinary differential equation

$$\mathrm{d}[1/a\mathrm{d}R_\alpha/\mathrm{ds}]/\mathrm{ds} = S_\alpha, \qquad \alpha = x, y, z \tag{5.5.6}$$

where $S_\alpha = aR_\alpha - aE_\mathrm{b}$.

At a bounding surface, the leaving flux F^+ is expressed by

$$F^{+} = \varepsilon_w E_b + (1-\varepsilon_w)F^{-} \tag{5.5.7}$$

where ε_w is the emissivity of the wall surface and F^{-} is the incident flux. Thus R_α at the wall boundary is given

$$R_\alpha = (F^{+}+F^{-})/2 = \varepsilon_w E_b/2 + (2-\varepsilon_w)F^{-}/2 \tag{5.5.8}$$

By rearranging above equation, we obtain

$$F^{-} = (2\,R_\alpha - \varepsilon_w E_b)/(2-\varepsilon_w) \tag{5.5.9}$$

From equation (5.5.7) we also have the relation below

$$F^{+} - F^{-} = \varepsilon_w(\,E_b - F^{-}) \tag{5.5.10}$$

Substituting for F^{-} from equation (5.5.9) in equation (5.5.10) gives

$$(F^{+} - F^{-})/2 = \varepsilon_w(E_b - R_\alpha)/(2-\varepsilon_w) \tag{5.5.11}$$

Finally, from equation (5.5.3) and equation (5.5.11) we have the boundary condition at the wall

$$\mathrm{d}\,R_\alpha/\mathrm{d}n = -a\varepsilon_w(E_b - R_\alpha)/(2-\varepsilon_w) \tag{5.5.12}$$

where n is the outward going unit normal direction to the solid surface.

The primary attraction of this model is that it is easily incorporated into the finite volume scheme of the numerical solution procedure adopted by fire field models and is much less demanding of computational power than other advanced radiation models such as the discrete transfer method.

5.5.3 Discrete transfer model formulation

The discrete transfer method was proposed by Lockwood and Shah[1981]. The radiative transfer equation is solved along a number of prescribed rays that discretise

the total 4π steradians. By ignoring the scatter effect, radiation along a ray is determined by

$$\frac{d}{ds} I(\Omega,r) = -a\, I(\Omega,r) + aI_b(r) \qquad (5.5.13)$$

where Ω is the ray direction; s represents the physical pathlength along Ω; r is the position of a point; $I(\Omega,r)$ stands for radiation intensity along Ω at position r; a is the absorption coefficient of the medium.

Each cell through which the ray passes is treated as isothermal, i.e., the temperature and properties are uniform in the cell. Thus the radiation intensity along the ray is calculated by the following recurrence equation that is the exact solution to equation (5.5.13) within the cell

$$I_{n+1} = I_n \exp(-a\delta_s) + [1-\exp(-a\delta_s)]I_b \qquad (5.5.14)$$

where I_n and I_{n+1} are respectively the radiation intensities of entering and leaving the cell along the ray and δ_s is the ray segment within the cell.

Assuming a grey wall surface, the wall boundary is calculated by

$$I = \varepsilon_w I_b/\pi + (1-\varepsilon_w)I^- \qquad (5.5.15)$$

where I^- is the incident radiation intensity at the wall surface.

The discrete transfer method is recognised as a method accurate, relatively economical and applicable to arbitrary geometrical configurations. It is now widely used in fire field models to calculate the radiative energy exchanges.

A standalone computer code for the DTM is developed in FORTRAN by the author.

The input includes the ray number, the directions of the rays, the black body radiative intensity or power(for the six-flux model) field, the absorption coefficient field, radiation intensities from bounding surfaces and emissivities of solid surfaces. If there is any solid object in the flow domain, its position, surface temperature and emissivity are required to be input into the code. The mesh used for the calculation of the radiation intensity or power(for the six-flux model) is the same one as for the flow domain. The rays used in the DTM are either particularly specified by users or are them described in section 5.6.2. The radiation intensity or flux after going through a cell along a ray is given by the recurrence equation (5.5.14). Along a ray, from each cell at a solid surface where the initial radiation intensity is given by equation (5.5.15), the calculation defined by equation (5.5.14) is continued until the ray reaches another solid surface. This procedure is gone through for all the rays and all solid surface cells. The linkage of the code with the selected CFD software lies on the fact that radiation creates source and sink terms in the enthalpy equation. This will be discussed in detail in section 5.6.3.

As will be shown in the following section, in a Cartesian co-ordinate system the six-flux model is, after some minor alterations, implemented using the same code developed for the DTM in which six rays parallel to the co-ordinate directions are used.

5.6 Incorporation of Radiation Models into the CFD Model

This section outlines some concrete considerations to implement the radiation models in the selected CFD software.

5.6.1 Modification of the conventional six-flux model

The absorption coefficient of a gas-soot mixture is involved in equation (5.5.12) that is the radiation boundary condition at a wall surface in the six-flux model. Actually, it is the limit value of the absorption coefficient of the gas-soot mixture at the wall surface. As the exact limit value is not known, approximations of it will be taken when numerically fulfilling the six-flux model. An approximation that is usually made in the standard six-flux model is to use the absorption coefficient in the cell next to the wall surface. However, since the absorption coefficient is dependent on the temperature of the gas-soot mixture and the temperature variation near the wall surface is possibly rapid in turbulent flows, this approximation may be crude. Furthermore, equation (5.5.12) makes the model predictions depend on the approximation of the limit value of the fluid absorption coefficient at the wall surface. This introduces an extra source of uncertainty and inaccuracy of the radiation model. This is highlighted by the following simple test case.

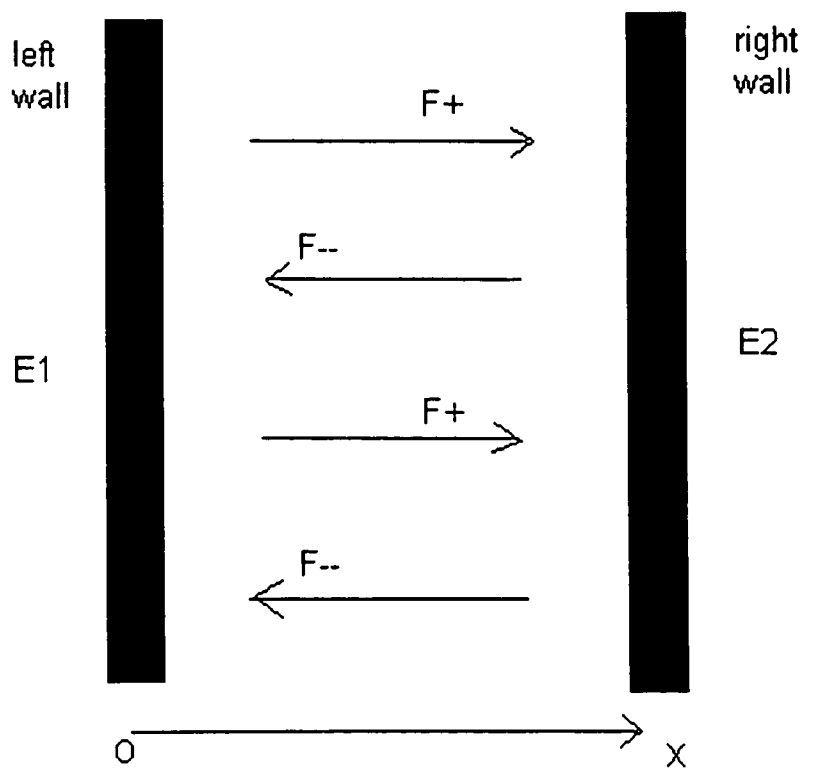

Fig. 5.6.1: The schematic view of the simple test case.

The test case involves two parallel walls separated by a distance of 1.0m(figure (5.6.1)). The wall emissivities are taken as one and the radiation fluxes emitting from the walls are E_1 (W/m^2) at the cooler left wall and E_2 (W/m^2) at the hotter right wall. The media between the walls has a variable absorption coefficient and constant blackbody radiation power of E_b (W/m^2). The absorption coefficient is formulated as

$$a = x \text{ (1/m)} \tag{5.6.1}$$

This is a simple one-dimensional problem. The formula for the conventional model is

$$d[1/x dR/dx]/dx = xR - xE_b, \tag{5.6.2}$$

with boundary conditions

$$dR/dx\,|_{x=0} = -a\varepsilon_w(E_1 - R)/(2-\varepsilon_w) = 0 \tag{5.6.3}$$

and

$$dR/dx\,|_{x=1} = a\varepsilon_w(E_2 - R)/(2-\varepsilon_w) = E_2 - R \tag{5.6.4}$$

For this simple test case there exist analytic solutions for the conventional model (equations (5.6.2), (5.6.3) and (5.6.4)). The analytical solutions are

$$R = (F^+ + F^-)/2 = E_b + C(E_1 - E_b)\,e^{-0.5x^2} + 0.5(E_2 - E_b)\,e^{-0.5}e^{0.5x^2} \tag{5.6.5}$$

where C is an arbitrary real number. Therefore the conventional model produces an ill-posed differiential problem since there are infinite number of solutions for it. This means, according to the conventional model, the radiation flux distribution in the medium has infinite possibilities. However in reality, the radiaton flux distribution in the medium is uniquely determined by the properties of the medium and the walls.

Another disadvantage is that the conventional model transforms the one-way

parabolic problem—equations (5.5.1) and (5.5.2)—to a two-way elliptic problem equation (5.5.6). When equation (5.5.6) is discretised over a control volume P(see figure(5.6.2)), the discretisation of the left-hand side of the equation is

$$\text{Left-hand side} = 1/a\,|_e\, dR/dx\,|_e - 1/a\,|_w\, dR/dx\,|_w \qquad (5.6.6)$$

Fig. 5.6.2: Three successive control volumes.

The absorption coefficient a at the cell faces e and w in equation (5.6.6) need be evaluated in terms of the values of the absorption coefficients at grid-point P, E and W. Thus the radiation flux value R at point P is partially determined by the properties in the cells of W and E. Since it is impossible to separate the radiation flux F^+ along the positive x direction and F^- along the negative x direction from R, equation (5.6.6) means that F^+ is partially determined by the properties in cell E that is in the down stream along the positive x while F^- is partially determined by the properties in cell W that is in the down stream along the negative x. Obviously, it is unrealistic that the one-way radiation flux F^+ or F^- is determined by the properties of the down stream. Errors due to the problem transformation are inevitably introduced by the discretisation for the conventional model. This is demonstrated in the following example.

The following test case is similar to the previous test case except for the specification of the absorption coefficient of the medium. In this test case the absorption coefficient is given by

$$a(x) = 0.2\, e^{20(x-0.5)^2}\ (1/\mathrm{m}) \tag{5.6.7}$$

The analytical solution for the conventional model is

$$R = (F^{+} + F^{-})/2 = E_b + 0.5(E_1 - E_b)\, e^{-\int_0^x a(x)dx} + 0.5(E_2 - E_b)\, e^{-\int_x^1 a(x)dx} \tag{5.6.8}$$

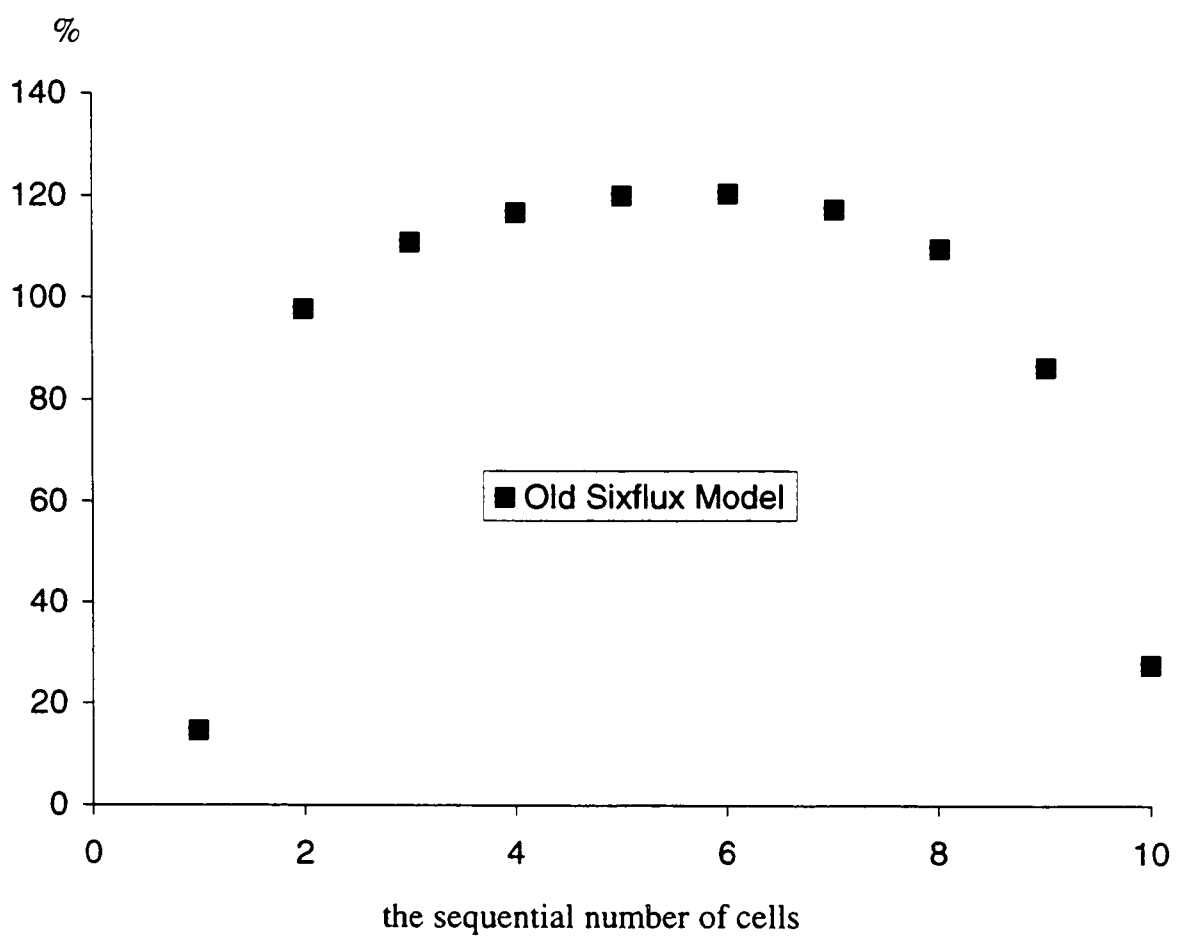

Fig. 5.6.3: The relative errors of the net gain of radiative energy in the cells.

For the numerical calculation of the conventional model, we assume that E_1 = 5000 W/m^2, E_2 = 8000 W/m^2 and E_b = 500 W/m^2. The differential form of the model is numerically solved using a mesh which is uniformally distributed with 0.1m cell length(the total cell number is 10). The errors produced by the model relative to the exact values for the net gains of the radiative energy in each cell are depicted in figure (5.6.3). The net gain of the radiative energy in each cell is defined by

$$E_{net} = (F^{+}_{out} - F^{+}_{in}) + (F^{-}_{out} - F^{-}_{in}) \tag{5.6.9}$$

where F_{in} represents the radiative flux arriving at the cell while F_{out} is the radiative flux leaving the cell. Figure (5.6.3) clearly demonstrates that the solution of the

conventional model has significant differences from the analytical solution. The maximum relative error produced by the conventional model is up to 120%.

As demonstrated earlier, the conventional six-flux model suffers two kinds of errors—the uncertainty due to the dependency of the boundary conditions at walls on the limit value of the absorption coefficient of the media and the unrealistic transformation from one-way parabolic problems to a two-way elliptic problem. Therefore, modification will be made while still adhering to the principles of the conventional method.

In the modified six-flux model, the equations (5.5.1) and (5.5.2), representing the quintessence of the conventional six-flux model, are still used in the flow domain. However, the variables in the model are F_x^+, F_x^-, F_y^+, F_y^-, F_z^+ and F_z^- rather than R_x, R_y and R_z, the average of the positive and negative flux along the coordinate directions. The boundary condition at the wall surface is therefore directly given by equation (5.5.7), i.e.,

$$F^+ = \varepsilon_w E_b + (1-\varepsilon_w) F^- \quad . \tag{5.6.10}$$

Since the incident flux F^- in the above equation is calculated from equation (5.5.1) or (5.5.2) depending on the position of the wall, an iterative method has to be employed to obtain radiation fluxes if the wall emissivities are not equal to one.

By comparing equations (5.5.1), (5.5.2) and (5.5.13), it is obvious that the modified six-flux model is almost identical to the DTM using six rays parallel to the coordinates. The difference between the two models is that in the modified six-flux

model $E_b = \sigma T^4$, the radiation power of black body, is used while in the latter model $I_b = \sigma T^4/\pi$, the radiation intensity of black body, is used. In each cell, if the temperature is assumed to be uniform, following the equations (5.5.1) and (5.5.2), the radiation flux after going through the cell along a direction parallel to one of the coordinates is given by the following recurrence relation.

$$F_{n+1} = F_n e^{-\int_s^{s+\delta s} a(x)dx} + (1 - e^{-\int_s^{s+\delta s} a(x)dx}) E_b \qquad (5.6.11)$$

where F_n and F_{n+1} are respectively the radiation fluxes of entering and leaving the cell through which the ray passes and δ_s is the ray segment within the cell and $E_b = \sigma T^4$ is the black body radiation power. If the absorption coefficient in the cell is further assumed to be uniform, equation (5.6.11) becomes

$$F_{n+1} = F_n e^{-a\delta s} + (1 - e^{-a\delta s}) E_b \qquad (5.6.12)$$

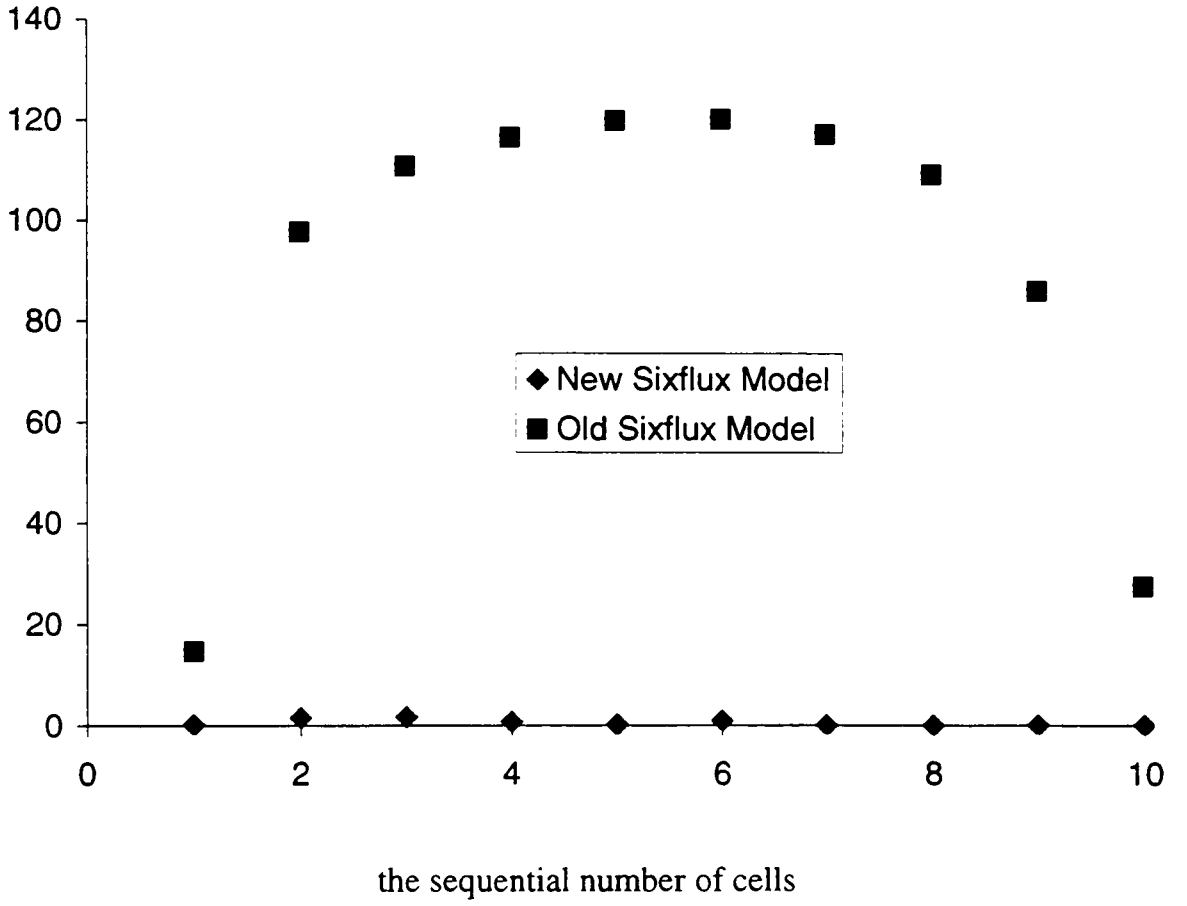

Fig. 5.6.4: The relative errors of the net gain of radiative energy in the cells.

Equation (5.6.12) is identical to equation (5.5.14) if using F_n, F_{n+1} and E_b to replace I_n,

I_{n+1} and I_b respectively. Therefore, there is no particular code developed for the modified six-flux model. The six-flux model is implemented using the same code developed for the DTM in which the ray number is defined particularly for the modified six-flux model as six and the directions of the rays are specified to be parallel to the coordinates and the black body power field is input. This is also another reason why the conventional model is modified.

The differences between the modified and the conventional six-flux models are demonstrated by the second test case described previously. For this simple test case there exist analytic solutions for both of the modified and conventional models. The analytic solution for the modified model is

$$F^{+} = E_b + (E_1 - E_b)\ e^{-\int_0^x a(x)dx} \tag{5.6.13}$$

$$F^{-} = E_b + (E_2 - E_b)\ e^{-\int_x^1 a(x)dx} \tag{5.6.14}$$

while the analytical solution for the conventional model is given by equation (5.6.8). The errors produced by the two models relative to the exact values for the net gains of the radiative energy in each cell are depicted in figure (5.6.4). In the calculations for the modified model, equation(5.6.11) is used, i.e., the absorption coefficient in each cell is not assumed to be uniform. Figure (5.6.4) clearly demonstrates that the errors of the numerical solution of the modified model to the analytical solutions is nearly zero while the solution of the conventional model has significant differences from the analytical solution.

In the following chapters, the six-flux model refers to the modified model defined in this section.

5.6.2 Selection of rays and weights for DTM

The rays and weights used in the DTM were recommended by Lathrop and Carlson[1965]. The rays are symmetric and are constructed to satisfy a number of key moments of the radiative intensity. Suppose that the 4π steradians are subdivided by N rays (μ_n,ξ_n,η_n), n = 1, ..., N and their weights are denoted by w_n, n = 1, ..., N. The required key moments are:

1) zeroth moment of full range($0 \le \theta \le \pi$ and $0 \le \phi \le 2\pi$), i.e. $\sum_{1}^{N} w_n = 4\pi$;

2) first moment of half range($0 \le \theta \le \pi/2$ and $0 \le \phi \le 2\pi$), i.e.

$$\sum_{1}^{N/2} \eta_n w_n = \int_0^{\pi/2} \left(\int_0^{2\pi} \cos\theta \sin\theta d\phi \right) d\theta = \pi; \qquad (5.6.15)$$

3) first moment of full range($0 \le \theta \le \pi$ and $0 \le \phi \le 2\pi$), i.e.

$$\sum_{1}^{N} \eta_n w_n = \int_{\Omega=4\pi} \cos\theta \, d\Omega = \int_0^{\pi} \left(\int_0^{2\pi} \cos\theta \sin\theta d\phi \right) d\theta = 0 . \qquad (5.6.16)$$

As the rays are selected symmetrically, all the rays can be classified into groups in terms of their symmetric relationship. The third requirement is automatically satisfied provided that the weights of the rays in the same group are designed to be equal.

Violation of these requirements will result in incorrect prediction of boundary heat flux, leading to improper numerical solid surface temperature. The quadrature rays and weights for 1, 3, 6 and 10 rays in the first quadrant are listed in table (5.6.1)[Fiveland, 1988].

Table 5.6.1: Rays and weights in the first quadrant.

	ordinates of rays			weights
	μ	ξ	η	w
1	0.5773503	0.5773503	0.5773503	1.5707963
1	0.2958759	0.2958759	0.9082483	0.5235987
2	0.9082483	0.2958759	0.2958759	0.5235987
3	0.2958759	0.9082483	0.2958759	0.5235987
1	0.1838670	0.1838670	0.9656013	0.1609517
2	0.6950514	0.1838670	0.6950514	0.3626469
3	0.9656013	0.1838670	0.1838670	0.1609517
4	0.1838670	0.6950514	0.6950514	0.3626469
5	0.6950514	0.6950514	0.1838670	0.3626469
6	0.1838670	0.9656013	0.1838670	0.1609517
1	0.1422555	0.1422555	0.9795543	0.1712359
2	0.5773503	0.1422555	0.8040087	0.0992284
3	0.8040087	0.1422555	0.5773503	0.0992284
4	0.9795543	0.1422555	0.1422555	0.1712359
5	0.1422555	0.5773503	0.8040087	0.0992284
6	0.5773503	0.5773503	0.5773503	0.4617119
7	0.8040087	0.5773503	0.1422555	0.0992284
8	0.1422555	0.8040087	0.5773503	0.0992284
9	0.5773503	0.8040087	0.1422555	0.0992284
10	0.1422555	0.9795543	0.1422555	0.1712359

5.6.3 Combination of the radiation model and the selected CFD software

Radiative energy exchanges create a source-sink term in the total energy conservation equation. The source-sink term can be expressed as

$$S_r = \int_0^\infty \int_{4\pi} a_\lambda [I_\lambda(\Omega) - I_{b\lambda}(\Omega)] d\Omega d\lambda \qquad (5.6.17)$$

where a_λ is the monochromatic absorption coefficient of the medium, $I_\lambda(\Omega)$ and $I_{b\lambda}(\Omega)$ are the monochromatic radiation intensity and the blackbody radiation intensity along the direction Ω respectively. The integration is over all wavelengths and throughout 4π steradians. Obviously, calculation of the integration (5.6.17) at all grid points of

the CFD mesh is extremely expensive and impractical at present. A simplificaiton widely used is the gray medium in which the absorption coefficient and radiant intensity are independent on wavelengths. Under the gray medium assumption, the source-sink term is rewritten as

$$S_r = a\int_{4\pi} [I(\Omega) - I_b(\Omega)]d\Omega \qquad (5.6.18)$$

Provided the flow field is known, the radiation intensity in the medium and the blackbody radiation intensity are computed according to the selected radiation model such as the six-flux model or the discrete transfer model described in the previous subsections. A code implementing the radiation model may be separated from the CFD code computing the flow field. Then the integration (5.6.18) is carried out to calculate the radiation source-sink term in the energy equation according to the radiant intensities resulted from the radiation model. In fact, after the completion of one outer iteration the tentative flow field is known. Using the radiation model the absorption coefficient of the medium and radiation intensities are then calculated from the tentative flow field. Then the radiation source-sink term is computed for the next outer iteration according to equation (5.6.18). When the DTM is used, the 4π steradians are discretised by the rays specified by the radiaion model. Numerical integration for equation (5.6.18) is carried out according to this discretisation, that is,

$$S_r = \sum_{rays} (I_{n+1} - I_n)\vec{\Omega}\cdot\Delta\vec{A}\Delta\Omega \qquad (5.6.19)$$

where $\vec{\Omega}$ is a ray direction and $\Delta\vec{A}$ is the normal face area of a cell volume. When the six flux model is employed, the integration is expressed as

$$S_r = a[(F_x^+ + F_x^- + F_y^+ + F_y^- + F_z^+ + F_z^-) - 6E_b]V \qquad (5.6.20)$$

where V is the volume of a cell.

5.6.4 Linearization of radiation source term in the energy conservation equation

To ensure a stable iteration to solve the governing equations of the flow the radiative heat loss source term in the energy conservation equation is linearized. Radiative heat losses are expressed as

$$\dot{q}_l'' = -\chi \varepsilon_m \int_{\Omega=4\pi} I_b \, d\Omega = -\chi \varepsilon_m \sigma T^4 \qquad (5.6.21)$$

where χ is a model constant, taken as 6 for the six flux model and 4 for the four flux model(a two-dimensional modification of the six flux model) and the DTM.

As the temperature of the gas-soot mixture is presumably a function of the enthalpy, $\dot{q}_l''$ can be linearized in terms of the enthalpy. Assume that $T = \Psi(h)$, where h stands for the enthalpy of the gas-soot mixture. Then by substituting $\Psi(h)$ for T, equation (5.6.21) becomes

$$\dot{q}_l'' = -\chi \varepsilon_m \sigma \Psi(h)^4 \qquad (5.6.22)$$

Thus the heat losses source term can be linearized in terms of enthalpy h.

5.7 Concluding Remarks

Sooting mechanisms were briefly examined and some soot models reviewed. A simple empirical treatment for the soot formation in fires was proposed. This sooting model is based on the experimental observations that soot formation takes place in the fuel rich side of chemical reaction region and the highest soot concentration is found in the same region. This model will be partially validated in chapter 6 by using it as a part of the model simulating one of the series of Steckler's room fire tests.

The principal concepts of radiation and key assumptions and models used in this study in the calculations of radiative properties were presented. All these assumptions and models have been proved by other modellers and users to be rational and capable of evaluating sufficiently accurate radiative properties of gas-soot mixture in fires.

Two radiation models—the six-flux model and the discrete transfer method (DTM) were discussed in detail. Some technical treatments in the six-flux model and the DTM model were described. Shortcomings in the conventional six-flux radiation model were highlighted. These involves the introduction of an extra source of inaccuracy and uncertainty due to the radiation boundary condition at wall surfaces and the unrealistic transformation from one-way parabolic problems to a two-way elliptic problem. These problems were demonstrated through a simple artificial test case. The problems were corrected in the modified six-flux model and the improved accuracy was demonstrated using the same test case. For the DTM, some recommendations for selecting rays are discussed. The aim of these treatments is to produce reasonable radiative heat flux.

The combination of the radiation models and the CFD code was discussed. The linearisation for the radiation loss term in the energy equation was recommended to enhance the stability of iterations.

Chapter 6

SIMULATIONS OF ONE OF STECKLER ROOM FIRES

6.1 Introduction

In chapter 3 a simple heat source fire field model was developed and its capabilities in simulating a room fire scenario were demonstrated. The demonstration consisted of a comparison of the model predictions with experimental data from the Steckler room fire tests[Steckler et al., 1982]. The model was found lacking in several areas with particular attention being drawn to

1) the lack of a description of gaseous combustion;

2) the lack of a radiation model;

3) the crude treatment of the wall thermal boundary condition.

In order to address the first two deficiencies a gaseous combustion model has been developed (see chapter 4) and two alternative radiation models have been developed in chapter 5. In this chapter the heat loss through the walls is addressed. Furthermore, all these components are integrated into a fire field model.

While field models of compartment fires incorporate increasing number of complex elements of physical and chemical processes which may occur, concerns are arising about the accuracy of the models and elaborate numerical methods essentially associated with these models. Although field models have many advantages over zone models[Galea, 1989], field models cannot be used with much confidence in enclosure fire situations until systematic comparison of fire field model predictions with experimental data (often called 'validation') is carried out. The validation of fire field

model predictions is essential to the continual development and acceptance of this complex procedure[Galea, 1989; Markatos and Cox, 1984]. By using the same Steckler room fire scenario as the one described in chapter 3, the performance of the integrated model is assessed by comparing with the experimental data of interest and the simple fire field model developed in that chapter. Comment is also made on the relative merits of the six-flux radiation model and the discrete transfer method.

6.2 The Integrated Model Description

The fire field model presented in chapter 3 using the volumetric heat source method to represent the fire source did not include a radiation model and treated the walls as a perfectly insulating (i.e. adiabatic) boundary. In this chapter we improve on these coarse treatments through the introduction of a gaseous combustion model, a radiation model and a heat loss calculation through the walls.

6.2.1 Representation of the fire source

The volumetric heat source model previously used to represent the fire is replaced with the gaseous combustion model described in chapter 4. The model is intended to simulate the gas phase combustion involved in enclosure fires. Two scalar variables represent the mixture fraction f and the fuel mass fraction m_f respectively. Assume that the one step global chemical reaction is

$$F + \nu O \rightarrow P + \text{heat} \qquad (6.2.1.1)$$

where F and O represent the reactants—the fuel and the oxidant respectively and P is the mixture of products. The oxidant mass fraction and product mass fraction are then

determined algebraically by equations

$$m_a = 1 - m_f - (f - m_f)/f_s \tag{6.2.1.2}$$

$$m_p = 1 - m_f - m_a \tag{6.2.1.3}$$

where f_s is the stoichiometric value of f. When the detailed information about the product is required, for instance that the mass fraction of water and carbon dioxide are wanted, the composition expression for the product is needed. Using the complete combustion assumption, the product can be expressed as

$$P = \nu_w H_2O + \nu_c CO_2 \tag{6.2.1.4}$$

where ν_w and ν_c are the stoichiometric values of water and carbon dioxide in the combustion product respectively. Let M_{fd} and M_{ad} denote the mole fraction of the inert dilutant in the fuel and oxidant respectively. And assume the dilutant molecular weight is W_d. The mass fractions of water and carbon dioxide, m_w and m_c, are then given by

$$m_w = 18.0\nu_w\, m_p/(18.0\nu_w + 44.0\nu_c + M_{fd}/(1-M_{fd})\, W_d + \nu\, M_{od}/(1-M_{od})\, W_d) \tag{6.2.1.5}$$

$$m_c = 44.0\nu_c\, m_p/(18.0\nu_w + 44.0\nu_c + M_{fd}/(1-M_{fd})\, W_d + \nu\, M_{od}/(1-M_{od})\, W_d). \tag{6.2.1.6}$$

The combustible gas fuel may be generated from the gasification of combustible solid fuels(see chapter 7 and 8) or provided by a gas burner for non-spreading fire tests. If the burning of a gas burner is intended modelled, the burner will be represented as an inlet from which the gas fuel is emitted. Under the assumption of complete combustion, the fuel mass flux $\dot{m}''$ from the inlet is determined by

$$\dot{m}'' = H_f/(aH) \tag{6.2.1.7}$$

where H_f is the burner strength, H is the heat of combustion of the fuel and a is the inlet area. The values of the two scalars used in the gas phase combustion model, the

mixture fraction f and the fuel mass fraction m_f, are both set to one at the inlet.

6.2.2 Representation of radiation

Two different radiation models are included in the integrated fire field model, the six-flux model and the discrete transfer method (DTM)(see sections 5.5 and 5.6). To calculate radiation flux or intensity according to the radiation model used, the emissivity or the absorption coefficient of the participating medium is required. Section 5.4 presented some methods to compute the radiative properties of the medium. Generally, the total radiative properties of the soot-gas mixture are calculated in terms of the soot and gases radiative properties. For most fires scattering can be neglected[Sarofim, 1986].

When the DTM is employed, it is necessary to specify the number of rays to be incorporated and the directions of the rays. The recommended number and directions of the rays are presented in table (5.6.1).

Both radiation models can be run with or without the soot formation sub-model described in sections 5.2.3. When soot formation is not modelled, it is necessary to specify a fixed value for the emissivity or the absorption coefficient of soot in the hot upper layer.

6.2.3 Heat loss through the walls

Since the heat losses through the non-combustible walls, floor or ceiling of a compartment affect the course of the fire spread within the compartment, the temperatures at these non-combustible solid surfaces need evaluating. From the computational cost point of view, however, it is uneconomic and unnecessary to calculate temperature distribution within the non-burning solid walls or ceiling by solving the conduction equation for the solid. An easy and economical way to calculate the solid surface temperature must be found and used. The integral method[Özişik, 1980] is simple, straightforward and easily applicable to transient heat conduction in non-combustible solid materials. It has been successfully used in fire modelling[Lockwood and Malalasekera, 1988; Bagnaro, 1983]. In this section the integral method is extended to be capable of dealing with the high non-linearity of the surface reradiation at the top surface and the convective heat loss at the bottom surface.

The non-steady conduction in the solid is described in the following mathematical form

$$\rho C_p \partial T/\partial t = k\partial^2 T/\partial x^2 . \qquad (6.2.3.1)$$

or

$$\partial T/\partial t = \alpha\partial^2 T/\partial x^2 . \qquad (6.2.3.1a)$$

where $\alpha = k/(\rho C_p)$. The boundary conditions are

1) at the top surface which is exposed to external incident heat flux

$$-k\partial T/\partial x \,|_{x=0} = q'' - h_T(T-T_0) - \varepsilon\sigma(T^4-T_0^4) = q''_{net} \qquad (6.2.3.2)$$

where ε is the emissivity of the solid surface, σ is the Stefan-Boltzmann constant, q'' is the incident radiative heat flux at the solid surface and h_T is the convective heat transfer coefficient at the surface.

2) at the bottom surface

$$-k\partial T/\partial x \big|_{x=L} = h_B(T-T_0) \qquad (6.2.3.3)$$

or

$$T\big/_{x=L} = T_0 \qquad (6.2.3.4)$$

where L is the thickness of the solid material, h_B is the convective heat transfer coefficient at the bottom surface and T_0 is the ambient temperature. The initial condition is

$$T(0, x) = T_0 . \qquad 0<x<L \qquad (6.2.3.5)$$

Let δ denote the thermal penetration depth. At x = δ, the following equations are held.

$$\partial T/\partial x \big|_{x=\delta} = 0 \qquad (6.2.3.6)$$

and

$$T\big|_{x=\delta} = T_0 \qquad (6.2.3.7)$$

The integral method assumes a prescribed temperature profile in the solid. Here we use a quadratic profile of the temperature distribution from 0 to δ, i.e., the one dimensional temperature distribution is presumed as

$$T(x, t) = a(t) + b(t)x + c(t)x^2 \qquad 0 < x <\delta \qquad (6.2.3.8)$$

and

$$T(x, t) = T_0 \qquad \delta < x <L \qquad (6.2.3.9)$$

By integrating equation (6.2.3.1a) with respect to the space variable from 0 to δ, we have

$$\int_0^{\delta} (\partial^2 T/\partial x^2)dx = 1/\alpha \int_0^{\delta} (\partial T/\partial t)dx \qquad (6.2.3.10)$$

Substituting equation (6.2.3.8) for T in equation (6.2.3.10) we obtain

$$da(t)/dt + 1/2\delta db(t)/dt + 1/3\delta^2 dc(t)/dt = 2\alpha c(t). \qquad (6.2.3.11)$$

From equations (6.2.3.2), (6.2.3.6) and (6.2.3.7) we have

$$b(t) = -q''_{net}/k \qquad (6.2.3.12)$$

$$b(t) = -2c(t)\delta \qquad (6.2.3.13)$$

$$T_0 = a(t) + b(t)\,\delta + c(t)\,\delta^2 . \qquad (6.2.3.14)$$

Since only surface temperature, denoted by T_s, is important for the flow domain calculation, we shall derive an equation in which T_s is a variable. From equation (6.2.3.8) $a(t)$ can be written as

$$a(t) = T_s \qquad (6.2.3.15)$$

Substituting equations (6.2.3.15) for $a(t)$ and equation (6.2.3.12) for $b(t)$ in equation (6.2.3.14) gives

$$c(t) = (T_s - T_0)/\delta^2 . \qquad (6.2.3.16)$$

From equations (6.2.3.13) and (6.2.3.14) we obtain

$$b(t) = -2(T_s - T_0)/\delta . \qquad (6.2.3.17)$$

The derivatives of $b(t)$ and $c(t)$ are then obtained

$$db(t)/dt = -2/\delta d(T_s - T_0)/dt + 2(T_s - T_0)/\delta^2 d\delta/dt \qquad (6.2.3.18)$$

$$dc(t)/dt = 1/\delta^2 d(T_s - T_0)/dt - 2(T_s - T_0)/\delta^3 d\delta/dt \qquad (6.2.3.19)$$

Substituting equations (6.2.3.15), (6.2.3.16), (6.2.3.18) and (6.2.3.19) in equation (6.2.3.11) gives

$$d[\delta(T_s-T_0)]/dt = 6\alpha(T_s-T_0)/\delta \qquad (6.2.3.20)$$

Since two variables, T_s and δ, are involved, an additional equation is required to determine these two variables. By substituing equation (6.2.3.17) we have

$$2(T_s-T_0)/\delta = q''_{net}/k = [\,q'' - h_T(T_s-T_0) - \varepsilon\sigma(T_s^4 - T_0^4)]/k \qquad (6.2.3.21)$$

Both equations (6.2.3.20) and (6.2.3.21) are used to determine the solid surface temperature when $\delta<L$. The initial condition for equation (6.2.3.20) is

$$[\delta(T_s-T_0)]_{t=0} = 0 \qquad (6.2.3.22)$$

When $\delta=L$, equations (6.2.3.20) and (6.2.3.21) will be invalid. δ becomes constant. Equations (6.2.3.11) and (6.2.3.12) are still held. The equation for T_s will be determined by the boundary condition at the bottom surface. If equation (6.2.3.4) is held for the bottom boundary condition, we have

$$T_0 = T_s + b(t)\,L + c(t)\,L^2\,. \qquad (6.2.3.23)$$

Thus

$$c(t) = [T_0 - T_s - b(t)\,L]/\,L^2 \qquad (6.2.3.24)$$

The derivatives of $b(t)$ and $c(t)$ are obtained from equation (6.2.3.12) and (6.2.3.24) respectively,

$$d\,b(t)/dt = -1/k\,d\,q''_{net}/dt\,, \qquad (6.2.3.25)$$

and

$$d\,c(t)/dt = -1/L^2 d(T_s - T_0)/dt - 1/L db(t)/dt$$

$$= -1/L^2 d(T_s - T_0)/dt + 1/(kL) d\,q''_{net}/dt \qquad (6.2.3.26)$$

Substituting equations (6.2.3.24), (6.2.3.25) and (6.2.3.26) in equation (6.2.3.11) gives

$$dT_s/dt = -3\alpha(T_s-T_0)/\,L^2 + 3\alpha/(Lk)\;q''_{net} + L/(4k)\,d\,q''_{net}/dt\,. \qquad (6.2.3.27)$$

From equation (6.2.3.2) we have

$$\mathrm{d}\,q''_{net}/\mathrm{dt} = \mathrm{d}\,q''/\mathrm{dt} - h_T \mathrm{d}T_s/\mathrm{dt} - 4\varepsilon\sigma T_s^3 \mathrm{d}T_s/\mathrm{dt} \qquad (6.2.3.28)$$

By substituting equation (6.2.3.28) in equation (6.2.3.27) we obtain

$$\mathrm{d}T_s/\mathrm{dt} = \mathrm{A/B} \qquad (6.2.3.29)$$

where

$$\mathrm{A} = -3\alpha(T_s - T_0)/L^2 + 3\alpha/(Lk)\ q''_{net} + L/(4k)\ \mathrm{d}\,q''/\mathrm{dt}$$

and

$$\mathrm{B} = 1 + Lh_T/(4k) + L\varepsilon\sigma T^3/k$$

If equation (6.2.3.3) is held for the bottom boundary condition, we have

$$b(\mathrm{t}) + 2c(\mathrm{t})L = -h_B[T_s + b(\mathrm{t})\,L + c(\mathrm{t})\,L^2 - T_0]/k \qquad (6.2.3.30)$$

Thus

$$c(\mathrm{t}) = -[h_B(T_s - T_0)/k + b(\mathrm{t})(1 + h_B L/k)]/(h_B L^2/k + 2L) \qquad (6.2.3.31)$$

and

$$\mathrm{d}c(\mathrm{t})/\mathrm{dt} = -[\ h_B \mathrm{d}T_s/\mathrm{dt} - (1 + h_B L/k)\mathrm{d}\,q''_{net}/\mathrm{dt}]/[L(h_B L + 2k)] \qquad (6.2.3.32)$$

From equations (6.2.3.2), (6.2.3.11), (6.2.3.25) and (6.2.3.32) we obtain

$$\mathrm{d}T_s/\mathrm{dt} = \mathrm{C/D} \qquad (6.2.3.33)$$

where

$$\mathrm{C} = 1 - Lh_B/3/(Lh_B + 2k) + (h_T + 4\varepsilon\sigma T_s^3)[L/(2k) - L(1 + Lh_B/k)/3/(Lh_B + 2k)]$$

and

$$\mathrm{D} = \mathrm{d}\,q''/\mathrm{dt}[L/(2k) - L(1 + Lh_B/k)/3/(Lh_B + 2k)]$$

$$-2\alpha[h_B(T_s - T_0) - (1 + Lh_B/k)\ q''_{net}]/(h_B L^2 + 2\,kL)$$

Let t_L denote the time when $\delta = L$. From equations (6.2.3.12) and (6.2.3.17) the top

surface temperature T_s at the time t = t_L is

$$T_s = T_0 + L q''_{net}/(2k) \tag{6.2.3.34}$$

Then the initial condition for equation (6.2.3.29) or (6.2.3.33) is

$$T_s(t_L) = T_0 + L q''_{net}/(2k) \tag{6.2.3.35}$$

We summarise the discussion above in brief. When the thermal penetration depth is less than the solid thickness, i.e., $\delta < L$, the surface temperature T_s and δ are determined from equations (6.2.3.20) and (6.2.3.21) with initial condition (6.2.3.22).

$$d[\delta(T_s - T_0)]/dt = 6\alpha(T_s - T_0)/\delta \tag{6.2.3.20}$$

$$2(T_s - T_0)/\delta = q''_{net}/k = [q'' - h_T(T_s - T_0) - \varepsilon\sigma(T_s^4 - T_0^4)]/k \tag{6.2.3.21}$$

$$[\delta(T_s - T_0)]_{t=0} = 0 \tag{6.2.3.22}$$

When $\delta = L$, T_s is calculated from equation (6.2.3.29) for the isothermal bottom boundary condition(i.e. equation (6.2.3.4))

$$dT_s/dt = A/B \tag{6.2.3.29}$$

where

$$A = -3\alpha(T_s - T_0)/L^2 + 3\alpha/(Lk)\ q''_{net} + L/(4k)\ d q''/dt$$

and

$$B = 1 + Lh_T/(4k) + L\varepsilon\sigma T^3/k$$

or from equation (6.2.3.33) for the convective bottom boundary condition(i.e. equation (6.2.3.3))

$$dT_s/dt = C/D \tag{6.2.3.33}$$

where

$$C = 1 - Lh_B/3/(Lh_B + 2k) + (h_T + 4\varepsilon\sigma T_s^3)[L/(2k) - L(1 + Lh_B/k)/3/(Lh_B + 2k)]$$

and

$$D = d\,q''/dt[L/(2k)-L(1+Lh_B/k)/3/(Lh_B+2k)]$$

$$-2\alpha[h_B(T_s - T_0)-(1+Lh_B/k)\ q''_{net}]/(h_BL^2+2\,kL)$$

The initial condition for both equations (6.2.3.29) and (6.2.3.33) is equation (6.2.3.35)

$$T_s(t_L) = T_0 + L\,q''_{net}/(2k)\ . \qquad (6.2.3.35)$$

Equations (6.2.3.20), (6.2.3.29) and (6.2.3.33) can be easily solved by the fourth-order Runge-Kutta method or more economically by the modified Euler method. The surface temperature T_s will be used to determine the boundary conditions at the interface between the solid and the flow.

6.3 The Simulations for the Steckler Room Fire

In order to demonstrate the integrated fire model described in section 6.2, the model is used to simulate the Steckler room fire scenario previously described in chapter 3. Here we outline the model specifications used to generate the results presented in section 6.4.

All the simulations in this chapter use the same mesh as the one used in chapter 3 consisting of 22×20×23(10120) cells. The mesh is non-uniformly distributed with refinements in the wall, floor, ceiling, fire and doorway regions. In order to correctly model the flow through the open door, the grid is extended by 1.6m to include a region outside the compartment. Fixed pressure boundary conditions are used on all external boundaries.

The simulations were run in transient mode until steady-state conditions were achieved. Only the steady-state results are considered here, typically requiring 200 time steps before reaching steady-state conditions. Steady-state is considered to be achieved when the maximum change between spot values falls to less than 1% between time steps. Within each time step, convergence is assumed if the mass source residual falls below 1×10^{-4} (and the other key residual measures, e.g. enthalpy by corresponding amounts). If the time step iteration is not stopped by these measures then a maximum of 100 iterations will be performed during the time step. These stopping criteria are the same as those used in chapter 3.

The floor is assumed to be well insulated and the temperatures of the walls and the ceiling are calculated by the integral model for non-combustible solid materials described in section 6.2.3. The external incident heat flux q'' calculated from the flow domain is input into the integral model. After the wall surface temperature T_s is obtained, the convective heat loss through the wall can be calculated by

$$\dot{q}_c'' = h_T(T_s - T_g) \tag{6.3.1}$$

where h_T is the convective heat transfer coefficient and T_g is the gas temperature next to the wall. The convective heat transfer coefficient h_T can be derived from the wall function for the turbulent flow(see section 2.4). Then the convective heat flux calculated in terms of equation (6.3.1) is used to set up the boundary conditions for the flow domain. In fact this reciprocal procedure is placed into the iterative process of the CFD software CFDS-FLOW3D software (Version 2.3.3) in each time step.

The fuel (commercial methane) is emitted from a square inlet which surface area is

the same as the burner used in the experiment. The inlet is in the centre of the floor and flush with the floor level. Under the assumption of complete combustion, the fuel mass flux $\dot{m}''$ from the inlet is determined by equation (6.2.1.7). Using 62.9 kW of the fire strength, 0.07065 m^2 of the inlet area and 45.5 MJ/kg of the heat of combustion of the fuel, the mass flux emitted from the inlet is 0.01957 kg/m^2s.

All the models presented in this section include the gaseous combustion model and wall heat loss calculation. In addition, the results in section 6.4 are generated from the following radiation model configurations:

(a) – Radiation is ignored

(b) – Two different radiation model options are examined, i.e., the six-flux radiation model and the DTM model(24 rays)

– Soot formation ignored and hence constant a soot absorption coefficient for the upper layer that assume the values: (i) 0.1; (ii) 0.2; (iii) 0.4

(c) – using the six-flux model with the soot formation model and hence the soot absorption coefficient for the upper layer depends on the soot volume fraction and temperature(equation (6.3.2))

(d) – as (c) but the radiation model is the DTM using 6, 8 and 24 rays.

When the DTM uses six rays, the rays are fixed to the co-ordinate directions, as in the six-flux model. When 8 or 24 rays is used, the directions of the rays are presented in table (5.6.1).

Where the sooting submodel is included, the absorption coefficient for soot is

calculated by equation (5.4.10)

$$\alpha_{soot} = C f_v T \tag{6.3.2}$$

where C is a constant, taken as 1114.5 in the simulations which was estimated from the measured mean soot volume fraction and mean soot absorption coefficient for methane fires[Hubbard and Tien, 1978; Yuen and Tien, 1977], f_v and T stand for soot volume fraction and temperature respectively. Where the soot formation is not modelled, constant values(0.4, 0.2 and 0.1) are assigned for soot absorption coefficient in the hot upper layer. These values are close to the range of pure soot absorption coefficient at temperature 400K estimated from the curves provided by Hubbard and Tien[1978] under the assumption that the upper layer is optically thin. While in the burner plume, the expression (equation (5.4.8)) for soot absorption coefficient is adopted

$$\alpha_{soot} = 3.6\gamma T/c_2 \tag{6.3.3}$$

with $\gamma = 0.002$ recommended by Yuen and Tien[1977].

The evaluation for the absorption coefficient of CO_2 and H_2O developed by Magnussen and Hjertager[1977](equation (5.4.3)) is used in the simulations, i.e.,

$$\alpha_g = 0.1(m_c + m_w) \tag{6.3.4}$$

where m_c and m_w are the mass concentration of CO_2 and H_2O respectively which are calculated algebraically by equations (6.2.1.5) and (6.2.1.6).

Finally, the absorption coefficient for the soot-gas mixture is given by[De Ris, 1979]

$$\alpha_m = \alpha_{soot} + \alpha_g \, . \tag{6.3.5}$$

6.4 Results and Discussion

In this section the predictions produced by the integrated fire field model (presented in section 6.2 and 6.3) are compared with experimental data from the Steckler fire scenario(described in section 3.2) and predictions produced by the base fire field model(see section 3.3). Throughout this section, the BASE MODEL (BM) will refer to the simple fire field model previously described in section 3.3 in which the gas phase combustion, the radiation heat exchanges and the heat losses through the walls are ignored.

The comparison with experiment includes the main trends of the induced flow, vertical temperature profiles in the corner and in the doorway central line and the vertical central velocity profiles in the doorway.

6.4.1 Main characteristics

Some main characteristics of a room fire observed by the experiment and the simulations are summarised in table (6.4.1) for comparison. The upper layer temperature, the neutral plane height and the mass flow rates are determined in the same manner as previously described in section (3.4). All the predicted values are in reasonably good agreement with the measured.

It is clear that the upper layer temperatures predicted by ignoring radiation are considerably higher than the measured and the predicted ones with radiation models. This indicates that radiation is very important to determine the hot upper layer

temperature and the radiative heat losses from the hot layer and the fire plume are significant.

Table 6.4.1. The predicted and experimental data of some main characteristics in the room fire.

Model Elements		Upper Layer Temperature		Neutral Plane Height		Inflow		Outflow	
		°C	err(%)	m	err(%)	kg/s^{-1}	err(%)	kg/s^{-1}	err(%)
Experiment Data		129	0.0	1.027	0.0	0.554	0.0	0.571	0.0
BASE MODEL		144	11.6	1.0	2.6	0.546	1.4	0.551	3.5
No Radiation		137	6.2	1.01	1.7	0.536	3.2	0.542	5.1
Six-flux Models									
Soot Model		115	10.9	0.935	9.0	0.523	5.6	0.534	6.5
No Soot Model	$\alpha_s = 0.1$	114	11.6	0.935	9.0	0.521	6.0	0.532	6.8
	$\alpha_s = 0.2$	111	14.0	0.933	9.2	0.519	6.3	0.530	7.2
	$\alpha_s = 0.4$	110	14.7	0.931	9.3	0.517	6.8	0.528	7.5
DTM(24 Rays)									
Soot Model		121	6.2	0.938	8.7	0.530	4.4	0.540	5.4
No Soot Model	$\alpha_s = 0.1$	118	8.5	0.942	8.3	0.524	5.6	0.534	6.5
	$\alpha_s = 0.2$	117	9.3	0.941	8.4	0.523	5.6	0.533	6.6
	$\alpha_s = 0.4$	115	10.9	0.938	8.7	0.521	6.0	0.532	6.8

Note: the error in the table represents the relative error between the prediction and the experiment.

It is noticeable that when radiation models are included, the predicted neutral plane heights fall in a narrow variation range(1cm). The type of the radiation model appears to have only slight effects on this value. However, a significant difference in the neutral plane was made when radiation is not taken into account. There is an approximate 7cm gap between the predicted neutral planes produced with and without radiation models. The model without radiation produces the best agreement with experiment.

The predictions of mass flux into and out of the room show good agreement with experimental data. Here again, the predicted mass fluxes (inflow and outflow) are in general sensitive to the radiative heat losses.

A common trend predicted by both the six flux model and the DTM for the upper layer temperature, the neutral plane height and the mass fluxes is that these values increase as the constant soot absorption coefficient in the upper layer (without the soot model) decreases and including the soot model generates the best results. In addition, the DTM creates predictions marginally closer to the measured than the six-flux model.

From the radiative energy exchange point of view, there are two competing mechanisms within the upper layer—the absorption of the radiative energy from the fire and the radiative heat losses to the cold lower layer. The decreasing trend of the upper layer temperature with the increasing absorption coefficient in this region indicates that the latter mechanism is dominant within this area compared with the former one. Since the two radiation models capture this characteristic of the two mechanisms in the upper layer, both of them predict the similar variation of the upper layer temperature changing with the absorption coefficient in this region.

One plausible explanation for the decreasing trend of the inflow mass flux lies in the following equation[Drysdale, 1985]

$$\dot{m}_a = 2/3 C_d B (h_0)^{3/2} \rho_0 [2g(\rho_0 - \rho_r)/\rho_0]^{1/2} \qquad (6.4.1)$$

where $\dot{m}_a$ is the inflow mass rate, C_d is a discharge coefficient, B is the width of the opening, h_0 is the neutral plane height, g is the scale of the gravitational acceleration, and ρ_0, ρ_r are the density of the ambient air and the hot gases respectively. Since the declining trend of the upper layer temperature results in higher values of the density in the upper layer, $(\rho_0 - \rho_r)/\rho_0$ decreases. Thus by combining the decreasing trend of the

neutral plane height, it is concluded from equation (6.4.1) that the inflow mass flux decreases as the upper layer absorption coefficient increases.

From table (6.4.1), it is obvious that the differences of predictions between the two radiation models are not significant. This indicates that similar magnitude of radiative energy exchange within the Steckler room scenario is predicted by both models. In fact, both models produce very close heat losses due to convective flow through the opening. For example, the simulation using the DTM and the soot model yields a convective heat loss of 48 kW while the simulation using the six-flux model and the soot model produce a 46 kW convective heat loss. This implies that both models predict similar quantities of radiation losses. Generally, the DTM is considered as more accurate model than the six-flux model. However, since the burner power (62.9 kW) of the selected Steckler fire test is relatively low, the extent of the total radiation is not sufficiently large. Furthermore, non-spreading fire is involved in Steckler fire tests. The accuracy of the incident heat flux at the walls and ceiling is not essential. The energy loss through radiation from the fire is more important. Thus it is not unexpected that both radiation models produce similar numerical results considering that they predict almost same radiation heat losses. It is nevertheless promising that the simpler six-flux model produces results that are equivalent of the DTM with 24 rays as the computational effort for the former is significantly less than that required by the latter(see section 6.5).

6.4.2 The vertical temperature profiles in the room corner

Figure (6.4.1) shows the vertical temperature profiles in the room corner produced by the simulations using the six-flux model and the DTM(24 rays). The comparison with the measured temperatures demonstrates that the predictions are in good agreement with the experimental data. However, the DTM produces results closer to the measured. It is appreciable that the simulations with radiation models captured the feature of nearly uniform vertical temperature distribution in the hot upper layer while the simulation ignoring the radiative heat exchange completely missed this feature. This suggests that radiation contribute a great part to creating a uniform upper layer.

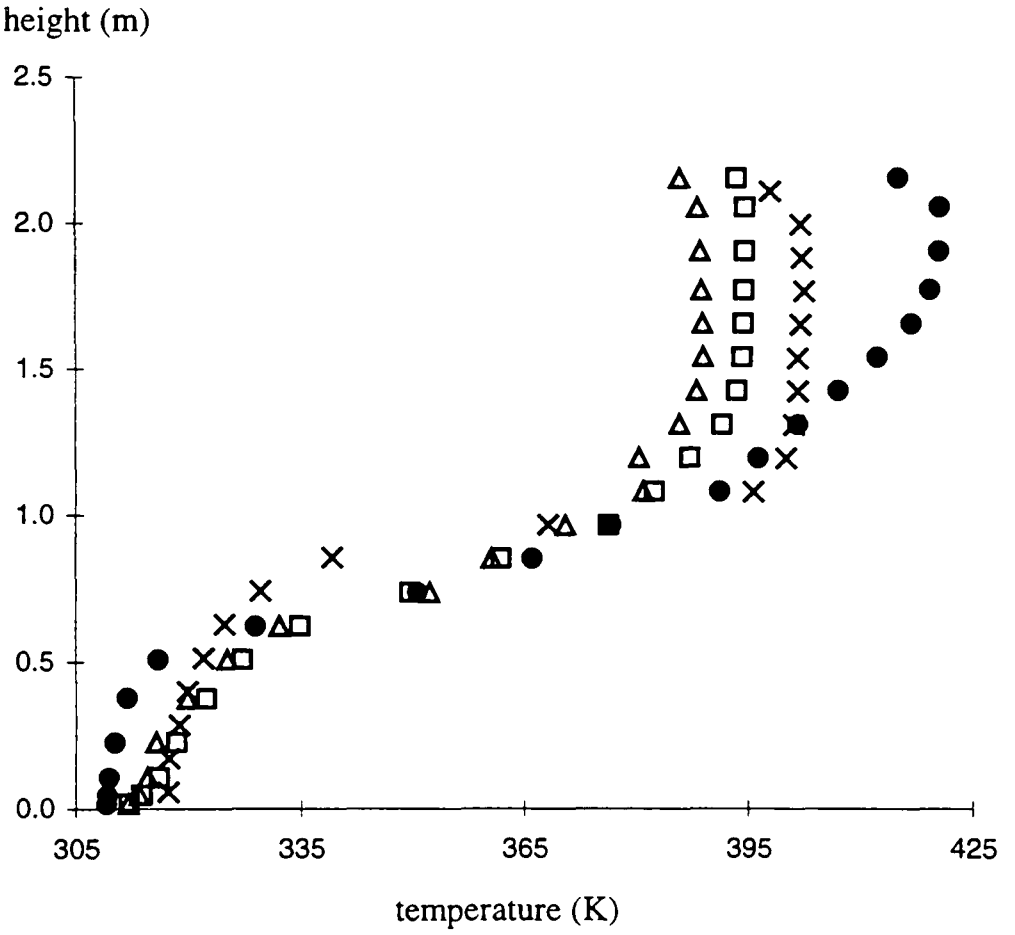

Fig. 6.4.1: The vertical temperature profiles in the corner predicted by
Δ: the six flux and soot model; □ :DTM and soot model;
• : the simulation without radiation models; × : measured.

Figure (6.4.2) depicts the stack temperature profile produced by the BASE MODEL and the simulation without radiation models but including the gas phase combustion

model and heat losses through the walls and the ceiling. This figure shows that only inclusion of the gas-phase combustion model and conductive heat losses through walls and ceiling is not able to sufficiently improve the vertical temperature predictions in the upper layer. However by taking the conductive heat losses through the ceiling, the temperature drop beneath the ceiling is predicted. Figure (6.4.2) also demonstrates that the temperature predictions at a position far from the burner fire seems not to be affected much by the gas-phase combustion model alone. The slight improvement of the upper layer temperature calculations is due primarily to the inclusion of the conductive heat losses through the walls and the ceiling. Comparing figure (6.4.2) with figure (6.4.1) illustrates that taking radiative energy exchanges into account will produce much better improvement for the predictions of the upper layer temperature.

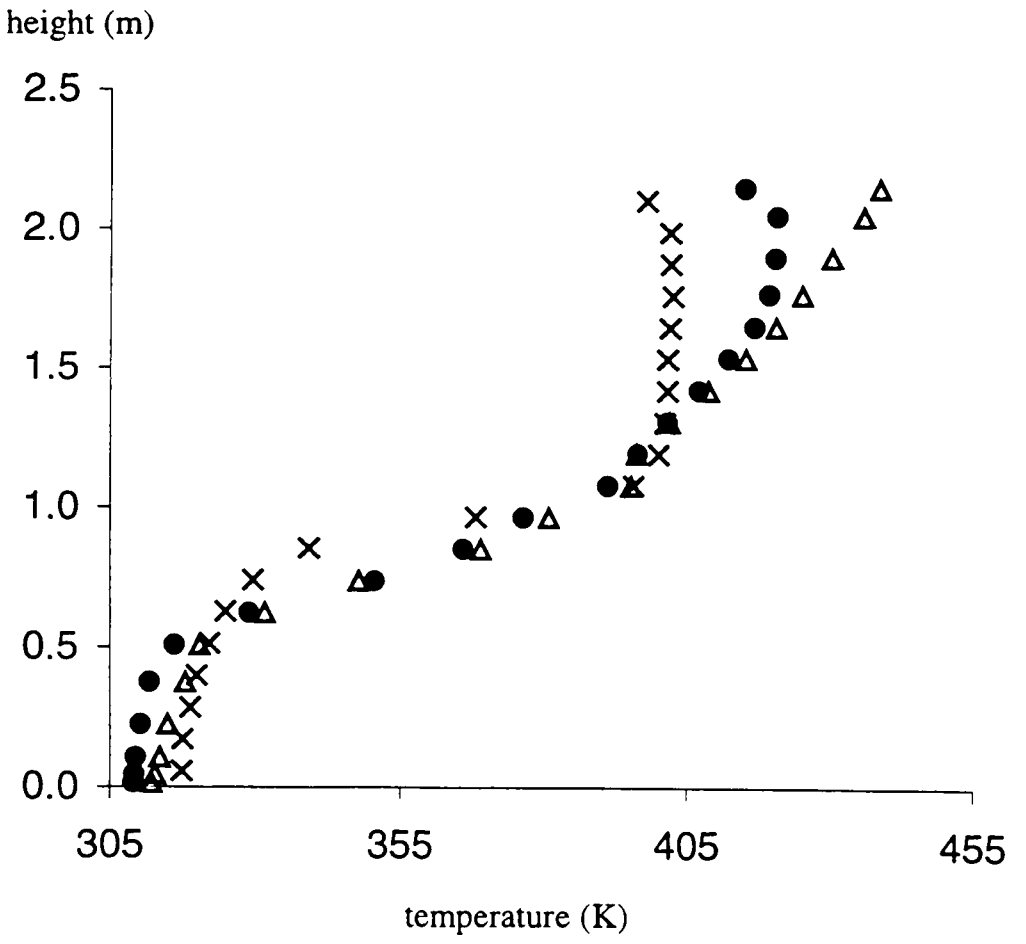

Fig. 6.4.2: vertical temperature profiles in the corner predicted by
× : measured; Δ: the BASE MODEL;
•: the simulation without the radiation models.

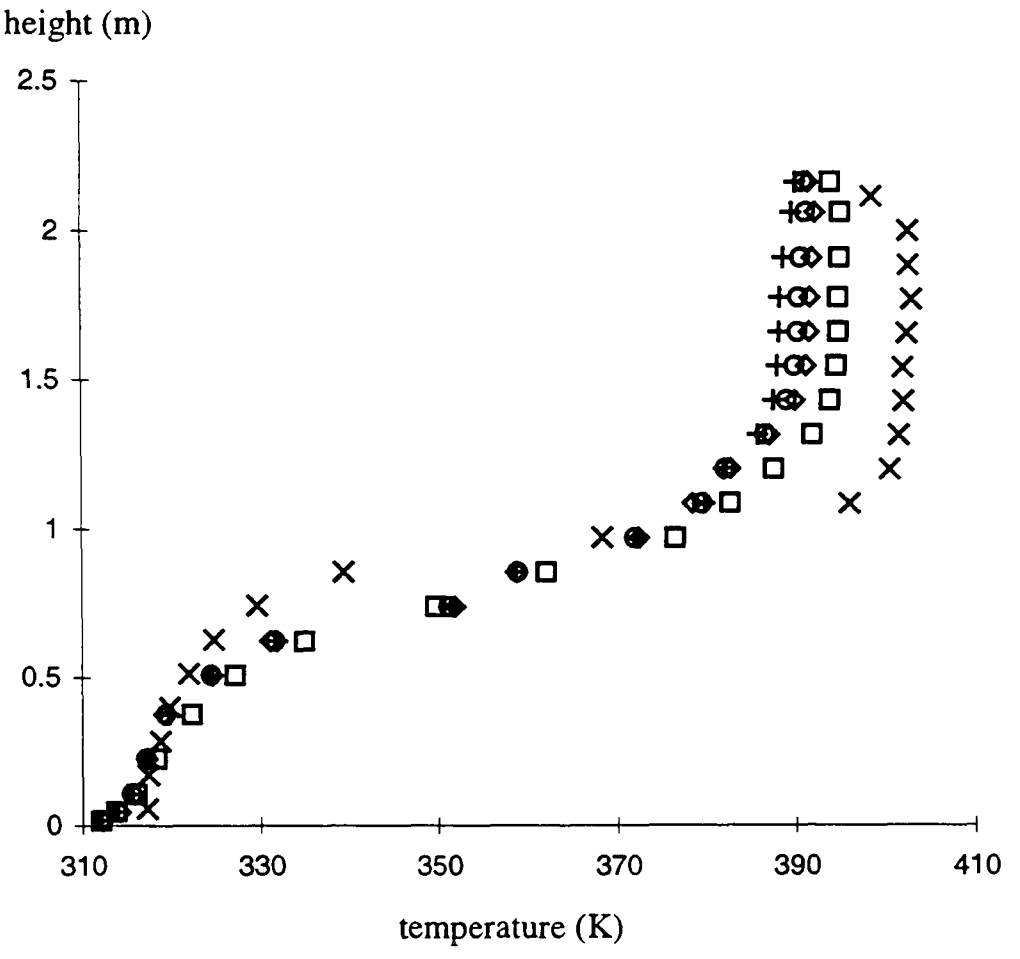

Fig. 6.4.3: Vertical temperature profiles in the corner predicted by DTM with/without soot model.
× : measured; □: predicted with the soot model;
without the soot model: + : $\alpha_s = 0.4$; o : $\alpha_s = 0.2$; ✧ : $\alpha_s = 0.1$;
where α_s stands for the constant absorption coefficient in the upper layer.

Figure (6.4.3) demonstrates the predictions of the vertical temperature distribution in the room corner yielded by simulations using the DTM with/without soot formation. The model inclusive of the soot formation produces better temperature predictions than the ones neglecting the soot formation. When soot formation is not taken into account, the temperature predictions appear not to be strongly sensitive to the variation of the constant soot absorption coefficient in the upper layer. The results from the simulations using the six flux model present the same features[figure (6.4.4)]. This indicates that the fire plume temperature interacting with its radiative heat losses controls the variation of upper layer temperature. In other words, the radiative heat losses in the fire plume are more important to determine the level of the temperature of the upper layer than the radiative heat losses in the same region. This

argument is further supported by the fact that the maximum flame temperature predicted without radiation models(1880K) is much higher than the ones predicted by inclusion of the radiative exchange(1360K). However, as ignoring radiation results in non-uniform temperature distribution in the upper region, the radiative energy exchange in this region may be primarily responsible for the temperature uniformity of the upper layer.

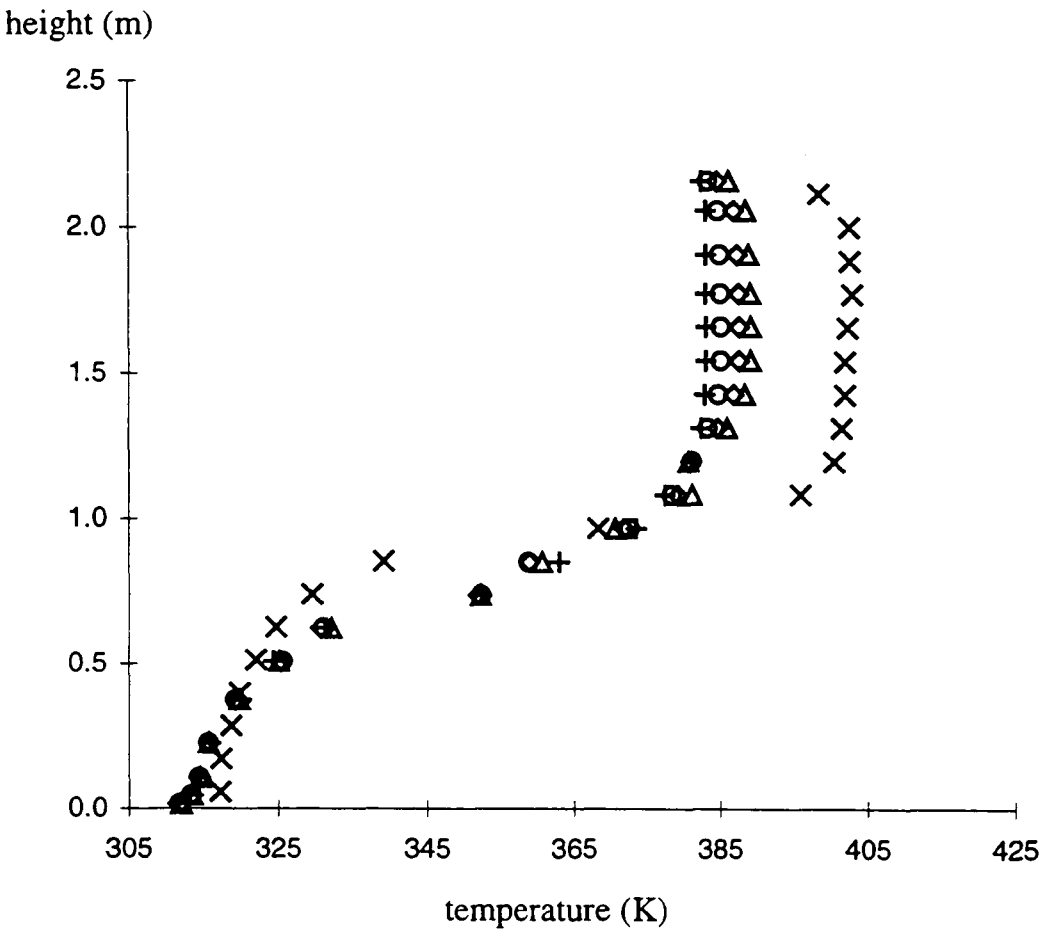

Fig. 6.4.4: Vertical temperature profiles in the corner predicted by the six flux model with/without the soot model.
× : measured; Δ: predicted with the soot model;
without the soot model: + : $\alpha_s = 0.4$; o : $\alpha_s = 0.2$; ✧ : $\alpha_s = 0.1$;
where α_s stands for the constant absorption coefficient in the upper layer.

Both figure (6.4.3) and (6.4.4) show that simulations incorporating soot formation yield better upper layer temperatures than the ones without the soot formation, no matter what kind of radiation model is used.

6.4.3 The temperature in the doorway central line

Figure (6.4.5) depicts the predicted and measured temperature profiles in the vertical middle line of the doorway. The predicted results come from the simulations using three different radiation model configurations as follows: the six-flux model and the soot model, the DTM and the soot model and no radiation model. The simulation quantities are reasonable agreement with experimental data. The figure shows clearly that the simulations capture the primary characteristic of flows induced by a room fire, that is, there exists an interface between the hot flow drifting out of the room and the cool flow entering into the room. However, due to neglecting the radiative heat losses, the simulation without radiation models generates much higher temperatures in the upper region. Once again, the simulations with soot and radiation models yield a better agreement with the measurements and the DTM simulation creates marginally closer results to the measured than the six-flux model simulation.

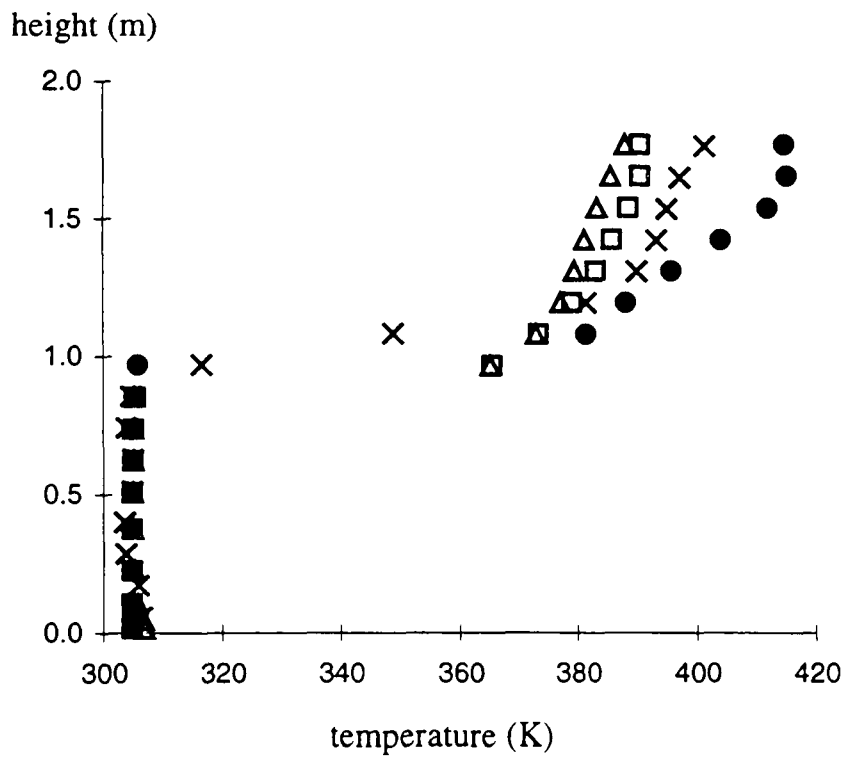

Fig. 6.4.5: Vertical temperature profiles in the doorway central line predicted by
Δ: the six flux and soot model; □: DTM and soot model;
• : no radiation models; × : measured.

6.4.4 The velocities in the doorway central line

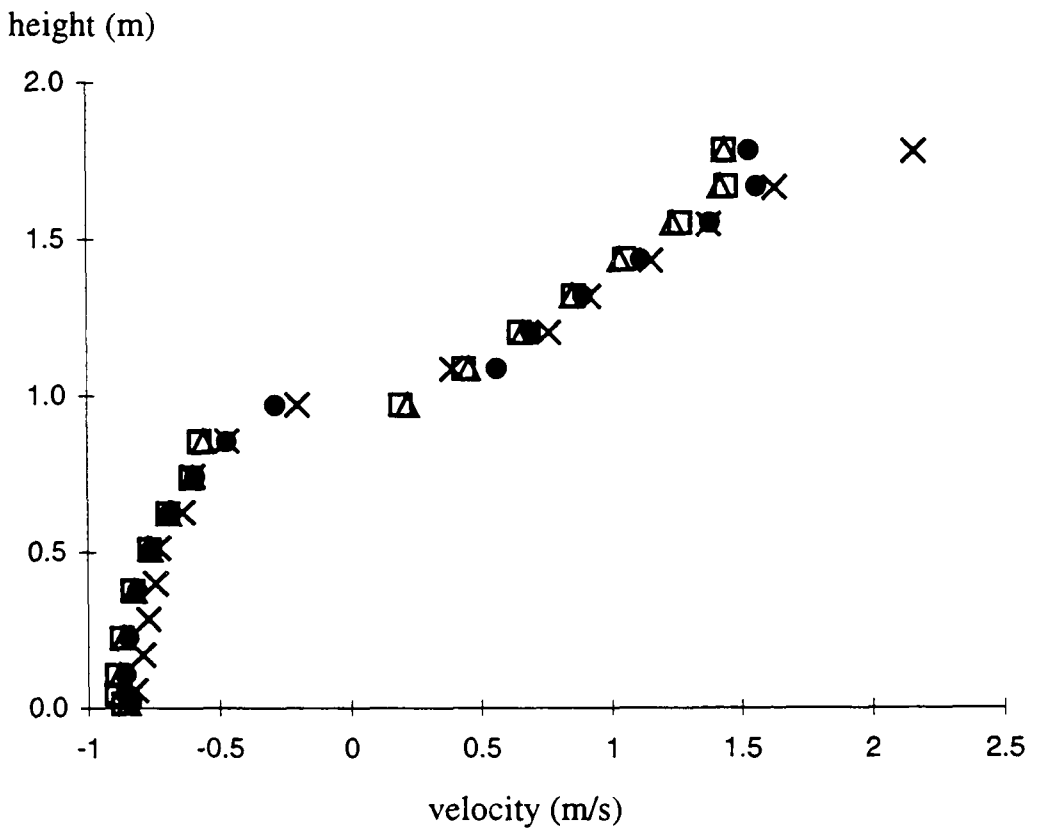

Fig. 6.4.6: The velocity profiles of the vertical middle line in the doorway predicted by
Δ: the six flux and soot model; □: DTM and soot model;
• : no radiation models; × : measured.

The vertical velocity profile in the middle of the door is depicted in figure (6.4.6). The predicted results come from the same simulations mentioned in the last subsection. Except just under the upper edge of the door the model predictions produce very good agreement with the experimental data. The velocity profiles do not appear to be model sensitive. The velocity just under the upper edge of the door is underpredicted. This behaviour was also found in the Kumar et al.[1991], Hadjisophocleous[1993] and Kerrisonn et al.[1994].

6.4.5 The predicted temperature and velocity contours

This subsection presents some velocity and temperature contours predicted by the simulation using 24 ray DTM, the six-flux model and the soot model. They will be

compared with the corresponding contours presented in chpater 3 which were predicted by the simple BASE MODEL.

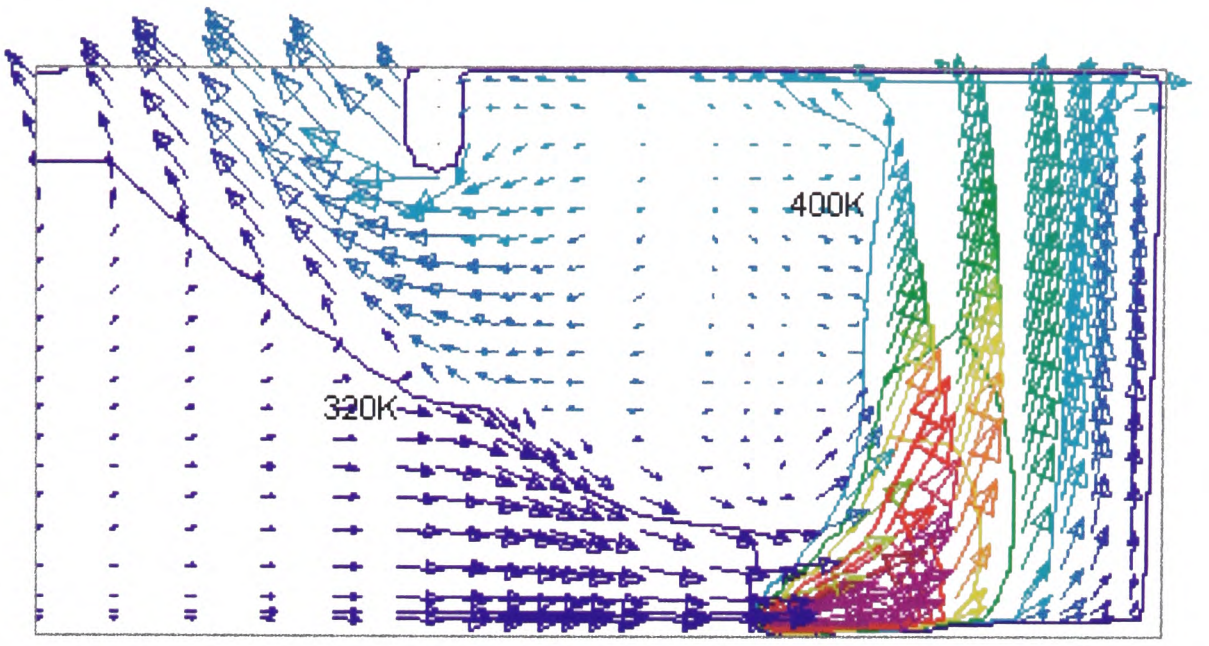

(a)

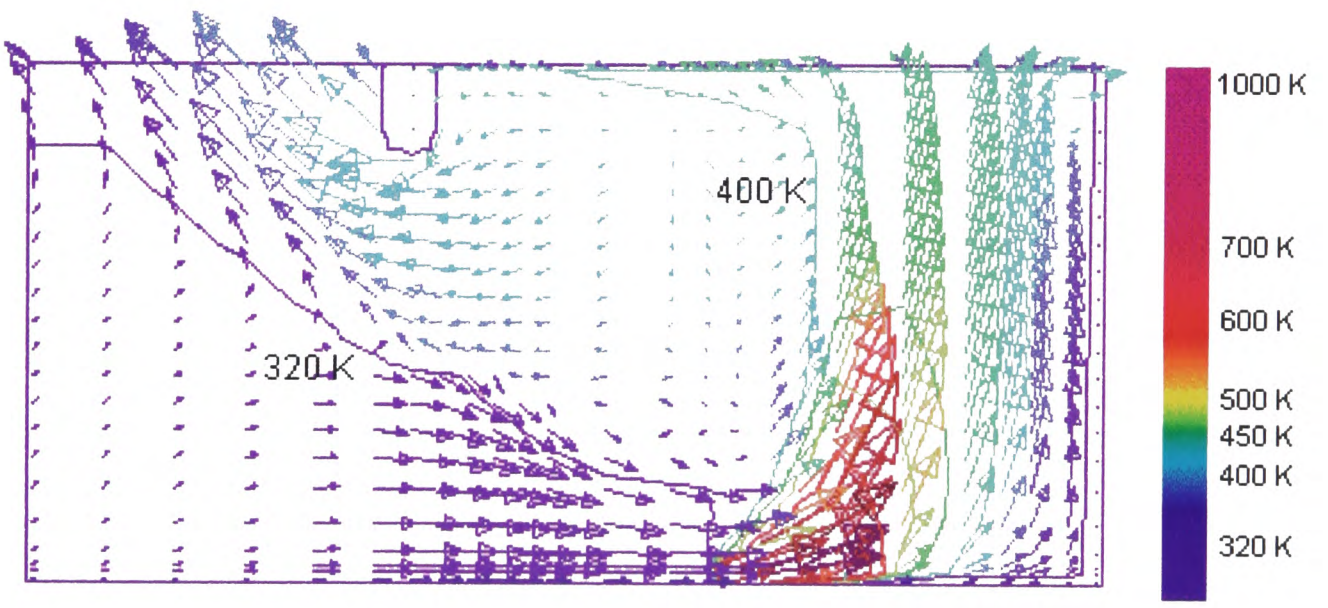

(b)

Fig. 6.4.7: The predicted flow velocities in the plane passing through the doorway central line and the centre of the Steckler room
as predicted by (a): DTM(24 rays) and (b) the six-flux model.
Note: the solid lines in the figure are temperature contours. The colour of the velocity vectors represents the flow temperature.

Figure (6.4.7) plots the predicted flow velocities in the plane passing the doorway central line and the center of the Steckler room. The two radiation models used produced very close velocity fields. Comparing these two figures with figure (3.4.4), we can find that the flow patterns predicted by the BASE MODEL and the two

radiation models are quite similar. However, in figure (6.4.7), the colour of the upper part of the fire plume indicates that the upper part of the fire plume predicted by the models here is cooler than that predicted by the BASE MODEL. As discussed previously, this is because radiative heat losses from the fire are taken into consideration in the simulations of this chapter. This means less energy is pumped into the upper layer through the fire plume. As a result, the 400K temperature contour originates from the front of the fire base, then following the fire plume reaches and vanishes at the ceiling inside the compartment, while in figure (3.4.4) the 400K temperature contour extends out of the room. Figure (6.4.7) also indicates that the flow predicted here within the doorway above the neutral plane is cooler than that predicted by the BASE MODEL.

In figure (6.4.8), the velocities in the xy plane 0.15m behind the burner are depicted. As obseved in figure (3.4.5), the flow of the upper part of the fire plume is deflected due to the confinement of the ceiling and there are two recirculation region flanking the fire plume in the upper layer. However, in figure (3.4.5), the yellow colour flow representing approximate 500K temperature impinges the ceiling, while in figure (6.4.8) much cooler flow (around 400K) touches the ceiling. Furthermore, in the core of the fire plume the red flow indicating higher temperatures is much bigger and higher in figure (3.4.5) than in figure (6.4.8). In addition, the 400K temperature contour in figure (6.4.8) is in much higher position than that in figure (3.4.5). Once again, these differences are attributed to the radiation heat losses from the fire and the hot upper layer.

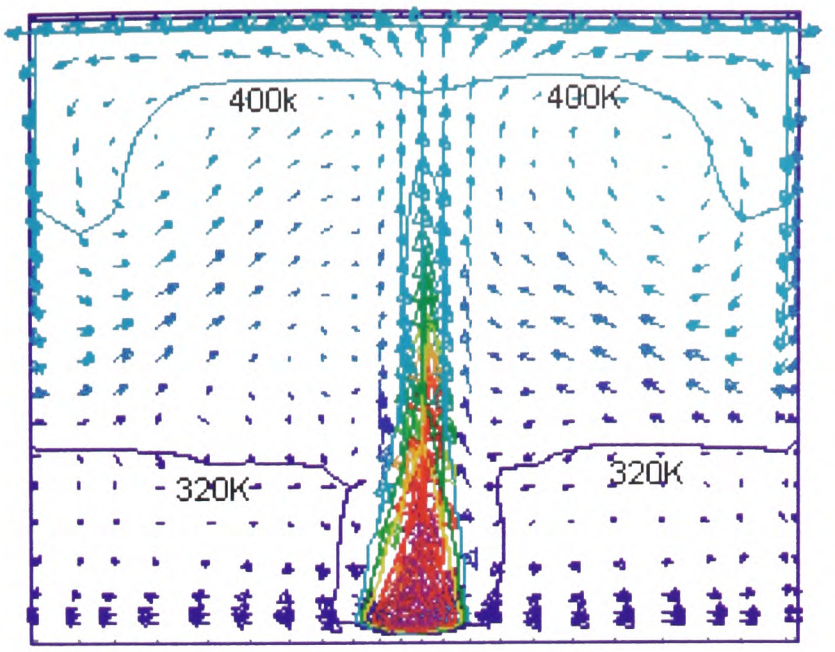

(a)

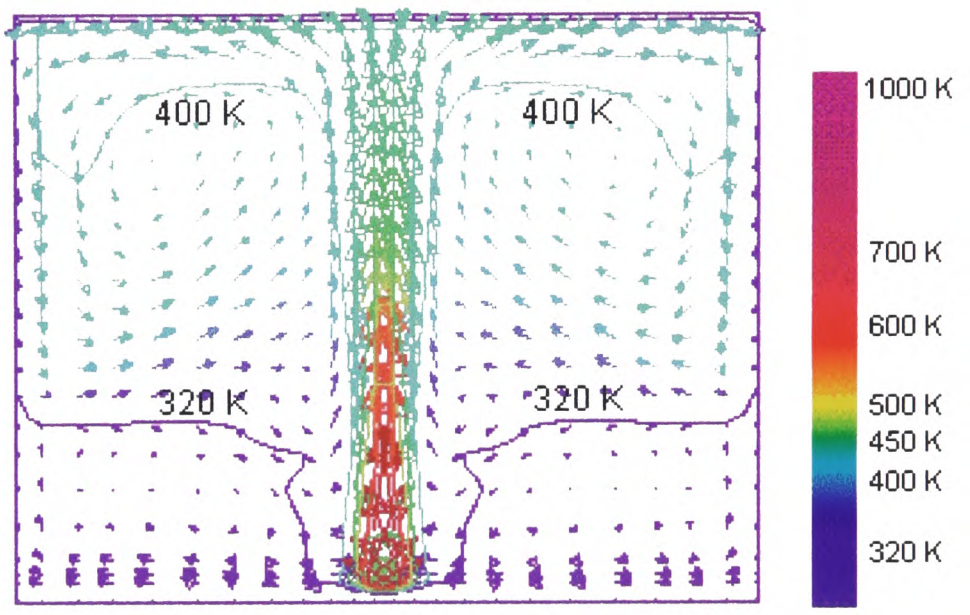

(b)

Fig. 6.4.8: The flow velocities in the xy plane 0.15m behind the burner as predicted by (a): the DTM(24 rays) and (b): the six-flux model. Note: the solid lines in the figure are temperature contours. The colour of the velocity vectors represents the flow temperature.

Figure (6.4.9) presents the temperature contours produced by the DTM(24 rays) in the plane passing the doorway central line and the center of the Steckler room. From it, it is observed that the fire plume is blown backwards by the incoming flow induced by the fire. From this figure, the angle of inclination of the fire to the horizontal can also be estimated. This is estimated to be approximately in the range of 32^{o} to 42^{o}. This estimation is very close to the flame angle range of 33^{o} to 43^{o} observed by Quintiere et

al.[1981] in an earlier series of experiments using an identical experiment setup. It is also a better estimation than the approximate range of the flame angle between 40° to 44° obtained from figure (3.4.6).

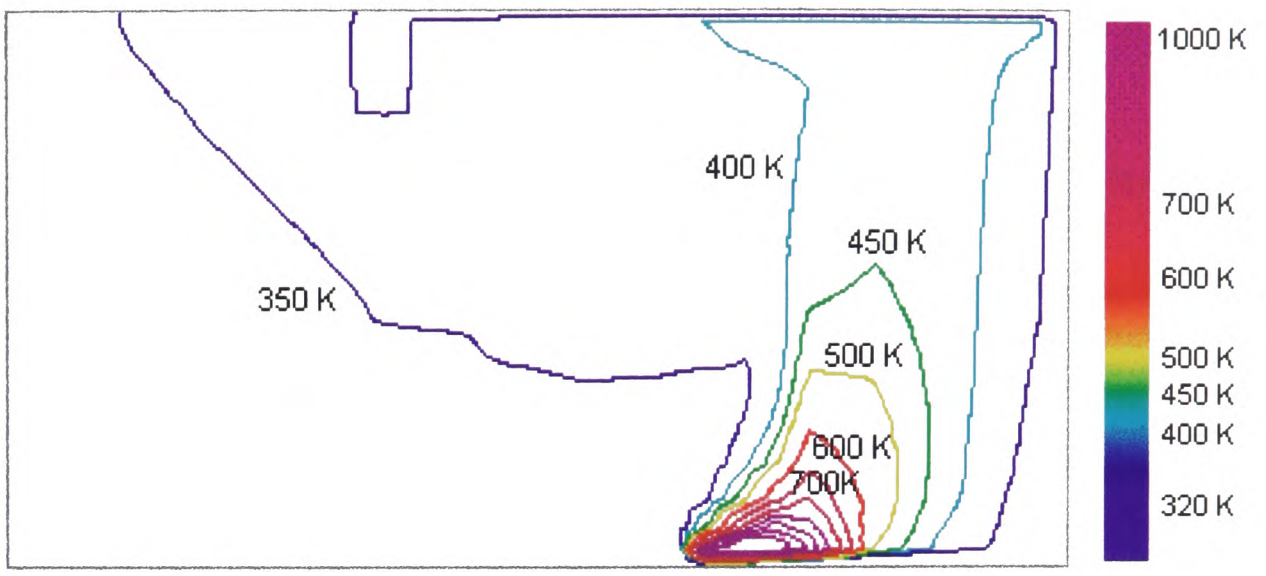

Fig. 6.4.9: the temperature contours in the plane passing the doorway central line and the centre of the Steckler room as predicted by the DTM(24 rays). (Unit: K).

6.5 Efficiency and Accuracy Comparisons for Radiation Models

It is important for modellers to balance the accuracy and the cost when an appropriate numerical method is being sought. In this section, the computational costs of the simulations of the selected Steckler's fire test using the six-flux model and the DTM are investigated. All the simulations in this section include the simple soot model described in subsection (5.2.3). One of the simulations uses the six-flux model while another three simulations include the DTM as the radiation sub-model. In the three DTM simulations the numbers of rays used are 6, 8 and 24 respectively. In the DTM model using six rays the six rays are parallel to the positive and negative directions of the three coordinates respectively. In the DTM models using 8 and 24 rays the directions of the rays are presented in table (5.6.1).

The average time consumed performing 100 iterations using a particular radiation model is presented in table (6.5.1). For each radiation model, a simulation of ten time steps with 100 iterations in each time step is carried out. Then the average consumed time is obtained dividing the total time consumed in ten time steps by ten.

Table 6.5.1: the time consumed by the simulations in preforming100 iterations.

Radiation model	Six-flux	DTM (6 rays)	DTM (8 rays)	DTM (24 rays)
Time (s)	91.1	94.9	134	255

As might be expected, the computational cost using the six-flux model is approximately the same as that using the six-ray DTM model. But as the number of rays used in the DTM model increases, the DTM becomes more and more expensive. The computer time using 24 rays in the DTM is approximately three times that of using 6 rays.

Table 6.5.2: Times consumed in performing 200 time step simulations for the Steckler room fire using various radiation models.

Radiation model	six-flux	DTM (6 rays)	DTM (8 rays)	DTM (24 rays)
Time (min)	126	139	181	372

As a reference, the times consumed by performing a 200 time step(one second time long of each time step) simulation for the selected Steckler room fire test using the soot model and different radiation models are presented in table (6.5.2). Once again, the use of the 24 ray DTM is most expensive and the time consumed by this radiation model is much longer than other radiation models using less number of rays in the DTM and the six-flux model.

While the computational costs of different radiation models concern modellers,

another central consideration is the accuracy of the selected model. What we are concerned with here is if the predictions for the Steckler fire scenario are significantly improved by using more sophisticated radiation models.

Some main features of the room fire are presented in table (6.5.3). The simulation using the six-flux model produced very similar results to those of the simulations using the DTM and the predictions are not improved much by increasing the ray number of the DTM.

Table 6.5.3: Main features of the Steckler's room fire.

Model Elements		Upper Layer Temperature	Neutral Plane Height	Inflow	Outflow
		°C	M	kg/s^{-1}	kg/s^{-1}
Six-flux		115	0.935	0.523	0.534
DTM	6 rays	124	1.0	0.512	0.520
	8 rays	127	1.01	0.525	0.534
	24 rays	121	0.938	0.530	0.540
Experiment		129	1.027	0.554	0.571

Figure (6.5.1) plots the stack vertical temperature profiles predicted by the simulations using different radiation models. The upper layer temperature predictions of these simulations are quite similar. The simulations using the DTM models with 8 rays and 24 rays predicted better temperature profiles than the simulation using the six-flux model. But the improvement is not significant. The 24 rays DTM produced an upper layer having a thickness closer to the measured than the 8 rays DTM. The simulation using 6 rays DTM missed the feature of the nearly uniform temperature distribution in the upper layer. It is not unexpected since the 6 rays in DTM is extremely coarse to discretise the total 4π steradians. Although the modified six-flux model has in appearance an identical formulation to that of 6 rays DTM, one fundamental difference between them lies in the fact that the former uses the concept of the

radiative flux which represents the total hemispherical power per unit area while the latter employs the concept of the radiative intensity which stands for the total radiant intensity per unit area in per solid angle along a prescribed beam. Therefore it is not surprising that the six-flux model and the 6 rays DTM produced different results, particularly in the upper region where stronger radiative exchanges take place.

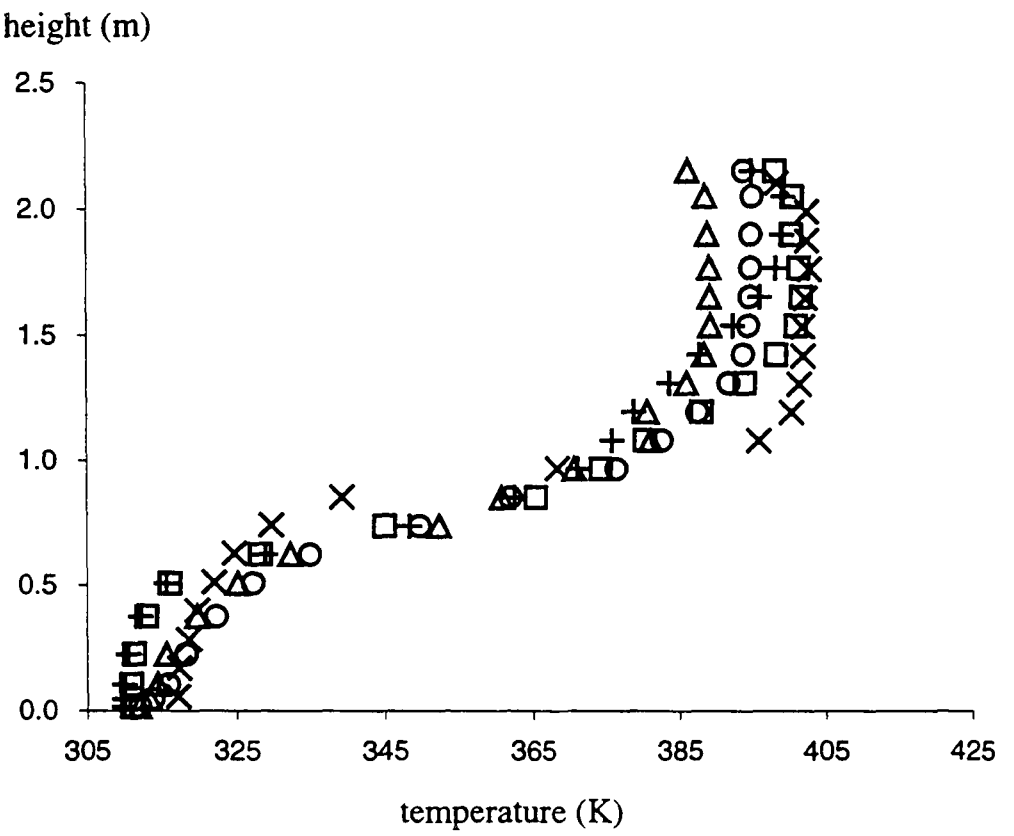

Fig. 6.5.1: the vertical temperature profiles in the corner predicted using the different radiation models.
× : measured; Δ: predicted with the six-flux model;
DTM: + : 6 rays; □ : 8 rays; o : 24 rays.

Since the accuracy of the prediction of the radiation heat flux at the walls and the ceiling is not crucial for the simulations of the Steckler's room fire and more important are the radiative heat losses from the burner plume and the upper layer, it might be expected that the predictions of the simulations are not much improved on the whole by increasing the ray number in the DTM models. Good agreements with the experimental data of the predictions produced by the simulations using different radiation models only demonstrate that the six-flux model and the DTM models can give the correct order of radiative heat losses in the gas phase. However when fire

spread over combustible solid surface is involved, more accurate predictions of radiation heat flux at the solid surface become important due to the central role of heat transfer in the processes of flame spread. Under these circumstances, the intention of modellers is generally to use larger number of rays in the DTM model.

The final part of this section is a short comparison of time consumed by using and not using the simple soot model. The table below presents the times used by performing 100 iterations of the different simulations on a 400 MHz DEC alpha workstation.

Table 6.5.4: The times consumed by different models.

Model Type	Six-flux		DTM (24 rays)	
	with soot model	without soot model	with soot model	without soot model
time (s)	91.1	90.7	255	244

It is clear that inclusion of the simple soot model in simulations is affordable.

6.6 Conclusions

An integrated fire field model was developed to address the weakness of the simple base model developed in chapter 3. The integrated model included three new components—the gas phase combustion model, radiation models and convective heat losses through the walls and ceiling. The first two components have been described in chapters 4 and 5 while the last one was addressed in this chapter.

An integral method capable of dealing with the nonlinear surface reradiation at the top surface and the convective heat loss at the bottom surface was outlined for non-combustible solids. Since the wall surface temperature is the only concern to set up

the boundary condition for the flow domain in a field fire model, the calculation of the solid surface temperature rather than the coefficients of the prescribed temperature profile was the central attention of the presentation of the integral model.

This integrated model was used to simulate the same Steckler room fire test as the one in chapter 3. The model was assessed by comparing the model predictions with the experimental data. Simulations were carried out with systematic variation of the radiation model configurations as follows:

(a) – Radiation is ignored

(b) – Two different radiation model options are examined, i.e., the six-flux radiation model and the DTM model(24 rays)

– Soot formation ignored and hence constant a soot absorption coefficient for the upper layer that assume the values: (i) 0.1; (ii) 0.2; (iii) 0.4

(c) – using the six-flux model with the soot formation model and hence the soot absorption coefficient for the upper layer depends on the soot volume fraction and temperature(equation (6.3.2))

(d) – as (c) but the radiation model is the DTM using 6, 8 and 24 rays.

The field model predictions capture the main trends of the flow induced by the room fire. The predicted neutral plane height, the mass flow in and out of the room and the average upper layer temperature are in good agreement with the experimental results. These predictions are strongly sensitive to radiative heat exchange. It was found that radiation is very important to determine the hot upper layer temperature and the radiative heat losses from the hot layer and the fire plume are significant.

The approximately uniform temperature structure of the upper layer is predicted by the simulations including radiation models. In contrast the simulation neglecting radiation completely misses this feature. By comparison of the predicted temperature profiles in the upper layer produced by simulations with/without radiation models and the systematic changes of the soot absorption coefficient in the upper layer, the predicted results indicate that the radiative heat losses in the fire plume are more important to determine the level of the temperature of the upper layer than the radiative heat losses in the upper layer. In addition, the radiative energy exchange in the upper layer may be primarily responsible for the temperature uniformity in this region.

The two-layer structure in the doorway is predicted by all the simulations. However, inclusion of radiation improves the upper layer temperature predictions. The velocity profiles are not model sensitive.

Generally, inclusion of soot formation slightly improves the predictions and simulations using the DTM produce predictions giving marginally better agreement with experiment than the ones using the six-flux model.

The integrated model produced predictions in better agreement with the experimental data than the simple model developed in chapter 3 where the burner was represented by a volumetric heat source and radiation and convective heat losses through the walls were neglected.

The computational cost and accuracy of the six-flux model and the DTM models

using different number of rays were also investigated. The DTM model becomes more and more expensive as the number of rays used increases. The DTM with 24 rays is about three time as expensive as the six-flux model. It was found that for the Steckler's room fire the simulation using the six-flux model produce similar predictions by the simulations using the DTM model and predictions are not much improved by increasing the ray number in the DTM model. This may be expected as the accuracy of the predictions of radiation heat flux at the solid surface is not crucial while more important are the heat losses through the radiation from the burner plume and the upper layer. Both the six-flux model and the DTM model can produce the correct order of the radiative heat losses in the fire plume and the upper layer but the later consumes in general more computer time. In addition, inclusion of soot formation does not significantly increase the computing time.

In this chapter, a non-spreading fire model was developed and tested. The spreading fire however, represents more severe and dangerous situation, in particular the fires spreading over solid fuels. In the next chapter the combustion of solid fuels is examined. Models used for this process are reviewed and models for non-charring and charring materials are proposed, developed and tested.

Chapter 7

MODELS FOR COMBUSTIBLE SOLID MATERIALS

7.1 Introduction

When a solid fuel is exposed to a high enough external heat flux, it will be gasified to release combustible gases. This process is called pyrolysis. Gasification of solid fuels involves very complex chemical decomposition processes. Some simplifications are required to model solid fuel pyrolysis. Since the present study is aimed at simulating fire spread over solid fuel surfaces, the major task of a pyrolysis model is to predict the mass loss rate of the pyrolizing material. The chemical decomposition involved in pyrolysis is thus ignored and the solid fuel is assumed to be chemically inert. Modelling pyrolysis (the mass loss process) of solid fuels is the first step to simulate the growth of the enclosure fires in which fire spread over the surfaces of combustible solids is involved. In this chapter, discussions are concentrated on the pyrolysis of solid fuels and its modelling under the assumption that the solid fuel is chemically inert. The fire spread process will be further discussed in chapter 8. A discussion of the detailed chemical processes involved in pyrolysis and the wide variety of degradation products is beyond the scope of this thesis and hence a brief description of the pyrolysis processes of charring and noncharring materials is presented in section 7.2 according to experimental observations and measurements. Section 7.3 reviews the pyrolysis models. In section 7.4, two pyrolysis models for non-charring and charring materials are developed. In section 7.5 and 7.6, both the non-charring model and the charring model presented in section 7.4 are validated comparing the model predictions with experimental measurements.

7.2 Solid Fuel Pyrolysis

When a solid fuel is exposed to a high enough external heat flux, chemical decomposition in which solid material is converted to combustible gases will take place and hence the solid will lose its mass. Some solid fuels produce a layer of carbonaceous residues known as char. As the gasification process of a solid fuel is endothermic, the mass loss rates of the condensed fuel depend on the value of the external heat flux. If sufficient combustible volatiles are generated in the pyrolysis process to form a fuel/oxidizer mixture within flammability limits, the fuel/oxidizer mixture may be ignited by a pilot heat source such as pilot flames, sparks, hot wires, thermal radiation and so on[Blasi, 1993]. Sustained burning after ignition needs sufficient excess heat to overcome heat losses.

7.2.1 Pyrolysis of non-charring materials

Unlike charring fuels, there are no carbonaceous residuals left after non-charring fuels are gasified. Consequently thermal degradation of a non-charring fuel is relatively simple and hence will be dealt with first. Polymethylmethacrylate (PMMA) is a non-charring fuel widely used to investigate the characteristics of thermal degradation of non-charring fuels both experimentally and theoretically. In an investigation of the mass loss processes for PMMA, Vovelle *et al.*[1984] observed that a regression of the exposed surface occurs so that "heat balance remains unchanged and the mass loss rate tends towards a stationary value". Whereas, the charring fuels can not reach such a quasi-stationary state as the char layer formed after the original material is removed is actively involved in the degradation and pyrolysis processes and has a significant

impact on the heat and mass transfer processes and relevant chemical processes[Blasi, 1993].

A relationship between the burning rate($\dot{m}''$) of a non-charring fuel and the heat flux($\dot{Q}''$) was obtained by Tewarson and Pion [1976]

$$\dot{m}'' = (\dot{Q}'' - \dot{Q}_0'')/L \tag{7.2.1}$$

where $\dot{Q}_0''$ is a critical heat flux under which no thermal degradation is observed and L is the heat of pyrolysis of the material. This empirical expression was further investigated for PMMA by Vovelle *et al.* [1984]. It was found that in an inert atmosphere it is valid at every stage of the overall phenomenon that the mass loss rate is directly propotional to the effective heat flux penetrating into the material [Vovelle et al., 1984]. A similar linear expression to equation (7.2.1) was established

$$\dot{m}'' = k(\dot{Q}'' - \dot{Q}_0'') \tag{7.2.2}$$

However, the slope k varies with time and only at the maximum mass loss rate is its value equal to the inverse of the pyrolysis heat of the material. In air, it was found that due to the effect of oxygen on the pyrolysis processes the situation becomes slightly more complex and the results are affected by the level of the incident heat flux[Vovelle et al., 1984].

When PMMA undergoes degradation processes, a thin molten film near the heated surface develops. The liquefied film acts as a barrier preventing degradation products from escaping through the surface. Bubbles are formed beneath the exposed surface and move to it. When they are close to the surface, they burst directly through it creating small holes. The holes aid oxygen to diffuse into the melted layer, permitting

oxygen to have an effect in the further depth of the layer[Kashiwagi and Ohlemiller, 1982]. The presence of the viscosity gradients affects the movements of bubbles within the molten thin layer[Kashiwagi *et al.*, 1990]. Oxygen in the environment remarkably reduces the viscosity of the molten layer, leading to a high bubble frequency. Kashiwagi and Ohlemiller[1982] observed that the presence of oxygen significantly increases the mass loss rate of the PMMA sample and its effect is lessened with increasing the level of the external heat flux. Based on this observation they concluded that the oxygen effect becomes weaker when the flow of degradation products increases. The same trend was observed by Vovelle *et al.*[1984]. They suggested that only the initial stages of the pyrolysis be affected by the oxygen presence at high values of the flux while the maximum mass loss rate is nearly independent of this parameter.

7.2.2 Pyrolysis of charring materials

Most natural solid fuels char when burnt. In this process the solid fuel forms a layer of carbonaceous residues known as char over the virgin material when it is heated. The char layer not only protects the virgin material from pyrolyzing but also results in increasing surface reradiation losses as the temperature at the char surface increases. Furthermore, complicated chemical reactions take place within the char layer as it reacts with atmospheric oxygen and is oxidized. The combustible volatiles yielded from pyrolysis undergo secondary reactions when they pass through the high temperature char layer.

Wood is the most representative of char materials. Its nonisotropic structure results in

material properties that vary with direction. It is a complex mixture with basic components of cellulose(~50%), hemicellulose(~25%) and lignin(~25%)[Madorsky, 1964]. These proportions are quite different from one species of wood to another. It also contains a certain amount of moisture and other inorganic impurities.

The pyrolysis processes of wood are extremely complex. The components of wood have different tendencies for decomposing and charring. The three basic constituents of wood have different decomposition temperatures, typically Hemicellulose 200-260°C, Cellulose 240-350°C and Lignin 280-500°C[Roberts, 1970]. Cellulose and hemicellulose produce high yields of volatiles at temperatures above 300°C, whereas the lignin content more readily forms char[Blasi, 1993].

The composition of wood pyrolysis products is also very complex. They are generally divided into three groups: char, tar and gas. Char is the solid carbonaceous residual most readily associated with burnt wood. Tars are the volatile products of high molecular weight, with levoglucosan as major constituent, that may condense near room temperature[Agrawal, 1988]. The principal volatiles included in the gaseous products of wood gasification are CO, CO_2 and water vapour.

The rate of heat transfer to the wood fuel not only affects the absolute yield of combustible volatiles, but also changes the composition of the pyrolysis products. It is more likely to occur for the char-forming process at conditions of low rates of heat, or relatively low temperature while at high temperatures (from 400-600°C), the tar generation increases[Scott et al., 1988].

The nature and concentration of inorganic impurities such as fire retardants have significant effects on the decomposition of wood. Fire retardants considerably enhance the yields of char[Brenden, 1967] which not only protect the virgin wood but leads to high surface temperature creating greater reradiation heat losses as well.

The formation of char starts at temperatures above 200-250°C. Small fissures and cracks appear in the char as pyrolysis continues. As the char accumulates, the size and number of cracks increase. The combustible gases and water vapour generated by the pyrolysis process flow towards both the char layer and virgin wood. Due to much higher gas permeability of the char, most of gaseous products are forced to pass through the affected layer. Secondary reactions occur when volatiles run through the high temperature char layer. While some of volatiles and water vapour travel towards the relatively cold virgin wood, they may condense in it.[Blasi, 1993]

As the depth of char increases, the residence time of the volatiles created in the primary pyrolysis is prolonged, which enhance the possibility of the occurrence of the secondary reactions within the char layer. In contrast, the increasing size and number of cracks and fissures in the char counteract this effect by allowing the volatiles to escape more easily through the affected layer[Blasi, 1993].

Radiation and convective heat flux may penetrate through the porous structure of the char[Blasi, 1993]. The cracks and fissures also provide a path for oxygen to diffuse into it. As a result, the char layer is oxidized. The exothermic char oxidisation as well as the enhanced radiation and convective heat transfer partly compensates the high reradiation heat losses by contributing heat to the endothermic decomposing process.

The moisture contained in wood may also affect the mass loss rates. At low incident heat flux ($2.5W/cm^2$), two stages in the history of the mass losses were observed[Kashiwagi *et al.*, 1987]: an initial small hump caused by evolved sample moisture and a subsequent larger peak. However, this small plateau of mass loss rates appears to vanish as the incident heat flux increases from $2.5W/cm^2$ to $4W/cm^2$. The moisture content also reduces the heat release rate(HRR) of the burning wood. Experimental results show that exposed to 50 kW/m^2 irradiance a 9% moisture content is responsible for about 23% change in the 60 second HRR and 41% change in the 300s HRR[Tran, 1992].

Another important observation is that the char layer does not have the same shape as the original wood. Surface regression and internal shrinkage are possible. More complicated is the dependence of the physical structure changes on the level and direction of incident heat flux. If the incident heat flux has a low intensity and is parallel to the wood grain direction, negligible surface regression occurs. If the incident heat flux is at a high level, surface regression and internal shrinkage are significant. At perpendicular high heat flux, these structural changes become greater than the parallel heating case.[Lee *et al.*, 1976]

7.3 Review of Existing Pyrolysis Models

Many efforts have been made to understand the chemical and physical processes of pyrolysis. A number of models have been proposed to treat the complex chemical and physical changes in the pyrolyzing solid fuels. Excellent reviews describing the mechanisms and models of the thermal degradation processes were given by Blasi[1993] and Kashiwagi[1994].

The chemical processes of pyrolysis can be represented by kinetic mechanism models. These mechanism models try to describe the routes, stages and products of the chemical processes. A discussion of these chemical mechanism models is beyond the scope of the present text. An excellent review for the models of kinetic mechanism of pyrolysis was given by Blasi[1993]. The simple one-step global model of pyrolizing mechanism is widely used. The evolution of the material thermal degradation is described by

$$\text{solid} \rightarrow \text{volatiles} + \text{char (for charring material)}$$

or

$$\text{solid} \rightarrow \text{volatiles} + \text{char} + \text{tar (for charring material)}$$

and

$$\text{solid} \rightarrow \text{volatiles (for noncharring material).}$$

A relationship between the burning rate($\dot{m}''$) and the heat flux($\dot{Q}''$) was obtained by Tewarson and Pion [1976]

$$\dot{m}'' = (\dot{Q}'' - \dot{Q}_0'')/\Delta H_g \qquad (7.3.1)$$

where $\dot{Q}_0''$ is a critical heat flux under which no thermal degradation is observed and ΔH_g is the heat of pyrolysis of gasification of the material, defined as

$$\Delta H_g = L + \int_{T_0}^{T_p} C_p dT, \tag{7.3.2}$$

where L is the heat of pyrolysis of the material, C_p is the heat capacity of the material, T_0 and T_p are the reference temperature and pyrolysis temperature respectively. The equation (7.3.1) was successfully used in some zone models to simulate and analyse the fire growth in enclosures. However, further investigations[Vovelle et al., 1984; Sibulkin, 1985] show that the heat of gasification varies throughout the burning period for both charring materials and noncharring materials. It depends on not only the heat losses through the material but also the environmental variables such as the level of external heat flux and the presence of oxygen. Therefore, more accurate approaches based on the thermophysical and thermochemical properties of the material are required.

Under the assumption of the one-step global model, there are numerous models based on the partial differential equations for conservation of mass, momentum and energy. However, the momentum equation is usually obviated by the assumption of no resistance to the flow of the degradation products within the condensed phase[Kanury, 1995]. Consequently mass transport in the sample is neglected partially or completely. Thus,

$$\frac{\partial \rho}{\partial t} + \frac{\partial \dot{m}''}{\partial x} = 0 \tag{7.3.3}$$

$$\frac{\partial}{\partial t}(\rho C_p T) + \frac{\partial}{\partial x}(\dot{m}'' \; C_p T) = \frac{\partial}{\partial x}(\lambda \frac{\partial T}{\partial x}) + \dot{q}''' \tag{7.3.4}$$

$$\dot{q}''' = -L\frac{\partial \rho}{\partial t} \tag{7.3.5}$$

[Kanury, 1995], where ρ is density, $\dot{m}''$ is mass flux of the degradation products, C_p is specific heat, T is temperature, λ is conductivity, L is heat of pyrolysis, t is time and x is depth normal to the exposed surface. In general, these models can be classified into two regimes: kinetic and ablative. The kinetic models try to incorporate the kinetic mechanisms of the thermal degradation of solid fuels. While ignoring the complex chemical reactions in the pyrolyzing material the ablation models are much simpler than the kinetic models. In effect, this approach assumes that the kinetics of the degradation mechanism occur at an infinitely fast rate[Staggs and Whiteley, 1996].

There are two fundamental assumptions used in this model. The first is that solid fuels are gasified only at the surface regions (for noncharring materials) or at the char/virgin interface (for charring fuels). Secondly, combustible gaseous products are released only when the solid surface is heated to the critical pyrolysis temperature (ignition temperature) and the temperatures of the pyrolyzing regions remain at the pyrolysis temperature throughout the period of mass loss.

The chemical changes within the pyrolyzing regions are not taken into account. The solid fuel is considered to be chemically inert. The mass transfer in the barrier layer(char or melt film) over virgin material is ignored. Only heat transfer within the condensed phase is treated.

The mathematical expressions for the thermal degradation rate in ablative models are very similar. The mass loss rate is determined by the energy balance at the solid

surface or at the boundary of char and virgin material. It is expressed as

$$\dot{q}'' = \lambda_v \frac{\partial T_v}{\partial x} + L\dot{m}'' \tag{7.3.6}$$

where $\dot{q}''$ is the net heat flux at the solid surface or at the interface between char and virgin. However the models differ in their assumptions and the solution methods. The integral model developed by Delichatsios et al.[1991a] for noncharring materials uses exponential temperature profiles across the sample thickness for the heat-up stage and pyrolysis stage. The use of these specified temperature profiles transforms the governing partial differential equations for the solid fuel into ordinary differential equations with variables θ(surface temperature rise), δ(thermal length) and δ_p(the depth of the material pyrolyzed). Following the same approach, Chen et al.[1993] presented an integral model for charring materials using exponential temperature profiles in virgin and char layer. The energy equation(a partial differential equation) and its boundary conditions are transformed into a set of ordinary differential equations by introducing the first two moments of the energy equation. The numerical difficulty generated from the ill-conditioned matrix for the transformed equations is overcome by a special numerical method. A similar integral method using quadratic rather than exponential temperature profiles within the solid was employed to derive integral models by Quintiere[1992], Quintiere and Iqbal[1993] and Moghtaderi *et al.*[1996]. Another approach[Yan and Holmstedt 1996] is to numerically solve the heat conduction equation in the condensed phase and the boundary conditions using the finite difference method. The temperature profiles in the solid (both char and virgin) are not prescribed. Careful treatment for the region near the boundary of char and virgin is given by using a fine grid in this region. The mass loss at each node depends on the energy balance at this point.

Kinetic models use kinetic laws to represent the mass loss rates of solid fuels rather than an energy balance equation at the solid surface or the interface of char and virgin material. The Arrhenius form of kinetic laws is widely used which is expressed as

$$\frac{\partial \rho}{\partial t} = \rho A \exp(-E/RT) \tag{7.3.7}$$

In this case, the pyrolysis temperature is not used and it is obvious according to equation (7.3.7) that pyrolysis occurs over a temperature range. As a result, unlike ablative models in which the material is assumed to be gasified within an extremely thin layer at the surface or the boundary of char and raw material, a finite depth of the sample is involved in decomposition processes. In Kung's model[1972], the density of the active material is time-dependent and the total density is determined by the active density and the char residue density. The decomposition rate of the active material is in Arrhenius form. Heat convection of volatiles within the material is taken into account in the transient conduction equation for the solid. According to the variable density the specific heat is also varied with the density. This model was then used to investigate the effects of slab thickness, char conductivity and decomposition endothermicity. These parameters were shown by the model predictions having a pronounced effect on the pyrolysis rate.

Similar models were proposed by Blasi[1994] and Ritchie et al.[1997] in which the thermal conductivity and heat capacity of the solid fuel vary with the composition of char and virgin. Staggs and Whiteley[1996] presented a very general treatment for the kinetic law. The description of this general kinetic law below follows the article of Staggs and Whiteley[1996]. The general kinetic law is expressed as

$$\mathbf{m}_t = -\mathbf{f}(\mathbf{m}, T) \tag{7.3.8}$$

"where **m** is a vector of mass fraction values, and **f** is a vector that is characteristic of the degradation process. **m** can be viewed as a vector describing the state of the solid at any given spatial location and any given instant of time". "Let **L** be a vector describing the energy change associated with a change of state in the solid d**m**. Thus the net energy required or given out in order to change the state of the solid from **m**(t) to **m**(t+dt) will be given by $M(t)\langle \mathbf{L}, \mathbf{m}_t \rangle$, where M is the mass of the slice and $\langle \mathbf{u}, \mathbf{v} \rangle$ denotes the inner (or scalar) product of the two vectors **u** and **v**." Thus the corresponding energy required for the conversion process will be given by

$$\dot{q}''' = \rho \langle \mathbf{L}, \mathbf{m}_t \rangle. \tag{7.3.9}$$

More sophisticated models were developed to include the effect of moisture and mass transfer in pore structure[Parker, 1986; Fredlund, 1993; Yuen, 1997]. In Parker's approach[Parker, 1986], the sample is divided by several slices parallel to the surface. The mass loss and water evaporation are described by the mass retention fraction and the moisture retention fraction at each slice. Char shrinkage is taken into account but char oxidation is ignored. The energy equation contains the effects of the change rate of enthalpy, heat conduction, internal heat generation or absorption and convective cooling by the flow of pyrolysis volatiles and water vapour. The water vapour production rate and the pyrolysis rate of wood are controlled by Arrhenius laws. The thermal properties are assumed to be a function of the temperature and the total mass retention fraction of each slice. This model is also able to incorporate multiple component thermal degradations. In Fredlund's model[Fredlund, 1993], the production rate of volatile pyrolysis products is given by the Arrhenius expression and the production rate of water vapour is a function of temperature, pressure gradient and

the densities of the volatile pyrolysis products and water vapour. "The fundamental assumption made is that vaporisation is sufficiently rapid for complete saturation of water vapour in the pores to be possible." The water vapour and pyrolysis volatiles are driven within the pore system of the sample by the gradients of concentration, temperature and pressure. As the driving force produced by temperature gradient is small compared to the one due to pressure gradient, the effect of temperature gradient on mass transfer is neglected. Thus mass transfer equation in the solid fuel is derived in terms of pressure gradient and concentration gradient. The heat transfer in the condensed phase occurs as thermal conduction and internal convection. The energy absorbed by water vaporisation and the movement of the pyrolysis products and water vapour in the pore structure of the wood sample is taken into account. Char oxidation is included. The thermal properties of the solid sample are calculated "as weighted mean values of the concentration of the constituent materials at the time under consideration". In the two-dimensional model, the anisotropic properties of wood due to its grain structure are included by introducing properties dependent on the directions of the coordinates. A more complicated model in three dimensions is proposed by Yuen et al.[1997] by inclusion of up to six first-order reactions representing the competing thermal degradation reactions of various constituents such as the cellulose, hemicellulose, lignin and other minor constituents. This model incorporated the evaporation of the moisture content, anisotropic and variable properties of wood and the internal movement of gases.

7.4 Pyrolysis Model Development

Some pyrolysis models have been reviewed in the previous section. Generally these models are in two regimes: kinetic and ablative. The kinetic models try to incorporate the kinetic mechanisms of the thermal degradation of solid fuels. However, the values used for the kinetic parameters are a considerable scatter particularly for wood and hence there are uncertainties in the numerical predictions produced by the kinetic pyrolysis models[Vovelle *et al.*, 1984]. While ignoring the complex chemical reactions in the pyrolyzing material the ablation models are much simpler than the kinetic models. This approach can be considered a limit situation of the kinetic regime, i.e., the kinetics of the degradation mechanism occur at an infinitely fast rate[Staggs and Whiteley, 1996]. However, this approach requires only a few quantities describing the condensed phase: the pyrolysis temperature, the heat of pyrolysis and the thermal inertial properties. Comparisons with experimental results show this approach is capable to producing reasonably good predictions of mass loss rates[Delichatsios et al., 1991a; Hopkins Jr and Quintiere, 1996; Yan and Holmstedt, 1996; Jia et al., 1999b,c]. The aim of this thesis is to develop an integrated flame spread model for engineering applications. The model is therefore expected to be economical and possess a strong flexibility and a wide range of applications. Thus, the ablation regime of pyrolysis models is selected to simulate the mass loss processes of solid fuels.

There are two fundamental assumptions used in this model. The first is that solid fuels are gasified only at the surface regions (for noncharring materials) or at the char/virgin interface (for charring fuels). Secondly, combustible gaseous products are released

only when the solid surface is heated to the critical pyrolysis temperature (ignition temperature) and the temperatures of the pyrolyzing regions remain at the pyrolysis temperature throughout the period of mass loss.

While the concept of an ignition temperature is considered by some to be controversial, it is a useful idea when properly applied[Williams, 1976]. This approach is best suited to situations involving flaming combustion. In addition, this concept has been demonstrated both experimentally and theoretically to be a fair approximation to the pyrolysis process for various materials[Delichatsios *et al.*, 1991; Kindelan and Williams, 1975].

Furthermore, it is important to note that the chemical changes within the pyrolyzing regions are not taken into account. The solid fuel is considered to be chemically inert. The mass transfer in the barrier layer(char or melt film) over virgin material is ignored. Only heat transfer within the condensed phase is treated.

In the following subsections, the mathematical formulas of two pyrolysis models—one for charring materials and the other for non-charring materials—are presented. Then standalone codes implementing these two models separate from the selected CFD software are described. The self-contained codes for the models facilitate the examination of the sub-model performances by avoiding the influences coming from the gas phase where too many parameters are involved. However, the standalone codes for the pyrolysis models can be easily incorporated into the selected CFD software through appropriate boundary conditions at the exposed solid surface. This incorporation is further discussed in chapter 8.

7.4.1 The pyrolysis model for non-charring fuels

A melted thin film may form when a noncharring fuel is exposed to a large incident heat flux. The molten layer is not taken into account in the model presented here and the bubble movement described in section 7.2.1 is hence neglected. Experimental results show that the effect of the movement of the in-depth degradation products within the molten layer on the gasification rate is not significant except at low external radiant flux[Kashiwagi *et al.* 1990]. Considering the radiation heat transfer is the dominant mode of heat transfer and the range of radiant heat flux to solid surfaces is generally above 2 W/cm^2 in large enclosure fires, the omission of the effect of the molten layer and bubble movement within it appears reasonable. A diagram schematically describing the pyrolysis model of a non-charring fuel is depicted in figure (7.4.1).

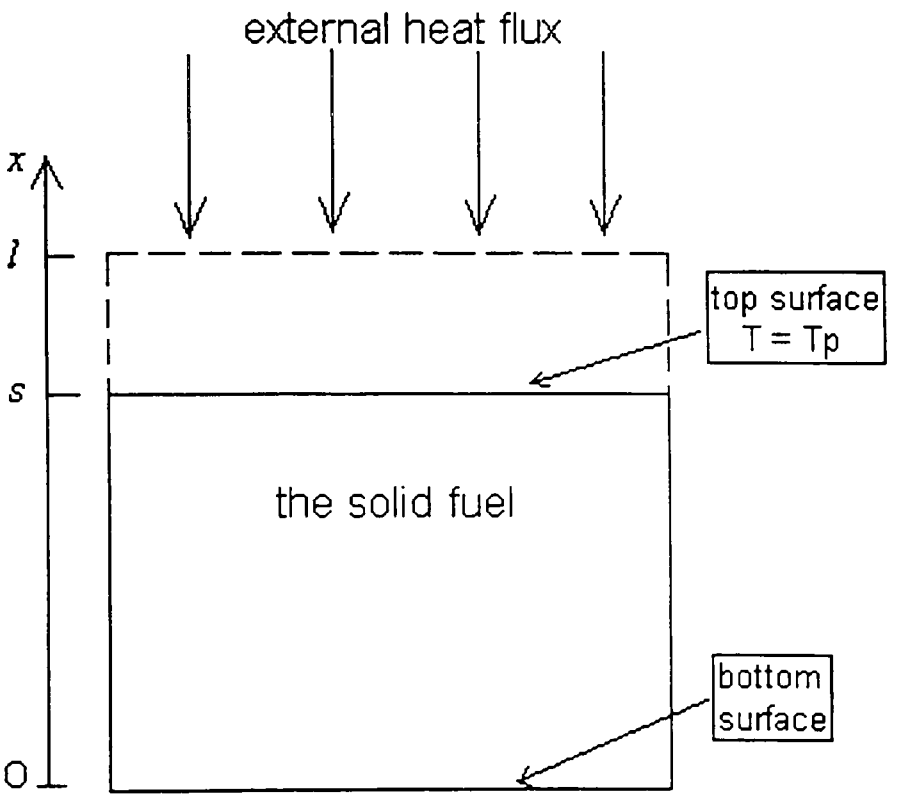

Fig. 7.4.1: The schematic diagram of the non-charring pyrolysis model. The mass in the region confined by the broken line has been removed due to gasification. *l* is the thickness of the original material while *s* shows the current location of the surface.

The deformation of the fuel due to the thermal expansion is also neglected. The thermal properties are assumed not to vary with temperature. Under these conditions and the assumptions described at the beginning of the section 7.4, the pyrolysis model belonging to the ablation regime takes the mathematical form below.

The heat transfer within the solid fuel is

$$\frac{\partial T}{\partial t} = \frac{\partial}{\partial x}(\alpha \frac{\partial T}{\partial x}) \qquad (7.4.1.1)$$

with boundary conditions at the heated surface

a) before pyrolyzing

$$\lambda \frac{\partial T}{\partial x} = \dot{q}'' - \dot{q}''_{rr} \qquad (7.4.1.2)$$

b) after pyrolyzing

$$T = T_p \qquad (7.4.1.3)$$

$$\lambda \frac{\partial T}{\partial x} = \dot{q}'' - \dot{q}''_{rr} + \rho L \frac{\partial s}{\partial t} \qquad (7.4.1.4)$$

where $\dot{q}''_{rr} = \varepsilon\sigma(T^4 - T_a^4)$ is the surface reradiation losses, s is the position of the regressing solid surface and L is the heat of pyrolysis of the solid fuel, and at the bottom

$$-\frac{\partial T}{\partial x} = 0 \qquad x = 0 \qquad (7.4.1.5)$$

If heat losses at the back surface due to surface reradiation and convection are considered, the boundary condition at the bottom may be altered to

$$-\lambda \frac{\partial T}{\partial x} = h_c(T_a - T) + \varepsilon\sigma(T_a^4 - T^4) \qquad x = 0 \qquad (7.4.1.5a)$$

and initial conditions

$$s\,(0) = l \tag{7.4.1.6}$$

$$T(x, 0) = T(x) \tag{7.4.1.7}$$

where s represents the position of the top surface of the solid fuel and l is the original thickness of the solid fuel.

Finally, the mass loss rate is obtained by

$$\dot{m}'' = -\rho \frac{\partial s}{\partial t} \tag{7.4.1.8}$$

The movement of the top surface of the solid fuel is determined by equation (7.4.1.4). After spatial and sequential discretizations are established, equation (7.4.1.4) is replaced with the equation below by combining equations (7.4.1.1), (7.4.1.3) and (7.4.1.4)

$$\rho L \Delta s/\Delta t + c_p \rho/\Delta t \int_{s-\Delta s}^{s} (T_p - T)\mathrm{d}x = \dot{q}'' - \dot{q}''_{rr} - \lambda \frac{\partial T}{\partial x}\Big|_{x=s-\Delta s} \tag{7.4.1.9}$$

where Δs is the regression length of the solid surface during the time interval Δt. The first term in the left side represents the energy required to gasify Δs length solid fuel and the second term stands for the enthalpy increase of the gasified part of the material, while the right side is the net energy left to pyrolyze the solid. As the solid surface remains at a constant temperature (the pyrolysis temperature T_p), Δs can be easily obtained iteratively from equation (7.4.1.9).

A standalone code separate from the CFD software is developed to implement the model presented above. The equation (7.4.1.1) describing the heat transfer within the solid fuel is solved using the finite difference method. Before pyrolyzing, the

boundary condition (7.4.1.2) is applied to the surface exposed to the external heat flux. After pyrolyzing, the boundary condition (7.4.1.3) is imposed on the exposed surface. Some mass is removed from the top of the solid due to gasification. The new position of the top surface of the solid is determined by iteratively solving equation (7.4.1.9). The integration and derivative in equation (7.4.1.9) are replaced with numerical integration and derivative. A fixed-grid rather than moving-grid mesh is used to discretise the solid due to its easier implementation and more economical use of computer resources. The fixed grid, while necessarily fine, is more economical than the moving grid as the fixed-grid methods do not require regeneration of the mesh and re-evaluation of the system matrices at each time step. The input of the standalone code includes the ambient conditions(the ambient temperature and the external heat flux), the material properties(density, specific heat, conductivity, the heat of pyrolysis and the emissivity of the surface) and the original thickness of the solid fuel.

7.4.2 The pyrolysis model for charring fuel

In the char model, char residuals are assumed to be inert, acting only as an insulation layer. Oxidation and secondary reaction of the primary gaseous products within the char are ignored. In fact, in an air environment, if the flame encloses the pyrolyzing solid fuel, the quantity of oxygen diffused into the solid is negligible[Kanury, 1972]. The deformations due to thermal expansion, formation of cracks and fissures and shrinkage of the char layer are also not taken into account. A schematic diagram describing the charring pyrolysis model is plotted in figure (7.4.2).

Under these assumptions plus the assumptions made at the beginning of section 7.4,

the complex degradation processes of charring fuels are simplified as a heat transfer process. The mathematical expression of this simplified heat transfer is presented below. In the following text the subscripts c and v represent the char layer and the virgin material respectively.

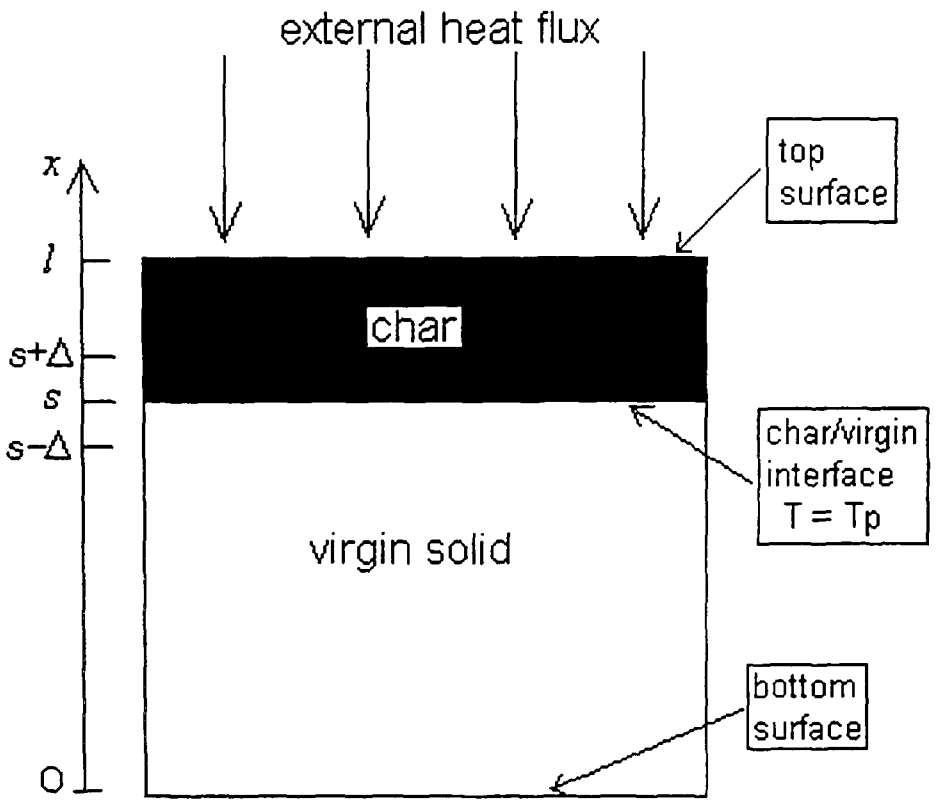

Fig. 7.4.2: The schematic diagram describing the charring pyrolysis model.

In the char layer

$$\frac{\partial T}{\partial t} = \frac{\partial}{\partial x}(\alpha_c \frac{\partial T}{\partial x}) \qquad s < x < l \qquad (7.4.2.1)$$

and in the virgin material

$$\frac{\partial T}{\partial t} = \frac{\partial}{\partial x}(\alpha_v \frac{\partial T}{\partial x}) \qquad 0 < x < s \qquad (7.4.2.2)$$

with boundary conditions

a) at the gas/char surface

$$\lambda_c \frac{\partial T_c}{\partial x} = \dot{q}'' - \dot{q}''_{rr} \qquad x = l \qquad (7.4.2.3)$$

where $\dot{q}''_{rr} = \varepsilon\sigma(T_c^4 - T_a^4)$ is the gas/char surface reradiation losses and l is the original

thickness of the solid fuel.

b) at the char/virgin interface

$$T = T_p \qquad x = s \qquad (7.4.2.4)$$

$$-\lambda_c \frac{\partial T_c}{\partial x} = -\lambda_v \frac{\partial T_v}{\partial x} + \rho L \frac{\partial s}{\partial t} \qquad x = s \qquad (7.4.2.5)$$

where s stands for the position of the char/virgin interface and L is the heat of pyrolysis of the solid fuel.

c) at the bottom of the virgin material

$$-\lambda_v \frac{\partial T_v}{\partial x} = 0 \qquad x = 0 \qquad (7.4.2.6)$$

If heat losses at the back surface due to surface reradiation and convection are considered, the boundary condition at the bottom may be altered to

$$-\lambda_v \frac{\partial T_v}{\partial x} = h_c(T_a - T_v) + \varepsilon\sigma(T_a^4 - T_v^4) \qquad x = 0 \qquad (7.4.2.6a)$$

where h_c is the convective heat transfer coefficient at the bottom surface. And the initial conditions are

$$s(0) = l \qquad (7.4.2.7)$$

$$T(x, 0) = T(x) \qquad (7.4.2.8)$$

Finally, the mass loss rate is obtained by

$$\dot{m}'' = -(\rho_v - \rho_c)\frac{\partial s}{\partial t} \qquad (7.4.2.9)$$

The equations from (7.4.1) to (7.4.9) are similar to the so-called Stefan problems that arise in many engineering heat transfer applications such as casting and melting where phase change processes are involved. The standard Stefan problem can be written as:

$$\frac{\partial T}{\partial t} = \frac{\partial}{\partial x}(\alpha_1 \frac{\partial T}{\partial x}) \qquad s < x < l \qquad (7.4.2.10)$$

$$\frac{\partial T}{\partial t} = \frac{\partial}{\partial x}(\alpha_2 \frac{\partial T}{\partial x}) \qquad 0 < x < s \qquad (7.4.2.11)$$

with boundary conditions

$$T(l, t) = T_1(t) \qquad (7.4.2.12)$$

$$T(0, t) = T_2(t) \qquad (7.4.2.13)$$

$$T(s, t) = T_f \qquad x = s \qquad (7.4.2.14)$$

$$-\lambda_1 \frac{\partial T_1}{\partial x} = -\lambda_2 \frac{\partial T_2}{\partial x} + \rho L \frac{\partial s}{\partial t} \qquad x = s \qquad (7.4.2.15)$$

and initial conditions

$$s\,(0) = x_0 \qquad (7.4.2.16)$$

$$T(x, 0) = T(x) \qquad (7.4.2.17)$$

Unlike a standard Stefan problem, the thermal pyrolysis model mentioned above (equations (7.4.2.1) to (7.4.2.9)) is subjected to a nonlinear boundary condition at the gas/char surface due to surface reradiation losses. The nonlinear boundary condition combined with the moving interface between the char and virgin materials can results in numerical complications leading to instability. While a variety of numerical methods suitable for Stefan problems have been developed[Patera, 1984; Lynch, 1981; Meyer, 1981], few of them are ideal for the thermal pyrolysis model[Chen, 1993]. A new approach developed by the author is described below to overcome the difficulty by employing a technique for decoupling the non-linearity of the boundary condition and the movement of the char front.

There are two tasks to solve the thermal pyrolysis model described above. One is to calculate the temperature distribution in the char and virgin materials. The other is to

track the char/virgin interface. These two tasks are strongly coupled by the char/virgin boundary conditions. This is further complicated by the nonlinear gas/char boundary condition due to the surface reradiation losses. The core of the approach presented here is to decouple the two tasks by iteration in each time step.

In each iteration (of each time step) of this decoupling process, the position of the char/virgin interface is tracked according to the temperature distribution in the char and virgin fields obtained from the last iteration. In turn, a new temperature distribution in the char and virgin materials is calculated in terms of the new char front position. The temperature at the gas/char surface is a function of the char front position, and the amount of heat transported into the char layer is hence dependent on the char front position according to equation (7.4.2.3). Conversely, the char front position is determined by the amount of heat transported into the char layer. By performing the decoupling process, the interaction between the char front position and the amount of heat transported into the char layer will lead to convergence of the process.

In each iteration of the decoupling process, the char/virgin front is defined by a standard Stefan problem (equations (7.4.2.10) to (7.4.2.17)), where the temperature at the gas/char boundary (which is time-dependent), is obtained from the last iteration. An invariant embedding method proposed by Meyer[1981] is used to track the char front. This method takes advantage of fixed-grid meshes which is significantly more economical compared with moving-grid techniques[Lynch and O'Neill, 1981]. Numerical results also suggest it to be an extremely stable method for the standard Stefan problem[Meyer, 1981]. A variation of this method for the thermal pyrolysis

model is described below.

First, the time derivative is treated using backward difference quotient. Then by introducing the flux term $h = \alpha(\partial T/\partial x)$, the second-order heat transport equations (7.4.1) and (7.4.2) are converted to first-order systems. Thus, at time step t_n the standard Stefan problem (equations (7.4.10) to (7.4.17)) is approximated by

$$T' = h/\alpha \tag{7.4.2.18}$$

$$h' = [T - T_{n-1}(x)]/\Delta t \tag{7.4.2.19}$$

$$T(0) = T_0 \tag{7.4.2.20}$$

$$T(l) = T_l \tag{7.4.2.21}$$

$$\rho_c C_c h_c - \rho_v C_v h_v = -\rho_v L(s - s_{n-1})/\Delta t. \tag{7.4.2.22}$$

where subscripts c and v replace the original subscripts 1 and 2 to stand for char and virgin material respectively. The relation of T and h can be represented through the Riccati transformations

$$T_c = u_c h_c + w_c \tag{7.4.2.23}$$

$$T_v = u_v h_v + w_v \tag{7.4.2.24}$$

where

$$u_i' = 1/\alpha - u/\Delta t, \qquad i = \text{c or v} \tag{7.4.2.25}$$

with

$$u_c(l) = u_v(0) = 0 \tag{7.4.2.26}$$

and

$$w_i' = -u_i[w_i - T_{n-1}(x)]/\Delta t, \qquad i = \text{c or v} \tag{7.4.2.27}$$

with

$$w_c(l) = T(l) \tag{7.4.2.28}$$

$$w_v(0) = T(0). \tag{7.4.2.29}$$

where $T(l)$ and $T(0)$ are obtained from the last iteration of the decoupling process at time step t_n.

As the temperature at the char/virgin interface is T_p, from equations (7.4.2.23) and (7.4.2.24) the heat flux at the interface are given by

$$h_c = (T_p - w_c)/u_c \tag{7.4.2.30}$$

$$h_v = (T_p - w_v)/u_v. \tag{7.4.2.31}$$

Thus, the position of the interface at time step t_n is determined by the following equation

$$\rho_c C_c (T_p - w_c)/u_c - \rho_v C_v (T_p - w_v)/u_v = -\rho_v L(s - s_{n-1})/\Delta t. \tag{7.4.2.32}$$

It is important to note that the temperature derivatives at the char/virgin surface are not directly calculated using numerical difference methods. Since the char/virgin interface is determined by equation (7.4.2.5), it is obvious that the accuracy of the numerical calculations of the two temperature derivatives involved in the equation is critical to obtain the accurate position of the interface. Furthermore, to determine the char/virgin interface is central of the pyrolysis model. Thus it is a great advantage that in the invariant imbedding method the temperature derivatives at the char/virgin surface are not directly numerically tackled.

To reduce the computation overheads, a so-called local invariant imbedding method can be implemented. As the tentative temperature distribution in the solid material has been obtained from the last cycle of the iteration, and we are primarily concerned with

the new position of the char/virgin interface, we need only apply the front track technique described above within the region near the interface.

After the new char front is determined, the original problem decouples into two heat transport problems over each given interval—the char interval and the virgin interval respectively. Over the virgin interval, the heat conduction problem consists of equation (7.4.2.1) with equations (7.4.2.4) and (7.4.2.6) or (7.4.2.6a) as the boundary conditions, while over the char region, the heat transport problem is composed of equation (7.4.2.2) with equations (7.4.2.3) and (7.4.2.4) as the boundary conditions. The nonlinearity at the boundaries (equations (7.4.2.3) and (7.4.2.6a)) due to the surface reradiation losses needs be dealt with. The method proposed by Patankar[1980] can be used. In the Patankar's method, the heat conduction problem with non-linear boundary condition is solved iteratively and the non-linear boundary conditions are linearised at the current surface temperature. Thus in each iteration a nominally linear heat conduction problem which can be solved using conventional numerical methods is generated.

The decoupling method proposed here to solve the charring pyrolysis model (equations (7.4.2.1) to (7.4.2.8)) is summarised below.

1. using the tentative temperature field obtained from the last iteration to track down the position of the char/virgin interface.

   1.1) the tentative boundary conditions at the top and bottom surface are set according to the current temperature field, i.e., $T(l) = T^*(l)$, $T(0) = T^*(0)$. Thus a standard Stefan problem (equations (7.4.2.10) to (7.4.2.17)) is generated. If local tracking-down technique is adopted, two positions

around the current char/virgin interface are selected, say $s+\Delta$ and $s-\Delta$(see figure 7.4.2), to replace the top surface l and the bottom surface 0.

1.2) for the standard Stefan problem, the tentative char/virgin interface is tracked down using the invariant embedding method(equations (7.4.2.23) to (7.4.2.32)).

2. after the char/virgin interface is obtained, two heat conduction problems over the char interval and the virgin interval are solved respectively.

3. if stopping criterion is met, the computation for the current time step is end. Otherwise, go back to 1.

A standalone code separate from the selected CFD software is developed to implement the charring pyrolysis model described above. The input for the standalone code include the ambient parameters(the ambient temperature and the external heat flux), the raw solid fuel properties(the density, the specific heat, the conductivity, the heat of pyrolysis, and the emissivity of the surface), the char properties(the density, the specific heat, the conductivity and the emissivity of the char surface) and the thickness of the solid fuel.

7.5 Validation for the Non-charring Pyrolysis Model

In this section the standalone non-charring pyrolysis model will be tested. Model predictions are compared with exact analytical results for an idealised case (section 7.5.1) and with experimental data (section 7.5.3).

This work has appeared in the referred academic journal Applied Mathematical Modelling[Jia et al., 1999b].

7.5.1 Analysis of the numerical method used by the pyrolysis model

An exact general analytical solution for the partial differential equations (7.4.1.1) to (7.4.1.7) representing the pyrolysis process does not exist. However, under special conditions, Delichatsios and Chen [1993] obtained an exact analytical asymptotic solution as $\beta \rightarrow 0$ for equations (7.4.1.1) to (7.4.1.7) where,

$$\beta = C_s \Delta T_p / \Delta H \tag{7.5.1}$$

$\Delta T_p = T_p - T_a$, T_a is the ambient temperature, C_s is the specific heat of the solid, $\Delta H = L + C_s(T_p - T_a)$ and L is the heat of pyrolysis of the solid fuel. The assumptions are,

a) neglecting reradiation loss,

b) constant external heat flux, and,

b) uniform initial temperature distribution.

Under these assumptions, the exact analytical solution for $\beta = 0$ is given

$$\dot{m}'' \Delta H / Q = 2/\pi \tan^{-1}(2\sqrt{\frac{\tau}{\pi}}) \tag{7.5.2}$$

where, Q is the net heat flux reached at the solid surface and τ is the normalised time defined by

$$\tau = t\alpha_s/(k\Delta T_p/ Q)^2 \tag{7.5.3}$$

where α_s is the material thermal diffusivity and k is the material conductivity.

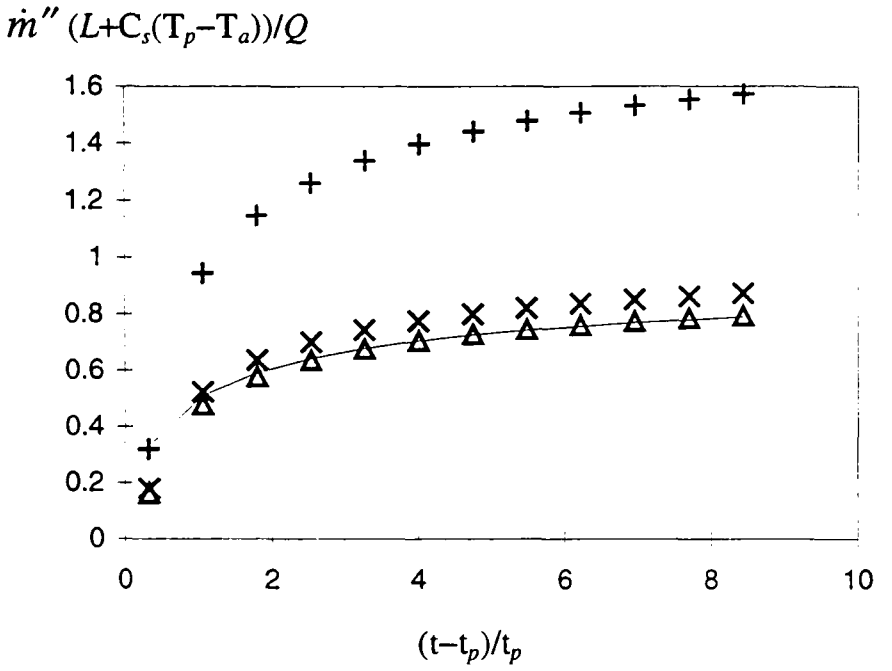

Fig. 7.5.1: The nondimensional mass loss rate against the nondimensional time.
— : exact analytical asymptotic curve; Δ : numerical solution for β = 0.01;
× : numerical solution for β = 0.1; + : numerical solution for β = 0.5.
t_p represents the time to ignition.

As a partial validation of the numerical method employed in the pyrolysis model, we generate a series of curves of the numerical mass loss rates which vary with the parameter β. These curves are produced by following the assumptions mentioned above and using a constant external heat flux of Q = 35 kW/m^2. This heat flux was selected as it represents a typical value among the range of heat flux encountered in compartment fire situations. The material properties are arbitrarily decided. They are ρ = 600.0 kg/m^3, C_s= 2678.0 J/(kgK), k = 0.1 W/(mK), T_p = 666.0 K, L = 0.95 MJ/kg. The uniform initial temperature is selected as 303 K. The one-dimensional solid with a thickness of 0.12 m is discretised by a mesh with a uniform cell length of 0.02 cm. We then compare the numerical solution with the exact analytical asymptotic solution for

the pyrolysis model. Figure (7.5.1) demonstrates that the numerical mass loss rates are in very good agreement with the exact asymptotic solution as $\beta \rightarrow 0$.

7.5.2 Grid sensitivity analysis for the solid mesh

A grid sensitivity analysis is performed to determine an appropriate number of cells to use within the solid mesh considering both numerical accuracy and computational efficiency. As a test case, a one-dimensional study describing a 12 mm thick piece of solid fuel initially at a temperature of 300K and exposed to an external heat flux of Q=35 kW/m^2 is undertaken. The results presented here consider a comparison of mass loss rates calculated from a mesh with cell size 0.2mm to a mesh with cell size 0.02mm. Figure (7.5.2) depicts the mass loss rate over time using both the coarse and fine meshes. Note that the coarse mesh produces a numerical mass loss rate very close to that from the extremely fine mesh. This suggests that the coarse mesh may be adequate to calculate the mass loss rate of the solid fuel during pyrolysis.

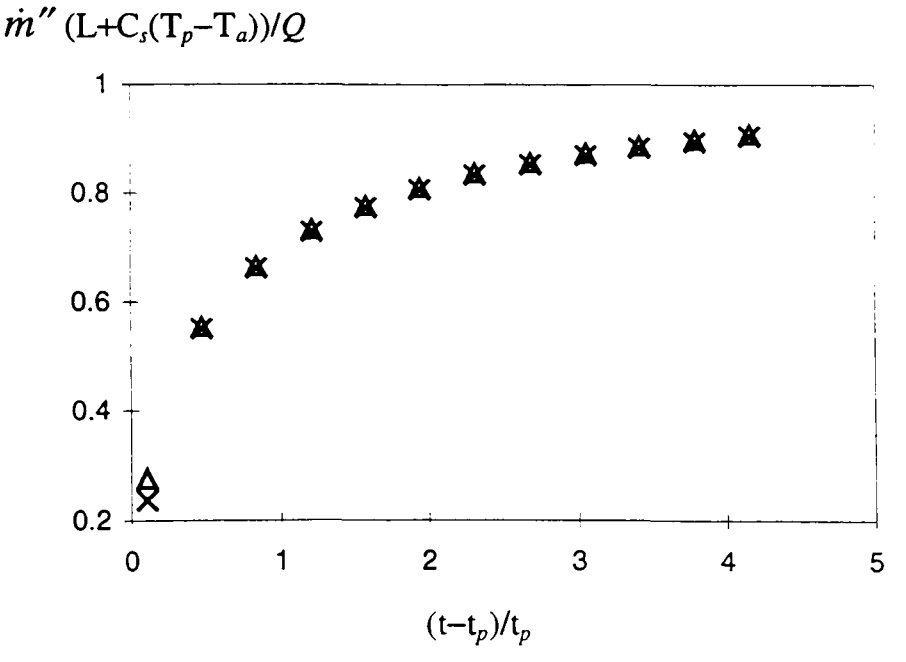

Fig. 7.5.2: The mass loss rates for 600 cells and 60 cells along the thickness of a 12mm thick solid material.
Δ : the mass loss rate for 600 cells; $\times$: the mass loss rate for 60 cells.

7.5.3 Comparison with experimental results

In this subsection, the non-charring pyrolysis model, represented by equations from (7.4.1.1) to (7.4.1.9), is compared with experimental results produced as part of a series of experiments conducted by Rhodes[1994].

7.5.3.1 Brief description of the experiments and the material

The sample used in the Rhodes's tests is black polycast PMMA. The sample size is 100×100×25 mm thick. A cone calorimeter heater assembly for irradiance ranging from 0-75kW/m^2 was used to measure the mass loss data, flame heat fluxes and surface temperature [Rhodes, 1994]. A schematic diagram of the cone heat apparatus is shown in figure (7.5.3).

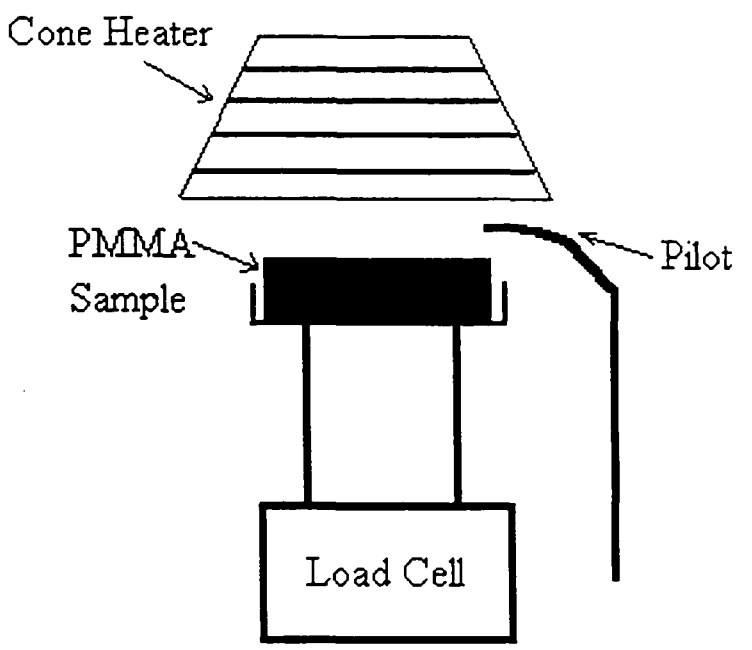

Fig. 7.5.3: A schematic diagram of a cone calorimeter.

The mass loss rates were obtained from the tests with three levels of irradiances of 25, 50, 75kW/m^2. The total heat flux from flame to the sample surface includes the

radiative and convective heat flux. Data from experiments using a 10cm square methane burner to simulate a sample burning under a cone calorimeter suggested that the flame heat flux is approximately constant for the cone calorimeter[Rhodes, 1994]. A theoretical analysis carried out by Rhodes and Quintiere[1996] also confirmed this conclusion. As for the tests using the black PMMA samples, the flame heat flux was estimated at a level of 27kW/m^2.

Based on the mass loss data, flame heat fluxes and surface temperatures measured from the tests, the properties of the black PMMA was derived by Rhodes and Quintiere[1996]. They are listed below.

ρ = 1190.0 kg/m^3, c= 4120.0 J/(kgK), λ = 0.432 W/(mK), T_p = 453.0 K, L=2000.0kJ/kg. The surface emissivity is 0.95.

7.5.3.2 Comparison of the predicted mass loss rates with the measurements

As the heat flux to the sample surface is nearly uniform, a one-dimensional simulation of the mass loss process is a reasonable first approximation. Along the direction of the incident radiation, the 25mm thick sample is discretised with the cell size 0.2mm. In the one-dimensional model the top (surface) is exposed to the incident flux, and the boundary condition at the bottom is described by equation (5.4.6), i.e. the bottom is assumed to be very well insulated.

The predicted and measured mass loss rates for the three levels of irradiances of 25, 50, 75kW/m^2 are presented in figures (7.5.4) to (7.5.6) respectively. All the predicted

mass loss rates for the three levels of irradiances are in very good agreement with the measured. For the 25kW/m^2 irradiance, the mass loss rate at the late stage appear to be underpredicted but still to agree well with experimental results, while for the two higher radiances, the agreement is excellent.

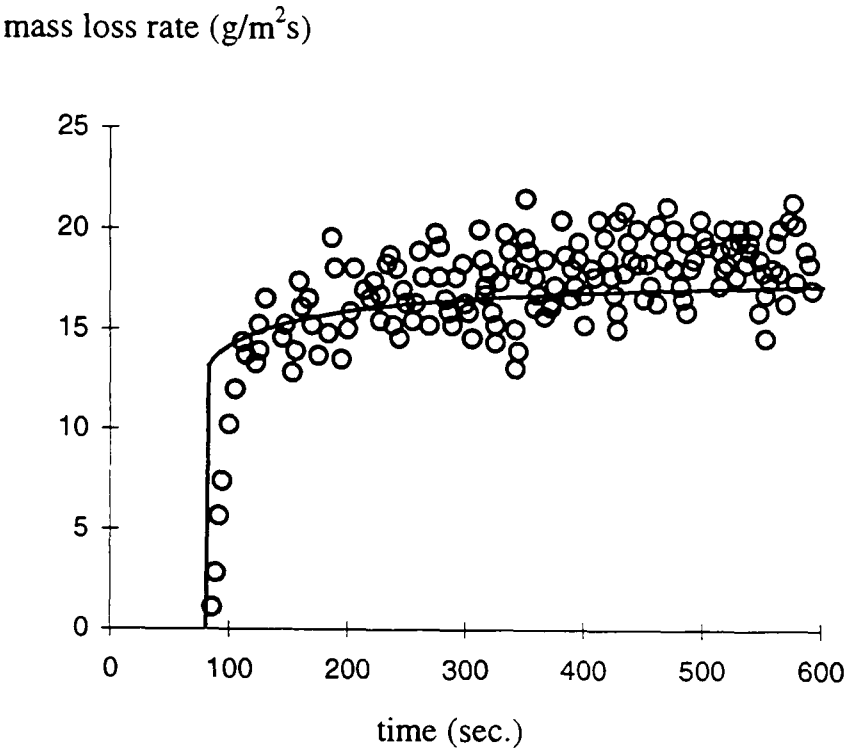

Fig. 7.5.4: Mass loss rates of PMMA exposed to a 25kW/m^2 cone irradiance.
o: measured, —: predicted

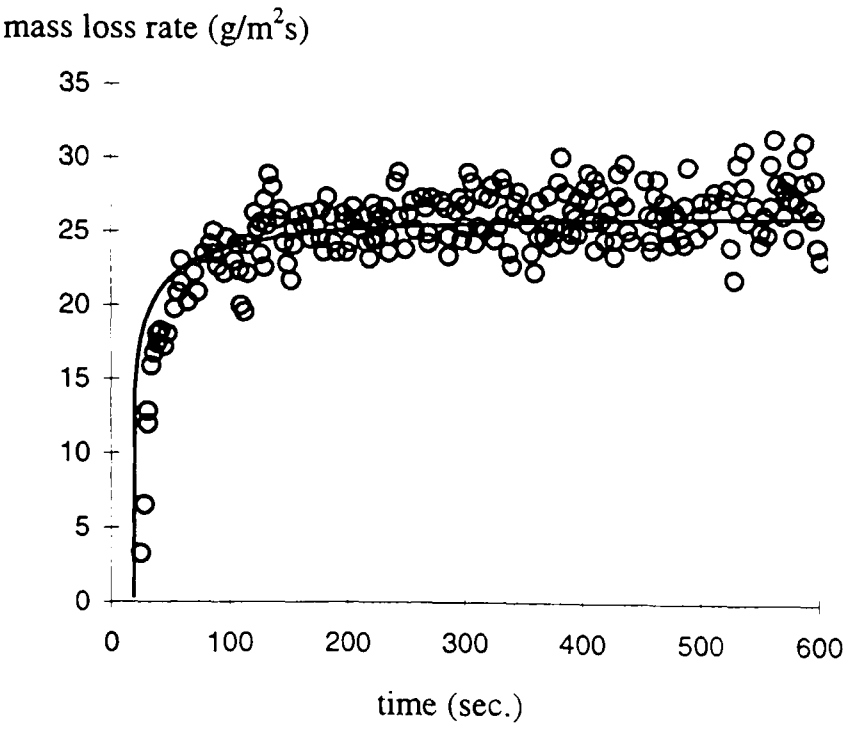

Fig. 7.5.5: Mass loss rates of PMMA exposed to a 50kW/m^2 cone irradiance.
o: measured, —: predicted

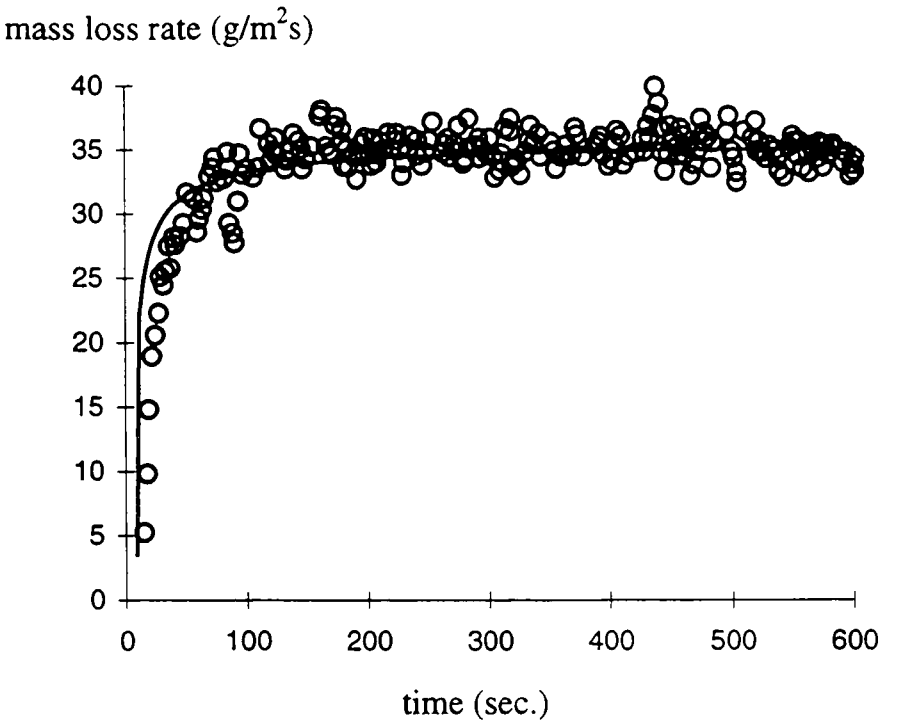

Fig. 7.5.6: Mass loss rates of PMMA exposed to a 50kW/m^2 cone irradiance.
o: measured, —: predicted

7.6 Validation of the Charring Pyrolysis Model

In the following section, the standalone pyrolysis model for charring materials, i.e. equations from (7.4.2.1) to (7.4.2.9) described in sub-section (7.4.2), will be tested. Model predictions will be compared with exact analytical results for several idealised cases (section 7.6.1) and with experimental data(section 7.6.3).

This work has appeared in the referred academic journal Fire and Materials[Jia et al., 1999c].

7.6.1 Accuracy of the decoupling technique for solving the charring model

The accuracy of the decoupling technique is demonstrated through comparing model predictions with two simple cases for which there are exact analytic solutions. These two cases were developed by Chen *et al.*[1993] to investigate the accuracy of their

integral approach methodology. The analytic solutions presented here can be found in [Chen *et al.*, 1993]

***Case* 1:** Comparison of numerical predictions with exact analytical solution for the case where surface reradiation losses are neglected.

The imposed external heat flux is given by,

$$\dot{q}_r'' = \dot{q}_0'' \exp[(\frac{\dot{q}_0''}{\rho L})^2 \frac{t}{\alpha}] \tag{7.6.1}$$

The initial conditions are

a) the virgin material is at the pyrolysis temperature;

b) $s = l$.

where s and l are the char/virgin interface and the thickness of the solid respectively(see figure (7.4.2)).

The thermal properties of the virgin and char materials are identical and are given by, $l = 0.1\text{m}$, $T_p = 640\text{K}$, $\rho_v = \rho_c = 600\ \text{kg/m}^3$, $C_v = C_c = 1500\ \text{J/kgK}$, $\lambda_v = \lambda_c = 0.2403\ \text{W/mK}$, $\alpha_v = \alpha_c = 2.67\times10^{-7}\ \text{m}^2/\text{s}$ and $L = 76520\ \text{J/kg}$. The parameter $\dot{q}_0''$ in equation (5.4.3) is $100.0\ \text{W/m}^2$.

The analytical solution of the char/virgin interface for this case is given by,

$$s = l - (\dot{q}_0'' t)/(\rho L) \tag{7.6.2}$$

The one-dimensional simulation uses a mesh with 0.02cm cell size to discretise 10cm thick of the solid. Figure (7.6.1) depicts the curves of the numerical results and the

exact analytical solution. As can be seen, the numerical predictions are in excellent agreement with the analytical solution. The maximum error is less than 0.01%. The average iteration number of each time step is 2.5, indicating that the numerical procedure rapidly converges to solution.

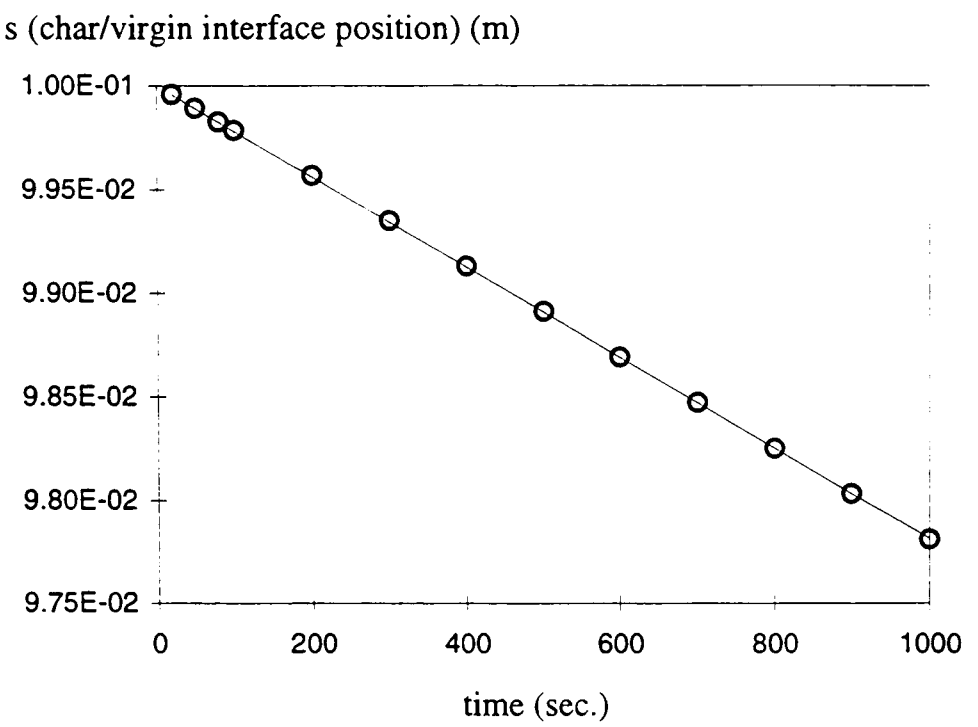

Figure 7.6.1: Comparison of the numerical prediction of the char/virgin interface with the exact solution in case 1.
O: the numerical solution; —: the exact analytic solution.

***Case* 2:** Comparison of numerical predictions with exact analytical solution for the case where surface reradiation losses are neglected.

The imposed heat flux is given by,

$$\dot{q}_r'' = \dot{q}_0'' / \sqrt{t} \tag{7.6.3}$$

and $\dot{q}_0'' = 5000$ W/m^2.

The initial conditions, the assumption of the surface re-radiation losses and the properties in this case are identical to those in case 1. The one-dimensional simulation uses the same mesh as the one in case 1.

The analytical solution for this case is

$$s = l - 2\mu\sqrt{\alpha t} \tag{7.6.4}$$

where μ is defined by

$$\mu e^{\mu^2} = \dot{q}_0'' / (\rho L \sqrt{\alpha}). \tag{7.6.5}$$

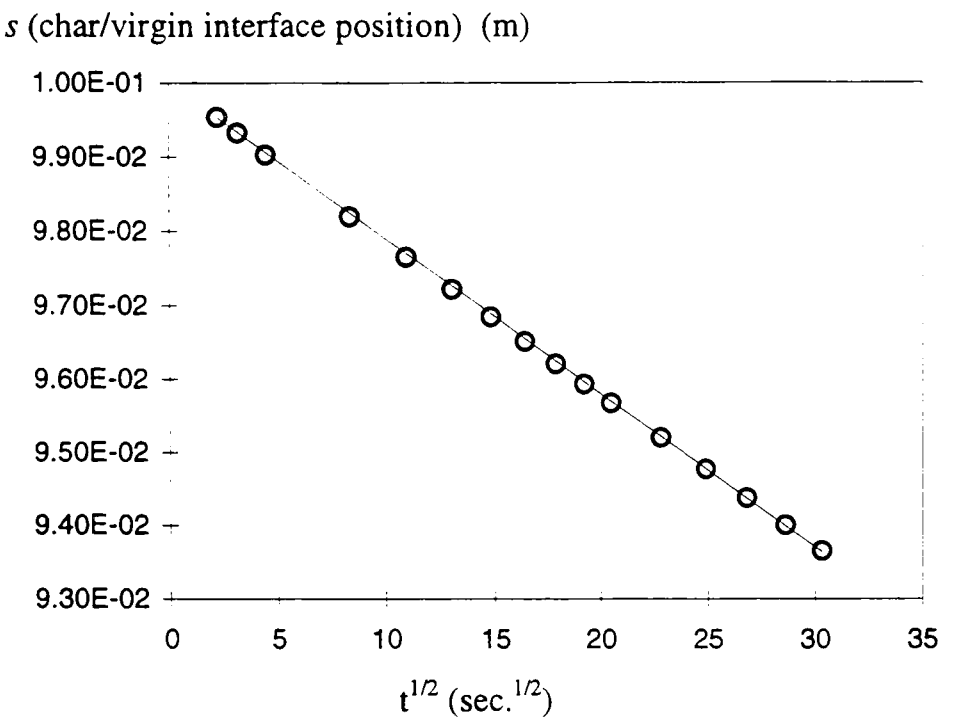

Figure 7.6.2: Comparison of the numerical prediction of the char/virgin interface with the exact solution in case 2.
O: the numerical solution; —: the exact analytic solution .

Figure (7.6.2) depicts the curves of the numerical results and the exact analytical solution.

As in case 1, the numerical char/virgin interface position is in very good agreement with the exact solution (see figure (7.6.2)). The maximum error is less than 0.05%. The average iteration number in each time step is 1.7, again indicating that the procedure rapidly converges.

7.6.2 Grid and Time Step Sensitivity Analysis

In this subsection, grid and time step sensitivity analyses are carried out. The solid material used in these analyses is white pine. The properties of white pine are taken from literature or derived from the data of experiments conducted by Kashiwagi et al.[1987]. ρ_v = 380 kg/m^3, C_v = 1150 J/kgK, λ_v = 0.34 W/mK, λ_c =0.2 W/mK, T_p = 603K and L = 1.2 MJ/kg. In addition, an extra parameter $\gamma = (\rho_c C_c)/ (\rho_v C_v)$ is introduced to represent the thermal property of the char material since experimental data regarding the char density and specific heat are less readily available.

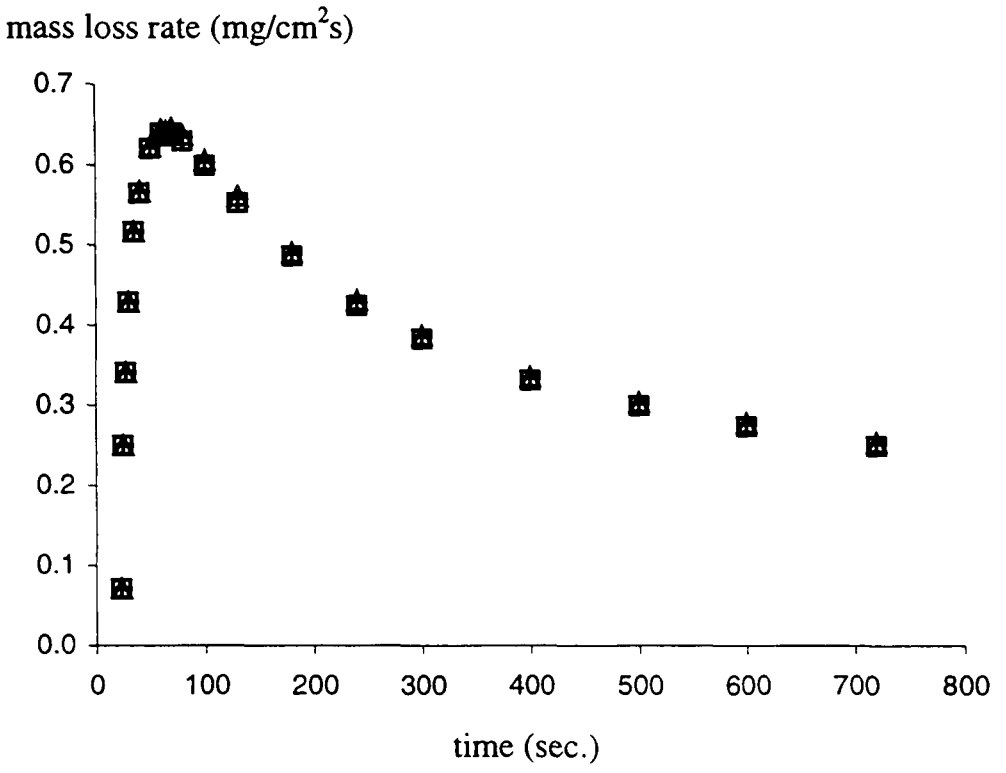

Fig. 7.6.3: The mass loss rates predicted using different values of γ.
γ = 0.1—triangle; 0.2—plus; 0.4—square.

In order to examine the sensitivity of the charring pyrolysis model to γ, three simulations using different values of γ (0.4, 0.2 and 0.1) are carried out. The simulations use the same mesh(0.02cm cell size to discretise 3.8cm thick of the solid) and the same time step(one second). The external heat flux is 40kW/m^2. Model predictions from the three simulations are depicted in figure (7.6.3). From figure

(7.6.3) it is clear that the pyrolysis model presented here is not sensitive to the variation of γ. Therefore in the following sections, it is assumed that $\gamma = (\rho_c C_c)/ (\rho_v C_v) = 0.2$.

7.6.2.1 Grid sensitivity analysis

The temperature distribution within a solid material exposed to a large external heat flux is generally nonuniform. The temperature variation within the solid material near to its surface can be quite large and so the accuracy of the numerical temperature prediction will depend on the resolution of the mesh within the solid material. This in turn directly impacts on the accuracy of the numerical mass loss rate of the solid fuel, which is the primary purpose of the pyrolysis model. However, for computational efficiency the number of cells within the solid mesh should be as small as possible - as long as it does not significantly affect the accuracy of the numerical mass loss rate.

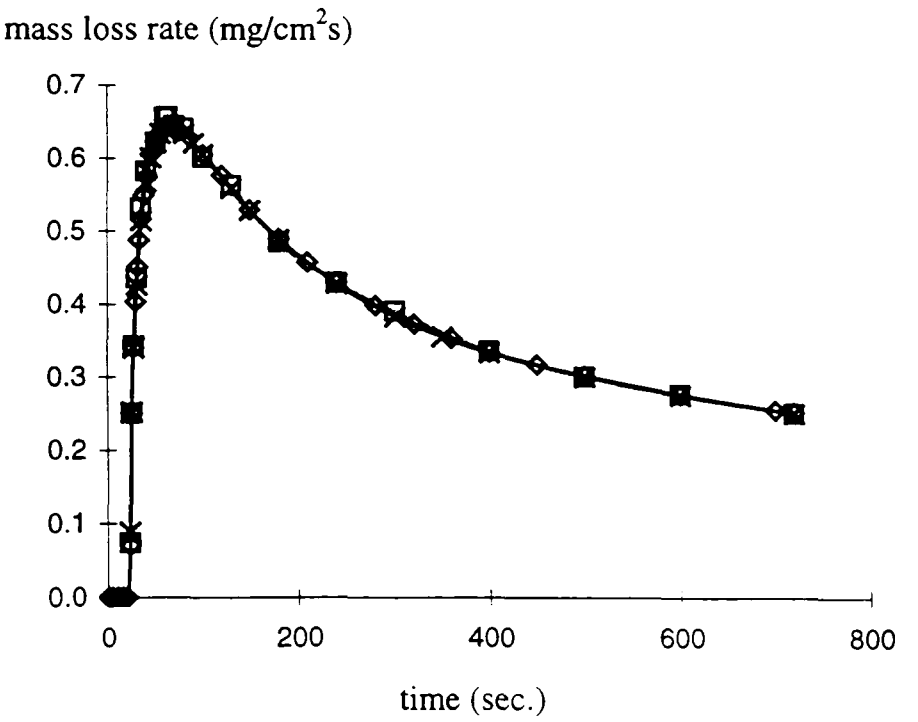

Figure 7.6.4: Numerical mass loss rates using three different meshes consisting of 380 cells - cross, 191 cells - diamond and 95 cells - square.

A grid sensitivity analysis was performed to determine an appropriate number of cells

to use within the solid mesh considering both numerical accuracy and computational efficiency. The study is intended to reveal the mesh sensitivity of the predicted mass loss rate. As a test case, a one-dimensional study describing a 38mm thick piece of solid fuel initially at a temperature of 300K and exposed to an external heat flux of $Q = 40kW/m^2$ was undertaken.

The model consists of equations (7.4.2.1) to (7.4.2.9) and the mass loss rate is determined by equation (7.4.2.9). The rear surface boundary condition uses equation (7.4.2.6a), i.e. convective and reradiation heat losses are taken into account. The convective heat transfer coefficient and the emissivity at the bottom surface are assumed to be 10 W/m^2K and 0.7 respectively. The ambient temperature is 300 K.

The results presented here consider a comparison of mass loss rates calculated from uniform meshes consisting of 95 cells, 190 cells and 380 cells representing the grid size of 0.4mm, 0.2mm and 0.1mm respectively. Figure (7.6.4) depicts the mass loss rates over time using these three meshes. Note that these three meshes produce almost identical mass loss rates. As a result, for the simulations presented in section 7.6.3, 190 cells(0.2mm grid size) covering 38mm thickness was selected.

7.6.2.2 Time step sensitivity analysis.

When a solid material is exposed to a large external heat flux, its temperature variation with time may be very rapid. Consequently, the size of time step may significantly affect the accuracy of the numerical simulation of mass loss rates. To investigate the dependence of the numerical mass loss rates on the time step, the

analysis of section 7.6.2.1 was extended to consider time step sensitivity. This involved comparing the numerical mass loss rates determined using three different time steps - 0.1 sec, 1.0 sec and 2.0 sec. The spatial mesh resolution used in these three simulations remained fixed at 190 cells.

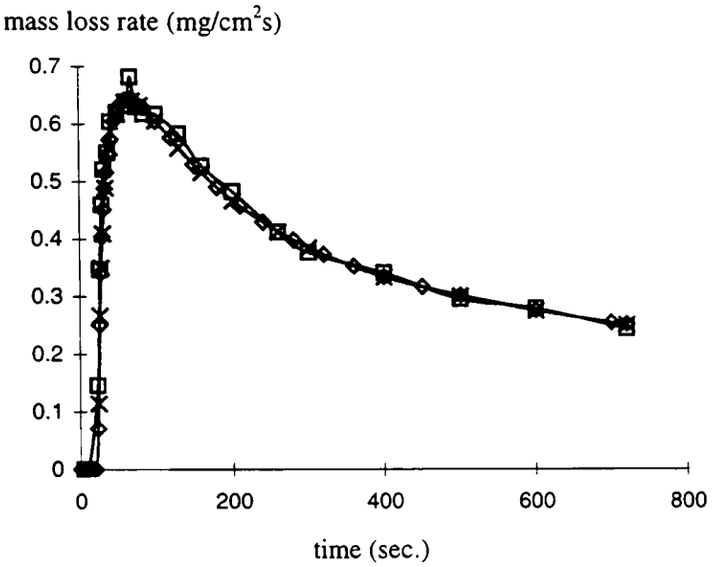

Figure 7.6.5: Numerical mass loss rates using three different time steps, 0.1second - square, 1.0 second - diamond and 2.0 second - cross.

Figure (7.6.5) shows that the numerical mass loss rates calculated from the three time steps are very close. As a result, for the simulations presented in section 7.6.3, a one second time step was selected.

7.6.3 Comparison with experimental results

In this subsection the charring pyrolysis model is compared with a set of experimental results produced as part of a series of experiments conducted by Kashiwagi et al. [1987].

7.6.3.1 Brief description of the experiments

Kashiwagi et al.[1987] conducted a series of experiments in which a 3.8cm cubic sample of white pine contained within three different atmospheres (pure nitrogen, 10.5% O_2 and 89.5% N_2 and air) were exposed to several levels of external radiation. The imposed radiant flux distribution over the sample surface was nearly uniform (a 5% variation was reported). The surface absorptivity of the virgin wood was reported as approximately 0.7 which increased to 0.95 after a layer of char formed.

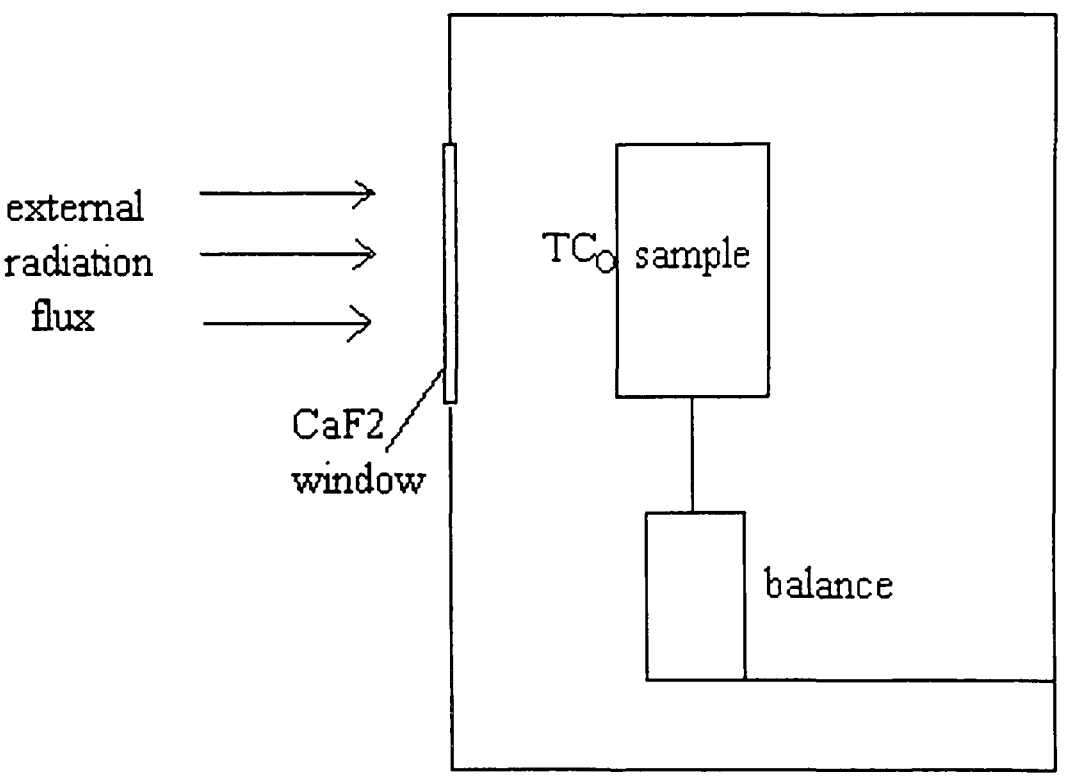

Figure 7.6.6: Schematic diagram of Kashiwagi et al. experiment.

The source of radiation is provided by a vertically positioned external radiation plate (see figure (7.6.6)). The sample is arranged so that only a single surface (front surface) is exposed to the external radiative heat flux which is nearly uniform over the sample surface. The bottom surface rests on an electronic mass scale and so is treated as insulating. The other four sides of the sample are uncovered. Through the centre of the sample (from front to rear surface) are three thermocouple locations, one at the

surface, one at a depth of 0.1 cm and the last at 0.5 cm. The sample is confined within a chamber whose inside surfaces are painted black and water-cooled. Kashiwagi et al. reported that temperature distributions within the sample approach spatially one-dimensional behaviour. Figure (7.6.6) is a schematic diagram of the experimental set-up.

Within an oxygen atmosphere several chemical reactions may occur. The char formed during pyrolysis is not chemically inert but reacts with the ambient oxygen. This reaction is strongly exothermic and causes a rapid increase in temperature. In addition, a gray ash is formed which lines part of the surface when the char is consumed by this reaction. Furthermore, gas phase ignition may occur if the gas phase temperature is high enough. Both of these factors will affect the heat feedback to the sample. As neither of these factors are included in the current model, the experimental data corresponding to samples in nitrogen atmospheres exposed to constant external radiative heat flux of 4 W/cm^2 are selected for comparison purposes.

7.6.3.2 One-dimensional simulation of mass loss rates

The properties of white pine used in this simulation are taken from the literature: ρ_v = 380 kg/m^3, C_v = 1150 J/kgK, λ_v = 0.34W/mK[Kashiwagi et al., 1987], λ_c = 0.2 W/mK[Mikkola, 1991]. The pyrolysis temperature of 603K is estimated from the measured surface temperature history. Figure (7.6.7)(copied from [Kashiwagi et al., 1987]) plots the experimental temperature histories at various locations in the sample at incident radiant heat flux of 4 W/cm^2. The three surface temperature profiles diverge at around 330 °C(603 K). This divergence indicates that the oxidation of the

char and burning of the sample within the atmospheres containing oxygen start up. Thus this point of temperature can be regarded as the pyrolysis temperature of the sample. The pyrolysis heat of wood varies broadly in the literature from 0.2~7 MJ/kg[Petrella, 1979; Delichatsios et. al., 1994; Mikkola, 1991]. A value of 1.2 MJ/kg is used in this simulation. It is also assumed that $(\rho_c C_c)/ (\rho_v C_v) = 0.2$.

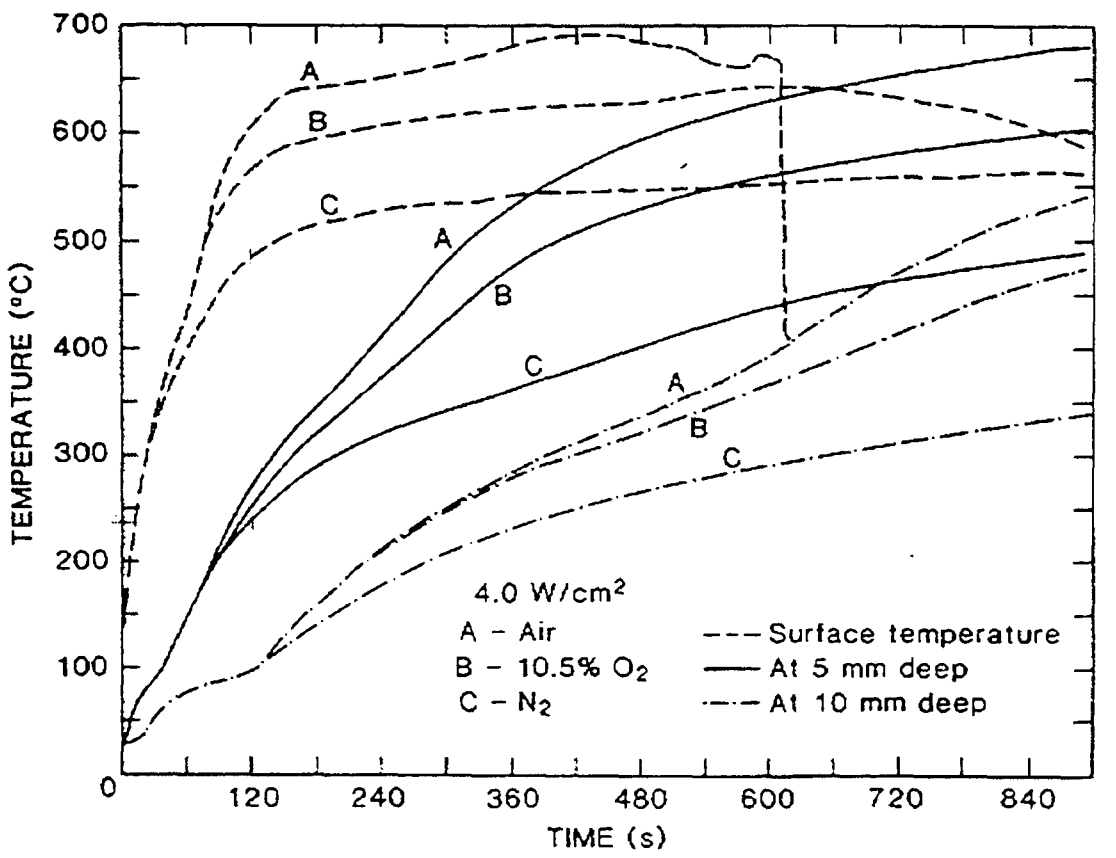

Fig. 7.6.7: Experimental temperature histories at various locations in the sample at incident radiant flux of 4 W/cm^2 (copied from [Kashiwagi et al., 1987]).

As the external radiative heat flux is nearly uniform, a one-dimensional simulation of the mass loss process is a reasonable first approximation. Along the direction of the incident radiation, the 38mm thick sample is discretised into 190 control volumes or cells. In the one-dimensional model the front (surface) is exposed to the measured flux of 4 W/cm^2. The surface absorptivity of the virgin wood is taken as 0.7 which increased to 0.95 after a layer of char formed. The heat losses at the rear surface are described by equation (7.4.2.6a), i.e. the convective and reradiation heat losses are taken into account. The convective heat transfer coefficient and the emissivity at the

bottom surface are assumed to be 10 W/m^2K and 0.7 respectively. The ambient temperature is 300 K. The model consists of equations (7.4.2.1) to (7.4.2.9) with the mass loss rate determined by equation (7.4.2.9).

The comparison between numerical predictions and experimental data is based on the time history of mass loss rates - the primary purpose of char models - and the time history of the temperature at three locations, the char surface, 0.5cm and 1.0cm below the char surface.

The curves of predicted and measured mass loss rates as a function of time are depicted in figure (7.6.8). As can be seen from figure (7.6.8), there is very good qualitative agreement between the predicted mass loss rates and those measured. The quantitative agreement is also reasonable.

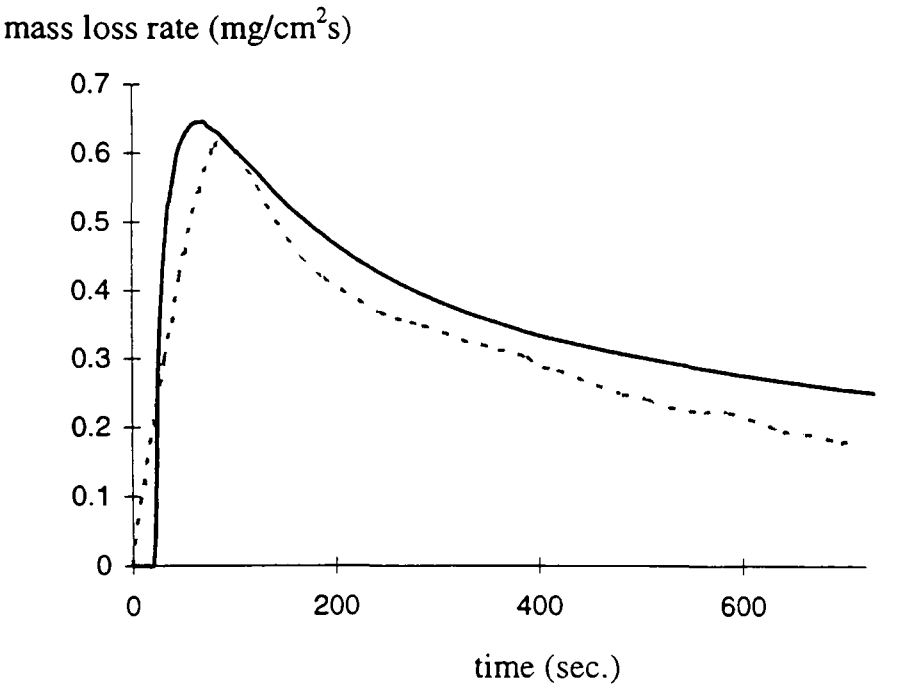

Figure 7.6.8: The predicted and measured mass loss rates for white pine at an irradiance $4W/cm^2$.
— : predicted mass loss rates; – – : measured mass loss rates.

The predicted peak mass loss rate value (0.65 mg/cm^2s) is in very good agreement with the measured value (approximately 0.62 mg/cm^2s). The predicted time (70

seconds) to attain this peak value is slightly earlier than the measured value (approximately 91 seconds). Furthermore, the numerical mass loss rate increases more rapidly than the measured values. These differences are probably due to the effects of moisture within the wood sample which are neglected in the charring model.

After the peak mass loss rate is achieved, the mass loss rate begins to decrease due to heat absorption of the char layer and enhanced surface reradiations which results from the high temperature at the char surface. During this decrease, the model predicts a smooth decline in mass loss rate which is higher than the measured mass loss rate. At 200 seconds the predicted mass loss rate is 0.47 mg/cm^2s compared with approximately 0.41 mg/cm^2s, at 400 seconds the predicted mass loss rate is 0.34 mg/cm^2s compared with approximately 0.29mg/cm^2s while at 600 seconds the predicted mass loss rate is 0.28 mg/cm^2s compared with approximately 0.22 mg/cm^2s.

Figure (7.6.9) depicts the comparison of predicted and measured temperature profiles at the top surface of the sample and at depths of 0.5cm and 1.0cm within the material. As can be seen from figure (7.6.9), the measured and the numerical top surface temperatures are in very good agreement. While the agreement between predicted and measured temperatures at the two deeper locations are not as good as at the surface, they are reasonably consistent.

These differences are thought to be due to several simplifications within the pyrolysis model. As heat absorption by moisture is neglected in the current pyrolysis model, more heat is conducted into the deeper portions of the wood. This causes the predicted temperatures at the 1.0 cm location to increase more rapidly than the measured values

after a brief (40 second) initial lag.

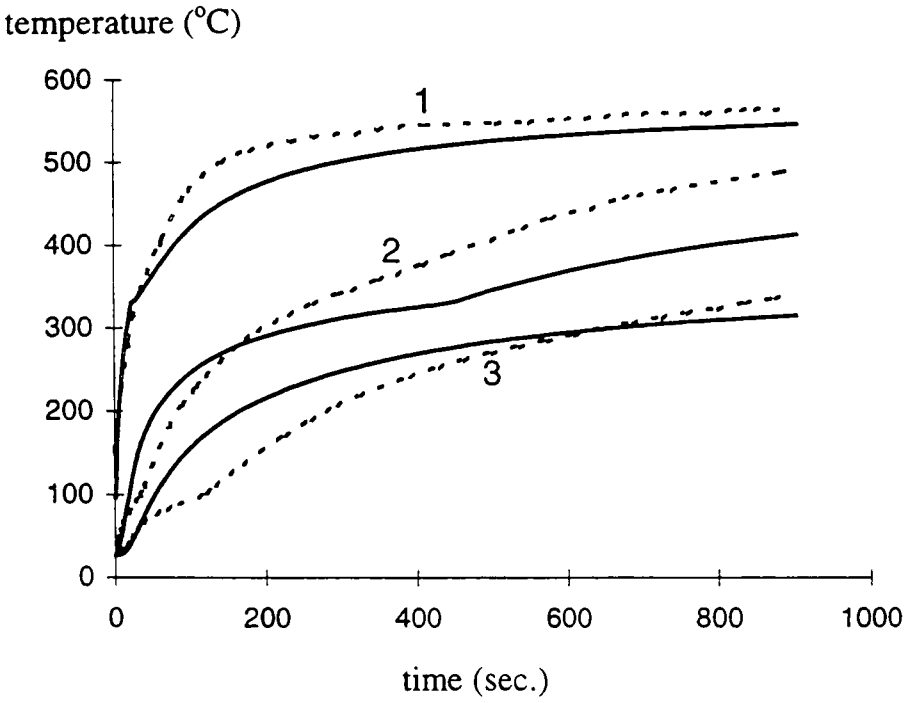

Figure 7.6.9: Measured and numerical temperature profiles.
1: at top surface; 2: at 0.5cm depth and 3: at 1.0cm depth.
— : numerical temperature profiles; – – : measured temperature profiles.

Another major difference in the predicted and measured temperature occurs at the 0.5cm depth during the late stage of pyrolysis. From the temperature history, it can be shown that this position is in char layer during the late stage of pyrolysis. The deformation in char layer and radiation flux penetrating through the char pores may affect the measured temperature. However these factors are not taken into account by the current model.

In the experiment, deformations within the char layer may result in the thermocouple - initially positioned at a depth of 5mm - being closer to the surface. This not only decreases the distance for heat transport but also brings the specified measuring location close to the hot surface. Furthermore, penetration of radiation flux through the char pores transports more heat within the char layer. Both these factors may contribute to the discrepancies noted at the 0.5 cm measuring location. The same arguments may also explain the slightly higher measured temperature at the 1.0 cm

depth during the last stage of pyrolysis.

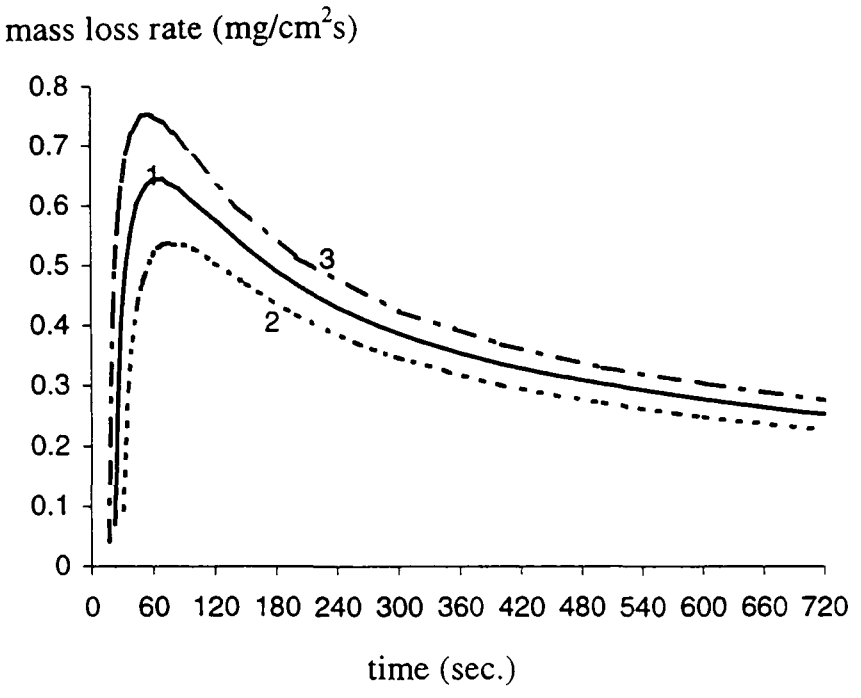

Figure 7.6.10: The variation of the mass loss rates caused by the changes of the ignition temperature for white pine at an irradiance 4W/cm^2.
1) T_p=603K; 2) (1+0.05) T_p; 3) (1-0.05) T_p.

It should be noted that the numerical results presented here are dependent on material properties which are estimated from experimental data, such as the pyrolysis temperature and pyrolysis heat. This is a feature common to all models using the pyrolysis temperature concept (e.g. [Chen *et al.*, 1993; Moghtaderi *et al.*, 1997]). A sensitivity analysis based on the pyrolysis temperature was performed to investigate the effects of the changes of this parameter on the model predictions. The ignition temperature was allowed ±5% variations around the 603K of the previously used ignition temperature(i.e.±30.15K). The mass loss rates produced by the changes of the ignition temperature are depicted in figure (7.6.10). It is clearly observed that during the early and late stages of the mass loss process the changes within the prescribed range of the ignition temperature do not cause significant differences in the mass loss rates. The magnitude and the trend of the mass loss during these two stages are quite similar and close. However, larger differences in the mass loss rate occur at the stage of peak mass loss rate. The peak mass loss rates vary within a range of ±17.1%.

However, it is worth to point out that the deviation of the peak mass loss rates also depends on the values of other parameters involved in the model, e.g., the pyrolysis heat and the specific heat. A full investigation into the influence of these parameters on the mass loss is considered beyond the scope of in this thesis and is left to later analysis.

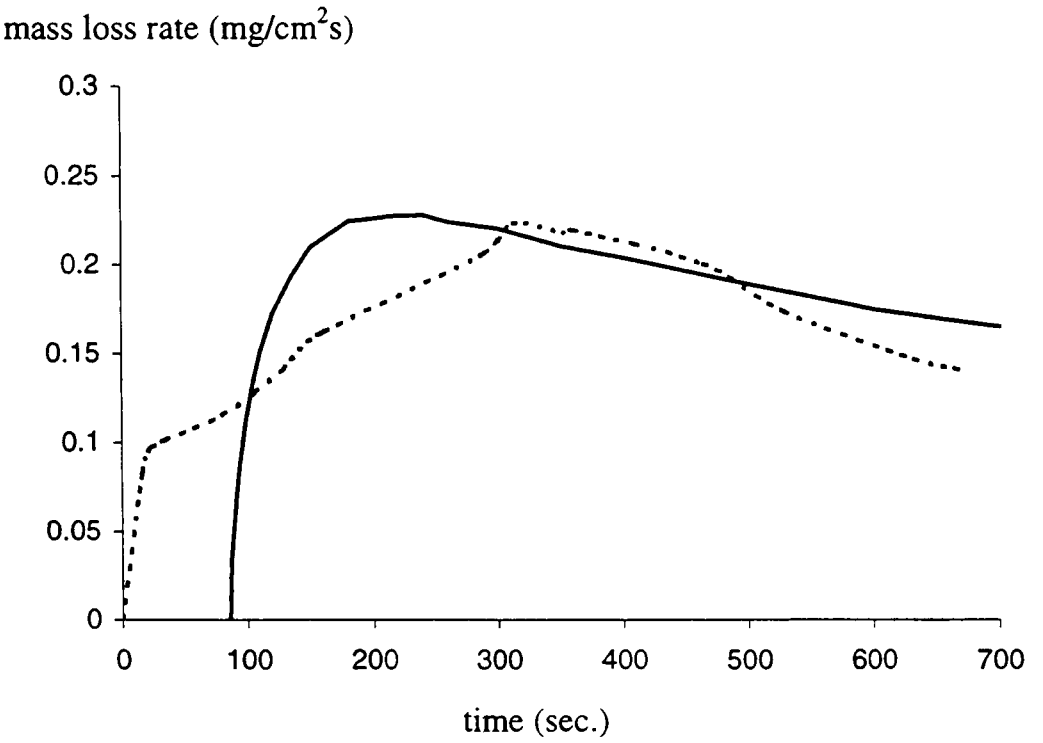

Figure 7.6.11: The predicted and measured mass loss rates for white pine at an irradiance $2.5 W/cm^2$.
— : predicted mass loss rates of the white pine sample;
– – : measured mass loss rates of the white pine sample.

In order to test the model capabilities for a different incident radiative flux, the model was compared with data generated by Kashiwagi et al.[1987] for an incident flux of $2.5\ W/cm^2$. This data corresponds to an identical experimental set-up as was used in the previous case. Furthermore, the same material properties are used in this simulation as in the previous case in order to predict the mass loss rates. The predicted and measured mass loss rates are presented in figure (7.6.11). As can be seen, the predicted peak mass loss rate is in very good agreement with that measured. Furthermore, the mass loss rates during the decay phase are also well predicted by the model. While the overall agreement is reasonable, there are two notable differences

between the model predictions and measured results.

Firstly, the degradation process is predicted to begin at a later stage than that observed. The delayed start to the degradation process predicted by the model is due to the simplicity of the ignition temperature concept. The model predicts no degradation within the sample until the surface temperature reaches the prescribed ignition temperature. However in reality, the degradation process can start before the ignition temperature is attained. This may lead to mass loss occurring at lower surface temperatures than predicted by the model. Secondly, at the initial stage of the degradation process, the model failed to re-produce the gradually increasing mass loss rates after the initial sharp starting process. Kashiwagi et al.[1987] argued that this small hump after the initial accelerated start was caused by evolved sample moisture. As the effects of moisture are ignored in the current model, this mechanism cannot be reproduced in the model.

7.7 Conclusions

The thermal degradation processes of solid fuels (charring and noncharring) involve extremely complicated chemical and physical changes within the fuels. There are strong interactions between transport phenomena and chemical reactions during the course of the thermal degradation. The mass losses not only depend on the nature of the material, but also are affected by the surrounding conditions.

Since there are uncertainties associated with the kinetic pyrolysis models due to the scatter of kinetic data, the relatively simple ablation models are selected to meet the

need of a strong flexibility and wide range application of the pyrolysis models. Another advantage of the ablation models is that it requires fewer material properties. The ablation pyrolysis models are based on two fundamental assumptions. First, it is assumed that solid fuels are gasified only at the surface regions(for noncharring materials) or at the char/virgin interface(for charring fuels). Second, presumably combustible gaseous products are released only when the solid surface are heated to the ignition temperature and the temperature of the pyrolyzing regions remains at this temperature throughout the period of mass loss. It is further assumed that the chemical processes associated with the pyrolysis process can be ignored.

The charring and noncharring pyrolysis models belonging to the ablation regime can mathematically be expressed in a set of partial differential equations. The pyrolysis models presented in this chapter were developed as standalone routines. They can be incorporated within the selected CFD software through the use of appropriate boundary conditions. For the charring model, a decoupling technique dealing with the tanglement of highly nonlinear surface reradiation and the movement of char/virgin interface was presented. Good accuracy of the decoupling technique was demonstrated by comparing the model predictions with the exact analytical solutions for two idealised cases. Comparisons with experimental results show the charring model presented here is capable of producing predictions of mass loss rates, surface temperature and interior temperatures in good agreement with measurements. The non-charring pyrolysis model was also compared with exact analytical solutions and experimental data. The model was found to produce excellent agreement with the analytical solution. The noncharring model also produced the numerical mass loss rates for PMMA in excellent agreement with the measured mass loss rates at three

different levels of the incident heat flux. In conclusion, the pyrolysis models presented in this chapter appear to be good candidates for incorporation into the CFD based fire models to simulate flame spread and fire propagation in enclosures.

Chapter 8

SIMULATIONS OF FIRE GROWTH AND SPREAD IN ENCLOSURES

8.1 Introduction

Since most of fuels involved in compartment fires are in condensed phase such as drapes, curtains, chairs, beds, desks, upholstered furniture, wood panelled walls, ceiling, floor and so on, the behaviour of these combustibles when they are exposed to or involved in fires is of great concern. The fire spread over the surface of continuous items such as lining materials may significantly speed up the process of fire propagation. In addition, standard tests for fire spread over wall and ceiling lining materials have been designed to assess the flammability of building materials. From the cost standpoint, it is desirable to use mathematical models to simulate fire spread over the surfaces of lining materials in a compartment. Due to the severity of flashover, this technique is expected to have the ability to predict this hazardous phenomenon. It is intended to predict the development and impact of fire within the compartment by the mathematical fire spread model in terms of measurable material properties, the geometric configuration of the compartment and the physical state of the environment. Since material properties can be derived from bench or small-scale experiments, mathematical modelling is an attempt to investigate fire propagation in the full scale by using the predictions from the model without the need to conduct full-scale experiments.

This chapter is an attempt by the author to develop a useful fire spread model to

simulate the course of the fire spread within a single compartment. Establishment of this model within the framework of CFD software is the main aim of the work presented here. The intention of this work is to integrate in the model some essential elements of compartment fires—the gaseous combustion, radiative energy exchange and solid fuel combustion. The models of these three phenomena have been presented, demonstrated and tested in chapter 4 to 7. Some validation of these models has been presented by the author or in other published research work. The validations show that each of these models is promising in simulating the according phenomenon. In this chapter these separate individual models will be synthesised together to form a combined model that is able to simulate the process of fire growth and spread within an enclosure. The integrated fire spread model will be then used to demonstrate fire spread in a compartment in two dimensions. As the two-dimensional predictions appear to produce realistic and plausible results, the model is then extended to three-dimensions. Predictions from the three-dimensional model are then compared with experimental data from two compartment fires, one involving PMMA and the other involving wood products.

8.2 The Flame Spread Model for a Compartment Fire

As mentioned in section 2.3, the flame spread model presented here for a compartment fire is an integrated model within the framework of the CFD software CFDS-FLOW3D(version 2.3.3). The entire model consists of the following sub-components, a gas-phase combustion model(the eddy dissipation concept model, equations from (4.4.1) to (4.4.10)), a radiation model(the six-flux model, equations (5.5.1), (5.5.2) and (5.6.1) or the discrete transfer method, equations from (5.5.13) to (5.5.15)) and a thermal

pyrolysis model(the non-charring model, equations from (7.4.1.1) to (7.4.1.9) or the charring model, equations (7.4.2.1) to (7.4.2.9)). Each individual model has been described in detail in previous chapters. The pyrolysis models for noncharring and charring materials have been verified by comparing numerical predictions with according experimental measurements(see sections (7.5) and (7.6) in the chapter 7). The integration of the gas phase combustion model and the radiation model has been validated by simulating a Steckler room fire test(see chapter 6). To evaluate radiative properties of the gas-soot mixture, the simple soot model described in chapter 5 is included in the integrated fire spread model. The mass loss processes of burning solid fuels is described by the pyrolysis models for noncharring and charring materials presented in chapter 7. However, the interplay between the gas phase and solid phase behaviours needs to be carefully dealt with. One of the major challenges in this work concerns how to efficiently incorporate the solid field calculations into the framework of CFDS-FLOW3D.

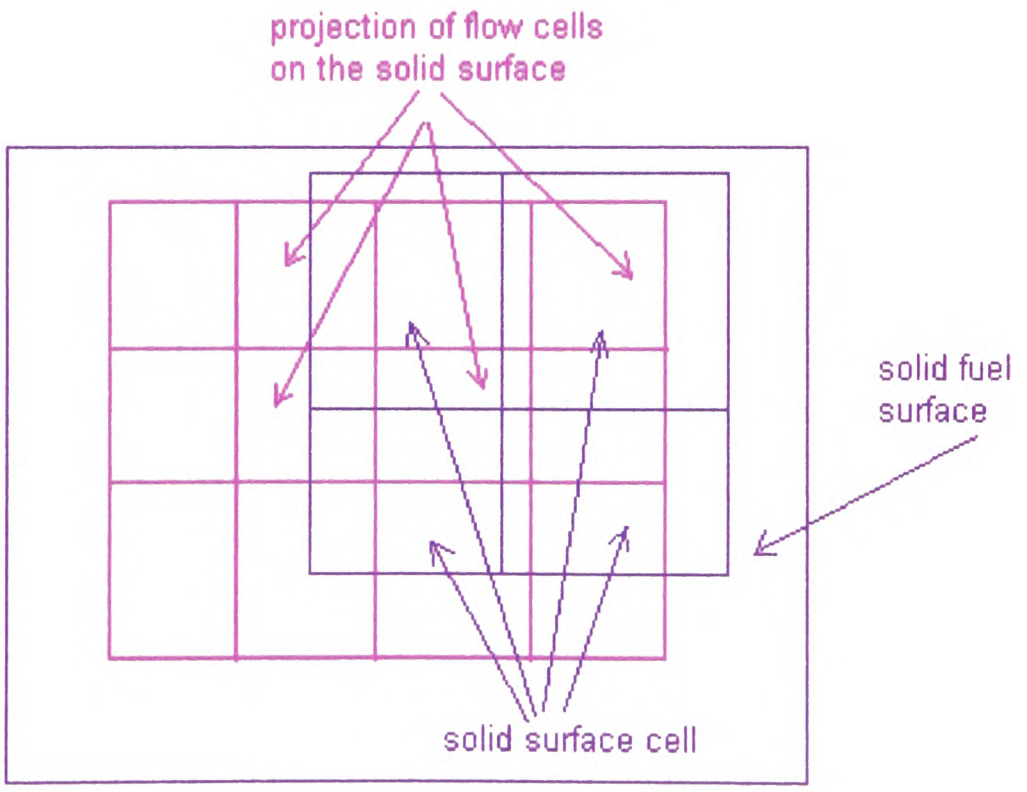

Fig. 8.2.1: the position relation between the flow cells and a solid cell.

The discretisation of solid field is separate from that of the flow domain. The mesh in the solid field can be made completely independent of that in the flow domain. An arbitrary representation of the relationship between flow and solid cells is depicted in figure (8.2.1). Physical quantities - such as heat flux - transferred from the flow domain to a particular solid surface cell must be obtained by averaging the contributions from the flow cells adjacent to the solid cell. Conversely, the contributions from the solid surface to the flow filed – such as radiation from the solid or combustible mass flux from the solid cells to the flow - must also be averaged, interpolated or summed. If computational cells in the solid and gaseous regions do not have a one-to-one correspondence - as shown in figure (8.2.1) - then a complex averaging procedure is required in order to preserve conservation. For simplicity and efficiency however, the surface of the solid is discretised according to the discretisation of the flow domain, thus maintaining a one-to-one correspondence and resulting in a simplified transfer procedure. While this process fixes the discretisation on the surface of the solid fuel, the number of cells along the thickness of the fuel is a free parameter. The number of the cells along the thickness of the solid is determined from a previous one-dimensional mesh sensitivity analysis in chapter 7. The manner in which the solid fuel is discretised is depicted in figure (8.2.2). Although the surface mesh of the solid region is dictated by the discretisation of the flow field, the actual computational mesh of cells used to discretise the solid fuel is separated from the flow domain. The mesh for the solid fuel is stored separately to the mesh for the flow domain. It does not make any contribution to the mesh in the flow domain. The advantage of this treatment is that the relatively fine mesh along the thickness of the solid fuel does not necessarily create a corresponding fine mesh in the flow domain.

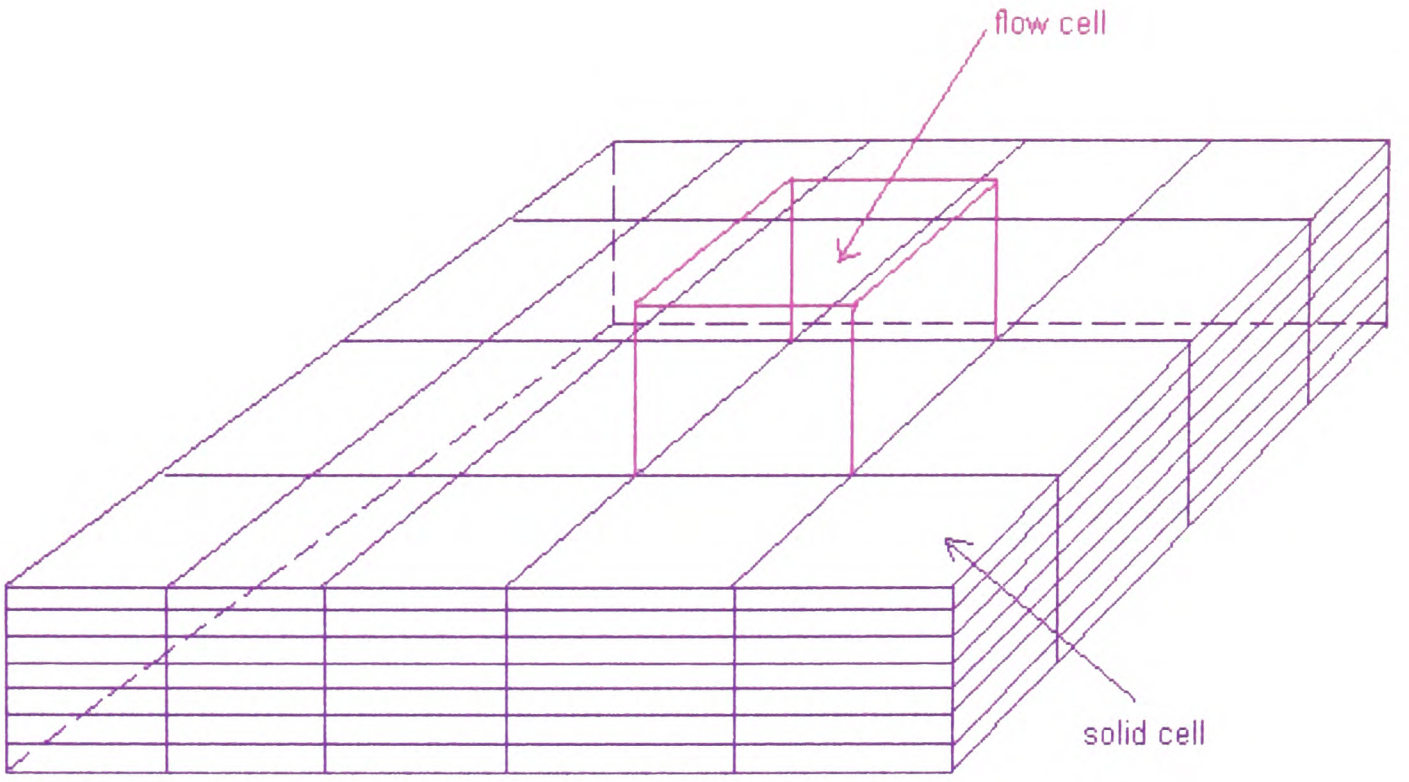

Fig. 8.2.2: The simple way of discretising the solid fuel.

Once the surface of the solid fuel is heated to the pyrolysis temperature T_p, it begins to be gasified. The gasified combustible products are allowed to enter the flow domain at the position of the burning solid cell. The rate at which the combustible pyrolysis products enter the flow domain at the position of the burning solid cell is equal to the mass loss rate of the solid fuel at the burning cell determined from the pyrolysis model. It is assumed that the combustible gas is blown-off the solid surface with a zero initial velocity. Once the solid has been gasified, the gaseous combustion model (the eddy dissipation model) is activated to simulate the flame spread process. For simplicity the gaseous specific heat and molecular weight are assumed to be constants.

If noncharring combustible solid is involved, mass losses of the target fuel due to gasification are described by regression of the solid surface. It is assumed that the reduction in solid surface does not impact on the gas motion near the solid surface. For charring combustible materials, the deformation of the target fuel is neglected.

The heat flux at the solid surface contains radiation heat flux and convective heat flux. Given all the values of the flow domain variables such as the velocities, turbulence variables associated the turbulence model, the temperature of the gas mixture and etc., the radiation part is calculated from the radiation model described in chapter 5 and the convective part is determined according to the wall function described in chapter 2 or empirical expressions. When combustible gas is released from the solid surface, the convective heat transfer coefficient should be corrected by $h_*/h = E(\phi)$[Bird et al., 1966; Atreya, 1995], where h_* is the corrected heat transfer coefficient and h is the heat transfer coefficient without mass transfer at the solid surface. $E(\phi)$ is given by

$$E(\phi) = \phi/(e^{\phi} - 1) \tag{8.2.1}$$

and ϕ is defined by

$$\phi = \dot{m}'' C_{pg}/h, \tag{8.2.2}$$

where $\dot{m}''$ is the mass flux coming out of the surface and C_{pg} is the specific heat capacity of the gas. However this correction is not implemented in the current spread model since uncertainties are brought about by using the wall function in fire environments in particular when the target solid fuel is placed at the ceiling.

Flame spread over the solid surface represents an interaction between gas phase and solid phase combustion. The interplay between the gas phase and solid phase behaviours needs to be carefully dealt with. This interaction is embodied in the boundary conditions on the interface between gas and solid. The boundary conditions for energy are

a) in virgin fuel region (in preheating stage)

$$T = T_s \tag{8.2.3}$$

$$\lambda_s \frac{\partial T_s}{\partial n} = \dot{q}_r'' - \dot{q}_{rr}'' + \dot{q}_c'' \tag{8.2.4}$$

where $\dot{q}_r''$ and $\dot{q}_c''$ are the radiation heat flux and the convective heat flux at the surface respectively and $\dot{q}_{rr}''$ ($= \varepsilon\sigma T_s^4$) is the surface re-radiation losses.

b) in pyrolysis region

1) for noncharring solid

$$T = T_s = T_p \tag{8.2.5}$$

$$\lambda_s \frac{\partial T_s}{\partial n} = \dot{q}_r'' - \dot{q}_{rr}'' + \dot{q}_c'' - \dot{m}'' L \tag{8.2.6}$$

2) for charring solid

at the gas/char surface

$$T = T_c \tag{8.2.7}$$

$$\lambda_c \frac{\partial T_c}{\partial n} = \dot{q}_r'' - \dot{q}_{rr}'' + \dot{q}_c'' \tag{8.2.8}$$

where $\dot{q}_{rr}'' = \varepsilon\sigma T_c^4$ is the gas/char surface re-radiation losses.

The boundary conditions for mass transfer in the pyrolysis region are

$$\rho D \frac{\partial m_f}{\partial n} = \dot{m}''(m_f - 1) \tag{8.2.9}$$

$$\rho D \frac{\partial m_o}{\partial n} = \dot{m}'' m_o \tag{8.2.10}$$

$$\rho v_n = \dot{m}'' \tag{8.2.11}$$

$$v_i = 0 \tag{8.2.12}$$

where n is the outward going unit normal direction to the solid surface, v_i represents the components of the velocity vector parallel to the solid surface, λ, D, ρ, m_f, m_o

are the thermal conductivity, diffusion coefficient, density, fuel mass fraction and oxidant mass fraction in gas phase respectively.

These conditions effectively link the gas phase variations to the solid phase variations and couple the two independent models for solid pyrolysis and gaseous phase flow, combustion and radiation.

At the surface of non-combustible walls or the ceiling or the floor, the boundary condition for heat transfer is

$$k_s \partial T_s / \partial x = q_r'' + \dot{q}_c'' - \varepsilon_s \sigma T_s^4 \tag{8.2.13}$$

$$T_s = T \tag{8.2.14}$$

where k_s, ε_s and T_s stand respectively for the conductivity, surface emissivity and temperature of the non-combustible solid, T is the temperature of the gas mixture and q_r'' and $\dot{q}_c''$ are the radiation flux and the convective heat flux at the solid surface respectively.

The convective heat flux can be expressed as

$$\dot{q}_c'' = h_T (T_s - T_g) \tag{8.2.15}$$

where T_g is the gas main stream temperature near the solid surface and the convective heat transfer coefficient h_T can be derived from the wall function for the turbulent flow(see section 2.4). The solid surface temperature T_s can be obtained from the pyrolysis model if the solid is combustible or from the integral model described in section 6.2.3 if the solid is non-combustible. If the non-combustible solid material is quite thin, for exmple a glass vision panel, the finite difference method can be

employed to obtain the solid surface temperature. However, the mesh for the solid is separate from the one for the flow. The same handling for meshes within the non-combustile solids as decribed earlier in this section for combustible solids is employed. The convective heat flux calculated in terms of equation (8.2.15) is then used to set up the boundary condition of heat transfer at the solid surface for the flow domain. In fact this procedure is placed into the iterative process of the CFD software CFDS-FLOW3D software (Version 2.3.3) in each time step.

8.3 Two Dimensional Simulations for Flashover and Backdraft

In this section we demonstrate the coupled gaseous/solid phase combustion model through two-dimensional simulations of flaming combustion in a room fire scenario involving a plywood ceiling. These simulations are only intended to provide a qualitative test of the model. As two-dimensional simulations are presented here, the four-flux radiation model, which is a two-dimensional version of six-flux radiation model, is used.

The work appearing in this section has appeared in two referred academic publications[Jia et al., 1997; 1999a], namely the Proceeding of the 5th International Symposium on Fire Safety Science(IAFSS) and the Journal of Fire Protection Engineering.

8.3.1 Scenario Description

The simulations concern a two-dimensional compartment(see figure (8.3.1)) measuring 3.6m in length and 2.4m in height and a non-uniform computational mesh consisting of 52×23 (1196) cells is used to discretise the flow domain(see figure (8.3.2)). The regions near the ceiling and the rear wall are refined with very small size of cells. The compartment has a 2.0m high door located in the end wall of the compartment. The solution domain is extended beyond the door - outside the compartment - where the boundary conditions are set as fixed pressure conditions thus allowing fresh air to flow in and combustion products out of the solution domain.

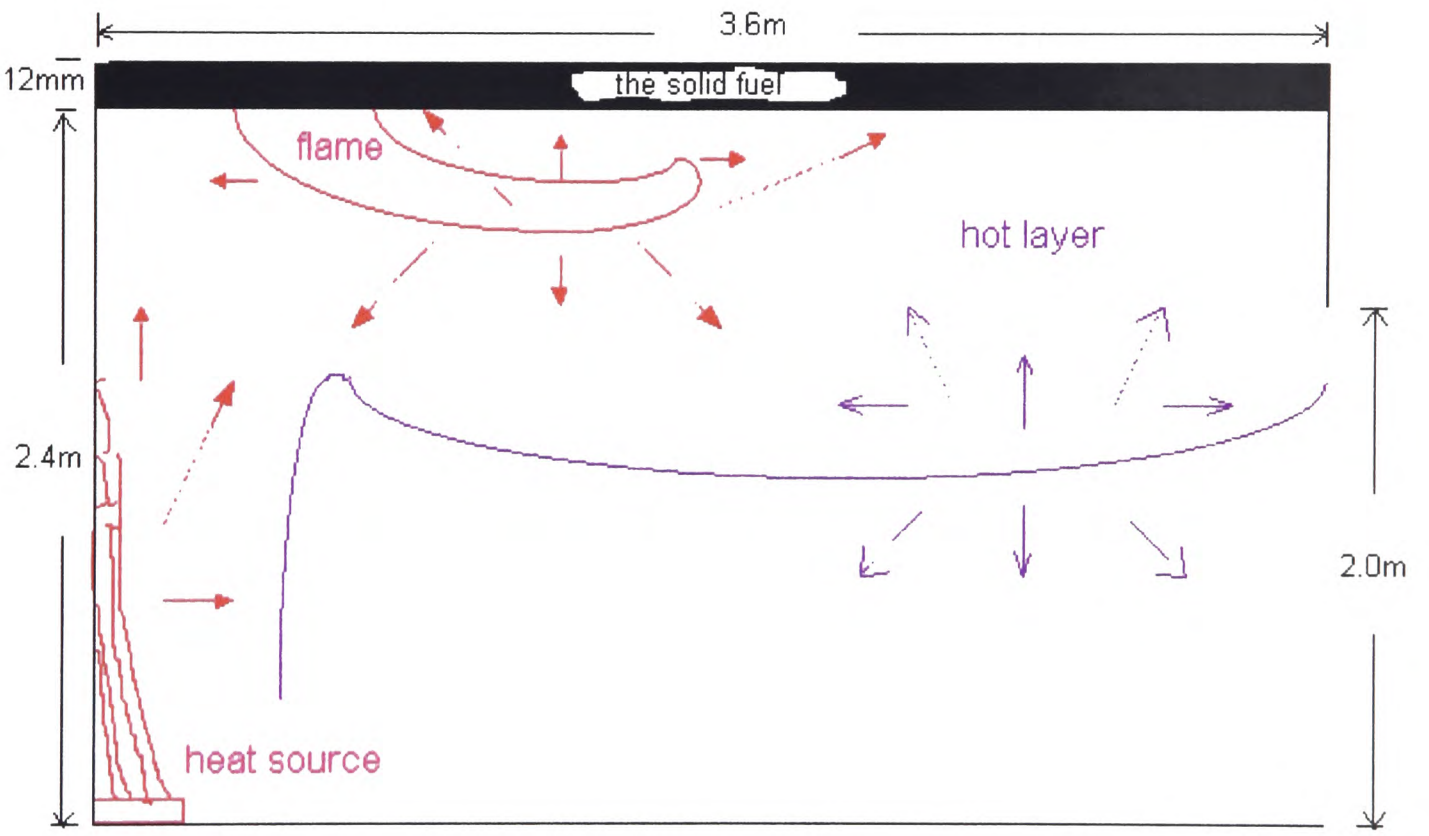

Fig. 8.3.1: The configuration of the two-dimensional compartment.
Note: Only the directions indicated by the solid line arrows are considered in the six-flux model.

The target solid fuel is located on the ceiling and consists of a 12mm thick cellulosic lining material that covers the entire expanse of the ceiling. Finally a mesh of 47×60 cells is used to discretise the solid material. Where the solid fuel has been totally consumed an adiabatic wall boundary condition is imposed.

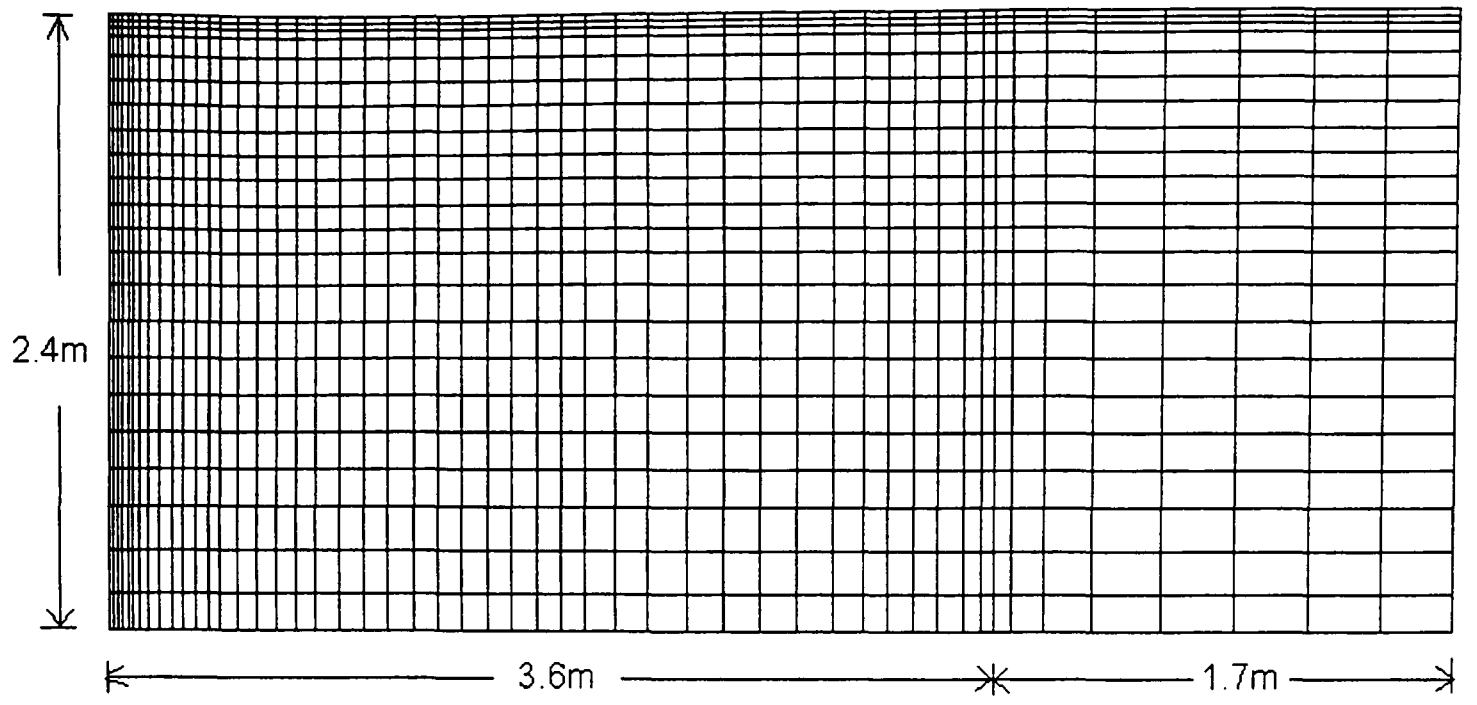

Fig. 8.3.2: The mesh used in the simulations.

The first case considers an open room scenario in which a "flashover" type phenomenon is predicted to occur. The second case considers a sealed room fire scenario in which the closed door is opened after some time. In this simulation a "backdraft" type phenomenon is predicted to occur.

***Case* 1**: Flame Spread Under Lined Ceiling -- Open compartment

In this scenario, the 2.0m high door is open throughout the simulation. A source of heat is artificially introduced into the calculation. This is achieved through the introduction of a 100 kW heat source located on the floor adjacent to the back wall. This is active throughout the simulation. It not only provides a heat source for initiating the fire spread along the solid fuel lining the ceiling, but also generates a gas flow to aid the fire spread. Run on a SUN SPARC 20/612 (60 Mhz processors) system, 100 seconds of simulation requires approximately 2.5 hours of computer time.

Case 2: Flame Spread Under Lined Ceiling -- Sealed compartment

The compartment geometry used in this case is identical to that of case 1. However, in this case the door to the compartment is initially closed and at some point in the simulation it is suddenly opened (door opens completely within one second). As in the previous calculation a 100 kW heat source is located on the floor adjacent to the back wall. However, unlike the previous case, its heat output is gradually reduced, reaching a value of zero when the fire spread in the ceiling material has reached a self sustaining level. After this point the heat source is not reactivated. Eventually, as the oxygen in the fire compartment is consumed, combustion of the pyrolysis products in the room atmosphere diminishes. Several seconds after the model predicts the gaseous combustion to nearly cease, the door to the compartment is opened, allowing fresh oxygen rich air to enter the room.

For the two cases described above, the same mesh plotted early in this subsection is used. The radiation model used in the integrated model outlined in the previous section is the six-flux model for these two particular cases. The soot model is not included in the simulations presented here. According to Hubbard and Tien [1978], the absorption coefficient a is a function of temperature T(K). Hubbard and Tien's curves for this dependence can be approximated using linear regression analysis. Using this approach the relationship between a and T can be roughly approximated by,

$$a = a_0 + b_0 T. \tag{8.3.1}$$

For wood, a_0 and b_0 take 0.0517 and 0.00052 respectively [Hubbard and Tien, 1978]. Using this relationship the absorption coefficient used in the radiation model becomes

temperature dependent.

The pyrolysis model used here is the non-charring model. The following solid fuel properties are assumed, ρ_s = 600.0 kg/m^3, c_s = 2678.0 J/(kgK), λ_s = 0.1 W/(mK), T_p = 666.0 K and L = 0.95 MJ/kg. These correspond to the material properties of plywood. The heat of combustion for the combustible gases is 10.35 MJ/kg.

The burner is modelled as a constant volumetric heat source as described in chapter 3. This model simply involves the burner represented as a heat source with constant heat release rate and is equivalent to the simplest form of fire field model used in practice. The wall and the floor of the compartment are assumed adiabatic while the boundary conditions at the ceiling where the target solid fuel is placed are specified by the equations from (8.2.3) to (8.2.12).

8.3.2 Results and Discussion

Case 1: Fire Spread Under Lined Ceiling -- "Flashover"

In order to provide a basis for comparison, first consider the results generated by the model without the solid fuel combustion component. All other components in the integrated model remain unchanged. In this simple representation of a compartment fire, the room reaches a steady-state after about 100 seconds and produces a maximum hot layer temperature of about 650K. Figure (8.3.3) shows the temperature distribution generated by the volumetric heat source model after 100 seconds.

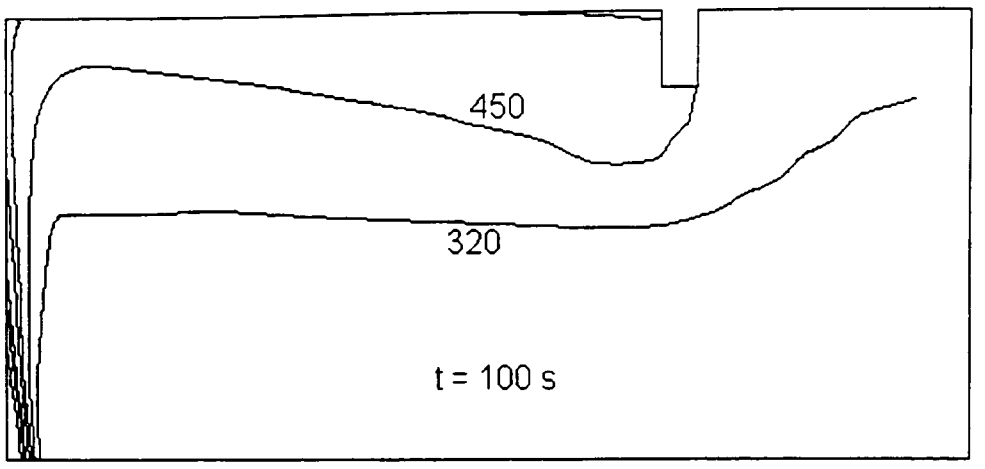

Figure 8.3.3: The temperature contours at steady state, where the only source of heat input is the volumetric heat source. Unit: K.

With the solid fuel combustion model and reactive ceiling included, the situation is very different. Unlike the previous case, steady-state conditions are not reached by this model. In fact, the temperature distribution attained by the simple model in steady-state conditions resembles the situation predicted by the more complex model after about 50 seconds (see figure (8.3.8)).

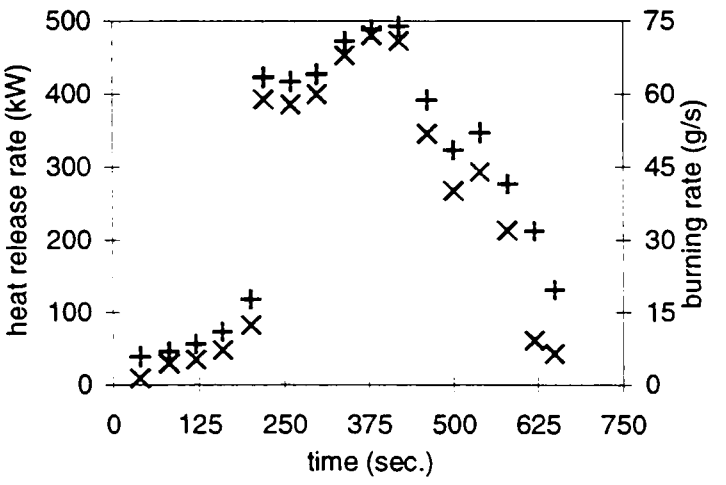

Figure 8.3.4: Heat release rate of gaseous combustion and burning rate of solid material in case 1.
+: the heat release rate of gaseous combustion (kW);
×: the burning rate of solid material (g/s).
Note: the 100kW heat source is not included in the heat release rate.

The fire progress is demonstrated by figures (8.3.4) to (8.3.9). Using the solid fuel combustion model, the fire development within the compartment appears to undergo a three stage development. This can most clearly be seen in figure (8.3.4) which depicts

the heat release rate due to gaseous combustion and the burning rate of solid fuel within the compartment.

The curves in figure (8.3.4) are clearly divided into three regions representing three phases of fire development, the initial growth phase, a rapid transition into the fully developed phase and finally the decay phase.

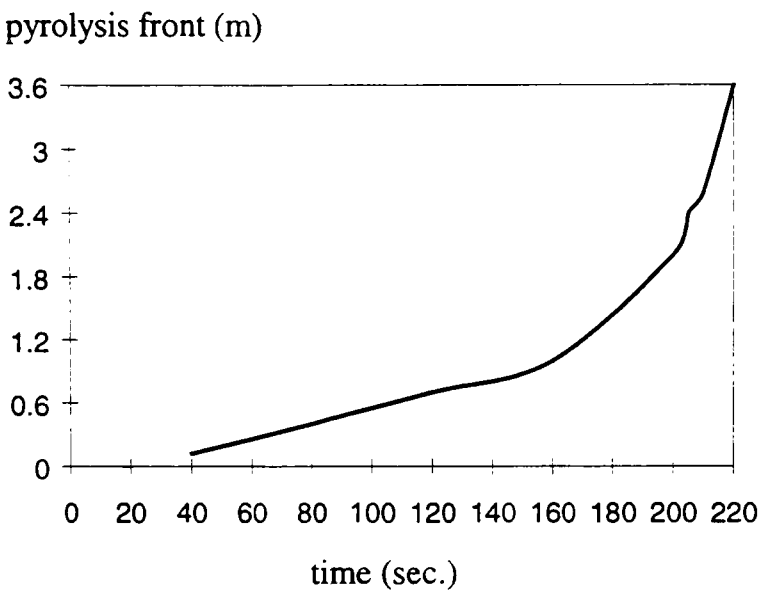

Fig. 8.3.5: The pyrolysis front position vs. time.

In the first phase, which lasts for the first 200 seconds, the heat release rate of gaseous combustion in the compartment increases at a slow and fairly constant rate. Figure (8.3.5) depicts the location (as measured from the back wall of the compartment) of the spreading pyrolysis front as a function of time. The pyrolysis front is identified by the solid cell undergoing pyrolysis which is furthest from the back wall of the compartment. Both figures (8.3.4) and (8.3.5) suggest that during the first 160 seconds the flame spread over the solid surface progresses at a constant rate. Between 160 and 200 second, as the fire progresses, the flame spread rate increases but remains relatively low. Figure (8.3.6) depicts the fraction of unburnt solid material remaining in the compartment as a function of time. Note that over the first 200 seconds, less than 5% of the solid material has been consumed by the fire. This is further emphasised in figure (8.3.7) which depicts

the changing profile of the unburnt ceiling material as a function of time. Over the 150 seconds only a small portion of material in the vicinity of the ignition source has been consumed.

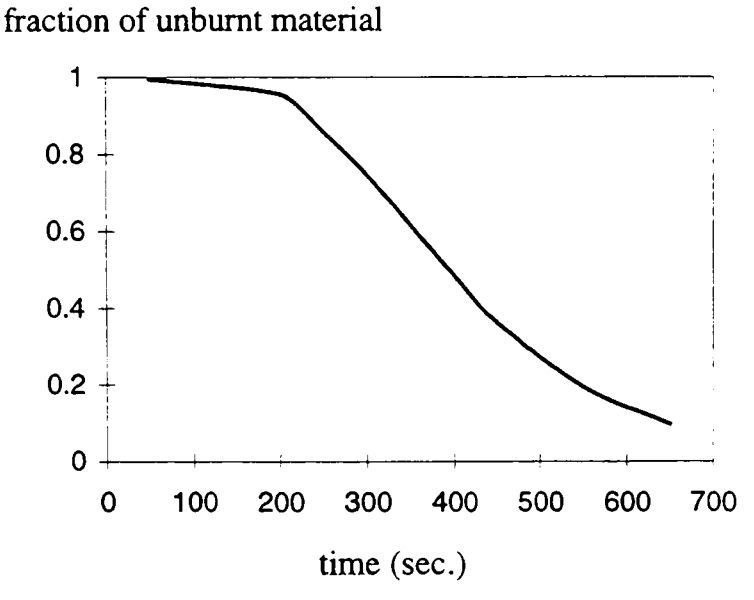

Fig. 8.3.6: Fraction of unburnt solid material vs. time.

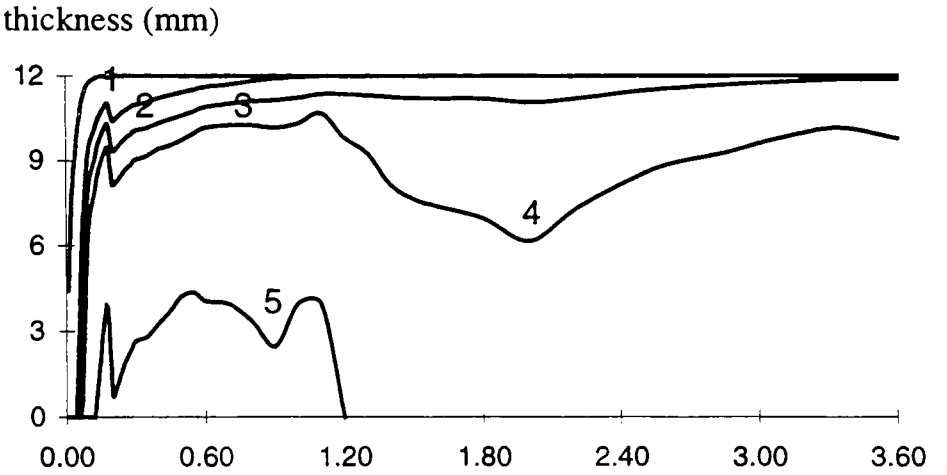

Fig. 8.3.7: The surface curves of remaining material at
1) 50 second, 2) 150 second, 3) 220 second,
4) 300 second, 5) 650 second.

During this phase the lining material is ignited and initially the fire spreads very slowly as there is a backward circulation of gases opposing the spread of hot combustion gases near the junction of the back wall and the ceiling. As the fire progresses, the hot combustion gases break out of this region and more of the ceiling material becomes involved in the combustion (see figure (8.3.8) at t = 150s). As the door soffit blocks the

flow of hot gases from spilling directly out of the compartment, hot gases begin to accumulate beneath the ceiling forming a stable layer (see figure (8.3.8) at t = 150s). This layer preheats the unburned materials and aids the fires progress.

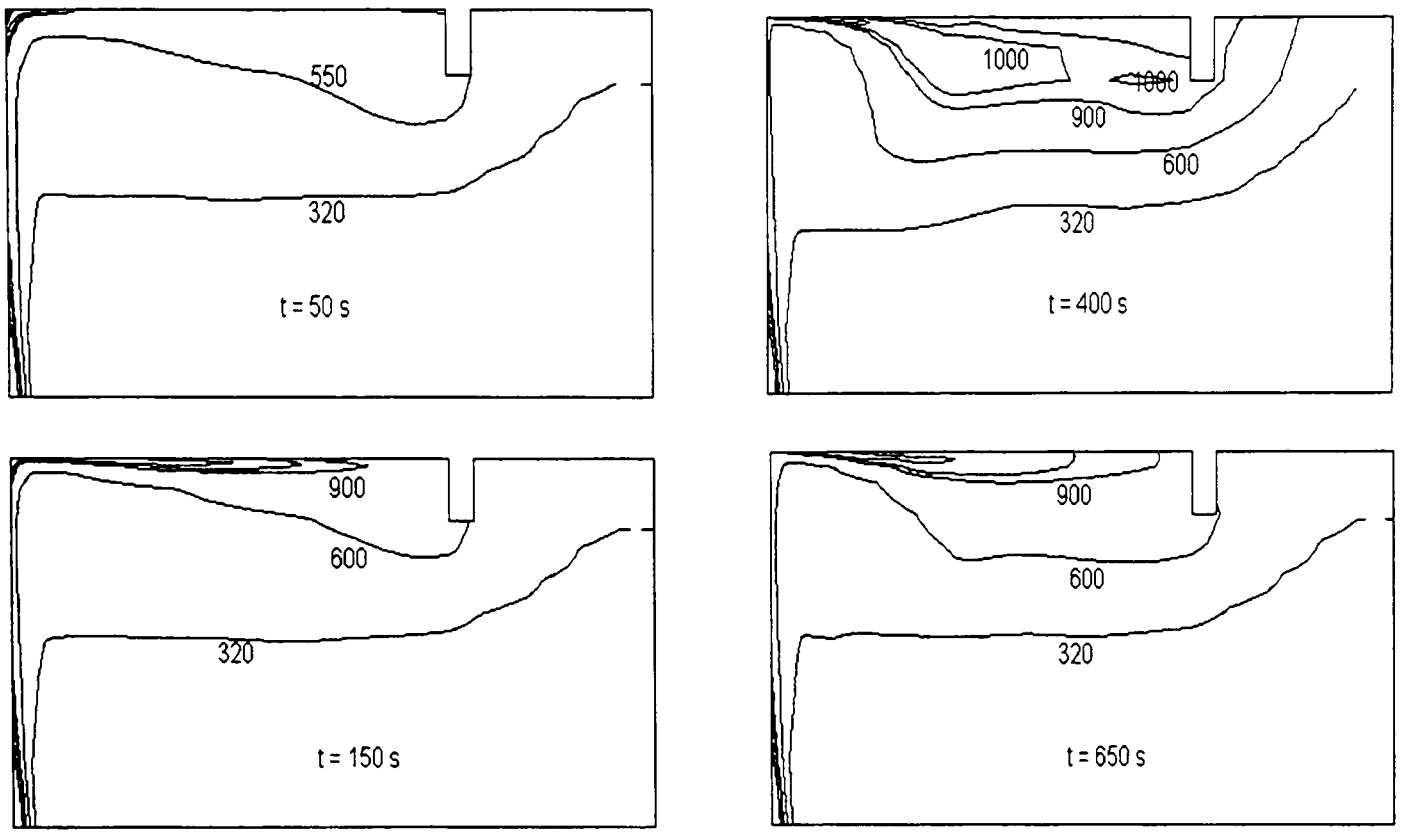

Figure 8.3.8: Temperature contours for case 1 after 50, 150, 400 and 650 seconds. Unit: K.

In this initial stage of fire development, as the advancing flame is quite small, the radiation view factor is also small; hence the radiative heat flux from the flame to the *unburnt* portions of ceiling surface is negligible. Furthermore, except for the ceiling region near the rear wall, the radiation from the 100 kW heat source can also be neglected due to the exponent form of radiation intensity. Therefore preheating of the unburnt ceiling region is mainly due to convective and radiative heat flux from the developing hot layer. In this situation, the four flux radiation model appears to produce reasonable predictions of radiative heat flux to the ceiling surface.

At about 220 seconds (see figure (8.3.4)) a critical point is reached where the fire rapidly

passes into the second phase of fire development and the heat release rate of gaseous combustion in the compartment undergoes a sharp increase (see figures (8.3.4), (8.3.5) and (8.3.9)). This rapid increase is a result of the entire combustible ceiling becoming involved in the fire. Figure (8.3.5) shows that at 200 seconds the pyrolysis front extends over approximately half the ceiling area. After a further 20 seconds the pyrolysis front has covered the entire ceiling and figures (8.3.5) and (8.3.7) show that the entire surface layer of combustible material has been burnt. Figures (8.3.4) and (8.3.5) show the speed of this transition and the marked increase in the rate of consumption of solid material.

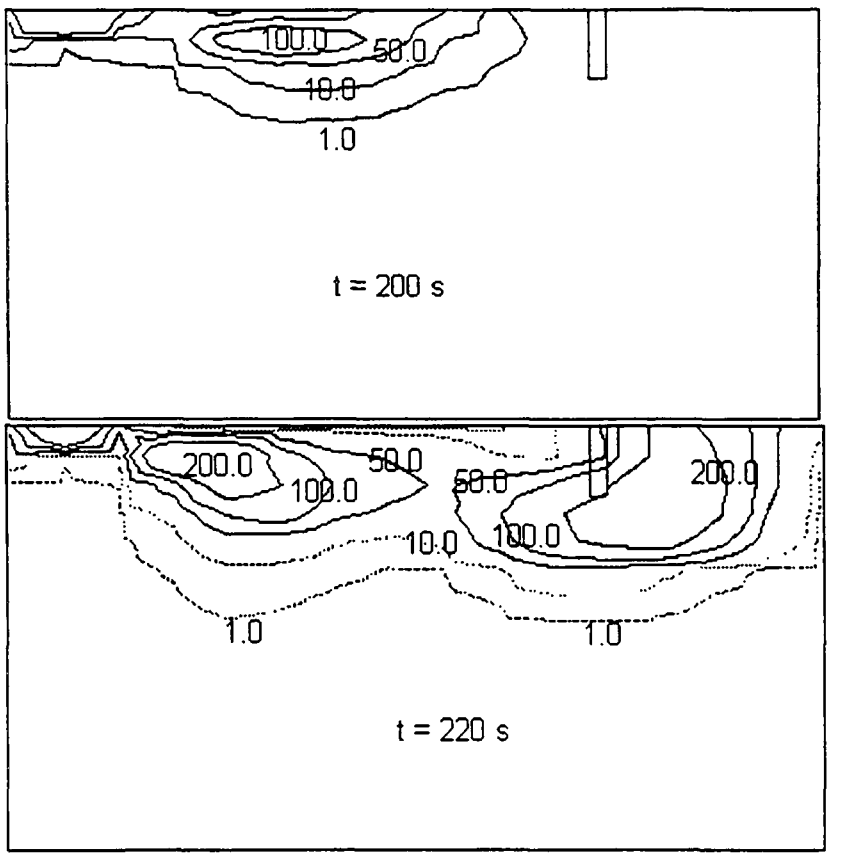

Figure 8.3.9: Contours of the heat release rate of gaseous combustion for case 1 preflashover (t = 200s) and during flashover (t = 220s). Unit: kW/m^3.

As a result, the flame erupts out of the compartment (see figure (8.3.9) at t = 220s), a phenomena often observed in experiments in which flashover occurs. During this short and rapid transition, combustion within the gaseous phase is more pronounced and involves a greater proportion of the compartment than is observed during the first stage (see figure (8.3.9)). During the transition, all available fuel within the compartment has

become involved.

Over the next period of about 200 seconds the heat release rate of gaseous combustion and the burning rate reach a maximum and maintain a reasonably stable state. Both figures (8.3.4) and (8.3.6) show that the mass loss rates remain nearly constant in this stage of fire development. The fire is fully developed in this period (see figure (8.3.8) at t = 400s). During this phase the gas temperature beneath the ceiling reaches a peak of about 1100K. Figure (8.3.7) suggests that, after 300 seconds, the fastest burning region of solid material is in the middle of the ceiling. From figure (8.3.8) at t = 400 seconds we note that this region corresponds to that portion of the hot layer which is both relatively thick and at an extremely high temperature. Radiation from this thick high temperature region below the ceiling results in the rapid burning of the ceiling material directly above it.

The third phase of fire development occurs approximately after 460 seconds, where the heat release rate begins to rapidly decrease (see figure (8.3.4)). At the beginning of this phase, there is approximately 40% unburnt material remaining in the ceiling (see figure (8.3.6)). Figures (8.3.6) and (8.3.7) show that during this phase nearly all of the remaining solid fuel is consumed. However the heat source driving the flow remains.

From figure (8.3.4) we note that during the first phase of fire development, the burning rate is less than 15 g/s , this rapidly increases to approximately 68 g/s during the second phase, remains approximately constant for a period before entering the third and final phase where it decreases as the fire begins to decline. This result is consistent with a general principle suggested by several experiments[Waterman, 1968; Hagglund et al.,

1974] that there is a limiting burning rate which must be exceeded for a flashover occurrence.

In real enclosure fires, three phases of fire development generally occur:

a) growth stage, in which the local fire grows smoothly, the end of this phase is usually followed by flashover which is marked by a sharp increase in fire growth rate;
b) fully developed stage, in which all combustible materials are involved in combustion, this is marked by a period of almost steady burning, and finally;
c) decay stage, in which the fire begins a rapid decline having consumed most of the fuel.

While the submodels described here are limited by a simple treatment of radiation and an equally simple treatment of gaseous and solid combustion, behaviour similar to this is predicted to occur.

Case 2: Fire Spread Under Lined Ceiling –"Backdraft"

When the door to the fire compartment is closed, the initial increase in room temperature and ceiling fire spread are more rapid than those noted in case 1. As the door is closed, there is no source of fresh air - and hence oxygen - to replenish the oxygen consumed by the combustion. In this case, while the pyrolysis process continues, combustion is incomplete and more and more unburned fuel gases accumulate within the room (see figure (8.3.10)). Figure (8.3.10) depicts curves for the heat release rate due to gaseous combustion and the amount of combustible fire products accumulating within the compartment.

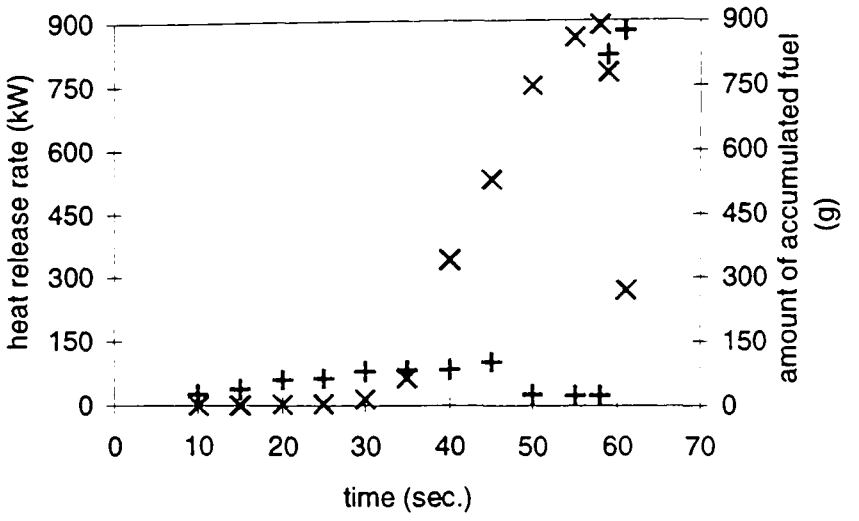

Figure 8.3.10: Heat release rate of gaseous combustion and amount of fuel accumulating within the compartment for case 2.
+: heat release rate of gaseous combustion (kW);
×: amount of fuel accumulating within the compartment (g).

Compared with case 1, instead of a sharp increase in heat release rate as the fire spreads, the heat release rate increases slowly however there is a rapid increase in the amount of fuel accumulating within the compartment (see figure (8.3.10)). Figure (8.3.10) suggests that even as the fire dies down, the amount of fuel accumulating in the compartment continue to increase. This suggests that the pyrolysis process continue as the hot gas mixture provides sufficient energy for the endothermic process to continue.

After approximately 45 seconds, the heat release rate due to flaming combustion begins to decrease due to the reduction in oxygen concentration within the compartment. It should be recalled here that the EDC gaseous combustion model is insensitive to the concentration of oxygen required to sustain combustion. As such the simulated gas phase combustion does not completely die away - even though the oxygen concentration levels have fallen to a sufficiently low level so as to prevent combustion - but continues at a very low level in pockets where fuel and oxygen coexist.

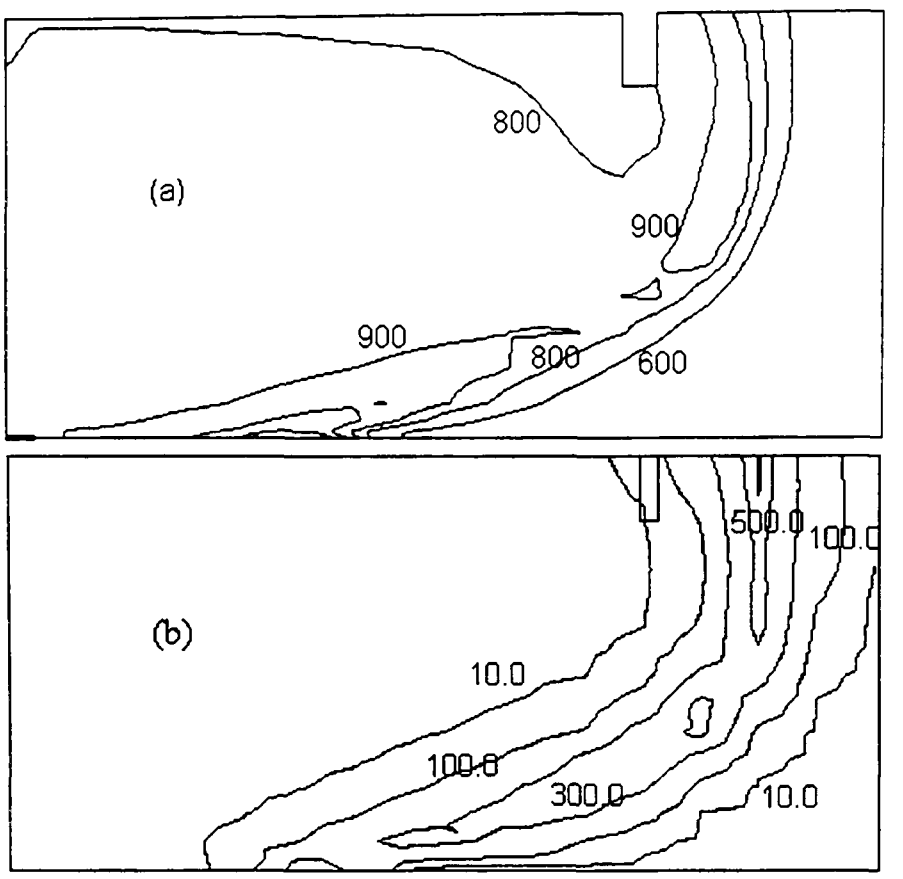

Figure 8.3.11: Contours of temperature and heat release rate of gaseous combustion for case 2 at one second after the door is opened.
(a): temperature contours (unit: K); (b) heat release rate contours (unit: kW/m^3).

After 59 seconds, the door of the compartment is opened suddenly. Oxygen rich air is entrained into the room through the lower reaches of the door while the hot fuel rich gas mixture flows out the room through the upper reaches of the door, under the soffit (see figure (8.3.11a)). Almost immediately, this motion of hot fuel rich gases and cool oxygen rich air re-initiates the combustion process (see figure (8.3.11b)). Figure (8.3.11b) suggests that initially (i.e. one second after the door is opened), gaseous combustion primarily takes place in the upper layer outside the room, in the doorway and in the lower layer just inside the room. This is due to the nature of the mixing process between the hot fuel rich gases leaving the room and the fresh oxygen rich air entering the room. It should be noted that as this is a two-dimensional simulation it represents a compartment in which the door opening is as wide as the compartment. This influences the nature of the entrainment into the compartment - in essence, the flow is unable to entrain air from the sides. This will in turn influence the nature of

the re-initiated combustion front.

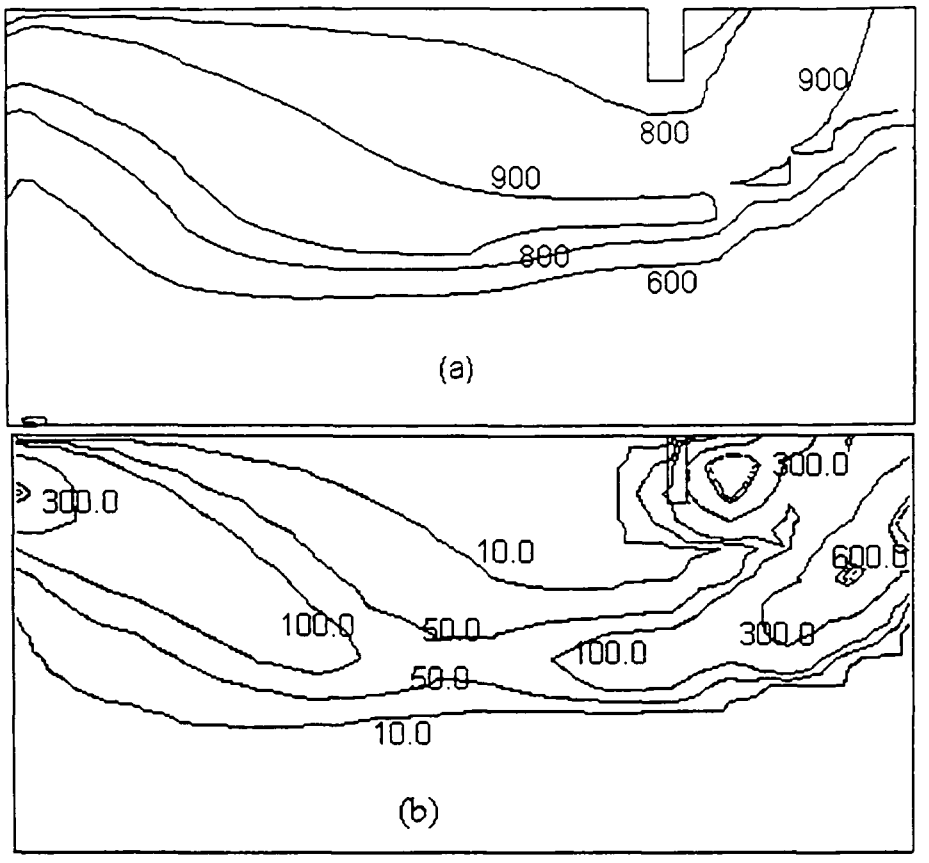

Figure 8.3.12: Contours of temperature and heat release rate of gaseous combustion for case 2 at three seconds after the door is opened.
(a): temperature contours (unit: K); (b) heat release rate contours (unit: kW/m^3).

As a great amount of fuel has accumulated within the compartment (see figure (8.3.10)), the gaseous combustion is tremendously intense. Furthermore, considerable amounts of combustible gases spill out from the top region of the doorway in a very short space of time generating a large combustion region outside the compartment i.e. the flame protrudes from the compartment (see figure (8.3.12)). As oxygen rich air mixes with the fuel rich products of solid combustion within the room, flaming combustion erupts through a greater proportion of the compartment in a matter of seconds (see figure (8.3.12)). These processes result in the marked rapid drop in combustion gases noted in figure (8.3.10).

This type of behaviour is similar in nature to the hazardous phenomenon known as backdraft[Bukowski, 1995; Fleischmann et al., 1994]. If there is insufficient oxygen

to allow flaming combustion to continue, or flashover to occur, the fire will be throttled back and vitiated burning may develop. This is extremely hazardous, for while flaming combustion may be greatly reduced, pyrolysis of the fuel will continue to produce combustible gases within the hot compartment. A sudden in rush of fresh air created by for example, the opening of a door or breaking of a window by a fire fighter, may cause the room to erupt into flame with large flames emerging from the opening posing a significant threat to firefighters [Bukowski, 1995]. This process is known as backdraft.

As in the previous example, while the submodels described here are limited by a simple treatment of radiation and an equally simple treatment of gaseous and solid combustion, the behaviour exhibited by this model is similar to the highly transient behaviour observed in real backdraft cases. Consider for example the series of scale experiments conducted by Fleischmann et al.[1994]. While these experiments involve a different scenario and mechanism of reignition to that described in the above numerical simulation, the nature of the backdraft observed in both cases shares several common features, namely;

a) the reignited flame burns along the front of entrained air;
b) sizeable flames are observed to emerge from the fire compartment due to the motion of the combustible gases as they escape through the open door;
c) flames emerge from within the compartment in an extremely short period of time - approximately two seconds from the opening of the compartment in both the experiments and the presented numerical predictions;
d) once the door to the compartment is opened, there is a rapid drop in the amount of combustible fire products accumulated within the compartment.

As the two-dimensional integrated fire spread model demonstrates promising capacity to predict the broad qualitative features of fire development in a compartment, we now investigate the models' quantitative capabilities through comparing with experimental data of enclosure fire growth and spread involving non-charring(see section 8.4) and charring (see section 8.5) solid fuels. The two-dimensional model can be regarded as a particular case of the three dimensional counterpart since the third dimension is supposed to be 1m long. Therefore there are no special difficulties encountered in extending the two-dimensional model to a situation in three dimensions.

8.4 Simulations of Fire Growth in a Small Compartment—Noncharring Material Involved

Quintiere et al.[Quintiere et al., 1979] conducted a series of fire growth tests within a small compartment using PMMA as the solid fuel. In this section, the integrated fire spread model is used to reproduce the experimental results from a selection of the test series.

The work appearing in this section has appeared in two referred academic publications[Jia et al., 1999b; 1999d], namely the Applied Mathematical Modelling and the Proceeding of the 6th International Symposium on Fire Safety Science (IAFSS).

8.4.1 The experiments

Square slabs of PMMA were burned in a small compartment constructed of low density alumina silica block. The internal dimensions of the enclosure were 0.30m×0.30m×0.56m deep with a doorway height of 0.225m and widths ranging from 0.015 m to 0.285m (see figure 8.4.1). PMMA samples of various sizes were burned, ranging in face area from $0.0025m^2$ to $0.0225m^2$ with a constant thickness of 0.013m. The PMMA was burned on a platform 0.03m above the floor and centred 0.40m from the doorway. The weight was continuously recorded by a load cell that supported the platform. Two bare chromel-alumel thermocouples were used to measure the upper gas and ceiling temperatures (see figure (8.4.1)). The ceiling thermocouple was pressed flush into the surface. A water-cooled heat flux sensor was used to record the incident heat flux to the floor. Pressure differences across the compartment wall were measured using an electronic manometer.[Quintiere et al., 1979]

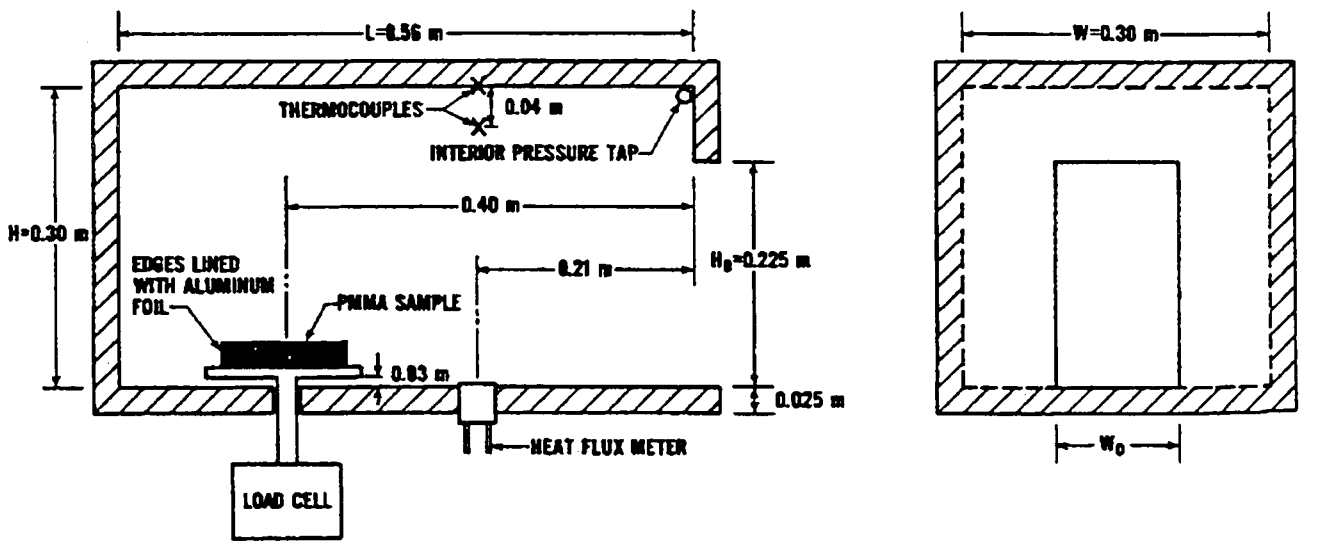

Fig. 8.4.1: The experimental arrangement (from [Quintiere et al., 1979]).

8.4.2 The simulations

The burning of the PMMA square samples is simulated by the noncharring pyrolysis

model described in section (7.4.1). The material properties used in the simulations take the values provided by Quintiere et al.[Quintiere et al., 1979]. They are: ρ = 1192.0 kg/m^3, c = 1460.0 J/(kgK), λ = 0.19 W/(mK), T_p = 636.0 K, L = 1008.0kJ/kg.

The radiative heat transfer is modelled by the six-flux radiation model. The calculation of the absorption coefficient of the hot air in the upper layer follows the suggestion of Quintiere et al.[Quintiere et al., 1979], that is,

$$k_g = 0.30+4.64\,\dot{m}_b\,(\dot{m}_a + 0.6\,\dot{m}_b). \tag{8.4.1}$$

The soot absorption coefficient is evaluated using the expression proposed by Yuen and Tien [Yuen and Tien, 1977],

$$k_s = aT/T_m \tag{8.4.2}$$

where a takes the value of 1.3 m^{-1} which is the flame absorption coefficient and T_m is 1400.0K which is the average temperature of the flame temperature. Both a and T_m were given by Quintiere et al. The total absorption coefficient of the soot-gas mixture is given by

$$k = k_s + k_g. \tag{8.4.3}$$

The convective heat transfer coefficient of the walls and ceiling is calculated using the expression [Quintiere et al., 1979],

$$h_w = 1.44(\dot{m}_b\,\Delta H)^{1/3}\ . \tag{8.4.4}$$

The floor convective heat transfer coefficient is 10 which was suggested by Quintiere et al. The walls, ceiling and floor are treated as conductive regions with properties given by ρ_w = 260kg/m^3, k_w = 0.14W/mK. The thickness of the wall, ceiling and floor

is 0.025m.

The smaller PMMA samples combined with the narrower door openings produce laminar-like flame plumes. However, the gas-phase combustion model is based on the turbulent dissipation concept. Thus, only the two larger sample sizes of $0.0225m^2$ and $0.0156m^2$, and four larger door openings of 0.285m, 0.185m, 0.115m and 0.077m, are selected for simulation. As a result a total of seven tests were simulated.

The platform where the PMMA samples were placed is treated as a nonconducting region. As no information concerning the surface area of the platform was available, the platform is assumed to have the same surface area as the sample in each individual test. The actual height of the platform is 0.03m. Since surface regression of the samples is neglected, the platform height is assumed to be 0.043m that is the sum of the actual platform height and the thickness of the sample.

The computational meshes used in these simulations for the flow domain vary with the individual test. The maximum number of cells used in these simulations consisted of 17×16×32 while the minimum number of cells consisted of 15×16×30. The mesh used in one of the simulations is presented in figure (8.4.2).

The discretisation of the PMMA sample is dependent on the size of the sample. The surface of the PMMA sample was discretised using either 5x5 cells (small sample) or 7x5 cells (larger sample). In each case, a cell thickness of 0.2mm was used as recommended in section (7.5.2) resulting in 65 cells through the thickness of the sample.

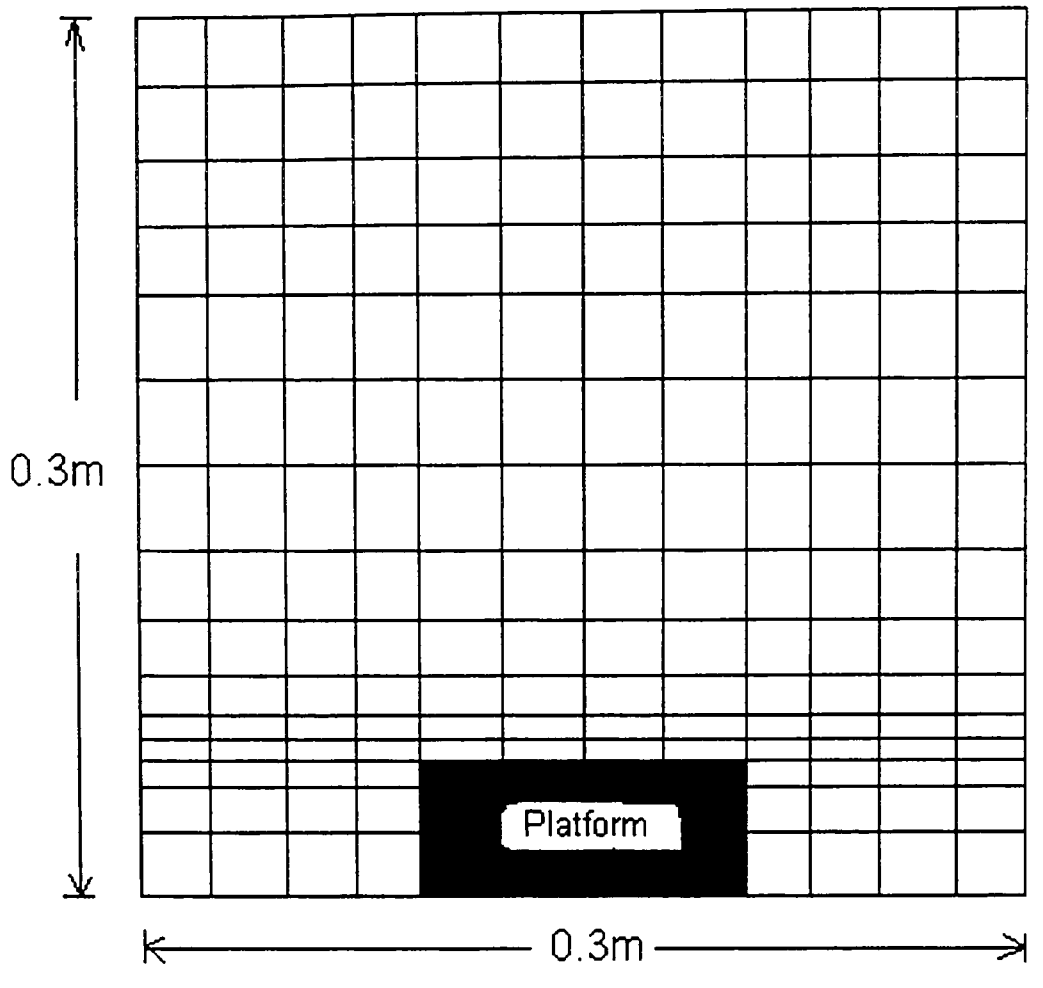

(a)

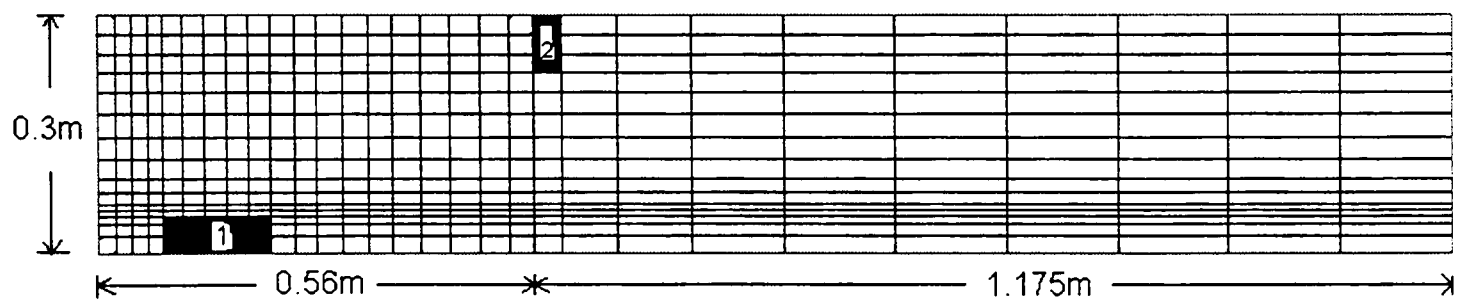

(b)

Fig. 8.4.2: The mesh used in one of the simulations.
(a): the mesh in xy plane; (b) the mesh in yz plane.
The black regions in (b) represent solid regions:
1) the platform to support the PMMA sample; 2) the soffit of the compartment.

8.4.3 Simulation results and discussion

The numerical predictions and corresponding experimental results are presented in table (8.4.1). The experimental values presented in table (8.4.1) refer to average values of the variable concerned, as measured during the period of maximum steady

burning. In addition to these maximum values, their deviation during this period is also listed. The corresponding numerical predictions listed in table (8.4.1) are determined in a similar way. In table (8.4.1), the experimentally derived rate of entrained air flow was calculated by Quintiere et al. using other measurements such as upper layer gas temperature, PMMA mass loss rate and the pressure rise across the compartment wall. The numerical predictions for the entrained air rate presented in table (8.4.1) are determined by summing the mass flow rates into the compartment throughout the open doorway.

Table 8.4.1: Comparison of numerical predictions with experimental results.

Test No.		31A	14A	30A	23A	29A	22A	27A
Door Width (m)		0.077		0.115		0.185		0.285
Fuel Area (m^2)		0.0156	0.0225	0.0156	0.0225	0.0156	0.0225	0.0225
$\dot{m}_v$ g/s	Pred.	0.69	0.759	0.848	1.1	1.0	1.39	1.69
	Exp.	0.79	0.875	1.0	1.225	0.908	1.5	1.56
T_g °C	Pred.	853	869	990	906	1136	1056	1050
	Exp.	910±50	902±50	993±25	902±50	973±25	950±75	1022±25
T_w °C	Pred	750	823	906	823	813	807	820
	Exp.	865±50	854±35	937±25	854±50	863±25	902±50	$925 \pm^{25}_{50}$
$\dot{q}''_F$ W/cm^2	Pred.	6.7	9.04	11.55	9.07	8.49	8.40	9.09
	Exp.	9.88±.65	8.05±1.2*	11.0±0.8	9.62±.78	$8.45 \pm^{1.0}_{2.6}$	10.8±.78	10.4±1.3
Δp N/cm^2	Pred.	1.56	1.57	1.65	1.64	1.71	1.79	1.69
	Exp.	[0.72±.2]	1.8±.12	[1.0±.2]	2.24±.08	[1.16±.08]	1.88±.08	1.92±.12
$\dot{m}_a$ g/s	Pred.	3.45	3.46	5.18	5.0	7.89	7.42	11.01
	Exp.	--	2.53	--	7.26	--	7.29	11.9
HRR kW	In	9.62	9.56	13.89	13.69	18.97	20.08	25.96
	Out	4.96	6.09	5.13	7.68	4.46	8.99	10.35

Note:
$\dot{m}_v$ is the average mass loss rate in the period of maximum steady burning; T_g is the gas temperature in the upper layer temperature; T_w is the ceiling temperature; $\dot{q}''_F$ is the incident heat flux at the floor; Δp is the pressure rise across the compartment wall; $\dot{m}_a$ is the rate of the entrained air flow and HRR is the heat release rate of the gas-phase combustion.
[]:pressure tap clogged; *: water coolant hose melted.

As can be seen from table (8.4.1), the agreement between the predicted and corresponding measured values are good. Some differences occur, for instance, for the

pressure rises of test 29A, 23A, 30A and 31A. However, among the tests except for test 23A, the measured pressure rises are not reliable due to pressure taps being clogged. For the other three tests (14A, 22A and 27A), the predicted pressure rises are close to the measured ones.

Given the range of measurement errors in the experimental results, the general trends predicted by the numerical model appear to follow those produced in the experimental results. These trends concern the change in T_g and $\dot{q}''_F$ as the door width is kept constant but the fuel size is increased and conversely when the fuel size is kept constant and the door width is increased.

For the tests with doorway width of 0.115m (i.e. tests 30A and 23A) and 0.185m (i.e. 29A and 22A), the predicted and measured upper layer gas temperatures and the heat flux at the floor for fuel surface area of $0.0156m^2$ (i.e. tests 30A and 29A) are generally greater than the predicted values for fuel face area of $0.0225m^2$ (i.e. 23A and 22A). At first sight this may be contrary to expectation, as the larger fuel sample would be expected to produce the higher temperatures and heat fluxes. As explained below, this phenomenon may result from the combustion regime involved in these cases and hence the diluting effects of the unburnt solid degradation products. The combustion process taking place in these cases is ventilation controlled, this can be seen by close inspection of figures (8.4.3) to (8.4.5).

The transient history of the mass loss rate and heat release rate within and outside the compartment for test 22A is depicted in figures (8.4.3) and (8.4.4). Only the results for test 22A are presented as the results for the other test cases are similar in nature. Note

the rapid increase in heat release rate within the compartment (see figure (8.4.4)) and the corresponding rapid increase in mass loss rate (figure (8.4.3)). However, as the heat release rate reaches a maximum, quasi-steady value, the mass loss rate continues to increase steadily. As this is occurring, the rate of air flow entrained into the compartment also remains nearly constant (see figure (8.4.5)).

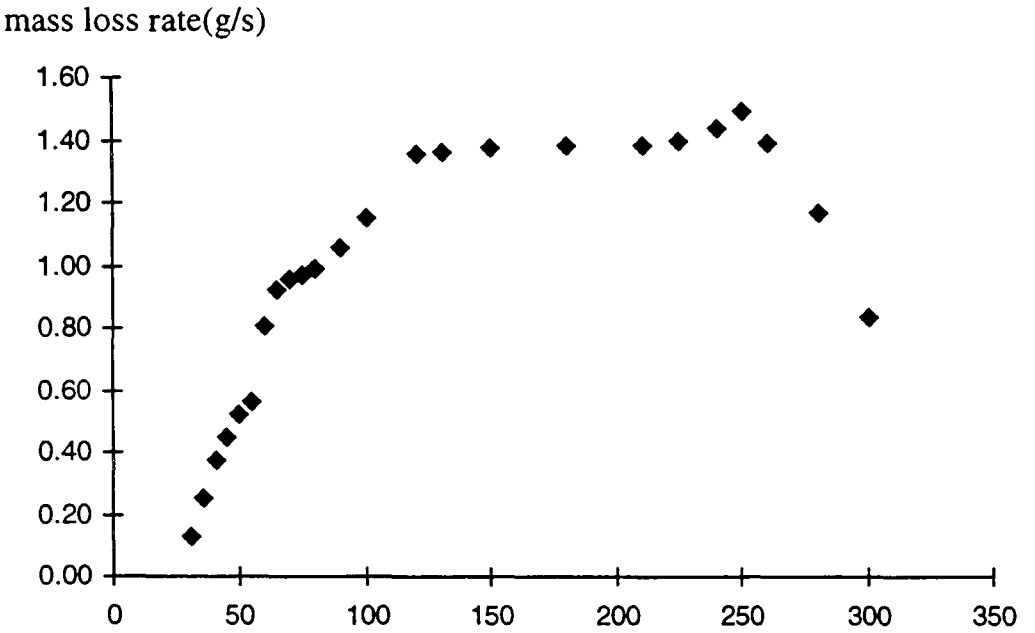

Fig.8.4.3: Predicted mass loss rate vs. time for the test conditions with 0.185m doorway width and 0.0225m^2 PMMA sample (i.e. test 22A).

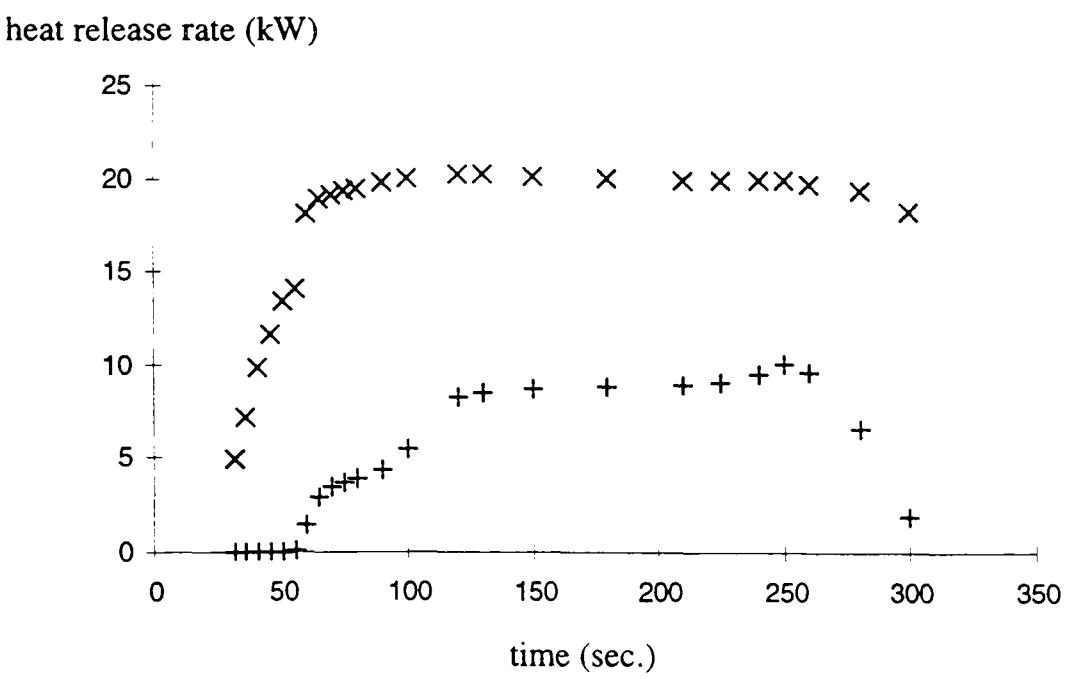

Fig.8.4.4: Predicted heat release rate within (symbol: x) and outside (symbol: +) the compartment for test conditions with 0.185m doorway and 0.0225m^2 PMMA sample (i.e. test 22A).

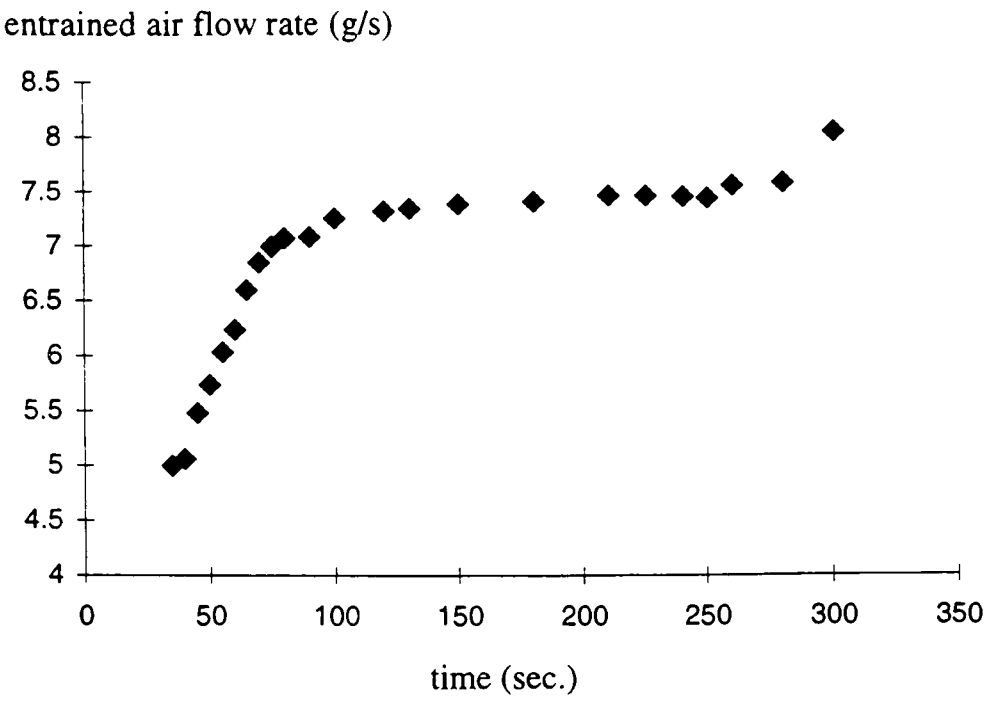

Fig. 8.4.5: Predicted rate of entrained air flow vs. time for the test conditions with 0.185m doorway width and 0.0225m^2 PMMA sample (i.e. test 22A).

These occurrences suggest that the fire is ventilation controlled. As described by Quintiere et al.[1979], "...so much fuel is vaporised that it can not be burned within the compartment due to insufficient oxygen. This excess fuel serves to dilute the products of combustion and hence to reduce the temperature and rate of heat flux received by the fuel surface from the compartment." For the same doorway width, the larger fuel sample produces more combustible volatiles. Consequently, the effect of dilution due to unburned vaporised fuel is also greater and causes a lower upper layer gas temperature and heat flux at the floor. The numerical predictions also show that slightly more fresh cool air is entrained into the compartment ($\dot{m}_a$) for the tests using smaller samples, which also helps to reduce the upper layer temperature.

However, for the tests with 0.077m doorway width (i.e. tests 31A and 14A), the cooling effect due to unburnt pyrolysis products is not great enough as the mass loss rates are not sufficiently large. As a result, the test using the larger sample (i.e. test 14A) creates higher upper layer temperatures and heat flux at the floor than the test

with the smaller sample size (i.e. test 31A).

Another interesting observation from figures (8.4.3) and (8.4.4) concerns the onset and development of "flashover" type conditions. Within a very short time period, the mass loss rate and heat release rate within the compartment undergo rapid increases. The end of this short growth period approximately corresponds to when the flux of entrained fresh air into the compartment reaches a steady state. At this stage the amount of entrained fresh air limits the burning rate and the combustion within the compartment becomes ventilation controlled. While this is occurring, the mass loss rate continues to increase steadily. As a result the heat release rate within the compartment remains nearly constant while the heat release rate outside the compartment continues to increase (see figure (8.4.4)) suggesting flames emerging from the compartment. All these observations are consistent with the flashover phenomena.

After the heat release rate within the compartment reaches a steady state, the mass loss rate from the solid fuel continues to increase until it attains a quasi-steady state. At this point, the heat release rate outside the compartment also maintains a quasi-steady state. This is to be expected as the total heat release rate of the gas-phase combustion is controlled by the generation rate of the combustible vapour which is approximately constant during this period. Eventually, the heat release rate of the internal fire begins to diminish as the fuel is exhausted, note however, that the external combustion is exhausted prior to the internal combustion.

The computer generated fire development described above corresponds to the classic

description of compartment fire development. After ignition, an initial growth period is followed by a rapid transition (or flashover) into the fully developed fire. The fully developed fire is characterised by a steady burning fire within the compartment with flames emerging from within the compartment. Such fires are often ventilation controlled. Finally, as the combustible fuel is exhausted, the fire enters the decay phase.

According to Babrauskas[Babrauskas, 1980] and Thomas[Thomas, 1981], the energy release rate required for flashover in a compartment is estimated by,

$$Q = 750 A_o \sqrt{H_o}\,, \tag{8.4.5}$$

or

$$Q = 0.78 A_T + 378 A_o \sqrt{H_o} \tag{8.4.6}$$

where A_T is the total internal surface area.

These equations suggest that for a small scale compartment, such as the one used in these experiments (0.56m×0.3m×0.3m), conditions suitable for the development of flashover may easily develop due to the low heat release rate required. For the test with 0.185m door width, the heat release rate required for flashover is 14.8kW and 14.1kW respectively estimated from equations (8.4.5) and (8.4.6). Although the scale of the small compartment concerned here may be out of the range applying equation (8.4.5), the figure calculated from it can provide a reference to the condition required for flashover. The simulation predicted approximately 12kW of the heat release rate at the onset of the flashover assuming that flashover is defined by the short transition from a fuel controlled fire to a ventilation controlled fire. This low level of heat

release rate is consistent with the estimations from equations (8.4.5) and (8.4.6).

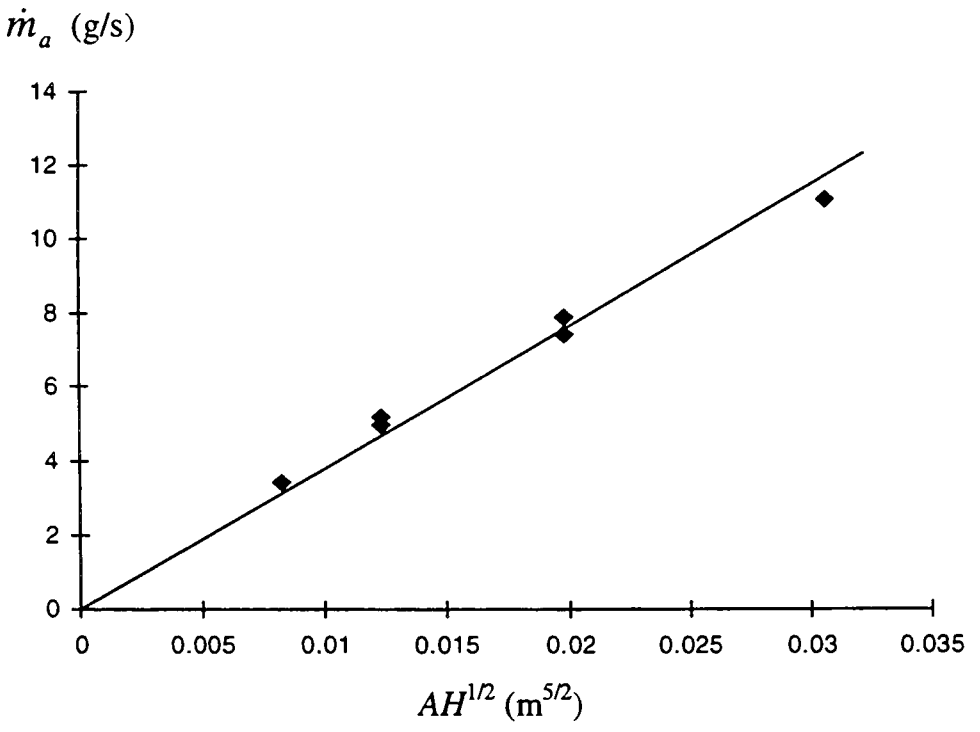

Fig.8.4.6: The rate of air flow entrained into the compartment vs. the ventilation factor. diamond: predicted values; straight line: the best fit line.

Using data generated from the numerical predictions, it is possible to suggest a relationship between the predicted entrainment rates and the ventilation factor $A_oH_o^{1/2}$ for the compartment. The predicted rates of entrained air flow versus the ventilation factor $A_oH_o^{1/2}$, where A_o is the area of the door opening and H_o is the height of the door are plotted in figure (8.4.6). The entrained air flow rates are determined during the period of maximum steady burning and hence are in the post-flashover phase of fire development. The figure strongly suggests a proportional relationship for post-flashover fires between the rate of entrained air flow and the ventilation factor. The same trend for post-flashover fires was shown by Rockett[1976]. He calculated the constant of proportionality to be in the range 0.4 to 0.61 $kg/sm^{5/2}$ depending on the selected discharge coefficient for the opening. Using the line of best fit in figure (8.4.6), we determine the constant of proportionality to be 0.38 $kg/sm^{5/2}$. This value is very close to the lower limit obtained by Rockett. Therefore, the entrained air rate at the post-flashover stage can be approximately expressed as

$$\dot{m}_a = 0.38 A_o H_o^{1/2} \tag{8.4.7}$$

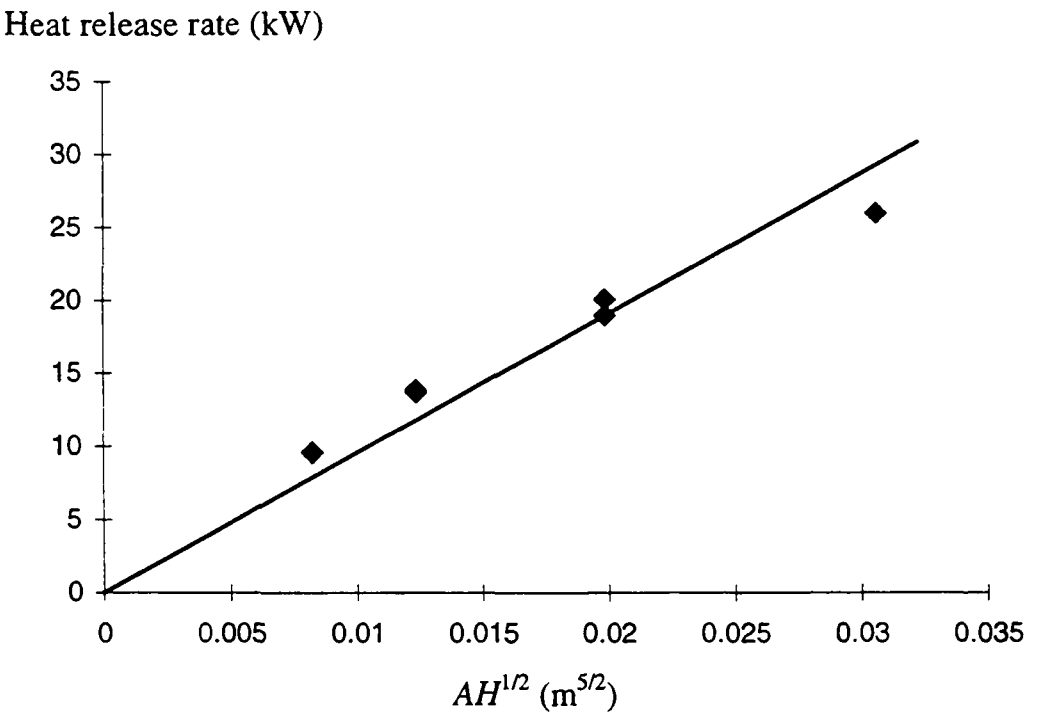

Fig. 8.4.7: The heat release rate of gas-phase combustion within the compartment predicted by the gas-phase combustion model versus the ventilation factor.
diamond: predicted values; straight line: the best fit line.

Since the rate of air flow entrained determines the combustion rate within the compartment and the heat of combustion per unit mass of air consumed is approximately constant by assuming constant oxygen concentration(23%) in air, the heat release rate due to combustion within the compartment at a steady state is, like the rate of air flow entrained, expected to have a linear relationship with the ventilation factor. Figure (8.4.7) plots the heat release rate of gas-phase combustion predicted by the gas-phase combustion model versus the ventilation factor. It demonstrates that a nearly linear relationship exists between the predicted heat release rate and the ventilation factor.

Finally, table (8.4.1) demonstrates that the predicted heat release rates within the compartment are very similar for those tests with different size samples but with the same doorway width. This is to be expected as the predicted entrained air flow rates

for tests with the same door width are very similar. As the rate of entrained air establishes an upper limit on the burning rate within the compartment, similar rates of the entrained air flow result in similar heat release rates within the compartment. However, the predicted heat release rates outside the compartment increase with increases in sample size for a given doorway width. This is because the tests with larger samples release more combustible gases than the tests with the smaller samples. While more gases are released, as discussed above only a certain amount of gas can be consumed within the compartment. Consequently, the excess combustible gases are vented out of the compartment where they burn on contact with the abundant ambient oxygen, resulting in a greater heat release rate outside for the tests with larger samples.

8.5 Simulation of Fire Spread within an Enclosure—Charring Material Involved

Several small scale tests simulating fire in a compartment were carried out specially for the purpose of this study by the Fire Research and Development Group, Home Office Fire Experimental Unit with the assistance of the author. The objectives of the tests were to obtain experimental data of fire spread over ceiling lining material within a small-scale compartment. These data were used to verify the integrated fire spread model developed in this thesis. This section will describe the experiments and report the simulation results for the tests.

A paper[Jia et al., 1999e] concerning this work will appear in the referred academic journal—the Journal of Applied Fire Sciences.

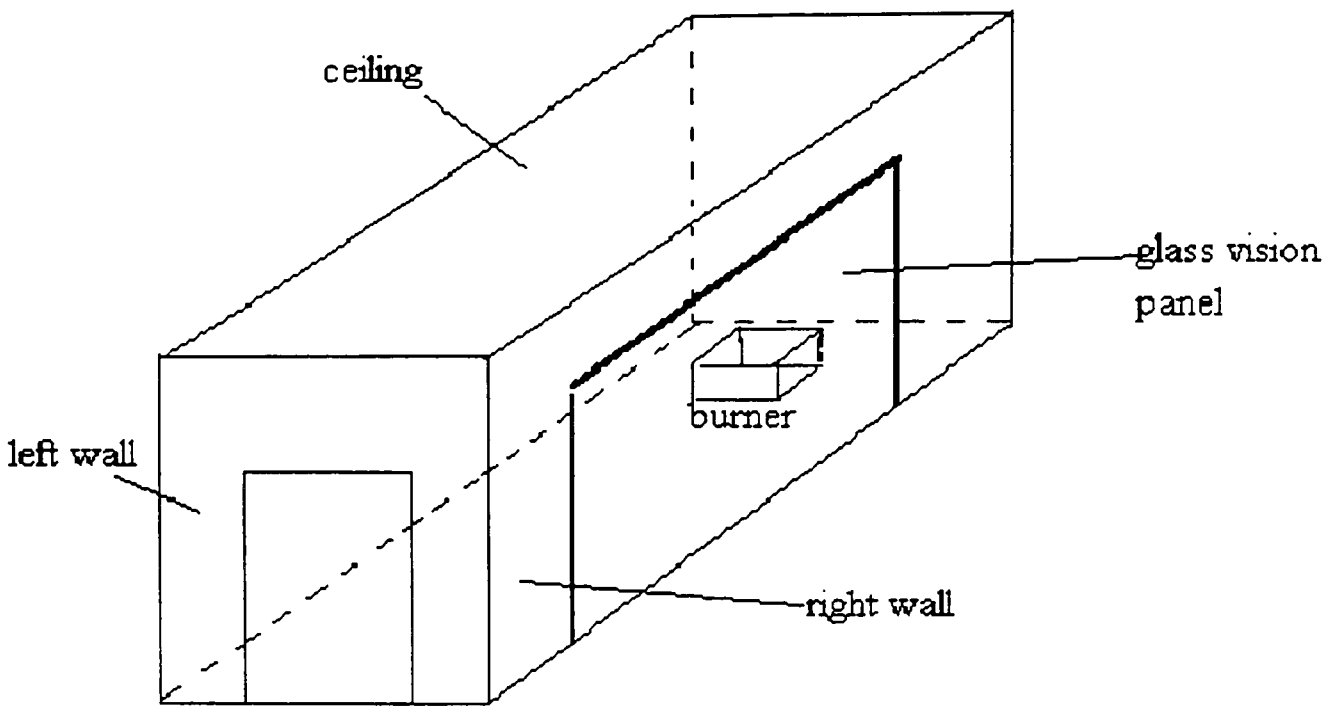

Fig. 8.5.1: The schematic view of the half scale compartment.

8.5.1 Description of the experiments

The fire spread tests were conducted in a specially designed half-scale compartment. The internal dimension of the compartment is 1.2m(wide)×1.2m(high)×2.4m(long). Figure (8.5.1) shows the schematic of the half scale compartment. The compartment had a door located in the end wall opposite the fire measuring 0.38m (wide) × 0.99m (high), the door was open throughout the experiment. The 6mm thick glass vision panel is 1700mm long by 961mm high. The inside walls were covered with silver fire blankets. A methane burner was placed inside a steel tray 300mm×300mm×150mm which was mounted on legs 150mm high. It was centrally placed 17.5cm away from the rear wall. A sheet of 18mm thick standard chipboard was suspended beneath the ceiling of the compartment. The chipboard was 98cm wide by 235cm long. It was 113cm high from the floor and the left edge of the chipboard sheet was against the left wall. Strengthening battens were fixed to the back of the sheet to prevent warping or sagging of the wood. To prevent flame spread around the edges of the wood, fibre

blankets was used to pack between the wood and compartment walls.

A thermocouple tree with five thermocouples labelled from TCT1 to TCT5, was placed at the corner 40cm from the front wall and 20cm from the left wall. The heights of the five thermocouple are 20cm, 40cm, 60cm, 80cm and 100cm. To measure the temperature in the hot layer, two thermocouples labelled as TCH1 and TCH2 respectively were installed along the centreline of the chipboard. They were 10cm below the ceiling and 140cm and 80cm away from the front wall respectively. Another four thermocouples were installed close to the left wall. Two of them labelled as TCLW1 and TCLW2 were 30cm away from the left wall, 90cm away from the rear wall and 60cm and 100cm high respectively. The other two thermocouples labelled as TCLW3 and TCLW4 were 20cm from the left wall, 120cm away from the rear wall and 60cm and 100cm high respectively. Six thermocouples labelled here from TCW1 to TCW6 were used to measure the temperature within the chipboard. They were equally spaced along the centreline of the chipboard at 0.39m, 0.78m, 1.17m, 1.56m, 1.95m and 2.33m from the rear wall. Each of the thermocouples was fixed at a depth of 2mm from the front surface using a small amount of glue and sawdust.

Six radiometers were used to measure the radiation heat fluxes at different positions and orientations. They are labelled as RAD1, RAD2, RAD3, RAD4, RAD5 and RAD6. The locations of the radiometers are plotted in figure (8.5.2). All the radiometers faced up to the ceiling except RAD5. RAD5 faced to the fire. RAD1, RAD2 and RAD3 were 21 cm high from the floor. RAD4 was 20 cm away from the right wall, RAD5 was 30 cm from the left wall and RAD6 was 20 cm from the left wall.

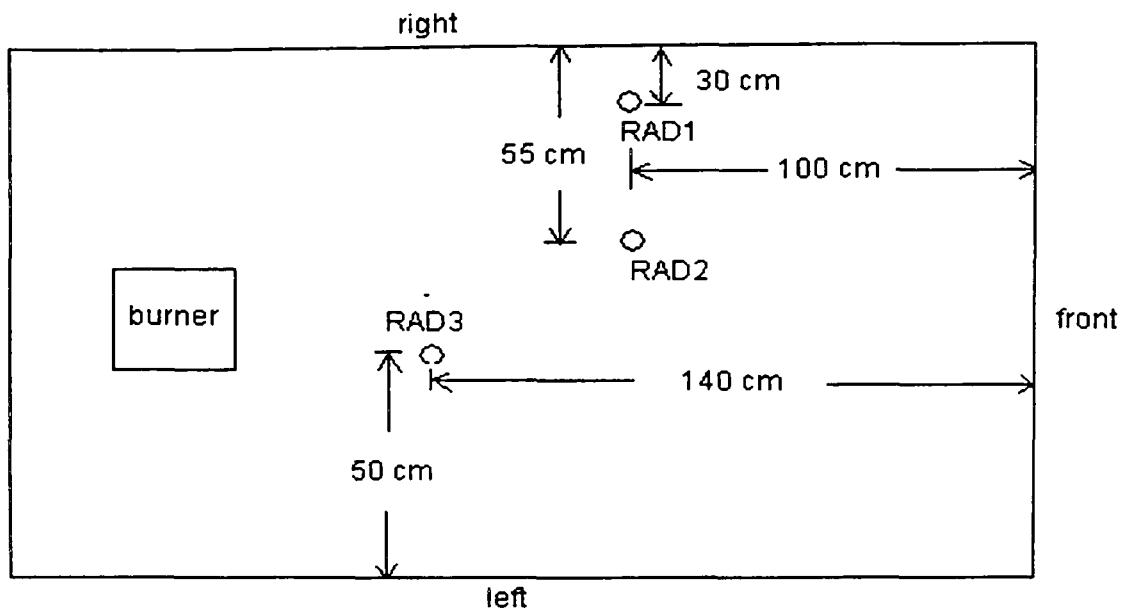

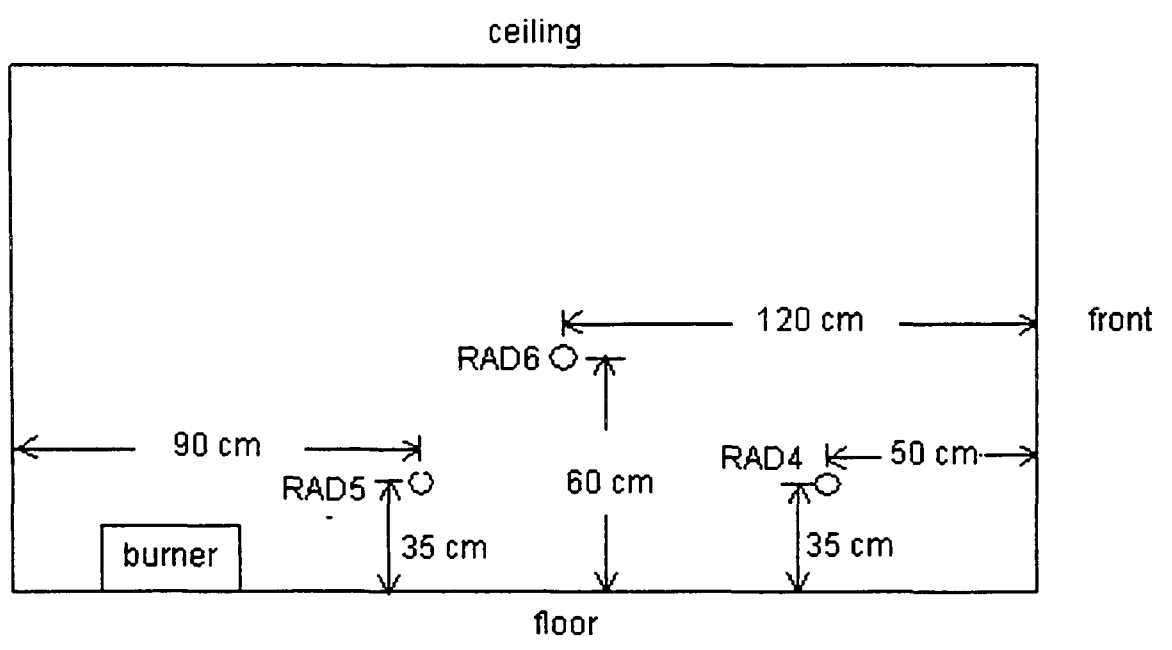

Fig 8.5.2: The locations of the radiometers.

A total of five tests were conducted. The first three tests were tentative to find the suitable burner power for this small-scale compartment for safety reasons. Finally it was decided to use a burner output of approximate 48kW. Test 4 was the first test with the 48kW burner. In order to check the reproducibility of the experiment an extra test(test 5) was conducted with the same burner power. Very good agreement between the measurements was obtained for test 4 and test 5. Test 5 was chosen for simulation purpose and the results of the simulation are compared with the experimental data.

8.5.2 Simulation of the test

The integrated fire spread model described in section 8.2 is used for the simulation. Some specifications for this particular simulation are outlined here.

The walls of the compartment are assumed adiabatic since they are well insulated by fire blankets. The glass vision panel and the floor are modelled as conduction regions. The glass temperature is calculated by solving the discretised conduction equation for the glass while the floor temperature is calculated by using the integral method described in section 6.2.3(equations from (6.2.3.20) to (6.2.3.22)).

The burner is simulated as a volumetric heat source of approximately 48kW. The burner is represented by a rectangular heat source of surface area equal to that of the burner used in the experiment.

The six-flux model and the discrete transfer method(DTM) are used to calculate the radiative heat exchanges. The DTM made use of 54 rays. The absorption coefficient of soot is evaluated by equation (5.4.10)

$$\kappa = a f_v T \qquad (5.4.10)$$

where a takes the value of 1275.95 which was determined from previously published experimental data of soot concentration and the absorption coefficient from wood fires[Yuen and Tien, 1977; Hubbard and Tien, 1978], f_v and T are the soot volume fraction and the temperature of the soot-gas mixture predicted by the model at a point of space. A scalar variable for the soot concentration is used and the soot concentration is calculated from the soot model described in section 5.2.3. The

absorption coefficient of water and CO_2 is given by equation.(5.4.3)

$$\alpha_g = 0.1(m_c + m_w) \tag{5.4.3}$$

where m_c and m_w are the mass concentration of CO_2 and H_2O respectively.

The mass loss of the chipboard is simulated using the charring pyrolysis model described in section 7.4.2, i.e., the equations from (7.4.2.1) to (7.4.2.9). The material properties of chipboard are selected from the literature[Yan and Holmstedt, 1996; Delichatsios and Chen, 1994]. The properties used in the simulation are:

$\rho_v = 670$ kg/m^3, $C_v = 3000$ J/kgK, $\lambda_v = 0.22$W/mK, $\lambda_c = 0.17$ W/mK, $T_p = 590$ K and the pyrolysis heat of 1.3 MJ/kg.

Although smouldering combustion may occur at the initial ignition stage, it is very difficult to simulate this process in the current model. A simple treatment to account for this is to slightly reduce the pyrolysis temperature, to allow combustible gases released slowly when the solid is being exposed to low external heat fluxes. Thus, the pyrolysis temperature of the solid material in the area directly above the burner is reduced from 590K to 550K and it is kept at this value throughout the simulation.

The flow domain mesh used in the simulation is presented in figure (8.5.3). It is comprised of 13,320 cells (20 (w) × 18 (h) × 37 (l)). It is not uniformly distributed with refinement near the walls and the ceiling. The set-up of the mesh in the combustible solid region has been described in section (8.2). It consisted of a mesh of 26,880 cells (16 (w) × 28 (l) × 60 (d)) with a cell thickness 0.02cm.

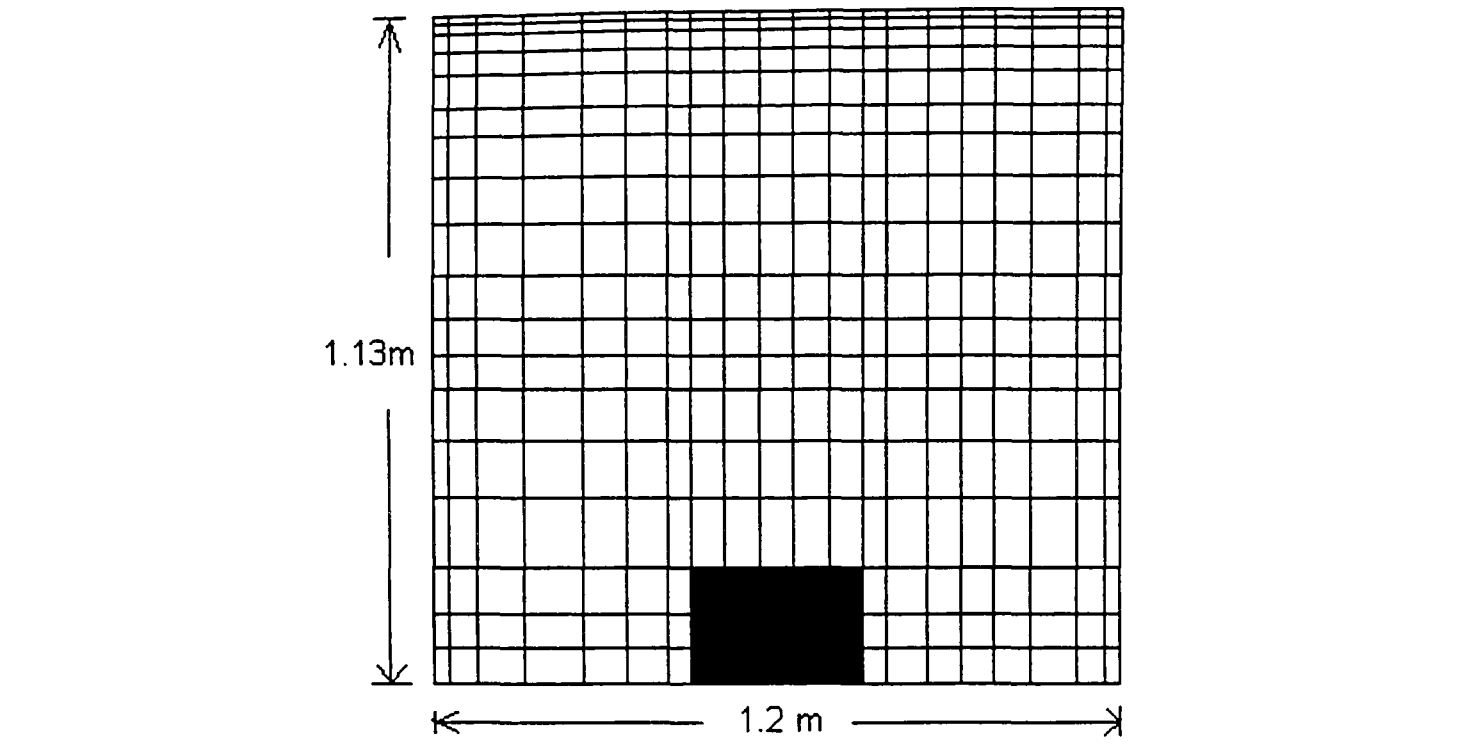

Fig. 8.5.3: The mesh used in the simulation.
(a) The mesh in the xy plane. (b) The mesh in the yz plane.
The black regions in (a) and (b) represent the burner position.

There are several uncertainties in the simulation. Firstly, the walls and the floor of the compartment were made from composite materials. The heat losses through them are quite difficult to model. Since the walls are protected by fire blanket covered by silver films, the walls are assumed well insulated and are modelled as adiabatic boundary conditions. This treatment is somewhat unrealistic and may result in faster fire spread. However, given the uncertainties and complications involved in performing any other treatments, this appears to be expedient. Secondly, the heat losses through the glass panel may be substantial. Although conduction loss is simulated, the radiative loss due

to its transparency is not easily handled. Thirdly, the chipboard properties used in the simulation are found from the literature. They may be not suitable to the particular material used in the test.

Under these uncertain circumstances, qualitative agreement between the experiment and the simulation is first expected. Quantitative agreement may be considered to be fortuitous.

8.5.3 Results and Discussion

The fire spread within the test compartment progressed through four distinct stages – preheating, ignition and rapid spread, fully developed and finally decay. The process of fire spread in the compartment may be represented by the history of the upper layer temperature as measured by the two thermocouples suspended just beneath the ceiling, TCH1 and TCH2(see figure (8.5.4)). The preheating stage lasted approximately 9 minutes. During this phase only the burner was active within the compartment, with no involvement of the ceiling material. The ignition stage was very short and was followed by a rapid spread of fire. It took approximately one minute for the fire to reach its peak. Figure (8.5.5) is a photograph taken at a moment of the peak stage. Large flames compared to the scale of the compartment were seen emerging from the open compartment door(see figure (8.5.5)). The fire remained at its peak for approximate one to two minutes and then began to decay. The decay stage lasted approximately one and a half minutes. The total test time was almost 14 minutes.

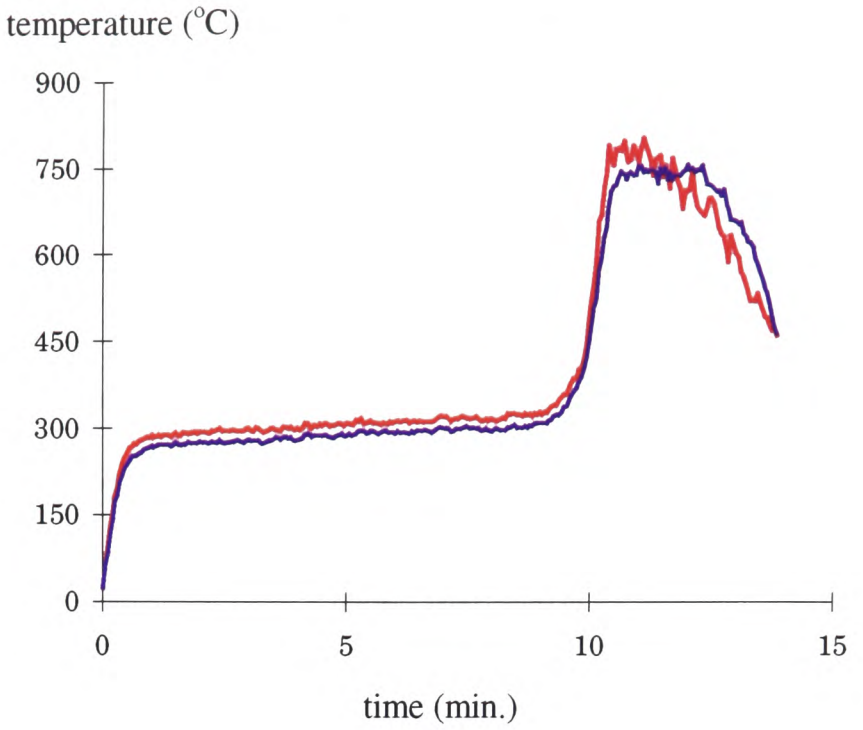

Fig. 8.5.4: the measured upper layer temperatures.
red line: measured by TCH1; blue line: measured by TCH2.

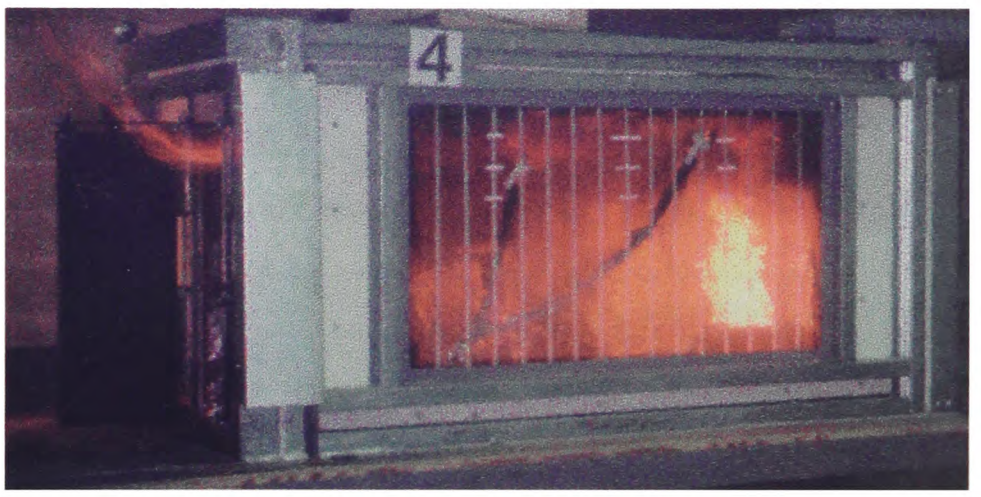

Fig. 8.5.5: a photograph taken at a moment of the peak stage.

Figure (8.5.6) depicts the measured and predicted upper layer temperatures. Table (8.5.3.1) displays the comparison of the predictions with the measurements for the peak values of TCH1 and TCH2 and the time to ignition. As can be seen, the simulation qualitatively reproduced the progress of the fire spread within the compartment. In the preheat stage the predicted temperatures agree very closely with the measured values. The peak temperatures are also reasonably close to the measured peak values. In addition, the predicted time to ignite the chipboard agrees very well with the experimental observation.

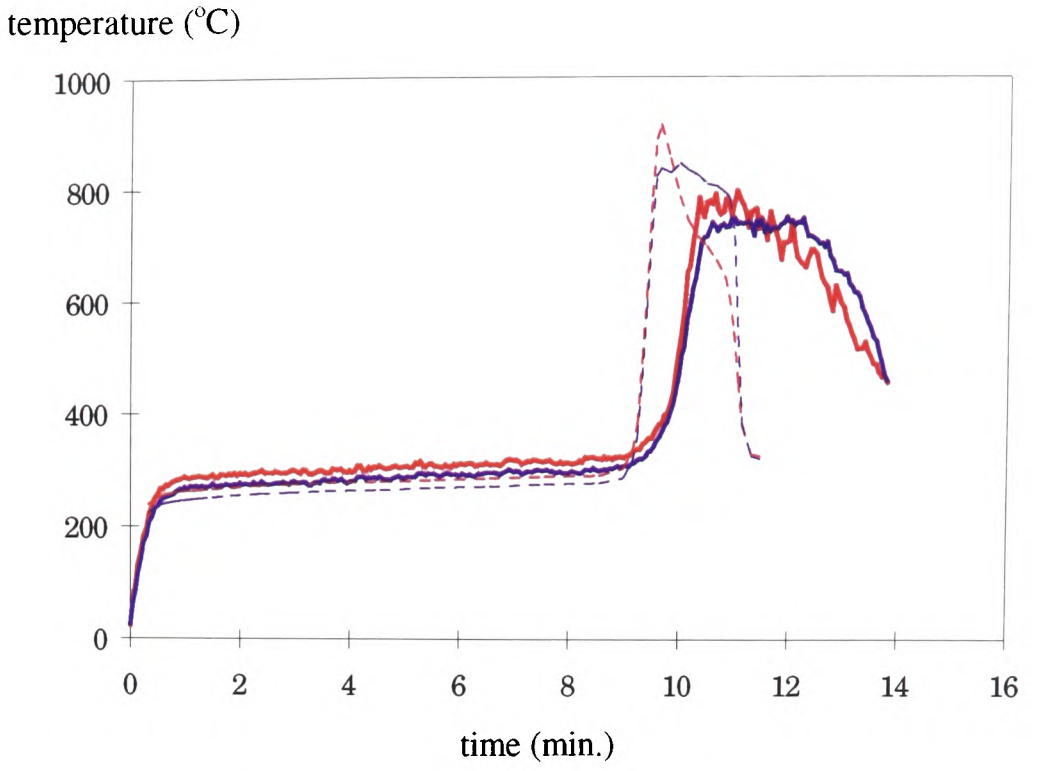

Fig. 8.5.6: the predicted and measured temperature curves
at the positions of TCH1 and TCH2 in the upper layer.
red: temperatures at TCH1 position; blue: temperatures at TCH2 position.
solid: measured; broken line: predicted.

Table 8.5.3.1. The time to ignition and peak temperatures
at thermocouple locations TCH1 and TCH2.

	Measurements	Predictions
Approximate time to ignition	9.6 min	9.2 min
Approximate peak temperature of TCH1	800°C	910°C
Approximate peak temperature of TCH2	750°C	850°C

For the first 11.5 minutes, the experimental measurements suggest that temperatures measured by TCH2 are lower than those measured by TCH1. This is consistent with the relative locations of the thermocouples, with TCH2 being located further away from the gas burner and the point where the fire first takes hold of the ceiling material. However, as the fire spreads forward along the ceiling, temperatures measured by TCH2 increase, and eventually exceed those measured by TCH1. In addition, temperatures at TCH2 remain at the their peak value longer than those at TCH1. While these trends are reproduced by the numerical prediction, the simulated fire appears to spread more rapidly than the real fire. Furthermore, the simulated fire appears to decay

earlier and more rapidly than the real fire. During the decay phase, both the experiment and the numerical prediction indicate that temperatures measured at TCH1 decrease more rapidly than TCH2.

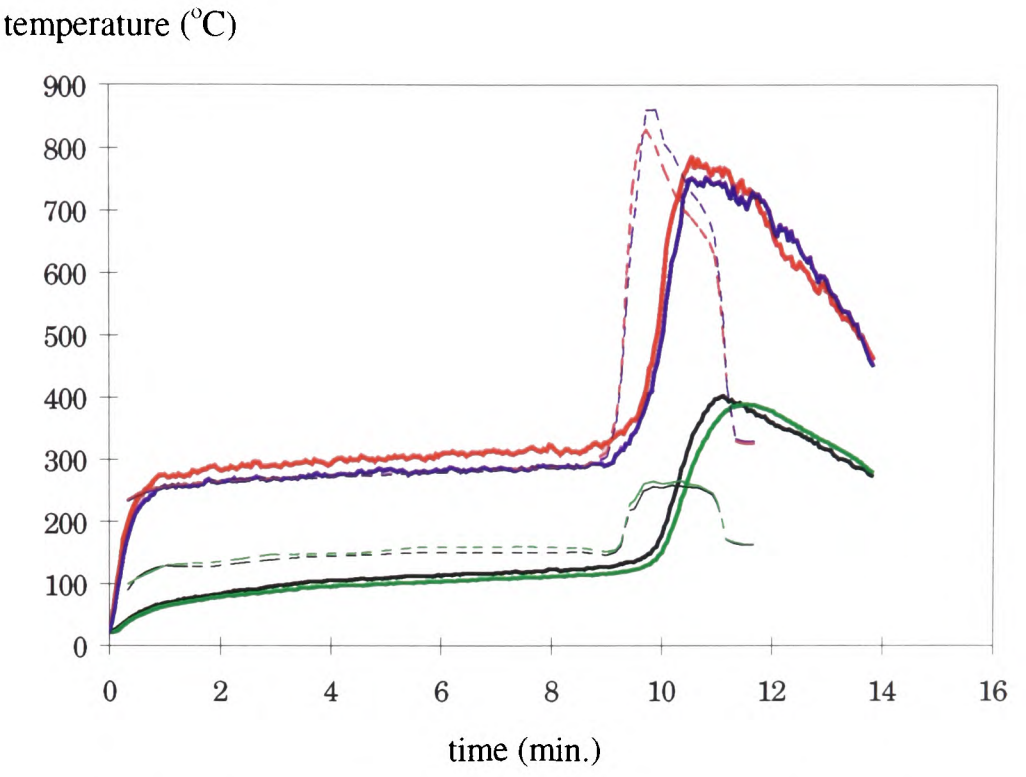

Fig. 8.5.7: the temperature curves at the positions of TCLW1 to TCLW4.
red: TCLW2; black: TCLW1; blue: TCLW4; green: TCLW3.
solid: measured; broken: predicted.

Table 8.5.3.2. Peak values of temperatures measured and predicted at thermocouple locations TCLW1—TCLW4.

	Measured Temperatures (°C)	Predicted Temperatures (°C)
Approximate peak value of TCLW1	400	260
Approximate peak value of TCLW2	780	830
Approximate peak value of TCLW3	390	265
Approximate peak value of TCLW4	750	860

The curves in figure (8.5.7) represent the measured and predicted temperatures at the locations of TCLW1 to TCLW4. The peak values of TCLW1-TCLW4 are presented in table (8.5.3.2). These thermocouples are located close to the left wall of the compartment. The shapes of the predicted temperature curves are similar to those of the measured temperature curves. In addition, the predicted peak temperatures at

thermocouple locations TCLW2 and TCLW4 are in reasonably good agreement with the measured peak temperatures. Once again however, the predicted temperature curves indicate an early and quick decay of the simulated fire. Furthermore, the peak values of the predicted temperatures for TCLW1 and TCLW3 are quite a bit lower than those of the corresponding measured temperatures. It is thought that the location of these thermocouples may have contributed to this discrepancy. These thermocouples are located 0.6m above the floor and are thus in the transition region between the lower cool layer and the upper hot layer. Temperatures in this region are very sensitive to changes of height. As a result, they are most likely to suffer from poor predictions.

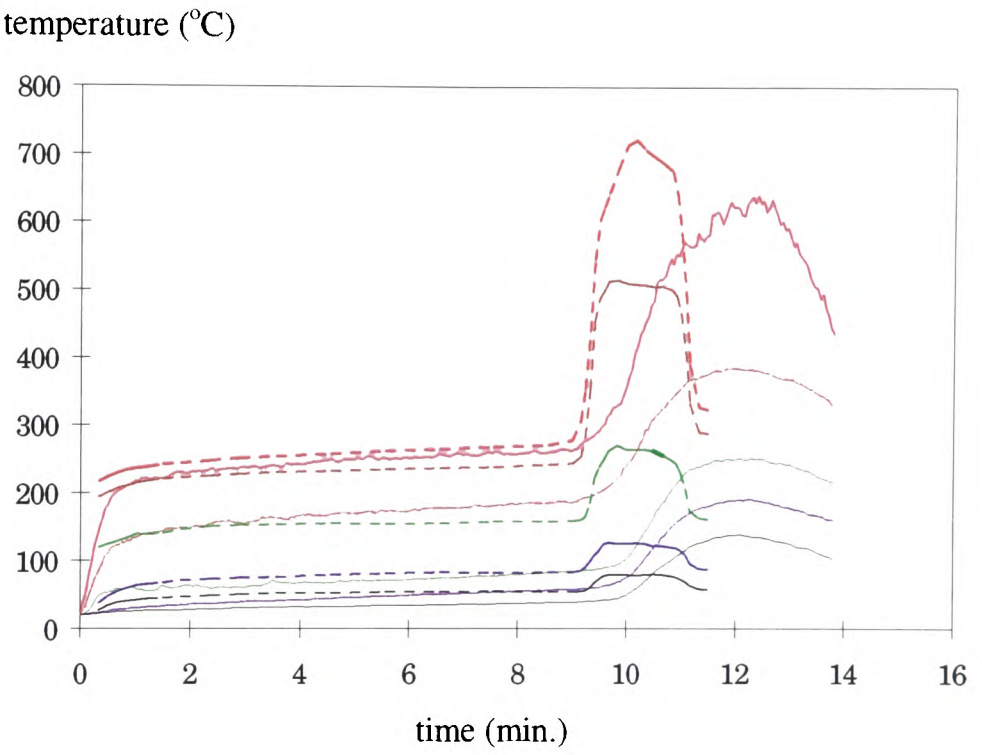

Fig. 8.5.8: the temperature profiles of the TC tree.
red:1.0m; brown: 0.8m; green: 0.6m; blue: 0.4m; black: 0.2m
solid: measured; broken: predicted.

The predicted and measured temperature profiles of the TC tree are plotted in figure (8.5.8). The predictions are in qualitative agreement with the experiment. As the walls are assumed adiabatic, in the preheating stage, the numerical temperatures are higher than the measured. After the chipboard is ignited, the predicted temperatures at the three higher locations are higher than the experiment while at the two lower positions

the temperatures are under predicted. As the simulated fire spreads more rapidly and decays more quickly than the actual fire, the peaks of the predicted temperature profiles shift backwards in time, i.e. occur earlier.

The curves of the measured and predicted radiative fluxes are drawn in figure (8.5.9). Good qualitative agreement with the experiment is achieved for the predictions. The predicted peak values are reasonably close to those of the measurements. Rapid decline of the predicted radiative fluxes indicates a quick decay of the simulated fire.

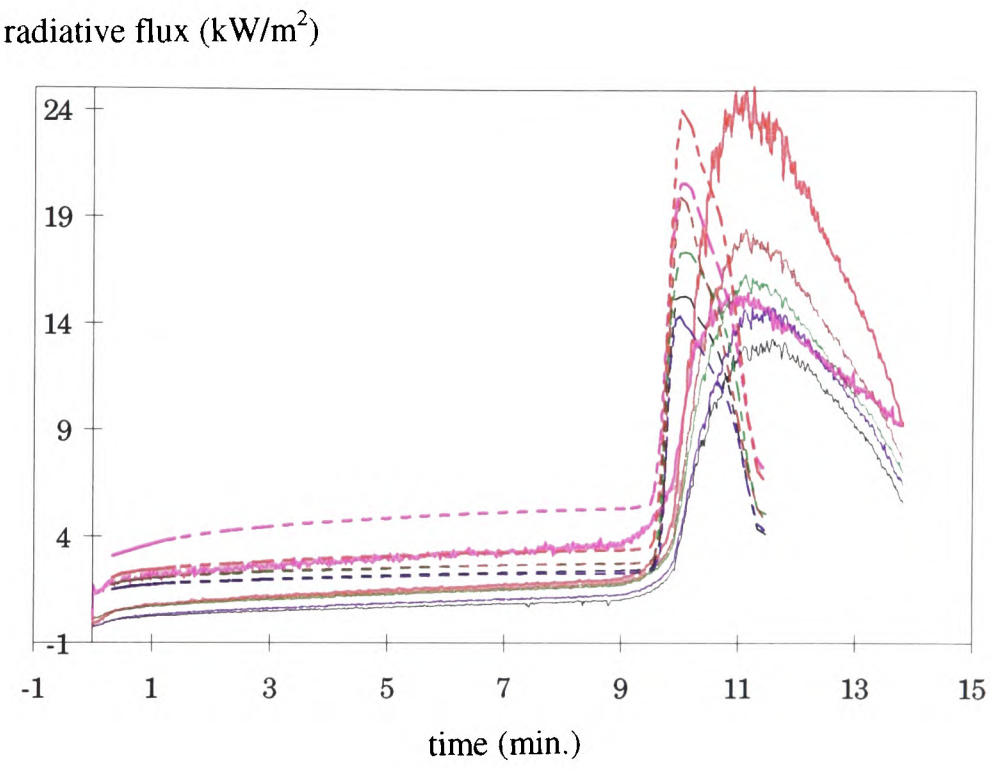

Fig. 8.5.9: the curves of radiative fluxes.
red: rad6; brown: rad2; green: rad1; pink: rad5; blue: rad4; black: rad3
solid: measured; broken: predicted.

Predicted and measured temperature profiles within the chipboard ceiling material are depicted in figure (8.5.10). The simulation produces qualitative agreement with the experiment. The more rapid increase in the predicted temperatures within the chipboard once again indicates that the simulated fire spreads more rapidly.

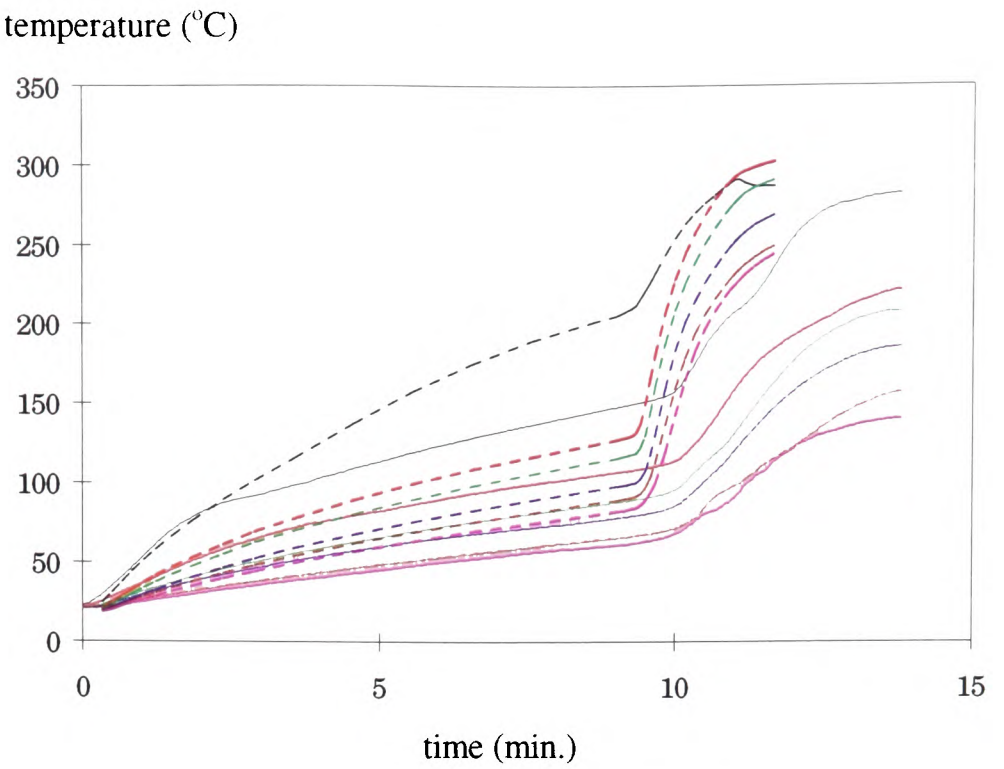

Fig. 8.5.10: the temperature profiles within the chipboard.
black: TCW1; red: TCW2; green: TCW3;
blue: TCW4; brown: TCW5; pink: TCW6.
solid: measured; broken: predicted.

The shorter duration of the simulated fire can be explained as a result of its more rapid progress. The char layer formed when the chipboard is burning protects the virgin material from further pyrolysis. As a result, there is a rapid decline in the mass loss rate of the charring material after it reaches its peak. The more rapidly the fire spreads, the faster the rate at which the chipboard surface area is covered with a layer of char, resulting in a more rapid decline of the mass loss rate from the entire chipboard. Consequently, the simulated fire decays more rapidly than the real one.

In summary, good qualitative agreement between experiment and predictions are achieved. In addition, some reasonable quantitative agreements between the simulation and the experiment are obtained, for example, the peak values of the upper layer temperatures and the radiative heat fluxes. Prior to the ceiling material being involved in the combustion, quite good quantitative agreement between predictions and experiment are produced. The predicted time to the involvement of the ceiling

material is also in very good agreement with that measured. However, the simulated fire spread more rapidly than the experimental fire and consequently, the duration of the simulated fire spread is much shorter than that measured.

These differences may result from the inappropriateness of the model assumptions. For example, the model did not take into account the moisture in the fuel. Moisture in wood may substantially reduce the heat release rate when the wood is burned. Another key assumption concerns the imposition of a constant pyrolysis temperature. Measurements suggest that the pyrolysis temperature is dependent on the external heat flux (i.e. the greater the external flux, the higher the resulting pyrolysis temperature). High pyrolysis temperature may significantly decrease the mass loss rate of the solid fuel since more surface re-radiation heat losses occur. Another plausible explanation for the differences between the numerical and experimental results concerns the use of improper char properties. This may result in the char layer being unable to provide sufficient insulation to the virgin material resulting in higher mass loss rates. Char properties may also vary with temperature. In addition, the secondary reactions of the combustible gases when going through the hot char layer change the composition of the volatiles and may hence reduce the heat release rate of the combustible gases. Finally, uncertainties in the basic material properties of the compartment building materials may also contribute to the observed differences.

It is worth noting that the simulations were also attempted using the six-flux radiation model in place of the discrete transfer radiation model. The attraction of the six-flux model is that it is more computational efficient in that it consumes considerably less computational power than the discrete transfer model. In these calculations, the six-

flux model required 26 minutes compared with the discrete transfer models 90 minutes to perform ten time steps with 100 iterations in each time step on a 400 MHz DEC alpha workstation.

However, in using the six-flux model, the simulations failed to predict the fire spread within the fire compartment. Although the burning in the region directly above the burner was produced, the simulated fire was not able to spread out of that region. This may at first appear somewhat surprising as the six-flux radiation model was successfully used for the examples in sections 8.3 and 8.4. However, these cases made use of the non-charring pyrolysis model.

The current case included charring which creates a much more difficult fire spread situation. Furthermore, a more accurate prediction of the incident heat flux at the ceiling is required for the current case as a much longer span of target material is used here compared with the situation in section 8.4 where only a small square sample of non-charring material was involved. In addition, the incident heat flux at the ceiling in the region normal to the burner is generally overestimated by the six-flux model, causing a faster growth of the insulation layer—the char layer which protects the material from further burning. Consequently, the mass loss rates in the mentioned region plummet. However, the burning in this region is crucial for the simulated fire spreading during the earliest stage of fire spread. This would suggest that under these conditions, the six-flux radiation model should not be used.

8.6 Concluding Remarks

This chapter concerned the development and demonstration of a fire field model intended to simulate the spread of fire within a compartment involving solid fuels. The fire model incorporated a gas-phase combustion model, a thermal radiation model that included the effect of soot, and a charring pyrolysis model, all within the context of a CFD based fire field model. Particular attention was paid to express the interplay between the gas-phase and the solid-phase behaviours. This interplay can be represented by the boundary conditions at the surface of the solid material.

At the initial stage of developing this integrated model, two two-dimensional models were established to simulate fire spread over ceiling lining material within an opened and sealed room respectively. These two models were expected to be able to qualitatively predict flashover type phenomena(opened room scenario) and backdraft type phenomena(sealed room scenario)—the two most severe hazards in enclosure fires. The two-dimensional fire spread models demonstrated qualitatively agreement with experimental observations for flashover and backdraft. These two models appeared to be promising in the simulation of the fire spread within enclosures. Therefore the approach was followed and extended into three-dimensional form. The model was used to simulate real fire experiments and to be further validated by comparing model predictions with experimental data.

The first three-dimensional fire spread model was developed to simulate some of the series of fire tests conducted by Quintiere et al.[1979]. In the series of tests PMMA samples were used and the sample size and the ventilation opening were

systematically changed. In total seven tests were selected from the series of tests to be modelled. Simulations of these tests can be regarded as a part of the systematic validation of the model developed in this thesis. Basically model predictions were in good agreement in every aspect with the experimental data provided. Based on the predicted data, the linear relationship between the ventilation factor and the entrained air flow rate was derived and was very close to the result obtained by Rockett. The heat release rate required for flashover was also calculated from the numerical data and closely matched the analyses of Babrauskas[Babrauskas, 1980] and Thomas[Thomas, 1981].

The second three-dimensional fire spread model was used to simulate a fire test within a half-scale fire compartment. The ceiling of the test compartment was lined with chipboard, a material that chars when exposed to fire. The model produced predictions that were in good qualitative agreement with the experimental data. Some quantitative agreement between numerical and experimental data was also achieved, in particular the peak values of the upper layer temperatures and radiation fluxes. In addition, the simulation was able to produce good agreement with the experimental observations during the growth stage of the fire, and the model was able to predict to reasonable accuracy when the ceiling material became involved in the fire. However, the simulated fire spread more rapidly than the real fire. Consequently the duration of the simulated fire spread is much shorter than that of the real fire. These differences may result from the nature of some of the model assumptions. For example, the model ignores the moisture content of the wood fuel, assumes a constant pyrolysis temperature, lacks detailed thermal properties of the char, assumes that the char thermal properties are temperature independent and finally, assumes values for the

thermal properties of the compartment wall materials.

It was noted during the course of these investigations that the six-flux radiation model was not suitable for applications involving the spread of fire along a large expanse of combustible solid material that chars. In order to capture this behaviour, it is necessary to incorporate a discrete transfer radiation model utilising some 50 rays. While this incurs a significant computational overhead, the alternative approach using the six-flux model is unable to simulate the spread of the combustion front.

Chapter 9

CONCLUDING REMARKS AND FUTURE WORK

9.1 Summary

The main objective of this thesis was to develop relatively simple but reasonable engineering models within a CFD software framework to simulate gas fire in a compartment and fire growth and propagation in enclosures in which solid combustibles are lined on walls or ceiling. The commercial CFD software CFDS-FLOW3D (Version 2.3.3) was selected as a numerical tool to solve the discretised equations derived from the differential governing equations.

However, this version of the CFDS-FLOW3D did not include sub-components representing the principal elements in fire growth and development in enclosures such as gas-phase combustion, radiation and solid combustion. Traditionally, the simplest engineering fire models are described by a simple heat prescribed source model. This approximation while appearing crude can produce reasonable agreement with experimentally derived temperature measurements for room fire scenarios, but it still ignores some main characteristics of enclosure fires. In particular, it lacks the ability to perform predictive simulations of the dominant component of enclosure fires, the spread of fire over combustible solid fuels. In addition, radiation is the dominant mode of heat transfer in a full-scale room fire. The radiative properties of the gas-soot mixture will not be appropriately evaluated without the simulation of gas-phase combustion since the concentrations of soot, CO_2 and H_2O are centrally important for the evaluation. The gas-phase combustion models are also required to simulate fire spread over solid fuel surfaces since the gas-phase combustion is one of the two

central mechanisms to control the flame spread over a solid surface.

This study has focused on developing individual sub-models representing the three principal elements mentioned above of fire growth and propagation in room fire scenarios and fit these model codes into the selected CFD software. At the heart of this study is integration of all the three sub-models and other auxiliary calculations such as the evaluation of the radiative properties of gas-soot mixture, temperature calculation for non-burning solid surfaces and so on into a complete fire spread model.

Chapter 1 simply outlined the objectives for the PhD study.

Chapter 2 reviewed the existing CFD fire spread models relevant to the study. The governing equations for turbulent flames were also described in this chapter. The relationships between the basic governing equations and the sub-models representing the gas-phase combustion, radiation and solid combustion were discussed.

In Chapter 3, the simple heat source model was used to simulate a compartment fire test in which a methane fuelled burner was centrally placed on the floor of the compartment. The weaknesses of this approximation were identified. This chapter was devoted to find further directions of the study.

Chapter 4 described the basic characteristics of turbulent diffusion flames. A gas-phase combustion model based on the eddy dissipation concept was presented. To partially validate the model, this model was used to simulate a jet diffusion flame in

the Harwell furnace which is a standard test case included in the CFDS-FLOW3D (version 3.3) software. The model results were compared with the ones obtained from the built-in combustion model in the CFDS-FLOW3D (version 3.3) software. Excellent agreements were achieved.

In Chapter 5, soot formation processes were outlined. A simple soot model was proposed on the basis of the facts observed from experimental measurements: that soot formation is in the fuel rich side of chemical reaction region and the highest soot concentration is found in the same region. The measured mean soot concentration in the region of soot formation is considered as a final result of soot formation processes: nucleation, surface growth, coagulation and oxidation. Therefore, in this region soot concentrations are assumed to remain constant, taking the measured mean values. While outside the soot formation region it is assumed that soot formation and oxidation has ceased due to lower temperatures and soot particles are transported by convection.

The same chapter also provided a fundamental introduction to radiation theory. The methods used in this study to evaluate the radiative properties of gas-soot mixture were described. Some special treatments in the study to the widely used radiation models—the six-flux model and the DTM—were presented. The radiation source term was linearised in terms of the enthalpy to enhance the convergence and stability of the numerical solution procedure. The rays in the DTM were specified to minimise the error of predicted radiative heat flux at the solid surfaces. Shortcomings in the conventional six-flux radiation model were highlighted and corrected in the modified six-flux model.

In Chapter 6, the gas-phase combustion model and the radiation model were incorporated into the CFD software CFDS-FLOW3D (Version 2.3.3) to form a model to simulate a compartment fire test. The soot model was also included in the integrated model to evaluate the radiative properties of the gas-soot mixture.

An existing integral method for the calculation of temperatures within solids was extended in this chapter to be able to cope with the reradiaiton losses at the surface exposed to a fire and the convective heat loss at the opposite surface. The integral method is economic and simple to calculate for non-combustible solids like the walls, the floor, or the ceiling of a compartment.

The compartment fire test used in this chapter was one of the Steckler's room fire tests, the same as the one in chapter 3 to demonstrate the extent of the improvement of the simulations. The conductive heat losses through the walls and ceiling were taken into account in this model. Good agreements were achieved in many aspects of the compartment fire: the neutral plane in the doorway, average temperature in the hot upper layer, mass flux-in and mass flux-out, vertical stack temperature profile, temperature profile and velocity profile in the doorway vertical centreline.

In this chapter, it was found that the use of the gas-phase combustion model alone was not able to produce sufficient improvement of the predictions especially the predictions to the upper layer temperatures. The simulations without radiation models still lost the characteristic of the vertical uniform temperature distribution in the upper layer. However, this feature was captured by inclusion of the radiation models. This fact indicates that radiative energy exchanges play an important role to create a

uniform temperature distribution in the upper region.

The computational costs of the six-flux radiation model and the DTM radiation model were also examined in this chapter by applying these radiation models in the simulations of the selected Steckler's room fire test. The computational cost using the six-flux model is approximately the same as that using the six-ray DTM model. The differences of the two models in predictions are not remarkable. It is not surprising because the modified six-flux model is quite similar to the DTM using six ray parallel to the coordinates. In fact, the six-flux model produced slightly better results. But as the number of rays used in the DTM model increases, DTM becomes more and more expensive. The computer time of the simulation using 24 rays in the DTM is approximately three times that using 6 rays. Meanwhile, in return for the price expended, the improvement of predictions of the DTM was smoothly made with increasing the ray number. While in this case, it could be argued that the improved accuracy achieved using the DTM did not justify the additional computational costs, the improvement in accuracy may be justified in cases involving larger fires or cases where solid fuel combustion is considered.

Chapter 7 introduced the mass loss processes of solid fuels—charring materials and noncharring materials. Experimental observations for pyrolizing solid fuels were presented. Two pyrolysis models for charring and noncharring materials respectively were described in terms of the pyrolysis temperature. Numerical methods for these two models were proposed. They were validated by comparing the model predictions with experimental data. The noncharring pyrolysis model produced numerical mass loss rates of PMMA in the Cone Calorimeter scenario in excellent agreement with the

measured mass loss rates. The charring model was capable of predicting the mass loss rates and temperature distribution within wood samples producing reasonable agreement with experimental data. Sensitivity analyses for grid size in the solid and time step length were also carried out to obtain the proper grid size and time step length practically used in the simulation of the mass loss processes of solid fuels.

Chapter 8 was concerned with integrating all the sub-models described in preceding chapters to form a complete fire spread model to simulate fire development involving solid fuel combustion in the room fire scenario. Developing such an integrated fire spread model was the main objective of this thesis. Attention was paid to express the interplay between the gas-phase and the solid-phase behaviours. This interplay can be represented by the boundary conditions at the surface of the solid material.

At the initial stage of developing this integrated model, two two-dimensional models were established to simulate fire spread over ceiling lining material within an opened room and sealed room respectively. These two models were developed to investigate the qualitative behaviour of the integrated model. In particular if the model could demonstrate some of the key features of enclosure fire behaviour. The model produced very good qualitative agreement with such behaviour that the characteristic enclosure fire heat release rate curves were produced indicating that the fire underwent the typical three-stage development. Indeed, in the open room case the model predicted a flashover type behaviour while in the closed room case the model developed back-draft type conditions. These two models appeared to be promising in the simulation of the fire spread within enclosures. Therefore the approach was followed and extended into three-dimensional form. The model was used to simulate

real fire experiments and to be further validated by comparing model predictions with experimental data.

The first three-dimensional fire spread model was developed to simulate some of the series of fire tests conducted by Quintiere et al.[1979]. In the series of tests PMMA samples were used and the sample size and the ventilation opening were systematically changed. In total seven tests were selected from the series of tests to be modelled. Simulations of these tests can be regarded as a part of the systematic validations to the model developed in this thesis. Basically, model predictions were in good agreement in every aspect with the experimental data provided. Based on the predicted data, the linear relationship between the ventilation factor and the entrained air flow rate was derived and was very close to the result obtained by Rockett. The heat release rate required for flashover was also calculated from the numerical data and closely matched the analyses of Babrauskas[1980] and Thomas[1981].

The second three-dimensional fire spread model was to simulate the fire test carried out by Home Office Fire Experimental Unit involving fire spread over charring lining material on the ceiling. The model produced predictions which were in good qualitative agreement with the experimental data. Some quantitative agreements of the predictions with the experiment, in particular the peak values of the upper layer temperatures and radiation fluxes, were also achieved. The simulated time to fire spreads was also in very good agreement with the measured one.

9.2 Conclusions

1. An integrated fire spread model for room fire scenarios was established within a CFD framework. This model includes the principal elements of fire development within enclosures: gas-phase combustion, radiation and solid fuel combustion. The CFD compatible model has few limits to the geometrical configurations. Aimed at ease of use and flexibility, all the material properties required as input for the model are measurable from bench or small scale experiment or can be easily found from the literature. The sub-models addressed in this thesis representing the principal elements in fire spread are easily implemented within the framework of CFD software.
2. Qualitative and quantitative verifications for the integrated fire spread model were carried out. The model was demonstrated to be capable of both qualitatively and quantitatively predicting the two most severe hazards—flashover and backdraft. Two-dimensional simulation qualitative predictions for fire spread within the opened and sealed room compared favourably with real fire observations. For fire tests using PMMA the three-dimensional model produced quantitative predictions very close to the results of experimental fire tests and other analyses in the literature. In the simulation of the fire test involving charring material lined over the ceiling in a compartment, the model produced predictions which were in good qualitative agreement with the experimental data. Some quantitative agreements of the predictions with the experiment, in particular the peak values of the upper layer temperatures and radiation fluxes, were also achieved.
3. Pyrolysis models for noncharring and charring solid combustibles were developed. The mass loss rates produced by the noncharring model for PMMA

were in excellent agreement with experimental data. The charring model produced predictions for the mass loss rates and temperature distribution of a wood sample in very close agreement to that measured.

4. A new method was proposed to tackle the extreme difficulty caused by the movement of the char-virgin interface and the high non-linearity of reradiation at the char surface. Numerical analyses show this method is stable and accurate. It was demonstrated that this method is able to produce numerical mass loss rates and temperature distribution for wood samples in reasonable agreement with experimental results.
5. A simple empirical soot model was developed based on experimental observations that soot formation occurs in the fuel rich side of the chemical reaction region and the highest soot concentration is found in the same region. The soot model is important to evaluate the radiative properties of the gas-soot mixture in fires.
6. By incorporating the gas-phase combustion model, the radiation models and the soot model, substantial improvement in the upper layer temperature profiles was achieved in the simulations of one of the Steckler's room fire test. It is found that radiation plays an important, perhaps dominant role to create the nearly uniform temperature distribution in the upper layer.
7. The integral method to calculate temperatures of non-combustible solids was extended to be capable of dealing with the non-linearity of the reradiation at the solid surface(top surface) exposed to a fire and the convective heat loss at the opposite surface. The integral method is economic and simple for the calculation of temperatures of non-combustible solids.
8. Shortcomings in the conventional six-flux radiation model were highlighted. These involves the introduction of an extra source of inaccuracy and uncertainty

due to the radiation boundary condition at wall surfaces and the unrealistic transformation from one-way (parabolic) to two-way (elliptic) problems. These shortcomings were demonstrated through a simple artificial test case and corrected in the modified six-flux model. Improved accuracy was demonstrated using the artificial test case.

9. The computational cost and accuracy of the six-flux model and the discrete transfer method (DTM) using different number of rays were also investigated. The DTM model becomes more and more expensive as the number of rays used increases. The DTM with 24 rays is about three time as expensive as the six-flux model. It was found that for the Steckler's room fire where non-spreading fire was involved the simulation using the six-flux model produced similar predictions to the simulations using the 6 rays DTM model and predictions are not much improved by increasing the ray number in the DTM model. However when fire spread over combustible solid surfaces are involved, more accurate predictions of radiation heat flux at the solid surface become important due to the central role of heat transfer in the process of flame spread. Under these circumstances, the intention of modellers is generally to use larger number of rays in the DTM model. This was demonstrated by the test case in section 8.5 where fire spreads over combustible solid fuel and the six-flux model failed to produce reasonable predictions and hence the DTM using 54 rays was used. In addition, inclusion of soot formation will not significantly increase the computing time.

9.3 Proposed Further Work

While the integrated model developed here appears to provide a promising approach to the prediction of fire spread within enclosures, much work remains before it can be applied to engineering applications of fire field modelling. In the current model, the heat transfer calculation at the wall boundary is based on the wall functions which are strictly correct only for forced flow conditions where buoyancy effects are unimportant[AEA Technology, 1991]. The use of the wall functions leads to uncertainties in fire situations, in particular at the pyrolysing solid surface where mass flux comes out from the solid. Generally, buoyancy effects are important in fires. Experiments[Zhao and Fernandez-Pello, 1993] have shown that the ceiling flame spread processes are quite different from the floor flame spread processes due to buoyancy. "Buoyancy pushes the flame closer to the solid surface in the ceiling case and lifts the flame away from the surface in the floor case" [Zhao and Fernandez-Pello, 1993]. Therefore buoyancy will change the heat transfer to the surface from the flame according to the orientation of the solid fuel. Since convective heat transfer at the solid surface is particularly important at the initial stage of fire spread within enclosures, its calculation in fire situation needs further investigation and modelling.

Interaction between turbulence and radiation is actually ignored in the current model. However, it was observed that effects of turbulence/radiation interactions were significant for radiation emission[Gore and Faeth, 1988]. Although the current model predictions are encouraging despite neglecting these turbulence/radiation interactions, the level of accuracy affected by this neglect needs to be assessed.

The current model was only partially verified for the configurations in which solid combustibles were placed on the ceiling or on the floor. Vertical upward flame spread has been proved to be rapid and hazardous. In contrast, downward flame spread is much slower. Further validations for these two combustible orientations and combinations of different solid orientations are needed.

There is much room for improvement for each component of the integrated model. The charring model, for instance, does not include effects of moisture which is a very common content in wood products and has very significant effects on the heat release rate of wood products in some cases. This pyrolysis model also makes use of the relatively simple ignition temperature concept rather than more sophisticated kinetic law to simulate the mass loss process of solid fuel. The soot model is also simple and empirical. Since soot oxidation was not taken into account the soot concentration may be overpredicted in the fire zones and the region far from fire zones. All these simple treatments must be refined to improve the predictions of the simulation for the case in section 8.5. The effects of these simple treatments on the model predictions as a whole must be further assessed.

Systematic and overall scrutiny must be performed through comparing the model predictions with experimental results. The examination should be conducted for different orientations and positions of solid fuels and different type of fuels. In addition, the sensitivity of the solid fuel combustion model to parameters such as the ignition temperature(T_p), the pyrolysis heat(L), the specific heat(C_p), etc. must be evaluated in detail.

There are some other elements of fire spread within enclosures important to fire safety and protection. The production and movement of smoke and toxicity, for example, are for great concerned to fire safety professionals. Smoke and toxic gases are generated in almost all fires. Reduced visibility due to the presence of smoke makes the occupants difficult to escape from the fire. Inhalation of smoke and toxic gas further reduces the chance to survival. Aimed at developing a useful tool to predict fire spread within enclosures for engineering applications, the production and movement of smoke and toxicity must be addressed in the future work.

To model the production and movement of smoke and toxicity, incomplete combustion, ignition and extinction of fires should be investigated and simulated. Although the detailed chemistry incorporated in flamelet or PDF techniques may create good predictions in the flame structure and combustion products, it leads to tens, or even hundreds, of chemical steps and species that must be included in the computation. Such detailed chemical reaction data is not usually available in the literature for common building materials. Therefore, an alternative approach is required which does not completely lose the chemistry of the combustion of interest like the over-simplified one step global reaction. The chemistry may be represented by the measured correlation of the production of combustion products with the vitiated condition according to the fuel. A plausible representative of the vitiated condition is the local equivalence ratio which is defined as the mass ratio of the fuel to the air normalised by the mass ratio of fuel and air required for stoichiometric burning. In the CFD fire model the numerical local equivalence ratio can be calculated using the fuel and air concentration available at a node of the mesh. Empirical relations between the production of the combustion products and the equivalence ratio have been obtained on

the basis of experimental data. These relations may be used in the CFD fire spread model to predict the soot or smoke production rate. In fact, the production rates of soot and other combustion products can be considered to be a function of the local vitiated condition—the local equivalence ratio. This method may introduce empirical representation of combustion chemistry for a given fuel and help surmount the weakness of the over-simplified one step global chemical reaction.

Finally, the gaseous combustion model currently used in the study is not sensitive to the oxygen concentration. That means that even when the oxygen concentration is beyond the range of the flammability limit, the gas phase combustion model still predicts the occurrence of combustion. Another advantage of the local equivalence ratio approach is that it may alleviate this error of the gaseous combustion model by making it sensitively respond to the oxygen concentration.

Appendix

EXAMPLE OF USER DEFINED CODE IMPLEMENTATION WITHIN CFDS-FLOW3D ENVIRONMENT

CFDS-FLOW3D provides users with a set of subroutines allowing the addition of source terms into variable equations, the modification of boundary conditions at solid surfaces and the change of model parameters such as diffussivities of variables. The most often used and central subroutines in the present study to implement the integrated fire spread model are USRSRC and USRWAL. In this appendix, the implementation of the integrated model using these two subroutines is briefly described. The explanations of the functions of each self-developed subroutines are put into a format of FORTRAN code.

1. SUBROUTINE USRSRC

This user subroutine provided by CFDS-FLOW3D is used to add additional source terms into each governing equation.

```
      SUBROUTINE USRSRC(VARIABLES, ..., ...)

C---IN THIS SUBROUTINE, THE SOURCE TERMS OF GOVERNING
C---EQUATIONS FOR VARIABLES ARE ADDED. AND SOME BOUNDARY
C---CONDITIONS AT THE SURFACE OF THE COMBUSTIBLE SOLIDS
C---DUE TO THE RELEASE OF COMBUSTIBLE GASES FROM THE SOLIDS
C---ARE ALSO IMPLEMENTED.

C-------------------------------------------------------------------------------------------
C---ADDING THE MASS SOURCE AT THE COMBUSTIBLE SOLID SURFACE
C---INTO THE PRESSURE CORRECTION EQUATION DUE TO THE RELEASE
C---OF THE COMBUSTIBLE GASES FROM THE SOLID FUEL. A SELF-
C----DEVELPED SUBROUTINE NAMED MSLDSRC IS CALLED TO
C---IMPLEMENT THIS DUTY. IN THIS SUBROUNTINE THE EQUATIONS
C---(8.2.11) AND (8.2.12) FROM CHAPTER 8 ARE IMPLEMENTED.
```

```
      IF (IEQN.EQ.4.AND.ICALL.EQ.1.AND.LSOLID) THEN

C---WHERE EQUATION 4 IS THE PRESSURE CORRECTION EQUATION
C---DERIVED FROM THE CONTINUITY EQUATION.

         CALL MSLDSRC(SU, SP, VARSLD)

C---WHERE VARSLD STORES THE MASS LOSS RATE AT EACH SOLID
C---SURFACE CELL AND LSOLID IS A LOGICAL VARIABLE
C---REPRESENTING IF SOLID COMBUSTION IS INVOLVED IN THE
C---SIMULATION. IF LSOLID IS TRUE, THE MASS SOURCE TERM DUE TO
C---THE COMBUTIBLE GAS RELEASE FROM THE SOLID FUEL IS ADDED.

      ENDIF

C-------------------------------------------------------------------------------------------
C---COMPUTING THE RADIATIVE ENERGE EXCHANGE ACCORDING TO
C---THE RADIATION MODEL—THE SIX-FLUX MODEL OR THE DISCRETE
C---TRANSFER METHOD. A SELF-DEVELOPED SUBROUTINE NAMED
C---RADCAL IS CALLED TO IMPLEMENT THIS DUTY. IN THIS
C---SUBROUTINE THE EQUATIONS IN SECTION (5.5.3) FOR THE DISCRETE
C---TRANSFER METHOD AND THE EQUATIONS IN SECTION (5.6.1) FOR
C---THE MODIFIED SIX-FLUX MODEL ARE PERFORMED.

      IF (IEQN.EQ.8.AND.ICALL.EQ.1.AND.LRAD) THEN
C---WHERE EQUATION 8 IS THE GOVERNING EQUATION FOR ENTHALPY.

         CALL RADCAL(VARIABLES, ..., VARRAD, LSIXF)

      ENDIF

C---WHERE LRAD IS A LOGICAL VARIABLE REPRESENTING IF A
C---RADIATION MODEL IS USED. IF LRAD IS TRUE, THE SUBROUTINE
C---RADCAL IS CALLED. LSIXF IS A LOGICAL VARIABLE. IF LSIXF IS
C---TRUE, THE SIX-FLUX MODEL IS USED. OTHERWISE, THE DISCRETE
C---TRANSFER METHOD IS USED. VARRAD STORES THE RADIATIVE
C---ENERGY ABSORBED BY EACH CELL AND THE RADIATIVE HEAT
C---FLUXES AT SOLID SURFACES.

C-------------------------------------------------------------------------------------------
C---ADDING SOURCE TERMS INTO THE ENERGY EQUATION.

      IF (IEQN.EQ.8.AND.ICALL.EQ.1) THEN

C---WHERE EQUATION 8 IS THE GOVERNING EQUATION FOR ENTHALPY.

C-----1. ADDING THE SOURCE AND SINK TERM DUE TO RADIATION. A
C--------SELF-DEVELOPED SUBROUTINE NAMED RADSRC IS CALLED TO
C--------IMPLEMENT THIS DUTY. IN THIS SUBROUTINE THE EQUATIONS
```

```
C--------(5.6.19) FOR THE DISCRETE TRANSFER METHOD OR (5.6.20) FOR
C--------THE SIX-FLUX MODEL AND (5.6.21) ARE PERFORMED.

        IF (LRAD) CALL RADSRC(SU, SP, T, VARRAD, ...)

C-----2. ADDING THE ENERGY SOURCE TERM DUE TO THE RELEASE OF
C--------THE COMBUSTIBLE GASES FROM THE SOLID FUEL IF SOLID
C--------COMBUSTION IS INVOLVED IN THE SIMULATION. THIS SOURCE
C--------TERM STEMS FROM THE BOUNDARY CONDITIONS RELATED TO
C--------THE ENERGY EQUATION AT THE SOLID SURFACE. A SELF-
C---------DEVELOPED SUBROUTINE NAMED HSLSRC IS CALLED TO
C--------IMPLEMENT THIS DUTY. IN THIS SUBROUTINE THE
C--------COMBINATIONS OF THE EQUATIONS IN SECTION 8.2 FOR THE
C--------THERMAL AND MASS TRANSFER BOUNDARY CONDITONS DUE
C--------TO THE COMBUSTIBLE GAS RELEASE ARE PERFORMED.

        IF (LSOLID) CALL HSLDSRC(SU, SP,VARSLD, TSOLID)

C--------WHERE TSOLID STORES THE TEMPERATURES OF THE SOLID
C--------FUEL.

      ENDIF

C-------------------------------------------------------------------------------------------
C---ADDING A SOURCE TERM INTO THE SCALAR EQUATION
C---REPRESENTING THE MIXTURE FRACTION IF THE SOLID PYROLYSIS
C---MODEL IS EMPLOYED. THIS SOURCE TERM STEMS FROM THE
C---BOUNDARY CONDITIONS AT THE SOLID SURFACE DUE TO THE
C---RELEASE OF THE COMBUSTIBLE GASES FROM THE SOLID FUEL. A
C---SELF-DEVELOPED SUBROUTINE NAMED MFSLDSRC IS CALLED TO
C---IMPLEMENT THIS DUTY. IN THIS SUBROUTINE THE COMBINATION
C---OF THE EQUATIONS (8.2.9) AND (8.2.10) IN SECTION (8.2) ARE
C---PERFORMED.

      IF (IEQN.EQ.9.AND.ICALL.EQ.1.AND.LSOLID) THEN

C---WHERE EQUATION 9 (THE FIRST SCALAR EQUATION) IS SUPPOSED
C---TO BE THE GOVERNING EQUATION FOR THE MIXTURE FRACTION.

        CALL MFSLDSRC(SU, SP, VARSLD)

      ENDIF


C-------------------------------------------------------------------------------------------
C---ADDING SOURCE TERM INTO THE SCALAR EQUATION
C---REPRESENTING THE MASS FRACTION OF THE FUEL GAS IF THE GAS
C---PHASE COMBUSTION MODEL IS EMPLOYED.
```

```
      IF (IEQN.EQ.10.AND.ICALL.EQ.1) THEN

C---WHERE EQUATION 10 (THE SECOND SCALAR EQUATION) IS
C---SUPPOSED TO BE THE GOVERNING EQUATION FOR THE FUEL MASS
C---FRACTION.

C---1. ADDING A SOURCE TERM DUE TO THE CONSUMPTION OF THE
C------FUEL GAS BY THE GAS PHASE COMBUSTION. A SELF-DEVELOPED
C------SUBROUTE NAMED FCOMSRC IS CALLED TO IMPLEMENT THIS
C------DUTY. IN THIS SUBROUTINE THE EQUATION (4.3.16) IN SECTION
C------(4.3) IS PERFORMED.

         CALL FCOMSRC(SU, SP, SCAL)

C---2. ADDING A SOURCE TERM DUE TO THE RELEASE OF THE
C------COMBUSTIBLE GASES FROM THE SOLID FUEL. THIS SOURCE TERM
C------STEMS FROM THE BOUNDARY CONDITIONS AT THE SOLID
C------SURFACE. A SELF-DEVELOPED SUBROUTINE NAMED FSLDSRC IS
C------CALLED TO IMPLEMENT THIS DUTY. IN THIS SUBROUTINE THE
C------EQUATION (8.2.9) IN SECTION (8.2) IS PERFORMED.

         IF (LSOLID) CALL FSLDSRC(SU, SP, VARSLD)

      ENDIF

C-------------------------------------------------------------------------------------------
C---ADDING A SOURCE TERM INTO THE SCALAR EQUATION
C---REPRESENTING THE SOOT CONCENTRATION IF THE SOOT MODEL IS
C---EMPLOYED IN THE SIMULATION. THIS SOURCE TERM STEMS FROM
C---THE SOOT GENERATION DUE TO THE IMCOMPLETE COMBUSTION.
C---A SELF-DEVELOPED SUBROUTINE NAMED SOOTSRC IS CALLED TO
C---IMPLEMENT THIS DUTY. IN THIS SUBROUTINE THE SOOT MODEL IN
C---SECTION (5.2.3) IS PERFORMED.

      IF (IEQN.EQ.11.AND.ICALL.EQ.1) THEN

C---WHERE EQUATION 11 (THE THIRD SCALAR EQUATION) IS SUPPOSED
C---TO BE THE GOVERNING EQUATION FOR THE SOOT MASS FRACTION.

         CALL SOOTSRC(SU, SP, SCAL)

      ENDIF

      RETURN
      END
```

2. SUBROUTINE USRWAL

This user subroutine provided by CFDS-FLOW3D is used to modify the boundary conditions at solid surfaces.

```
      SUBROUTINE USRWAL(VARIABLES, ..., ...)

C---IN THIS SUBROUTINE, THE PYROLYSIS MODELS FOR COMBUSTIBLE
C---SOLIDS – NON-CHARRING AND CHARRING -- ARE IMPLEMENTED IF
C---THEY ARE EMPLOYED IN THE SIMULATION. AND THE INTEGRAL
C---METHOD FOR CALCULATING THE SOLID SURFACE TEMPERATURES
C---OF THE NON-COMBUSTIBEL MATERIAL IS ALSO IMPLEMENTED. THE
C---THERMAL BOUNDARY CONDITIONS ARE THEN OVERWRITEN
C---ACCORDING TO THE CALCULATED COMBUSTIBLE AND NON-
C----COMBUSTIBLE SOLID SURFACE TEMPERATURES.

        IF (LSOLID) ISOLID = 1 OR 2

C-------------------------------------------------------------------------------------------
C---IF ISOLID = 1, THE SUBROUTINE IMPLEMENTING THE PYROLYSIS
C---MODEL NAMED PYSOLID IS CALLED AT THE BEGINNING OF EACH
C---ITERAION.
C---IF ISOLID = 2, PYSOLID IS CALLED AT THE START OF A NEW TIME
C---STEP.

        IF (LSOLID .AND. IENTRY.EQ.ISOLID) THEN

          CALL PYSLD(VARIABLES, VARRAD, VARSLD, TSOLID, LCHARF)

C---WHERE LCHARF IS A LOGICAL VARIABLE REPRESENTING THE TYPE
C---OF THE SOLID FUEL USED. IF LCHARF IS TRUE, THE MATERIAL IS
C---CHARRING. OTHERWISE, IT IS NON-CHARRING. THE VARIABLES
C---INCLUDE ALL THE PARAMETERS REQUIRED TO CALCULATE THE
C---CONVECTIVE HEAT FLUX AT THE SOLID SURFACE.

C-------------------------------------------------------------------------------------------
C---THE THERMAL BOUNDARY CONDITIONS AT THE SOLID FUEL
C---SURFACE ARE OVERWRITEN ACCORDING TO THE SOLID SURFACE
C---TEMPERATURES OBTAINED FROM PYSLD. A SELF-DEVELOPED
C---SUBROUTINE NAMED BDYSLD IS CALLED TO IMPLEMENT THIS
C---DUTY. IN THIS SUBROUTINE THE EQUAITON (8.2.15) IN SECTION (8.2)
C---IS PERFORMED. THE WALL FUNCTION IS USED HERE TO CALCULATE
C---THE CONVECTIVE HEAT TRANSFER COEFFICIENTS AT THE SOLID
C---SURFACES.

          CALL BDYSLD(VARIABLES,TSOLID)
```

```
C---WHERE THE VARIABLES INCLUDE ALL THE PARAMETERS REQUIRED
C---TO CALCULATE THE CONVECTIVE HEAT TRANSFER COEFFICIENT AT
C---THE SOLID SURFACE AND TO SET UP THE THERMAL BOUNDARY
C---CONDITIONS FOR THE FLOW DOMAIN.

      ENDIF

C-------------------------------------------------------------------------------------------
C---THE SURFACE TEMPERATURES AT THE NON-COMBUSTIBLE SOLIDS
C---ARE CALCULATED BY A SELF-DEVELOPED SUBROUTINE NAMED
C---NSLDCAL USING THE INTEGRAL METHOD OR THE FINITE
C---DIFFERENCE METHOD. THEN THE THERMAL BOUNDARY
C---CONDITIONS AT THE SURFACE OF NON-COMBUSTIBLE SOLIDS ARE
C---OVERWRITEN BY A SELF-DEVELOPED SURBROUTINE NAMED
C---BDYNSLD ACCORDING TO THE CALCULATED SURFACE
C---TEMPERATURES. IN THIS SUBROUTINE THE EQUAITON (8.2.15) IN
C---SECTION (8.2) IS PERFORMED. THE WALL FUNCTION IS USED HERE
C---TO CALCULATED THE CONVECTIVE HEAT TRANSFER COEFFICIENTS
C---AT THE SOLID SURFACES.

      IF (LNSLD .AND. IENTRY.EQ.1) THEN

        CALL NSLDCAL(VARIABLES,VARRAD, TNCSLD)

C---WHERE TNCSLD STORES THE SURFACE TEMPERATURES OF THE
C---NON-COMBUSTIBLE SOLID AND LNSLD IS A LOGICAL VARIABLE
C---REPRESENTING IF THE NON-COMBUSTIBLE MODLE IS EMPLOYED IN
C---THE SIMULATION. THE VARIABLES INCLUDE ALL THE PARAMETERS
C---REQUIRED TO CALCULATE THE CONVECTIVE HEAT FLUX AT THE
C---SOLID SURFACE.

        CALL BDYNSLD(VARIABLES,TNCSLD)

C---WHERE THE VARIABLES INCLUDE ALL THE PARAMETERS REQUIRED
C---TO CALCULATE THE CONVECTIVE HEAT TRANSFER COEFFICIENT AT
C---THE SOLID SURFACE AND TO SET UP THE THERMAL BOUNDARY
C---CONDITIONS FOR THE FLOW DOMAIN.

      ENDIF

      RETURN
      END
```

REFERENCES

AEA Technology[1991], "FLOW3D Release 2.3.3: user manual".

Agrawal, R. K.[1988], "Kinetics of reactions involved in pyrolysis of cellulose I: the three reaction models", Canadian J. of Chmeical Engineering, Vol. 66, pp 403-412.

Atreya, A.[1995], "Convective heat transfer", in The SFPE Handbook of Fire Protection Engineering, 2nd edition, pp.1-39-1-54.

Babrauskas, V.[1980], "Estimating room flashover potential", Fire Technology, vol. 16, pp. 94-104.

Bagnaro, M., Laouisset M. and Lockwood F. C.[1983], "Fire model prediction of some room fires: steady and transient", Fire Dynamics and Heat Transfer, vol. 25, pp. 107-114.

Bird, R.B., Stewart, W.E. and Lightfoot, E.N.[1966], *Transport phenomena*, Wiley, New York.

Blasi, C. D.[1993], "Modelling and simulation of combustion processes of charring and noncharring solid fuels", Prog. Energy Combust. Sci., vol. 19, pp 71-104.

Blasi, C. D.[1994], "Processes of flames spreading over the surface of charring fuels: effects of the solid thickness", Combustion and Flame, vol. 97, pp. 225-239.

Bradley, D., Gaskell, P. H. and Gu, X. J.[1994], "Application of a Reynolds stress, stretched flamelet, mathematical model to computations of turbulent burning velocities and comparison with experiments", Combustion and Flame, vol. 96, pp. 221-248.

Brenden, J. J.[1967], "Effect of fire retardant and other salts on pyrolysis products of Ponderosa pine at 280°C and 350°C", U.S. Forest Service Research Paper FPL 80, US Department of Agriculture.

Brushlinsky, N.[1997], "Formulating statistics for a safer planet", Fire International, October/November, p. 26.

Bukowski, R. W.[1995], "Modelling a backdraft incident: the 62 watts st. (NY) fire", proc. of fire safety by design (ed. Butler, G.W.), 1995, University of Sunderland.

Buriko, Yu. Ya., Kuznetsov, V. R., Volkov, D. V., Zaitsev, S. A. and Uryvsky, A. F.[1994], "A test of a flamelet model for turbulent nonpremixed combustion", Combustion and Flame, vol. 96, pp.104-120.

Burke, S. P. and Schumann, T. E. W.[1928], "Diffusion flames", Industrial and Engineering Chemistry, vol. 20, pp.988-1004.

Burns, A.D and Wilkes, N.S[1987], "A finite-difference method for the computation of fluid flows in complex three dimensional geometries", U.K. Atomic Energy Authority Harwell Report. AERE-R 12342.

Canter, D.[1990], "Studying the experience of fires", in Fires & Human Behaviour(ed. by Canter, D.), 2nd ed., pp. 1-14.

Chen, Y., Delichatsios, M.A. and Motevalli, V.[1993], "Material pyrolysis properties, part 1: an integral model for one-dimensional transient pyrolysis of charring and non-charring materials", Combust. Sci. Tech, vol. 88, pp. 309-328.

Coppalle, A. and Joyeux, D.[1994], "Temperature and soot volume fraction in turbulent diffusion flames: measurements of mean and fluctuating values", Combustion and Flame, vol. 96, pp. 275-285.

Delichatsios, M.M., Mathews, M.K. and Delichatsios, M.A.[1991a], "An upward fire spread and growth simulation", Fire Safety Science-Proc. of the Third International Sym. pp. 207-216.

Delichatsios, M.A., Panagiotou, Th., and Kiley, F.[1991b], "Use of time to ignition data for characterizing the thermal inertia and the minimum(critical) heat flux for ignition or pyrolysis", Combust. Flame, vol. 84, pp. 323-332.

Delichatsios, M. A. and Chen, Y.[1993], "Asymptotic, approximate, and numerical solutions for the heatup and pyrolysis of materials including reradiation losses", Combust. Flame, vol. 92, pp. 292-307.

Delichatsios, M. A. and Chen, Y.[1994], "Flame spread on charring materials: numerical predictions and critical conditions", Fire Safety Science-Proc. of 4th International Sym. pp. 457-468.

Delichatsios, M.M., Wu, P., Delichatsios, M. A., Lougheed, G.D., Crampton, G.P., Qian, C., Ishida, H. and Saito, K.,[1994], "Effect of external radiant heat flux on upward fire spread: measurements on plywood and numerical predictions", Fire Safety Science-Proc. of 4th International Sym. pp. 421-432.

De Ris, J. [1979], "Fire radiation - a review", 17th Sym. (Int.) on Combustion, The Combustion Institute, pp. 1003-1016.

Di Blasi, C.[1993], "Modelling and simulation of combustion processes of charring and noncharring solid fuels", Prog. Energy Combust. Sci., vol. 19, pp. 71-104.

Di Blasi, C.[1994], "Processes of flames spreading over the surface of charring fuels: effects of the solid thickness", Combust. Flame, vol. 97, pp. 225-239.

Drysdale, D.[1985], *An introduction to fire dynamics*, John Wiley (1985).

Fairweather, M., Jones, W.P. and Lindstedt, R.P.[1992], "Predictions of radiative transfer from a turbulent reacting jet in a cross-wind", Combust. Flame, vol. 89, pp: 45-63.

Fernandez-Pello, A.C. and Hirano, T.[1983], "Controlling mechanisms of flame spread", Combustion Sciences and Technology, vol. 32, pp. 1-31.

Fiveland, W.A.[1988], "Three-dimensional radiative heat-transfer solutions by the discrete-ordinates method", J. Thermophysics, vol. 2, pp. 309-316.

Fleischmann, C.M., Pagni, P.J. and Williamson, R.B.[1994], "Quantitative Backdraft Experiments", (ed: T.Kashiwagi), Proceedings Fire Safety Science Fourth International Symposium, 1994, pp 337-348.

Fredlund, B.[1993], "Modelling of heat and mass transfer in wood structures during fire", Fire Safety J., vol. 20, pp. 39-69.

Frenklach, M., Clary, D. W., Gardiner, W. C. and Stein, S. E, "Effect of fuel structure on pathways to soot", 21st Sym. (Int.) on Combustion, pp1067-1076, 1986.

Galea, E.R.[1989], "On the field modelling approach to the simulation of enclosure fires", J. Fire Protection Engng, vol. 1, pp. 11-22.

Galea, E.R. and Markatos, N.C.[1991], "The mathematical modelling and computer simulation of fire development in aircraft", Int.J.Heat Mass Transfer, vol. 34, pp.181-197.

Galea, E.R, Hoffmann, N. and Berhane, D.[1993], "Large-Scale Fire Field Modelling - the Route to General Use via Parallel Processing", Interflam'93, Interscience, pp. 307-319.

Galea, E.R., Berhane, D and Hoffmann, N.A[1996], "CFD Analysis of Fire Plumes Emerging from Windows with External Protrusions in High-Rise Buildings", Proceedings Interflam'96, Compiled by C.Franks and S Grayson, ISBN 0 9516320 9 4, pp. 835-839.

Glassman, I.[1988], "Soot formation in combustion processes", 22nd Sym. (Int.) on Combustion, pp295-311.

Gore, J. P. and Faeth, G. M.[1988], "Structure and radiation properties of luminous turbulent acetylene/air diffusion flames", J. Heat Transfer, vol. 110, pp. 173-181.

Gore, J. P. and Jang, J.H.[1992], "Transient radiation properties of a subgrid scale eddy", J. Heat Transfer, vol.114, pp. 234-242.

Gottuk, D. T., Williams, F.W. and Farley, J. P., "The development and mitigation of backdrafts: a full-scale experimental study", Fire Safety Science- Proc 5th Int Symp, 1997, pp 935—946.

Hadjisophocleous G.V. and Cacambouras M.[1993], "Computer modelling of compartment fires", J. of Fire Prot. Engr., vol. 5 (2), pp. 39-52.

Hägglund, B., Jansson, R. and Onnermark, B.[1974], "Fire development in residential rooms after ignition from nuclear explosions", FOA Report C 20016-D6 (A3), 1974, Forsvarets Forskningsanstalt, Stockholm.

Harwell Laboratory[1994], "CFDS-FLOW3D version 3.3: user manual".

Hoffman, N. and Markatos, N.C.[1988], "Thermal radiation effects on fires in enclosures", Appl. Math. Modelling, vol. 12, pp. 129-140.

Hoffman, N, Galea, E.R. and Markatos, N.C.[1988], "A computer simulation of fire-sprinkler interaction: a two-phase phenomena", 12th IMACS World Congress.

Home Office Statistical Bulletin[1997], "Summary fire statistics United Kingdom 1995", ISSN 0143, 6384.

Honnery, D. R., Tappe, M. and Kent, J. H.[1992], "Two parametric models of soot growth rates in laminar ethylene diffusion flames", Combustion Science and Technology, vol., 83, pp. 305-321.

Hopkins Jr, D. and Quintiere, J. G.[1996], "Material fire properties and predictions for thermoplastics", Fire Safety J., vol. 26, pp. 241-268.

Hottel, H.C. and Sarofim, A.F.[1967], *Radiative transfer*, Mcgraw-Hill, N.Y., 1967.

Howell, J. R.[1968], "Application of Monte Carlo to heat transfer problems", in *Advances in Heat Transfer*, vol. 5, Academic Press, New York, pp. 1-54

Hubbard, G. L. and Tien, C. L.[1978], "Infrared mean absorption coefficients of luminous flames and smoke", J. Heat Transfer, vol. 100, pp. 235-239.

Jia, F., Galea, E. R. and Patel, M. K. and Hoffmann, N.[1995], "Combustion models of turebulent diffusion flames", ISBN 1 899991 08 5, Paper No. 95/IM/09, CMS Press, University of Greenwich.

Jia, F., Galea, E. R. and Patel, M. K.[1997], "The prediction of fire propagation in enclosure fires", Fire Safety Science- Proc 5th Int Symp, 1997, pp 345--354.

Jia, F., Galea, E. R. and Patel, M. K.[1999a], "Simulating "FLASHOVER" and "BACKDRAFT" Type Events Using Fire Field Models - A First Approximation", Journal of Fire Protection Engineering, vol. 9, no. 4, pp. 1-17.

Jia, F., Galea, E. R. and Patel, M. K.[1999b], "The numerical simulation of the non-charring pyrolysis process and fire development within a compartment", Applied Mathematical Modelling, vol. 23, pp. 587-607.

Jia, F., Galea, E. R. and Patel, M. K.[1999c], "Numerical Simulation of the Mass Loss Process in Pyrolizing Char Materials", Fire and Materials, vol. 23, pp. 71-78.

Jia, F., Galea, E. R. and Patel, M. K.[1999d], "The numerical simulation of noncharring thermal degradation and its application to the prediction of compartment fire development", to appear in Fire Safety Science- Proc 6th Int Symp, 1999.

Jia, F., Galea, E. R. and Patel, M. K.[1999e], "The Numerical Simulation of Fire Spread within a Compartment using an Integrated Gas and Solid Phase Combustion Model", J. of Applied Fire Scicences, vol. 8, pp. 291-316.

Jones, W. W.[1984], "Future directions for modelling the spread of fire, smoke, an toxic gases", in Fire Safety: Science and Engineering (ed. T. Z. Harmathy), pp. 70-96

Kanury, M. A.[1972], "Thermal decomposition kinetics of wood pyrolysis", Combustion and Flame, vol. 18, p. 75-83.

Kanury, A. M.[1995], "Flaming ignition of solid fuels", in *The SFPE Handbook of Fire Protection Engineering*, 2nd edition.

Karlsson, B.[1992], "Modeling fire growth on combustible lining materials in enclosures", 992, Report TVBB-1009, Lund University, Department of Fire Safety Engineering, Lund, Sweden, 1992.

Kaplan, C. R., Baek, S. W., Oran, E. S. and Ellzey, J. L.[1994], "Dynamics of a strongly radiating unsteady ethylene jet diffusion flame", Combustion and Flame, vol. 69, pp. 1-21.

Kashiwagi, T. and Ohlemiller, T. J.[1982], "Study of oxygen effects on nonflaming transient gasification of PMMA and PE during thermal irradiation", 19th symposium (international) on combustion, The Combustion Institute, p. 815.

Kashiwagi, T., Ohlemiller, T.J. and Werner, K.[1987], "Effects of external radiant flux and ambient oxygen concentration on nonflaming gasification rates and evolved products of white pine", Combustion and Flame, vol. 69, pp. 331-345.

Kashiwagi, T., Omori, A. and Nanbu, H.[1990], "Effects of melt viscosity and thermal stability on polymer gasification", Combustion and Flame, vol. 81, p. 188.

Kashiwagi, T.[1994], "Polymer combustion and flammability-role of the condensed phase", 25th symposium (international) on combustion, The Combustion Institute, p. 1423.

Kay, J. M. and Nedderman, R. M.[1985], *Fluid mechanics and transfer processes*, Cambridge University Press.

Kenndey, I. M., Kollmann, W. and Chen, J. Y.[1990], "A model for soot formation in a laminar diffusion flame", Combustion and flame, vol. 81, pp. 73-85.

Kent, J. H. and Honnery, D. R.[1987], "Soot and mixture fraction in turbulent diffusion flames", Combustion Science and Technology, vol. 54, pp.383-397.

Kent, J. H. and Honnery, D. R.[1990], "Soot formation rate map for a laminar ethylene diffusion flame", Combustion and Flame, vol. 79, pp. 287-298.

Kerrison, L., Mawhinney, N., Galea, E.R., Hoffmann, N. and Patel, M.K.[1994a], "A comparison of two fire field models with experimental room fire data", Fire Safety Science--Proc 4th Int Symp, pp. 161-172.

Kerrison, L., Galea, E. R., Hoffmann, N. and Patel, M. K.[1994b], "A comparison of a FLOW3D based fire field model with experimental room fire data", Fire Safety J., vol. 23, pp. 387-411.

Kim, B. S., Travelho, J., Jagoda, J. I. and Zonn, B. T.[1984], "Soot formation in an opposed flow polymer diffusion flame", 20th Symposium (Int.) on Combustion, the Combustion Institute, pp. 1113-1120.

Kindelan, M. and Williams, F.A.[1975], "Theory for endothermic gasification of a solid by a constant energy flux", Combust. Sci. Technol., vol. 10, pp. 1-19.

Kumar, S., Gupta, A.K. and Cox, G.[1991], "Effects of Thermal Radiation on the Fluid Dynamics of Compartment Fires", Fire Safety Science- Proc 3rd Int Symp, pp. 345-354.

Kumar, S. and Cox, G.[1985], "Mathematical modelling of fires in road tunnels", 5th Int. Conf. on Aerodynamics and Ventilation of Vehicle Tunnels, p. 61.

Kung, H.[1972], "A mathematical model of wood pyrolysis", Combustion and Flame, vol. 18, pp. 185-195.

Lathrop, K and Carlson, B.[1965], "Discrete-ordinates angular quadrature of the neutron transport equation in (x, y,z) geometry", Los Alamos Scientific Laboratory, Los Alamos, NM, Reports LASL-3186.

Lee, C. K., Chaiken, R. F. and Singer, J. M., "Charring pyrolysis of wood in fires by laser simulation", 16th symposium (international) on combustion, 1976, pp. 1459-1470.

Leung, K. M., Lindstedt, R. P. and Jones, W. P.[1991], "A simplified reaction mechanism for soot formation in nonpremixed flames", Combustion and Flame, pp. 289-305.

Lewis, M. J., Moss, J. B. and Rubini, P. A.[1997], "CFD modelling of combustion and heat transfer in compartment", Fire Safety Science- Proc 5th Int Symp, pp. 463-474.

Linan, A. and Williams, F. A.[1993], *Fundamental aspects of combustion*, Oxford University Press.

Lockwood, F.C. and Shah, N.G.[1981], "A new radiation solution method for incorporation in general combustion prediction procedures", 18th Symposium (Int.) on Combustion, the Combustion Institute, pp.1405-1414.

Lockwood F. C. and Malalasekera M. G.[1988], "Fire computation: the flashover phenomenon", 22nd Symp. (int.) on Combustion, the Combustion Institute, pp. 1319-1328.

Luo, M. and Beck, V.[1996], "Flashover fires in a full scale building: prediction and experiment", Proceedings Interflam'96, Compiled by C.Franks and S Grayson, ISBN 0 9516320 9 4, 1996, pp. 361-370.

Lynch, D.R., and O'neill, K.[1981], "Continuously deforming finite elements for the solution of parabolic problems, with and without phase change", Int. J. Numerical Methods in Engineering, vol. 17, pp. 81-96.

Lyons, J.W.[1985], *Fire*, Scientific American Books, Inc., New York.

Madorsky, S. L.[1964], *Thermal degradation of organic polymers*, Interscience, John Wiley, New York.

Magnussen, B. F. and Hjertager B. H.[1977], "On mathematical modelling of turbulent combustion with special emphasis on soot formation and combustion", 16th Symp. (Int.) on Combustion, the Combustion Institute, pp719-729.

Magnussen B. F., Hjertager B. H., Olsen, J. G. and Bhaduri, D.[1978], "Effects of turbulent structure and local concentrations on soot formation and combustion in C_2H_2 diffusion flames", 17th Sym. (Int.) on Combustion, pp1383-1393.

Markatos, N.C, Malin, M.R and Cox, G.[1982], "Mathematical modelling of buoyancy induced smoke flow in enclosures", Int J heat Mass Transfer, vol. 25, p. 63.

Markatos, N.C. and Cox, G.[1984], "Hydrodynamics and heat transfer in enclosures", Physico-Chem. Hydrody., vol. 5, pp. 53-66.

Meyer, G. H.[1981], "The method of lines and invariant imbedding for elliptic and parabolic free boundary problems", SIAM J. Numer. Anal., vol. 18, pp. 150-164.

McCaffrey B. J., Quintiere, J. G. and Harkleroad, M. F.[1981], "Estimating room temperatures and the likelihood of flashover using fire test data correlations", Fire Technology, vol. 17, pp. 98-119.

Mikkola, E.[1991], "Charring of wood based materials", Fire Safety Science- Proc 3rd Int Symp, pp 547-556 (1991).

Modak, A.T.[1979], "Radiation from products of combustion", Fire Research, vol. 1, pp. 339-361.

Moghtaderi, B., Novozhilov, V., Fletcher, D. and Kent, J. H.[1997], "An integral model for the transient pyrolysis of solid materials", Fire and Materials, vol. 21, p. 7.

Moss, J. B., Stewart, C. D. and Syed, K. J.[1988], "Flowfield modelling of soot formation at elevated pressure", 22th Sym. (Int.) on Combustion, pp. 413-423.

Moss, J. B., Stewart, C. D. and Young, K. J.[1995], "Modelling soot formation and burnout in high temperature laminer diffusion flame burning under oxygen-enriched conditions", Combustion and Flame, vol. 101, pp. 491-500.

Novozhilov, V., Moghtaderi, B., Fletcher, D. F. and Kent, J. H.[1996], "Computational fluid dynamics modelling of wood combustion", Fire Safety J., vol. 27, pp. 69-84.

Opstad, K.[1995], "Modelling of thermal flame spread on solid surfaces in large-scale fires", MTF-Report 1995:114(D), Department of Applied Mechanics, Thermo- and Fluid Dynamics, The Norwegian Institute of Technology, University of Trondheim.

Özişik, M. N.[1980], *Heat conduction*, John Wiley & Sons, Inc., New York.

Patankar, S. V.[1980], *Numerical heat transfer and fluid flow*, McGraw Hill, New York, 1980.

Patera, A.T.[1984], "A finite-element/green's function embedding technique applied to one-dimensional change-of-phase heat transfer", Numerical Heat Transfer, vol. 7, pp. 241-247.

Petrella, R.V.[1979], "The mass burning rate and mass transfer number of selected polymers, wood and organic liquids", Polym. Plast. Technol. Eng., vol. 13, pp. 83-103.

Pivovarov, M., Zhang, H., Ramaker, D., Tatem, P., and Williams, F.[1993], "Similarity solutions in buoyancy-controlled turbulent diffusion flame modelling", Combustion and Flame, vol. 92, pp. 308-319.

Quintiere, J. G., McCaffrey B. J. and Braven, K. D.[1979], "Experimental and theoretical analysis of quasi-steady small-scale enclosure fires", 17th Sym. (Int.) on Combustion, pp. 1125-1137.

Quintiere, J.G, Rinkinen, W.J and Jones, W.W,[1981], "The effect of room openings on fire plume entrainment", Combust. Sci. Tech, vol. 26, pp. 193--201.

Quintiere, J. G.[1992], "A semi-quantitative model for the burning of solid materials", NIST-4840, National Institute of Standards and Technology, June, 1992.

Quintiere, J. G. and Iqbal, N.[1993], "An approximate integral model for the burning rate of a thermoplastic-like material", Fire and Material, vol. 18, pp. 89-98.

Quintiere, J.G., Haynes, G. and Rhodes, B.T.[1995], "Applications of a model to predict flame spread over interior finish materials in a compartment", J. Fire Protection Engineering, vol. 7, pp. 1-13.

Rhodes, B.T.[1994], "Burning rate and flame heat flux for PMMA in the cone calorimeter", NIST-GCR-95-664, National Institute of Standards and Technology, 1994.

Rhodes, B.T. and Quintiere, J.G.[1996], "Burning rate and flame heat flux for PMMA in a cone calorimeter", Fire Safety J., vol. 26, pp. 221-240.

Ritchie, S.J., Steckler, K.D, Hamins, A., Cleary, T.G., Yang, J.C. and Kashiwagi, T.[1997], "The effect of sample size on the heat release rate of charring materials", Fire Safety Science—Proc. of 5th International Symp., pp. 177-188.

Roberts, A. F.[1970], "A review of kinetic data for the pyrolysis of wood and related substances", Combustion and Flame, vol. 14, pp. 261-272.

Rockett, J. A.[1976], "Fire induced gas flow in an enclosure", Combustion Science and Technology, vol. 12, pp. 165-175.

Rubini, P.A.(ed.)[1996], "SOFIE Users Manual", School of Mechanical Engineering, Cranfield University, UK.

Sanders J. P. H. and Lamers, A. P. G. G.[1994], "Modeling and calculation of turbulent lifted diffusion flames", Combustion and Flame, vol. 96, pp.22-33.

Sarofim, A. F.[1986], "Radiative heat transfer in combustion: friend or foe", 21st Sym. (Int.) on Combustion, The Combustion Institute, pp.1-23.

Scott, D. S., Piskorz, J., Bergougnou, M. A., Graham, R., and Overend, R. P.[1988], "Role of temperature in the fast pyrolysis of cellulose and wood", Industrial and Engineering Chemistry Research, vol. 27, pp. 8-15.

Sibulkin, M.[1985], "Heat of gasification for pyrolysis of charring materials", Fire Safety Science—proceeding 1st (Int.) Symp., pp. 391-400.

Simcox, S, Wilkes, N,S and Jones, I.P.[1992], "Computer simulation of the flows of hot gases from the fire at King's Cross Underground Station", Fire Safety J., vol. 18, pp. 49-73.

Spalding, D. B[1971], "Mixing and chemical reaction in steady confined turbulent flames", 13th Symp. (Int.) on Combustion, the Combustion Institute.

Spalding, D. B.[1979], *Combustion and mass transfer*, Pergamon Press.

Spalding, D.B[1981], "A general purpose computer program for multi-dimensional one-and two-phase flow", in Mathematics and Computers in Simulations, North Holland (IMACS), vol. XXIII, p. 267.

Sparrow, E. M. and Cess, R. D.[1978], *Radiation heat transfer*, McGraw-Hill Book Company, New York.

Staggs, J.E.J. and Whiteley, R.H.[1996], "Modelling the combustion of solid-phase fuels in cone calorimeter experiments", Proceedings Interflam'96, Compiled by C.Franks and S Grayson, ISBN 0 9516320 9 4, 1996, pp. 103-112.

Steckler, K.D, Quintiere, J.G and Rinkinen, W.J.[1982], "Flow induced by fire in a compartment", NBSIR 82-2520, National Bureau of Standards.

Stroup, D.W.[1995], "Using field modelling to simulate enclosure fires", in The SFPE Handbook of Fire Protection Engineering, 2nd edition, pp.3-152-3-159.

Tewarson, A. and Pion, R. F.[1976], "Flammability of plastics-I. burning intensity", Combustion and Flame, Vol. 26, pp. 85-103.

Thomas, P.H.[1981], "Testing products and materials for their contribution to flashover in room", Fire and Materials, vol. 5, pp. 103-111.

Tien, C.L., Lee, K.Y. and Stretton, A.J.[1995], "Radiation heat transfer", in the SFPE Handbook of Fire Protection Engineering, 2nd edition, pp. 1-65—1-79.

Tran, H.C.[1992], "Experimental data on wood materials", in Heat Release in Fires(ed. by V. Babrauskas and S. J. Grayson), London Elsevier Applied Science, pp. 357-372.

Tuovinen, H.[1995], Simulation of combustion and fire-induced flows in enclosures, Report Lutvdg(TVBB-1010), Department of Fire Safety Engineering, Lund University, Sweden.

Vovelle, C., Akrich, C. and Delfau, J. L.[1984], "Mass loss rate measurements on solid materials under radiative heating", Combustion Science and Technology, vol. 36, pp. 1-18.

Wang, H. and Fan, W.[1997], "Progress and problems of fire protection in China", Fire Safety J., vol. 28, pp. 191-205.

Waterman, T. E.[1968], "Room flashover--criteria and synthesis", Fire Technology, vol. 4, pp. 25-31.

Williams, F.A.[1976], "Mechanisms of fire spread", 16th symposium (international) on combustion, pp.1281-1294.

Yan, Z. and Holmstedt, G.[1996], "CFD and experimental studies of room fire growth on wall lining materials", Fire Safety J., vol. 27, pp. 201-238.

Yeoh, G. H., Chandrasekaran, V. and Leonardi, E.[1995], "Numerical prediction of fire and smoke", AIRAH Journal, vol. 49, pp.13-18.

Yuen, W. W. and Tien, C. L.[1977], "A simple calculation scheme for the luminous flame emissivity", 16th Sym. (Int.) on Combustion, pp1481-1487.

Zhou, L. and Fernandez-Pello, A.C.[1993], "Turbulent, concurrent, ceiling flame spread: the effect of buoyancy", Combustion and Flame, vol. 92, pp. 45-59.